UNIVERSIDAD COMPLUTENSE DE MADRID
FACULTAD DE CIENCIAS QUÍMICAS
Departamento de Ingeniería Química

TESIS DOCTORAL

Electrospray deposition of superhydrophobic carbon-based layers: Application in proton exchange membrane fuel cells

Depósito de capas superhidrófobas de carbón mediante electrospray: Aplicación en pilas de combustible de membrana protónica

MEMORIA PARA OPTAR AL GRADO DE DOCTOR

PRESENTADA POR

Julio J. Conde López

Directores:

Dra. Paloma Ferreira Aparicio

Dr. Antonio Martínez Chaparro

CIEMAT - Centro de Investigaciones Energéticas, Medioambientales y Tecnológicas

Madrid, 2019

UNIVERSIDAD COMPLUTENSE MADRID

DECLARACIÓN DE AUTORÍA Y ORIGINALIDAD DE LA TESIS PRESENTADA PARA OBTENER EL TÍTULO DE DOCTOR

D./Dña. Julio José Conde López,
estudiante en el Programa de Doctorado en Ingeniería Química,
de la Facultad de Ciencias Químicas de la Universidad Complutense de Madrid, como autor/a de la tesis presentada para la obtención del título de Doctor y titulada:

Electrospray deposition of superhydrophobic carbon-based layers: Application in proton exchange membrane fuel cells

Depósito de capas superhidrófobas de carbón mediante electrospray: Aplicación en pilas de combustible de membrana protónica

y dirigida por: Antonio Martínez Chaparro y Paloma Ferreira Aparicio

DECLARO QUE:

La tesis es una obra original que no infringe los derechos de propiedad intelectual ni los derechos de propiedad industrial u otros, de acuerdo con el ordenamiento jurídico vigente, en particular, la Ley de Propiedad Intelectual (R.D. legislativo 1/1996, de 12 de abril, por el que se aprueba el texto refundido de la Ley de Propiedad Intelectual, modificado por la Ley 2/2019, de 1 de marzo, regularizando, aclarando y armonizando las disposiciones legales vigentes sobre la materia), en particular, las disposiciones referidas al derecho de cita.

Del mismo modo, asumo frente a la Universidad cualquier responsabilidad que pudiera derivarse de la autoría o falta de originalidad del contenido de la tesis presentada de conformidad con el ordenamiento jurídico vigente.

En Madrid, a 2 de septiembre de 2019

Fdo.: _____

Esta DECLARACIÓN DE AUTORÍA Y ORIGINALIDAD debe ser insertada en la primera página de la tesis presentada para la obtención del título de Doctor.

Nom lhe ponhades chatas à obra namentres nom se remata.
O que pense que vai mal que trabalhe nela,
há sitio para todos.
Afonso Daniel R. Castelao

ACKNOWLEDGEMENTS

First and foremost, I would like to express my gratitude to Dr. Antonio Chaparro and Dra. Paloma Ferreira for giving me the opportunity to develop my doctoral thesis in their research group. My most sincere thanks for their continuous support and assistance throughout these years.

I would also like to thank all the persons who participated directly or indirectly on the development of this thesis, especially my fellow colleagues from Fuel Cell group at CIEMAT: Antonia Folgado for her assistance on fuel cell operation experiments, Marco Galarza and David de Rafael for their invaluable technical assistance, and Jose Serrano for his tireless help with electronics and software. Thanks to the rest of the group, especially to my beloved office mates.

Additionally, I want to show my gratitude to Gonzalo de Diego, Susana Merino, Cesar Maffiotte and Carlos Novillo, members of the Microstructural Characterization and Microanalysis Group at CIEMAT, for their help with the microscopic and XPS characterization of the samples. Manuel Benito help with ATR measurements and Andrea Pernas with the electrospray setup drawings are also greatly acknowledged. At a personal level, I am greatly pleased for the bunch of good and kind people I knew during my years at CIEMAT, without much effort, several dozens of people comes to mind.

My most sincere thanks also goes to Adam Weber for allowing me to work at Lawrence Berkeley National Laboratory. Thanks to Anamika Chowdhury and Ahmet Kusoglu for their help in the laboratory and the rest of the group for their warmth welcome in Berkeley.

TABLE OF CONTENTS

ABSTRACT

Fuel cells are electrochemical devices that allow the production of clean, safe and renewable electrical energy. Facing the uncertainty of the upcoming end of the oil era, fuel cells are highly regarded as strong candidates for future portable, transportation and stationary applications. In particular, proton exchange membrane (PEM) fuel cells use hydrogen fuel to produce energy with high efficiency and no greenhouse gasses emission. However, a widespread market deployment is limited by the cost and durability of the components, especially the catalyst layers that requires platinum. To overcome these problems, among other approaches, the use of more efficient methods to prepare PEM fuel cell catalyst layers is studied.

Electrospray is a method of liquid atomization based on the ejection of a solution or suspension under the influence of a strong electric field, without any additional physical force playing a role in the atomization process. It is a suitable technique to fabricate thin films of controlled morphology from colloidal suspensions of catalyst particles ('catalytic inks'), leading to particle monodispersity and homogeneous distribution on the substrate. Film morphology and properties strongly depend on particles disposition and stacking upon arrival to the substrate, so electrospray deposition allows the production of films of excellent quality, reducing the number of voids, flaws and cracks, and ensuring a homogenous thickness throughout the surface of the films. Electrospray is also very appropriate for depositing expensive materials, like platinum-based catalysts, because it allows high deposition efficiency of the target material, with minimal losses compared with regular ink-based methods.

Under an adequate tuning of the ink composition and the electrospray experimental conditions, the aerosol of charged particles produced by electrospray can achieve complete solvent evaporation, and thus producing a dry deposit on the substrate solely controlled by electrostatic interactions. The application of electrospray to the fabrication

of catalyst layers for PEM fuel cells is attracting a great deal of interest in the last years, but numerous issues about their structure and properties are still open questions. The layers depart from suspensions of the catalyst particles and an ionomer that are deposited on the gas diffusion layer or on the proton exchange membrane. This technique provides additional advantages for membrane deposition because of the absence of solvent reaching the substrate avoids membrane damage with ink organic solvents. The resulting layers present highly porous and dendritic morphologies with superhydrophobic surfaces and better ionomer distribution than other conventional methods, deduced from the halved ionomer content to achieve optimal performance. As a result of these special characteristics, PEM fuel cells with cathodic electrosprayed layers show improved performance with respect to conventional layers, especially under high current densities, leading to peak power densities 20 % larger.

The main objective of the research work compiled in this thesis is to gain a deeper knowledge on the electrospray deposition process of carbon black-based inks and its applications to PEM fuel cell technology. Within the main objective, three main secondary objectives were set in the study: the investigation of the origin of the special of electrosprayed carbon black-Nafion films, the analysis of mass transport and water distribution of electrosprayed catalyst layers, and the use of the superhydrophobic carbon black-Nafion films as corrosion protection for metallic components.

The dissertation is organized in five chapters. In the first chapter, the fundamentals of PEM fuel cell and fabrication of catalytic layers, including the state-of-the-art of electrospray application to PEM fuel cells is reviewed, and the scope of this study is detailed. The experimental work, the results and their discussion have been compiled in three next chapters. One of them (Chapter 2) is focused to analyze the exact nature of the enhanced properties of the electrosprayed carbon-based layers compared to regular methods by means of a fundamental study with carbon layers. The mass-transport properties and the effect on water distribution of electrosprayed catalyst layers in PEM fuel cells have been thoroughly investigated in Chapter 3. Additionally, the passive control of water distribution by means of hydrophobicity gradients inside the cell is

studied. The fourth chapter, on the other hand, is devoted to the application of the superhydrophobic character of electrosprayed layers as corrosion-protection coating for metallic surfaces, such as those in flow field plates or current collectors in fuel cells. Finally, the central conclusions of the work are compiled in the fifth and final chapter.

The studies conducted in this thesis have resulted in major advances not only on the knowledge of the effect of electrosprayed layers in PEM fuel cells, but on a deeper understanding of Nafion-carbon black interactions and the effect of hydrophobicity inside the porous structure of a PEM fuel cell. The fundamental study on carbon-based layers (Chapter 2) has revealed a strong and stable interaction between the sulfonic groups of the Nafion and the carbon black surface, which is probably the result of the fast desolvation of the adsorbed ionomer during the ionization process. This interaction favors a better coverage of the carbon surface with the polymer chains and leads to a particular arrangement of the Nafion with fluorocarbon backbones oriented towards the outer part of the aggregates. Electrosprayed layers in the cathode of a PEM fuel cell have been found to enhance the back diffusion of water from the cathode to the anode, due to the superhydrophobic character of the electrosprayed layer, which gives rise to operation under lower saturation conditions and lower water permeability compared with conventional layers (Chapter 3). The transport properties of electrosprayed catalyst layers have revealed an unprecedented reduction of mass-transport problems at low loadings. The water-uptake capability of the electrosprayed layers is enhanced due to the particular morphology and distribution of the ionomer phase. The enhanced water-vapor uptake of electrosprayed layers combined with their very low wettability and superhydrophobic character, allow for an optimal catalyst layer with low mass transport resistance and high ionic conductivity. On top of that, electrosprayed carbon-based superhydrophobic layers application as protective coatings on metal surfaces has been found to be resistant to corrosion in acidic mediums, opening the possibility to use them as coatings in some metallic fuel cell components (Chapter 4).

RESUMEN

Las pilas de combustible son dispositivos electroquímicos que permiten una producción de energía eléctrica limpia, renovable y de forma segura. La incertidumbre que provoca el inminente fin de la era del petróleo, hace que las pilas de combustible sean consideradas como firmes candidatas para ser utilizadas en aplicaciones portátiles, estacionarias o de transporte. En particular, las pilas de combustible de membrana protónica emplean hidrógeno como combustible para producir energía eléctrica con una gran eficiencia de conversión sin producir gases de efecto invernadero. Sin embargo, la penetración de esta tecnología en el mercado está limitada por el coste y la durabilidad de sus componentes, especialmente de los catalizadores, dado que se fabrican utilizando platino. Actualmente, para superar estas limitaciones, la investigación en pilas de combustible se centra, entre otras soluciones, en el uso de métodos más eficientes para la preparación de capas de catalizador.

El *electrospray* es un método de atomización de líquidos que se basa en la eyección de una disolución (o suspensión) bajo la influencia de un campo eléctrico, sin que ninguna otra fuerza participe en el proceso de atomización, siendo adecuada para fabricar capas delgadas de morfología controlada a partir de suspensiones coloidales de catalizador. Las propiedades y la morfología de las capas dependen fundamentalmente de la disposición de las partículas y de su ordenamiento al llegar al sustrato, por lo que el *electrospray* permite la fabricación de láminas de gran calidad, espesor homogéneo y bajo número de defectos. Además, es una técnica especialmente apropiada para materiales de alto coste ya que el proceso de depósito tiene una alta eficiencia, con pérdidas mínimas de material en comparación otros métodos.

Con una correcta optimización de la tinta catalítica, el *electrospray* es capaz evaporar todo el disolvente de la tinta antes de llegar al sustrato para producir depósitos en seco, que tendrán una morfología controlada únicamente por interacción electrostática. El uso del *electrospray* en la fabricación de capas de catalizador para pilas de membrana

protónica está despertando un interés creciente en las últimas décadas, sin embargo, aún existen muchas cuestiones sin resolver sobre su estructura y su efecto en la operación de las pilas. Aunque mediante esta técnica las capas catalíticas se pueden depositar tanto sobre la membrana como sobre la capa difusora de gases, la mayor ventaja se obtiene al depositar sobre la membrana, ya que la eliminación del solvente antes de llegar a la membrana evita que los disolventes orgánicos puedan dañar la estructura de esta. Las capas catalíticas producidas por *electrospray* presentan morfologías dendríticas de gran porosidad y superficies superhidrófobas, así como una mejor distribución del ionómero sobre la superficie del catalizador. Debido a estas características tan particulares, las pilas de combustible con electrodos fabricados con *electrospray* en el cátodo han mostrado una mejora de hasta un 20 % en la densidad de potencia máxima en comparación con otros métodos de depósito.

El objetivo principal de la investigación recogida en esta tesis comprende el estudio del proceso de depósito de tintas catalíticas de negro de carbón mediante *electrospray* y sus aplicaciones en pilas de membrana polimérica. Para alcanzar el objetivo principal, se platean tres objetivos secundarios: el estudio del origen de las propiedades características de las láminas de *electrospray* utilizando tintas de negro de carbón y Nafion, el estudio de las propiedades de transferencia de materia y transporte de agua de capas catalíticas preparadas mediante *electrospray* en pilas de combustible de membrana polimérica y el uso de las capas superhidrófobas de *composite* de negro de carbón y Nafion como barrera protectora contra la corrosión en sustratos metálicos. La tesis está divida en cinco capítulos que incluyen introducción, resultados, discusión y conclusiones. En el primer capítulo se presentan los aspectos fundamentales de las pilas de combustible de membrana polimérica junto con una revisión del estado del arte de la fabricación de electrodos centrada en el uso de la técnica de *electrospray*. Los resultados experimentales obtenidos se presentan en los tres siguientes capítulos uniendo las descripciones de los montajes experimentales y técnicas utilizadas, junto con los resultados y su discusión correspondiente. El primero de ellos, el Capítulo 2, se centra en el estudio del origen de las propiedades de las capas de carbón fabricadas mediante el uso de *electrospray* mediante un análisis fundamental de sus propiedades físicas y químicas. El Capítulo 3 se

centra en el análisis de las propiedades de transporte de masa y en el efecto sobre la distribución de agua provocado por el uso de capas de catalizador fabricadas mediante *electrospray*, además de analizar la posibilidad de controlar los flujos de agua de forma pasiva utilizando componentes con diferentes grados de hidrofobicidad. El Capítulo 4 se centra en la aplicación de las películas superhidrófobas de carbón para proteger superficies metálicas dentro de la pila, especialmente en placas difusoras de gases. Por último, en el Capítulo 5 se presentan las conclusiones globales del trabajo.

Los resultados recogidos en esta tesis han desembocado en importantes avances en el conocimiento de los efectos de las capas de catalizador fabricadas mediante *electrospray* en pilas de combustible de membrana polimérica, así como en las interacciones que provoca entre el negro de carbón y el Nafion. El estudio fundamental de las capas de carbón (Capítulo 2) revela una fuerte interacción entre los grupos sulfónicos del Nafion y la superficie del negro de carbón, probablemente causada por la rápida evaporación del disolvente durante el proceso de ionización, favoreciendo así una mejor distribución del Nafion sobre la superficie del carbón y orientando las cadenas fluorocarbonadas del Nafion hacia el exterior de los agregados. Las capas de *electrospray* en el cátodo de una pila de membrana polimérica han resultado en un aumento de la retrodifusión de agua desde el cátodo al ánodo de las pilas, debido al carácter superhidrófobo de las capas y que resultan en cátodos con menor permeabilidad y saturación de agua (Capítulo 3). El estudio de las propiedades de transporte de las capas de catalizador ha mostrado una gran reducción de las limitaciones de trasporte de masa a bajas cargas de catalizador, así como una mejora en la capacidad de absorción de agua de los catalizadores. El aumento de la capacidad de absorción de agua unida a la superhidrofobidad de las capas de catalizador, resulta en una capa de catalizador con condiciones óptimas de conductividad térmica y resistencia al transporte de masa. Adicionalmente, las capas superdrofóbicas de carbón fabricadas mediante *electrospray*, han demostrado ser resistentes a la corrosión en medio ácido (Capítulo 4), abriendo la posibilidad de ser utilizadas para proteger la superficie de componentes metálicos en el interior de las pilas de combustible.

CHAPTER 1
Introduction

The energy system of the industrialized countries since the industrial revolution has been based on the combustion of fossil fuels, such as coal, natural gas and oil. The global capitalist economy is based on mass production of goods using the cheap energy obtained from fossil fuels, but the economic and technological progress in the 20th century was made completely ignoring that fossil fuels are a finite resource, limited to a few areas of the world, and which massive use brings severe environmental problems. The massive consumption of fossil fuels for combustion is dramatically decreasing oil reservoirs and causing a severe increase of greenhouse gas emissions [1] and health problems [2]. Most of the scientific community agree that a large-scale climate change is under way as a result of human activities, and more specifically, because of the growing carbon emissions to the atmosphere [3]. Another concerning issue of the usage of fossil fuels as energy carriers is that carbon-containing materials are the raw material for the production of many essential ingredients for the chemical, such as syngas, aromatics and olefins; and pharmaceutical industries. However, more than 90 % of the extracted crude oil is used for energy purposes [4].

Fortunately, in the last part of the 20th century, the scientific community managed to raise awareness of the potential problems caused by greenhouse emissions due to the usage of fuel fossils. At the Paris climate conference (COP21) in December 2015, 195 countries adopted a binding global climate deal, in which the global community agreed to limit global warming to below 2 °C relative to pre-industrial levels and to pursue further efforts for limiting temperature increase to below 1.5 °C [5]. According to the International Energy Agency, this goal will only be achieved reducing CO_2 emissions by an 80 % accompanied with a profound transformation of the energy sector [6]. The

European Union is already taking actions through the '20-20-20' climate and energy targets, which aims for the 20 % reduction of greenhouse emissions [7], the achievement of a 20 % of the total energy production by renewable sources [8] and a 20 % improvement in energetic efficiency [9] by the year 2020.

The environmental problems caused by the energy sector can only be addressed by the use of non-fossil energy generation technologies to achieve more efficient and environmental friendly energy production, the so-called renewable energies. Renewable energies are defined as primary, domestic and clean or inexhaustible energy resources, such as biomass, hydropower, geothermal, solar, wind and marine energies [10]. However, one of their major drawbacks is the availability of a proper energy storage system to equalize production and demand, and storing large quantities of energy of exceedingly produced electricity by the renewable sources.

Energy storage is also a complex problem and there is not a universal solution for it. Electrical energy storage can be segmented in two different groups: small-scale (batteries and capacitors) and large-scale storage (pumped hydro, compressed air and chemical) [11]. Among the chemical storage systems, hydrogen is one of the most promising energy vectors. Although internal combustion engines can be adapted to run with hydrogen fuel, one of the most interesting features about hydrogen is that it can be directly transformed to electrical energy in fuel cells. Nowadays, most of the hydrogen is produced by steam reforming of natural gas and other fossil fuels [12], but the goal is to make the hydrogen a ‘clean’ energy vector, absorbing the excess energy produced by renewable sources for its production using water electrolysis.

Fuel cells can close this clean energy cycle by transforming back the hydrogen in electrical energy with a high efficiency and without producing greenhouse emissions. Another major advantage of fuel cells is their versatility, since the applications of fuel cell technology ranges from large stationary production to transportation and portable applications [13].

1.1 General aspects of fuel cells

Fuel cells convert the chemical energy stored in the fuel, generally hydrogen, to electrical energy by means of an electrochemical reaction. Most of the cells use hydrogen as fuel, but also hydrocarbons (mainly methane) or alcohols (mainly methanol) can be used in some types of cells. The ability of converting chemical energy directly to electrical energy is one of the most attractive characteristics of fuel cells, which are able to achieve much higher conversion efficiencies than any existing thermo-mechanical system [14].

A fuel cell can be imagined as a generator that obtains electricity and heat due to the electrochemical reaction combining a fuel with an oxidant gas, i.e. oxygen from the air. Fuel cells consist of two electrodes, anode and cathode, separated by an ion conducting electrolyte. Several types of ion-conducting electrolytes can be used depending on the type of the fuel cell. Figure 1-1 presents a basic scheme of the fuel cell components and feed gases with different electrolytes (The electrolytes used in the different fuel cells will be briefly discussed in Section 1.1.1).

To visualize the reactions inside a fuel cell, one of the simplest electrolytes is an aqueous acid. The overall electrochemical reaction between hydrogen and oxygen to produce electricity is the following [15]:

$$2H_2 + O_2 \rightarrow 2H_2O \qquad (1.1)$$

At the anode, hydrogen is oxidized to produce protons and electrons:

$$2H_2 \rightarrow 4H^+ + 4e^- \qquad (1.2)$$

At the cathode, the protons, which migrate through the acid electrolyte, combine with oxygen along with electrons transported through an external circuit from the anode to the cathode to produce water:

$$O_2 + 4e^- + 4H^+ \rightarrow 2H_2O \quad (1.3)$$

The electrons transported through this external circuit convey a direct electric current that can be used to power an electrical application. When using other types of electrolytes, analogous reactions are occurring with different mobile ions [2].

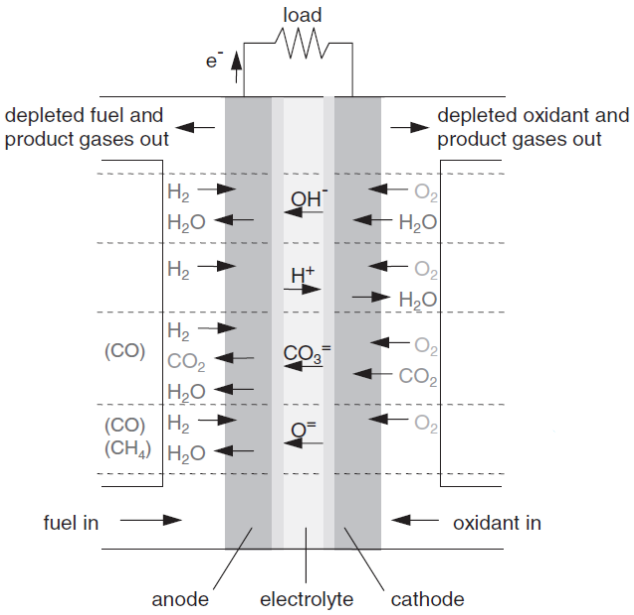

Figure 1-1: Schematic of a fuel cell with different electrolytes. Reprinted from reference 16 with permission from Elsevier, © 2011

Fuel cell systems present many advantages compared to internal combustion generators, namely [16]:

- **Reduction of conversion steps**: A traditional process of electricity generation includes several steps, such as fuel combustion of the fuel, generation of steam, production of mechanical energy with the steam and conversion to electrical energy. Instead, fuel cells can transform the fuel into electrical energy in a single step.

- **Zero emissions**: The inner reactions of the cell only produce water as by-product if hydrogen is supplied as a fuel.

- **High efficiency**: A combustion-based power plant usually generates electricity at efficiencies around 35 percent, while fuel cell systems can generate electricity at efficiencies up to 60 percent and can even be higher with cogeneration systems.

- **Wide range of applications**: They can be used for stationary applications, such as for backup power, power for remote locations, distributed power generation, and cogeneration. Fuel cells can also be used in substitution of batteries in any hand-held device or in transportation vehicles for personal mobility, trucks or buses.

- **Modular design**: Fuel cells systems are easily scalable since the cells can be connected in stacks in series to provide any required voltage.

- **No moving parts**: Mechanical vibration and noise can be avoided.

1.1.1 Types of fuel cells

Fuel cells can be classified using different criteria, such as the type of electrolyte, the conduction ions or the operating temperature. Based on the type of electrolyte, the most studied and most viable types of fuel cells are presented in Table 1-1:

Table 1-1: Summary of the different types of fuel cells. Reprinted from reference 15 with permission from John Wiley and Sons, © 2013

Fuel cell type	Mobile ion	Operating temperature	Applications and notes
Alkaline (AFC)	OH^-	50-200 °C	Used in space vehicles, e.g. Apollo, Shuttle.
Proton Exchange Membrane (PEMFC)	H_3O^+	30-100 °C	Vehicle and mobile applications, and for lower power CHP systems.
Direct Methanol (DMFC)	H_3O^+	20-90 °C	Suitable for portable electronic systems of low power, running for long times.
Phosphoric Acid (PAFC)	H_3O^+	≈ 220 °C	Large numbers of 200-kW CHP systems in use.
Molten Carbonate (MCFC)	CO_3^{2-}	≈ 650 °C	Suitable for medium- to large scale CHP systems, up to MW capacity.
Solid Oxide (SOFC)	O^{2-}	500-1000 °C	Suitable for all sizes of CHP systems, 2kW to multi-MW.

Proton exchange membrane (PEM) fuel cells have a solid electrolyte in which protons are mobile, so the chemistry is similar to the aqueous acid electrolyte. These cells run at low temperature and use a platinum-based catalyst. They are one of the simplest cells because of the use of a solid electrolyte. However, the hydrogen feed requires a high level of purity to avoid catalyst poisoning. With some modifications, PEM fuel cells can admit liquid methanol as supply, such cells are known as **direct methanol fuel cells**. Though these cells have low power outputs, they can be useful for a number of applications.

Alkaline fuel cells have a liquid alkali aqueous solution as electrolyte, generally 30 % KOH. They also run at low temperatures and use platinum based catalysts. Oxygen reduction takes place at a faster rate and less potential losses, but it requires high purity in supplies, especially with no CO_2 impurities to avoid the formation of carbonates.

Phosphoric acid fuel cells are run at a slightly higher temperature, around 200 °C, and use aqueous acid electrolyte. Platinum catalyst is also used, but these cells have higher resistance to impurities, except for sulfur compounds. Polibenzimidazole doped with phosphoric acid is being widely studied for medium-temperature fuel cells.

Solid oxide fuel cells operate at high temperatures, in the region from 600 to 1000 °C. Using these high temperatures, no noble catalysts are needed to improve the reaction kinetics, so cheaper catalysts are used. These cells use ceramic catalysts made of yttria stabilized zirconia in which the anion O^{2-} is mobile. The design of the cells is quite simple but the ceramic materials are difficult to handle and expensive for manufacturing. It is a quite interesting cell since natural gas can be used directly, because internal reforming of the fuel can take place inside the cell.

Molten carbonate fuel cells are run at high temperatures, over 650 °C, with a molten (liquid) mixture of lithium, potassium and sodium carbonates, in which the carbonate ion is transported through the electrolyte. Inexpensive catalysts, such as those based in nickel, can be used due to the high operation temperatures. Like in the solid oxide cells,

natural gas or even synthesis gas can be used as fuel directly without an external reformer. However, the molten carbonate electrolyte is highly corrosive.

1.1.2 Historical review of fuel cell development

In 1800, Anthony Carlisle and William Nicholson, discovered water electrolysis and were considered the first scientists to produce a chemical reaction by using electrical energy [17]. Later, in 1838, William Grove demonstrated the inverse process, by immersing two platinum electrodes in a solution of sulphuric acid and in contact with oxygen and hydrogen, current was found to be flowing between the electrodes [18]. Figure 1-2 shows a simplified sketch of the Grove's experiment, in which oxygen and hydrogen were produced by electrolysis, and later spontaneously recombined as the water level rose in both tubes as the current flowed. He also created the so-called *gas battery*, i.e. the first fuel cell, by combining pairs of electrodes connected in series to produce higher voltages.

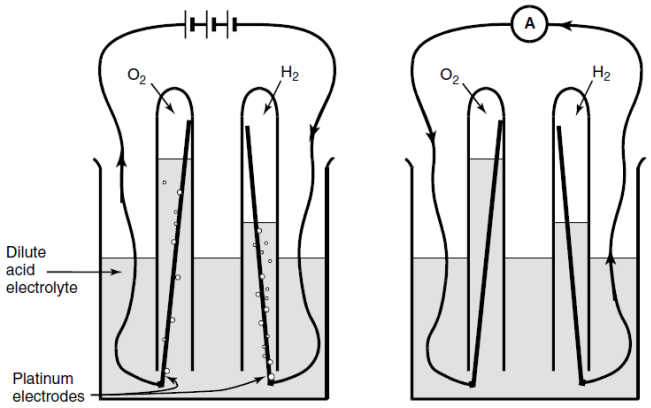

Figure 1-2: Simplified setup of Grove's experiments. Electrolysis process (left) and recombination of the produced hydrogen and oxygen (right). Reprinted from reference 15 with permission from John Wiley and Sons, © 2013

Grove realized himself that the highest area of contact between the electrolyte, the gaseous reagent and the electrocatalytic conductor, was crucial for actual practical use of his device. Trying to acquire this optimized reaction surface has remained the basis of fuel cell research and development ever since. In 1889, *fuel cell* name was actually

coined by Ludwig Mond and his assistant Carl Langer, which made the first fuel cell with three dimensional electrodes. They made a porous electrode structure, and rotated it by 90°, setting all the features of the modern fuel cells [19]. However, the porous electrodes had internal flooding problems, reducing the internal volume open to the gaseous reagent over time. Less than a decade later, in 1893, Friedrich Wilhelm Ostwald experimentally determined the interconnection of various components of a fuel cell: electrodes, electrolyte, oxidizing and reducing agents, anions and cations, giving a theoretical background to the processes observed by Grove [17]. Back then, Ostwald already pointed out to the huge energy loss of energy of the internal combustion engines compared to the electrochemical processes when transforming fossil fuels [19].

In 1896, William Jacques developed the first fuel cell with higher energy outputs (100 $mA \cdot cm^{-2}$ at 1 V) and increasing the durability from hours to months, using molted sodium hydroxide [20]. In 1900, Walther Nernst, first used zirconia as solid electrolyte. The first molten carbonate fuel cell was built by Emil Baur in 1921 using porous asymmetric electrodes to prevent liquid flooding. Baur and his group in ETH (Zürich) also studied zirconia-yttria and zirconia-ceria electrolytes and are considered pioneers in both solid oxide and molten carbonate fuel cells [21].

In England, Thomas Francis Bacon used activated nickel electrodes with an aqueous potassium hydroxide electrolyte and presented the results in 1939. After two decades of research, he ultimately presented a 5 kW alkaline fuel cell device with 60 % efficiency in 1959 [17, 22]. Meanwhile, in Germany, Justi and Winsel invented the *double-skeleton catalyst electrode* (DSK) with a bimodal porous structure [23], on which Siemens future technological fuel cell advances were based. Bacon continued to work in fuel cells up to the early 1960s when Pratt and Whitney Division of United Aircraft Corporation (now United Technologies Corporation) licensed his patents. Bacon's cell, as modified by Pratt and Whitney was the on-board power system for the Apollo lunar missions [19].

The polymer electrolyte fuel cell was invented by Thomas Grubb, a chemist who worked for General Electric (GE) Company in 1955 [24], using a membrane made of ion

exchange sulphonated polystyrene as an electrolyte. Leonard Niedrach, another worker of GE, further improved the cell by using platinum as a catalyst on the membranes [25]. The cell designed by Grubb and Niedrach was first used by NASA in the Gemini space mission in 1962. During this decade, this type of cells further improved by the discovery of Nafion. DuPont developed its perfluorosulfonic-acid membranes in the early 1960s and it was first used as electrolyte in fuel cells in 1966. A dramatic reduction in catalyst loadings also was achieved using perfluorinated ionomers in liquid form (dissolved in alcohol) to impregnate the electrodes, resulting in a higher electrochemical area [24].

In the 1960s the introduction of Teflon in fuel cells is also an important milestone for the improvement of acid (both liquid and solid) electrolyte [19]. The use of Teflon also made possible the development of the phosphoric acid fuel cells. In 1961, Elmore and Tanner published an article describing a cell using an electrolyte that was 35 % phosphoric acid and 65 % silica powder pasted into a Teflon gasket and non-wetting electrodes ‘by the use of Teflon’ [26].

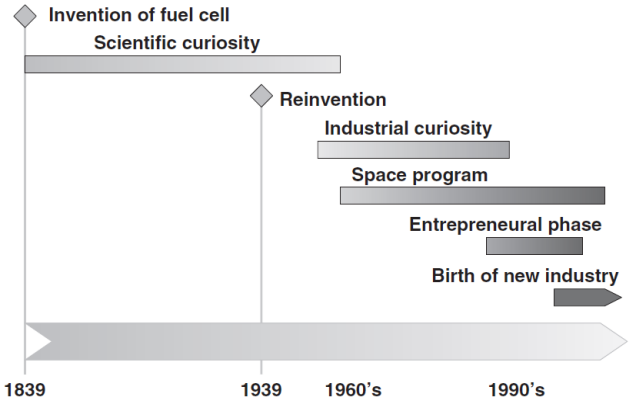

Figure 1-3: Simplified fuel cell history timeline. Reprinted from reference 16 with permission from Elsevier, © 2011

A simplified timeline of fuel cell development is shown in Figure 1-3. During the last fifty years the fuel cells have continued to get refined in many aspects, especially in the improvement of the catalyst (cost reduction and improvement of electrochemical area) and the increment of performance and lifetimes. Among them, PEM fuel cells were on

the main focus of research institutions and technological companies since its invention. Although PEM fuel cells continued to be used on a continuous basis until the present day in space ships, it was not until the 1990s when practical applications outside the space industry use started to surface. Perry Technologies together with Ballard successfully demonstrated a PEMFC-powered submarine in 1989. A few years later, in 1993, Ballard demonstrated fuel cell-powered buses and Energy Partners presented the first passenger car with a PEMFC-based engine [16]. Nowadays, PEMFC is the leading type of fuel cell in terms of industrial production. In 2016, of the 800 MW total fuel cell power deployed, two-thirds corresponded to PEM fuel cells [27]. Thus, the development of PEMFCs is currently an active area of research for stationary power generation, transportation applications, and as an alternative for batteries in portable electronics.

1.2 Proton exchange membrane fuel cells

Proton exchange fuel cells are characterized for the use of an ion exchange membrane as the electrolyte in which the mobile ion is H_3O^+, so the reactions occurring in the cell are essentially the same as for the acid electrolyte fuel cell. A standard PEM single cell (see Figure 1-4) consists of a protonic membrane separating two symmetrical chambers, the anode and the cathode, each one having a catalytic layer (CL), a gas diffusion layer (GDL) and a plate with mechanized gas channels. The anode-electrolyte-cathode assembly is usually called membrane-electrode assembly (MEA). It is also necessary to use gaskets to make the cells gas-tight, and, depending on the application, other auxiliary components such as cooling, forced convection or gas humidification systems.

The presence of a solid electrolyte eliminates the corrosive fluid hazards of other types of cells and also allows the cell to work in any orientation. However, the polymeric membrane must be hydrated to ensure proper ion conductivity, so water management is critical for efficient performance. The requirement of water imposes a temperature limitation on cell operation, usually below 80 °C, forcing the presence of platinum, a high activity electrocatalyst to ensure proper conversion kinetics at low temperatures.

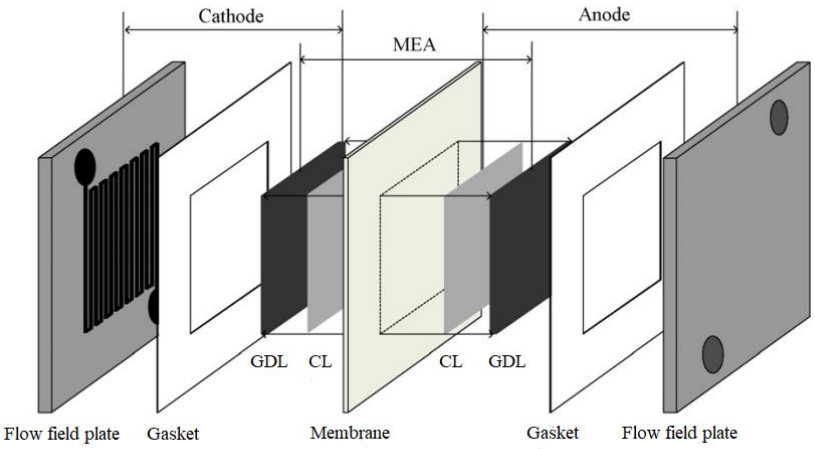

Figure 1-4: Simplified schematic of a proton exchange membrane fuel cell. Reprinted from reference 28 with permission from Elsevier, © 2010

Low working temperatures, allow a quick start and the thinness of the MEAs permits the fabrication compact fuel cells, making PEM fuel cell suitable for small stationary applications, transportation and also portable applications. However, low operation temperatures require high purity hydrogen, as the electrodes are easily poisoned by even trace levels of CO, sulfur species, and halogens [29].

All things considered, PEM fuel cells remain as one of the most promising candidates to be used as the main power sources in transportation [30] and portable applications [31] due to their high power density, easy scale up and low operation temperature.

1.2.1 Components

Electrolyte

The proton exchange membrane plays a fundamental role by transporting protons from anode to cathode and separating the oxidizing and reducing environments in the fuel cell. The essential requirements for a PEM fuel cell membrane are the impermeability to the feed gases and high protonic conductivity together with low electronic conductivity. The most common and well established solid polymer used in fuel cells is Nafion, which is a polyperfluorosulfonic acid (PFSA). Nafion is obtained in the copolymerization of

perfluorovinyl ether with a terminal $–SO_2F$ group and tetrafluoroethylene [32] and is often labeled as an ionomer, since according to IUPAC definition, an ionomer is a macromolecule in which a small but significant proportion of the constitutional units have ionizable or ionic groups, or both [33]. The chemical structure of Nafion, depicted in Figure 1-5, consists of a polytetrafluoroethylene backbone and regular spaced long perfluorovinyl ether pendant side chains terminated by a sulfonate ionic group [34].

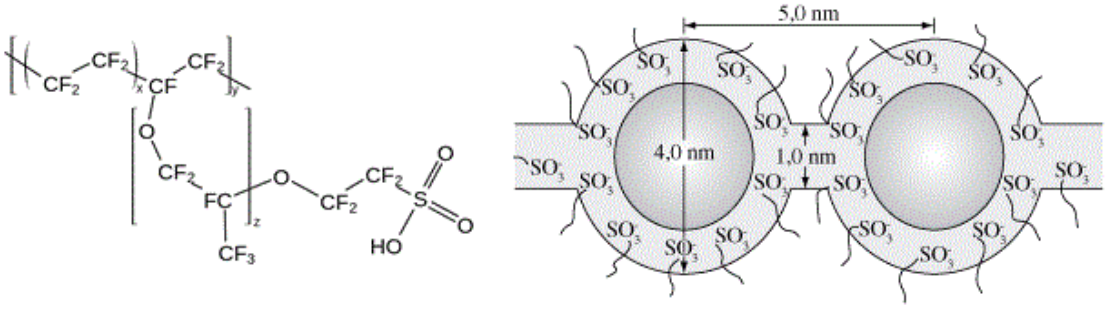

Figure 1-5 Chemical structure of Nafion (left) and cluster-network model for hydrated Nafion (right). Reprinted from reference 35 with permission from Elsevier, © 1983

The ion-conducting properties of the Nafion membranes are attributable to a structure that consists of a hydrophobic fluorocarbon, Teflon-like, backbone with side chains terminating in $-SO_3H$ groups. In the presence of water or other polar solvents, these sulfonic acid groups dissociate, protonating the solvent molecules and forming a hydrophilic phase [36]. The first model proposed for this behavior is the cluster-network model, shown in Figure 1-5, in which the sulfonate groups form into spherical inverted micelles clusters with 5 nm spacing upon hydration [35, 37]. Since then, several other models have been proposed [36], but probably the most accepted is the Gebel model, in which the structural evolution of Nafion is described depending on the water content, observing an inversion of the structure from a reverse micellar structure to a connected network of polymer rod-like particles for a water content larger than 50 % by volume [38].

The exact molecular weight of the Nafion is difficult to determine and is estimated to be between 10^5 and 10^6 Da [39]. Instead, Nafion is described by its equivalent weight and

membrane thickness. Equivalent weight (EW) is the ratio of the number of grams of polymer per mole of sulfonic acid groups of the material in the acid form and completely dry. Polymer mechanical properties are increased with higher EW ratios and proton conductivity is increased with lower EW ratio. The most common Nafion used in PEM fuel cell systems is 1100 EW since it has a reasonable balance of proton conductivity and mechanical integrity [40].

Catalyst layer

Platinum is the preferred electrocatalyst for PEM fuel cells due to its high activity at low operation temperatures and good stability. Platinum is used in both anode and cathode, but the most demanding challenge for the electrodes is the oxygen reduction reaction (ORR), which causes 70 % of the total overpotential losses [41], thus requiring a higher load of cathode catalyst. Up to this time, there are no other viable choices to substitute the platinum catalyst, even though there has been plenty of research on other types of metallic [42] and metal-organic frameworks electrocatalysts [43]. Platinum alloys have also been extensively studied to improve the catalyst activity, corrosion resistance and poisoning resistance of the platinum [44]. However, current platinum catalysts are far from perfect, since they suffer from oxidation, catalyst migration, loss of electrode active surface area, membrane degradation and corrosion of the carbon support [45].

PEM fuel cells catalyst layers are generally made of nanostructured platinum particles supported on high surface area carbon black and Nafion ionomer as a binder. This electrode configuration results in a three-phase interface, as shown in Figure 1-6, in which the ion conducting polymer electrolyte phase is in contact with the electronic phase and the reactants in gaseous phase. This interface comprises reactants in gas, solid and ionomer phase that, despite of being hydrated, behaves different from that of aqueous electrolytes and, although it has been a subject of great study, there is still little knowledge about the true nature of these interfaces [46].

The catalyst layers can be deposited either on top of the gas diffusion layer or directly onto the polymer membrane. In either case, catalyst particles should be next to the membrane to be connected on the ionic conductor level to provide a passage for the protons to be transported in or out [47]. An effective electrode should correctly balance three different transport properties: (i) proton migration between the catalyst and the membrane, (ii) the electron movement from or to the gas diffusion layer and (iii) reactant and product gas diffusion to and from the catalyst layer and the gas channels [48].

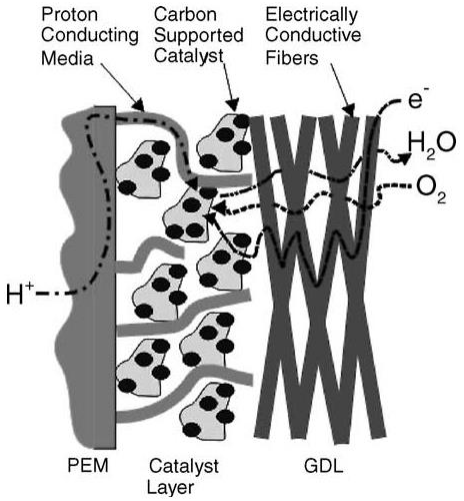

Figure 1-6: Schematic of the three-phase interface in the cathodic catalyst layer. Reprinted from reference 48 with permission from Elsevier, © 2004

Since electrochemical reactions are heterogeneous processes occurring at the interface between an electrode and an electrolyte, the catalytic active surface area will depend on the dispersion and the platinum particle size. In terms of mass activity, it has been found that platinum particles in the range from 2 to 4 nm provide the best performance [49]. The carbon support does not only fulfill the mission to disperse the catalyst particles, but also provides good electronic conductivity to enable the extraction of high current densities from the fuel cell. In the first stages of fuel cell development, catalyst loading was typically around 28 $mg \cdot cm^{-2}$ of platinum in the MEA. In recent years, the control of platinum particle size and dispersion, has allowed to reduce the catalyst loading to approximately 0.2 $mg \cdot cm^{-2}$ in the fuel cell [15].

Gas diffusion layer

The gas diffusion layers (GDLs) are not only used to homogenize the diffusion of the gas to the electrode, but to channel product water away from the electrodes while making a good electrical connection between the catalyst and the flow field plate. The GDLs are made of macroporous carbon-based materials, such as woven carbon cloth, carbon paper, carbon felt, or carbon foam. Although metals have been also studied as GDL material, carbon is widely used because of its chemical stability in acid environment, high gas permeability, good electronic conductivity and elasticity upon compression [50].

An optimization of the thickness of GDLs has to be achieved in order to ensure a proper performance. Whereas thinner layers are beneficial due to low gas diffusion losses, reducing it too much may cause mass transfer limitations, an increased contact resistance and weakness in mechanical properties [51]. The optimization of morphology and pore size is also essential to avoid water accumulation that causes mass transfer limitations. Mean pore sizes above 60 μm have been found to have a negative effect on cell performance due to water condensation [51]. Hydrophobic treatments, usually with PTFE, are also applied to the carbon materials to control the wettability of the GDL in order to ensure an effective removal of the water saturated in the cathode [52, 53].

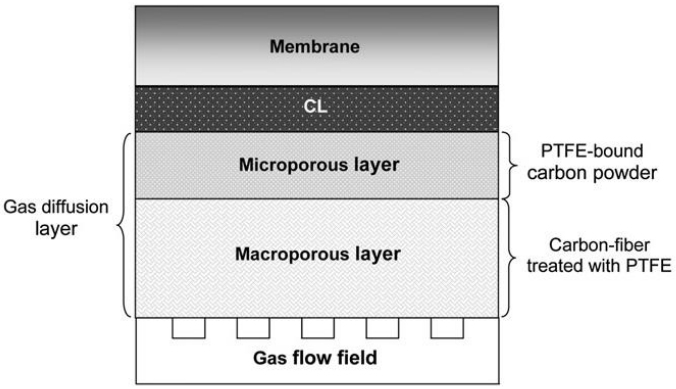

Figure 1-7: Schematic diagram of a dual-layer GDL. Reprinted from reference 50 with permission from Elsevier, © 2012

Another approach to reduce mass transfer limitations is the use of a dual-layer GDL, in which the macroporous structure is tailored with a microporous layer (MPL), made of carbon powder inks with hydrophobic fluoropolymer. As in Figure 1-7, the MPL is oriented towards the catalyst layer, reducing the contact resistance between the catalyst layer and the macroporous backing by forming a flat layer not permeable to the catalyst particles. In this way, the size and the saturation level of interfacial water droplets formed on the catalyst layer surface is reduced and the diffusion rate of reactants is increased [54]**.** Nowadays, state-of-the-art research is focused in adding hydrophilic materials to the hydrophobic MPL to implement wick effect and the use of dual-layer MPL with hydrophobicity gradients [50].

Flow field / bipolar plates and cell stacking

Flow field plates are used to extract the current produced in the electrochemical reaction while helping to maintain the mechanical integrity of the cell upon clamping. Its functions also include the accurate distribution of the feed gases throughout gas diffusion layers using gas channels while removing heat and excess water from the active area. Thus, flow field plate material must present a good chemical stability, high electrical and thermal conductivity; low contact resistance with the backing, good mechanical strength, low gas permeability, inexpensive total cost and allow uniform reactant gas distribution and product removal [55]. The most used flow field geometrical configurations are typically pin-type, parallel, serpentine and interdigitated designs [56], with patterns usually rectangular in cross-section and dimensions ranging from 1 to 2 mm in width and depth in order to reduce the fluid pressure loss due to friction losses [57].

When useful voltage is needed, single cell MEAs can be connected in series. Such arrangement is known as fuel cell stack and it can be attained by the use of bipolar plates. Bipolar plates are essentially the union of a cathodic and an anodic flow field plate in a single component to make an interconnection all over the area of the electrodes in order to minimize the voltage drops of the connections between single cells. At the same time, the bipolar flow field plates keep the function to feed the hydrogen to the anode and the

oxygen to the cathode through the channels in each side of the plate. A schematic of a fuel cell stack is presented in Figure 1-8, in which the bipolar plate is connecting two MEAs while flow field plates are still used in both ends of the stack. Following this scheme, virtually any number of single cells could be assembled in series.

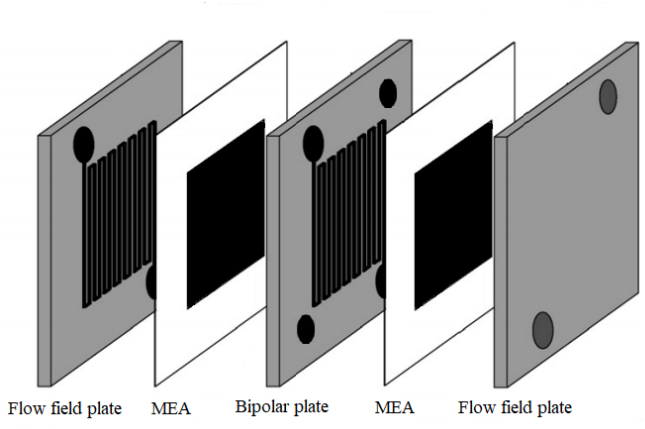

Figure 1-8: A two cell stack showing the bipolar plate connection

In the early stages of fuel cell development, graphite was the dominating material for current bipolar plates due to its very low resistivity and corrosion resistance. However, the lack of mechanical resistance, the high cost of mechanization and a certain degree of hydrogen permeability are major drawbacks for graphitic plates. Although there has been a good amount of research in carbon-based bipolar plates using carbon composites [58, 59], metallic materials are preferred due to higher mechanical strength, better resistance to shocks and vibration, and no gas permeability [60]. The main handicaps of the usage of metals are their proneness to corrosion processes and the increase of the total weight of the cell. Among all the types of metals, stainless steel is the most used due to existing availability for mass production and low cost. As a consequence, there are currently many research groups dedicated to solve the corrosion problems in metallic flow field plates [61].

1.2.2 Thermodynamics and kinetics

The maximum potential that a fuel cell may attain, disregarding existence of any liquid junction potential, is related to the Gibbs free energy (*G*) by the most fundamental equation of electrochemistry (Equation 1.4). Gibbs free energy can be defined as the energy available to do an external work, neglecting any work done by changes in pressure and/or volume. Specifically, in fuel cells, the external work involves moving electrons through an external circuit forced by a spontaneous ($\Delta G < 0$) chemical reaction like that in equation 1.1 [15]. The maximum amount of electrical work that can be obtained of a fuel cell is:

$$\Delta G = -nF E_{cell} \quad (1.4)$$

Where ΔG is the change in Gibbs free energy due to the cell reaction, *n* is number of electrons involved in the reaction, *F* is the Faraday constant (96485 C·mol^{-1}) and E_{cell} is the reversible cell potential or the electromotive force (EMF).

For PEM fuel cells, the reaction of production of water (Equation 1.1) has a ΔG of -237.1 kJ·mol^{-1} at standard conditions and liquid water as product. Thus, the cell standard potential (E^0) of a PEM fuel cell is 1.23 V. When the redox reaction is not occurring at standard conditions, the equilibrium state is governed by the Nernst equation:

$$E_{cell} = E^0 - \frac{RT}{nF} ln\left(\frac{C_R}{C_O}\right) \quad (1.5)$$

Where *R* is the ideal gas constant, *T* is the absolute temperature, C_R is the concentration of reduced species and C_O is the concentration of oxidized species. The reversible cell potential is the highest voltage that can be measured in a cell. When current is drawn from the cell, it is driven out of the equilibrium, the cell voltage decreases with current density (*j*) due to non-equilibrium losses, also known as overpotentials, which can be expressed by [62]:

$$V = E_{cell} - jR_{\Omega} - \eta_{an} - |\eta_{ca}| - \eta_{tx} \quad (1.6)$$

R_{Ω} stands for the ohmic losses, η_{an} and η_{ca} represent the activation losses on the anode and the cathode, respectively, and η_{tx} represents the voltage losses due to mass transport issues. In Figure 1-9, it can be seen the representation of the so-called polarization curve (V vs. j), which is the most common representation to characterize the operation of a fuel cell.

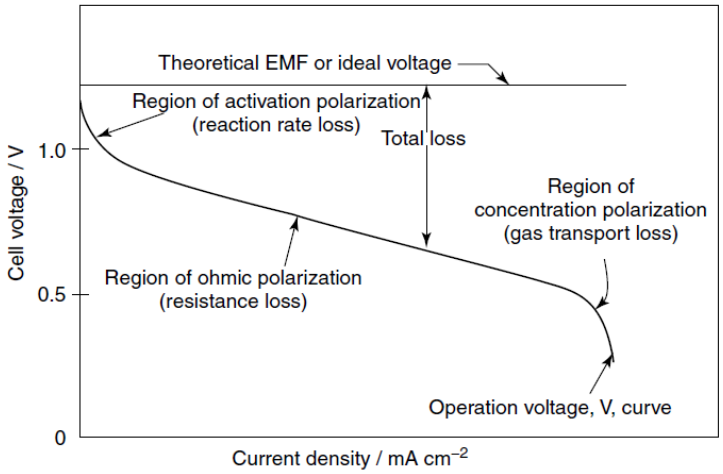

Figure 1-9: Typical polarization curve of a PEMFC. Reprinted from reference 62 with permission from John Wiley and Sons, © 2012

Activation losses are mostly related with kinetics and charge transfer in the catalyst layer. These losses are mostly controlled by the potential difference across the double layer and are described by the Butler-Volmer equation. This equation can be deduced from the state of equilibrium of an electrochemical system.

At equilibrium, the current densities of the forward and reverse reaction of a redox process are the same, implying that the net current density is equal to zero. The exchange current density of the reaction is defined by the following equation:

$$j_0 = j_1 = j_2 \quad (1.7)$$

In which the subscript *1* correspond to the forward and *2* to the reverse reaction. The Butler-Volmer equation represents the net current in a system away from the thermodynamic equilibrium, relating the exchange current density and the activation energies of the reaction.

$$j = j_1 - j_2 \tag{1.8}$$

$$j = j_0(e^{\alpha nF\eta/RT} - e^{-(1-\alpha)nF\eta/RT}) \tag{1.9}$$

Where η stands for the overpotential of the activation energy and α is the transfer coefficient, which signifies the fraction of the interfacial potential that reduces the energy barrier for the reaction. Note that equation 1.9 stands for a compact form of Butler–Volmer equation, although there is a more general form of the equation applicable to the mass transfer-influenced conditions [63].

For fuel cell practical application, the forward reaction can be approximated to an irreversible reaction when the activation overpotential is higher than 50-100 mV. Solving the equation for η yields the Tafel equation (Equation 1.11):

$$\eta = -\frac{RT}{\alpha nF} lnj_0 + \frac{RT}{\alpha nF} lnj \tag{1.10}$$

$$\eta = a + blogj \tag{1.11}$$

From the linear plot of the Tafel equation it is possible to obtain the kinetic parameters of the reaction: the Tafel slope, *b*, and consequently $\alpha \cdot n$ (*n* is the charge exchanged in the rate determining step), and j_0 to compare the kinetic performance of different cells.

Ohmic resistance losses are caused by all processes related with ionic and electronic transport: the ion-conducting resistance of the electrolyte and electrodes, and electronic resistance of the electrodes and the contacts. The variation of this resistance is linear and

responds to Ohm's law. Resistance losses can easily be determined by measuring the high frequency resistance of the cell.

At high current densities, **mass transport losses** are originated for various reasons; one is the excessive production of water that could lead to condensation, hindering the porous cathodic structure by creating a two-phase region in which oxygen permeation is impeded. Also, when the water transport rate from electroosmotic drag to sustain the reaction is increased, a partial dehydration of the anode together with cathode flooding is likely to happen [64]. The mass transport overpotential is described by equation 1.12:

$$\eta = \frac{RT}{nF} ln\left(1 - \frac{j}{j_{lim}}\right) \qquad (1.12)$$

where j_{lim} is the limiting current density due to oxygen depletion in the catalyst layer. The limiting current density is the higher current density that a fuel cell can produce at a given conditions and is exactly the point where the reactant concentration in the catalyst layer is zero [64].

There are also other sources of fuel cell irreversible losses, but have almost no impact in the performance. However, there should be taken into account because they can point out to cell malfunctions. Fuel crossover and internal currents through the electrolyte can be caused by fuel passing and/or from electron conduction through the electrolyte. Small ohmic currents can also be originated due to the oxidation of Pt, carbon support or even impurities.

1.3 Catalyst layers in PEM fuel cells

The vast majority of the research on catalyst layer fabrication is focused on the use of platinum supported on carbon (Pt/C) as catalyst, as it is active for both the hydrogen oxidation and oxygen reduction reactions. Supported platinum catalysts are commonly prepared by wet chemical methods, which consist in absorbing platinum containing precursors on high surface area carbon blacks produced by the pyrolysis of hydrocarbons.

Compared to other popular catalyst supports such as alumina or magnesium oxide, carbon is chemically stable in highly acidic media and a much better electronic conductor. The ability of carbon to be burnt off allows the recovery of the platinum, and therefore offers a clear environmental and ecological advantage. Although there has been a lot of research devoted to the study of carbon supports over the years, Vulcan XC72 carbon black was among the first carbons used for PEM fuel cells and remains as the most extendedly used support for this application [65].

Since the invention of PEM fuel cells until mid-1980s, the catalyst layer consisted in unsupported platinum (platinum black) particles mixed with Teflon and hot-pressed onto the membrane. Using this method, the catalyst loading was around 4 $mg \cdot cm^{-2}$ for state-of-the-art General Electric fuel cells [66]. Although, the use of electrodes with supported catalyst layers was common in alkaline and phosphoric acid fuel cells, the attempts to use supported platinum on carbon in PEM fuel cells were unsuccessful until I.D. Raistrick work in LANL (Los Alamos National Laboratory) was published in 1986 [67]. A major breakthrough on electrode fabrication was achieved after impregnating gas diffusion electrodes with Nafion ionomer solution and hot pressing it to the membrane. The use of Nafion ionomer opened the possibility to use supported catalyst and allowed a ten-fold catalyst loading reduction to 0.4 $mg \cdot cm^{-2}$ by increasing the protonic access to the majority of catalyst sites not close to the membrane [68]. Researchers at LANL continued to refine electrode preparation techniques and developed the modern membrane electrode assembly, as we know it nowadays, preparing catalyst inks by mixing the solubilized ionomer with the Pt/C catalyst in alcohols, allowing the fabrication of thin catalyst films and eliminating the use of Teflon as a binder in catalyst layers [69].

1.3.1 Catalyst layer fabrication methods

Litster and McLean divide the catalyst layer manufacturing methods among PTFE-bound, thin-film and emerging methods. Thin film classification includes all the methods that employ a catalytic ink maintaining the name given by the LANL researchers in the 1990s, while emerging methods include vacuum deposition or electrodeposition [48]. In

the literature, one can also find other type of classifications such as thin and ultra-thin deposition methods. However, these classifications are not intuitive at all. The author of this Thesis proposes here an actualization of the classification, with two main groups: ink-based and platinum deposition methods and its subdivisions, as shown in Figure 1-10.

PTFE-bound methods were excluded from the classification since their use is residual nowadays. This group of methods is characterized by the use of a hydrophobic PTFE structure to bind the catalyst particles and a later impregnation step by immersion, brushing or spraying with liquid Nafion ionomer. This type of preparation was conventional before the development of thin film layers, and, although there was some work in the 1990s using these methods, the platinum utilization was dramatically low in comparison with thin-film methods [70].

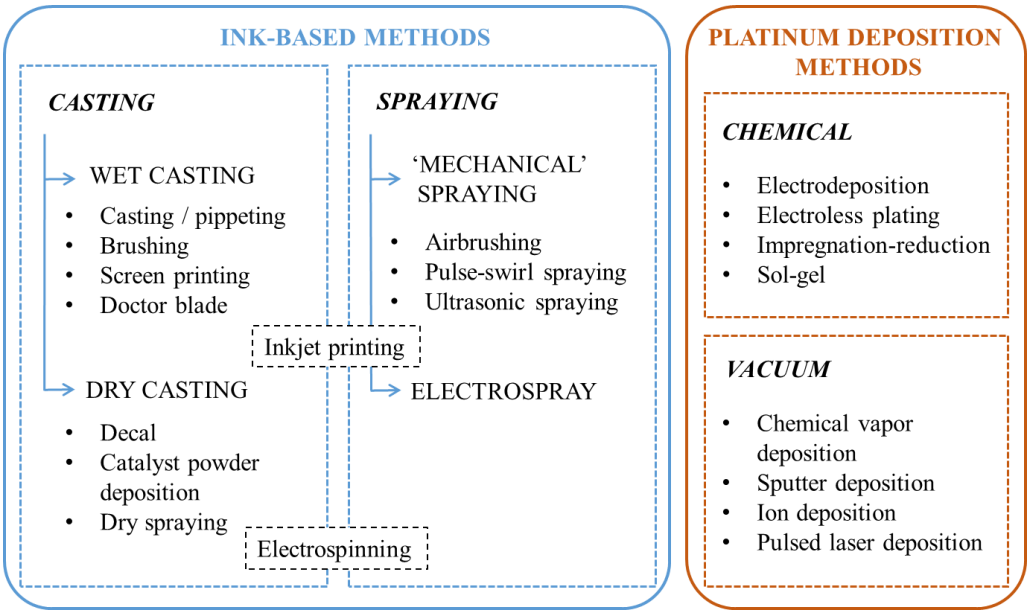

Figure 1-10: Classification of catalyst layer fabrication techniques

Ink-based methods are characterized for using Nafion as binding material with platinum supported catalysts. Using a binder of the same material as the membrane increases proton transport in the catalyst layer, causing an increase of the platinum utilization. This group of methods has at least two necessary steps: the ink preparation and its application. Within these modes, catalyst layers can be deposited either onto the GDL or onto the

membrane. Membrane deposition allows a better protonic conductivity between the membrane and the ionomer in the catalyst layer [71], but with the risk of damaging the membrane due to the chemical attacks of the solvents present in catalytic inks. To reduce the losses of ionic connection when depositing the catalyst onto the GDL, it is common to perform a hot-pressing procedure on the MEA before the assembly [72].

Ink-based methods include the **wet casting methods**. The simplest type of catalyst layer deposition, which is used for small-scale experiments, is the ***direct casting***, which simply consists on pouring or pipetting the catalyst ink followed by a drying process [73]. The process can be refined by using the ***brushing*** [74], ***screen printing*** [75] or ***doctor blade*** [76] methods to have a better control of the ink application onto GDL surface. Although these methods can be used for membrane deposits, the presence of a significant quantity of solvents can damage the membrane. ***Decal*** method can be used to overcome this problem, as the catalyst layer is previously casted on a PTFE blank and then transferred on to the membrane [69].

Dry casting methods eliminate the solvent from the catalyst layer fabrication and deposits dry catalytic layer mixtures. It is not among the most popular methods, but a couple of different variations were described in the literature. In ***catalyst powder deposition*** the components catalyst layer are mixed with a fast running knife under forced cooling and the catalytic dust is fixed to the membrane using hot rolling [77]. In ***dry spraying***, the dry mixture is ejected with the help of a nitrogen stream and also hot-rolled [78].

Spray methods involve the atomization of the catalyst ink and allow a better control and reproducibility of the deposition process. Spray methods are also able to eliminate the drying step when using low boiling point solvents that facilitate solvent evaporation due increased superficial area of the generated droplets. The simplest spray method uses the ***airbrush***, which uses pressurized air to create the ink atomization, and has been used for decades to prepare catalyst layers [79]. Until now, the technique evolved from the use of hand-held devices to more complex setups to increase the reproducibility of the method

[80]. Other types of spray techniques such as ***pulse-swirl spray*** [81] or ***ultrasonic spray*** [82] have also been investigated for layer preparation. ***Electrospray*** is a special type of spray technique; it does not use mechanical forces to generate the atomization of the liquid ink. The technique generates a mist of charged particles solely by application of high voltage between the ink source and the target material. Electrospray is also very appropriate for depositing expensive materials, like platinum-based catalysts, because it allows high deposition efficiency with minimal losses compared with regular airbrushing methods, due to the electric attraction of the charged particles to the target substrate. Although it shares the same physical principles with electrospray, ***electrospinning*** cannot be strictly considered a spray technique, because it produces dry solid fibers in the special situation of inks with sufficiently high molecular cohesion to not allow the liquid ink to break into droplets [83]. Spray methods are particularly interesting for industrial application due to its control and reproducibility over the resulting layer and the easy scale-up for mass production.

Inkjet printing is a technique originally developed for office document printers that was adapted to catalyst deposition. It has the ability to generate small droplets using a piezo-driven piston that displaces a controlled volume of liquid inside a capillary tube [84]. Inkjet printing is strictly a wet casting technique but lays in the middle of wet casting and spray methods for its ability to produce small droplets.

Platinum deposition methods are characterized for a direct deposit of platinum nanoparticles in a single step, aiming to deposit thin and resilient films of the platinum onto the substrate (either the membrane or the GDL), aiming to reduce the catalyst loading and improve the catalyst utilization. Moreover, the proximity of the layers to the membrane dissipates the requirement of the ionomer to act as a proton-conducting medium. As shown in Figure 1-10, these methods include vacuum and chemical deposition. **Chemical deposition** involves the deposition of platinum particles in a liquid medium by different types of chemical processes: ***electrodeposition*** [85], ***electroless plating*** [86], ***impregnation-reduction*** [87] or ***sol-gel*** [88]. **Vacuum deposition methods**

are a group of methods that use high vacuum to deposit thin layers of a material on top of solid surfaces and include techniques such as ***chemical vapor deposition*** [89], ***sputtering*** [90], ***ion deposition*** [91] or ***pulsed laser deposition*** [92]. Although the results obtained with those methods show good cell performances with reduced platinum loadings, the main drawback of the techniques is the inability of volume production and the requirement of expensive equipment of the vacuum methods. More detailed information of the most used direct platinum deposition methods can be checked in a review by Wee et al. [93].

1.3.2 State of the art of electrospray deposition for PEM fuel cells

The first reported application of the electrospray deposition technique in PEM fuel cells dates from 2005, when Baturina and Wnek deposited Pt/C catalyst layers on both sides of a Nafion 112 membrane, using an ink dispersed in ethanol with no MEA hot pressing. The results were promising and showed good performance at 80 °C and pressure of 3 bar [94]. Before that, they demonstrated the feasibility of the technique by depositing Pt/C onto glassy carbon and studying catalyst particle size distribution and dispersion, electrocatalytic activity and catalyst utilization [95]. In 2004, Wnek also participated in a publication in which Nafion membranes were fabricated using electrospray. The physical properties of the electrosprayed Nafion membranes (water uptake, dimensional changes and electrical conductivity) where similar to those of Nafion 117 films, with the exception of an unusually high water uptake, absorbing as much as 15 wt% water more than the commercial membrane [96]. At about the same time, Umeda et al. also explored the feasibility of the technique for deposition of catalytic inks on Nafion membranes using inks diluted in a mixture of methanol, isopropanol and water [97] and characterized the MEAs obtaining similar performances as cells prepared by air-spraying [98]. However, after those promising results, they stopped publishing works related to the electrospray deposition technique.

In parallel, the fuel cells group at CIEMAT also published their first work on the use of electrospray for the fabrication of catalyst layers for PEM fuel cells in 2005 and have

been using the technique ever since. In this first work, electrochemical characterization of electrosprayed layer was performed for the oxygen reduction reaction [99]. That year, the deposition of Pt/C catalyst layers on top of a gas diffusion layer was studied by using an ink dispersed in a complex mixture of solvents (butyl acetate, ethanol and glycerol), reporting a better distribution of the catalyst, higher platinum utilization and a performance increase when compared to regular deposition methods [100]. However, a later work showed that high boiling point solvents remain within the film, and although this mixture shows high mass specific area, pure isopropanol is preferred as solvent due to its lower boiling temperature [101]. Optimization of catalyst loading showed a maximum at 0.17 $mg \cdot cm^{-2}$ with Pt/C (20 wt% Pt), corresponding to the minimum value of catalytic layer resistance. Additionally, an optimal 15 % of Nafion concentration was found to be optimal for electrospray deposited electrodes, which is significantly lower than the values reported for standard preparations methods [102]. The use of electrospray resulted in catalyst layers with a better distribution of the Nafion around the catalyst particles and the formation of high macroporous structure [103]. Additionally, single cell testing demonstrated that catalyst layers deposited on top of the membrane showed better catalyst layer-membrane ionic contact than the layers deposited on the GDL, allowing a reduction internal resistance of the cell [104]. The ability of the electrospray to produce superhydrophobic layers was already reported with polymer coatings [105]. However, this property did not receive much attention until the last works at CIEMAT. In the latest studies, the hydrophobic properties of Pt/C layers are believed to favor a faster water removal that contributes to improve the performance and the homogeneity of cell response [106]. The superhydrophobicity of the catalyst layer is also believed to retard the kinetics of corrosion of the carbon support and thus reducing cathodic layer degradation [107].

Since 2010, Garcia-Ybarra group have also published about electrospray application for catalyst layer deposition, mainly focusing in the minimization of the platinum catalyst loading. They started to deposit the cathodic catalyst layers onto carbon papers, reporting platinum loadings as low as 0.012 $mg \cdot cm^{-2}$ with high power outputs per gram of platinum

[108] with a much higher optimum Nafion content, in the range of 30-50 wt%, with dry gases and a cell temperature of 80 °C [109]. They reported that the overall platinum utilization reached values larger than 30 $kW \cdot g_{Pt}^{-1}$ with catalytic layers with Pt loadings of 0.01 $mg \cdot cm^{-2}$ in both anode and cathode under certain conditions [110]. Moreover, they demonstrated the suitability of low loading electrosprayed catalyst layers for scaling-up process to elaborate electrodes up to 25 cm^2 [111] and for long-term and stable operation under non-humidified conditions [112]. Their results were confirmed by other research groups, which also observed that electrosprayed catalyst layers have the potential to improve the mass activity at 0.05 $mg \cdot cm^{-2}$ platinum loading, due to increased efficiency of gas mass transport [113] and reduced O_2 transport resistance with ultra-low platinum loading [114].

In recent years, some authors are also using the electrospray deposition technique to form carbon layers to be used in other parts of the fuel cell. For instance, Chingthamai et al. studied the optimal conditions for carbon black microporous layer deposition [115]. Other authors studied the effect of carbon layers next to the catalytic layer: Koh et al. reported the fabrication of nano-sized dense-structured layer to create a dual layered electrode that improves self-humidification operation [116], while Okuno et al. fabricated three-layered catalysts, alternating Pt/C and carbon layers, to examine the effect of platinum distribution on the cell performance [117]. Modifications of the standard cone-jet deposition process are also starting to be explored lately. One approach is to change the electrospray regime, such as the use of electrohydrodynamic jet deposition, which is formed at lowest potentials than the cone-jet, resulting in uniform deposition of fuel cell catalysts [118]. Another approach consists in the combination of the electrospray deposition with other processes, such as the modification of the deposited layers, via the use of surfactants, to create additional porous structures [119], or the use of simultaneous electrospinning/electrospraying technique to produce Pt/C coated Nafion fibers that improve cell performance with low platinum loadings [120, 121].

1.4 Scope of the research

Electrosprayed catalyst layers have been used for more than ten years for PEM fuel cell electrode fabrication exhibiting great performance and unique properties, such as superhydrophobicty and high macroporosity. This thesis focuses on the study of the electrospray deposition technique for the fabrication of carbon black-based layers and its application in PEM fuel cells aiming to expand the knowledge about electrospray deposition, stablish electrospray as a reference technique for electrode manufacturing and expand its application to other cell components. The investigation is divided in three distinct parts: a characterization study of the electrosprayed carbon black-Nafion composite layers, a study of carbon black-supported platinum catalyst layers in PEM fuel cells and the application of electrosprayed carbon-based deposits as metallic substrate coating for corrosion protection.

The first part aims to explain the superhydrophobicty and high macroporosity of electrosprayed layer by means of a thorough physicochemical study of carbon black-Nafion composites using scanning electron microscopy, X-ray photoelectron spectroscopy, attenuated total reflectance, water contact angle and thermal stability. This set of techniques attempt to unravel the interactions between the carbon black surface and the Nafion determining the characteristic structure and properties of the resulting layers.

The second part is devoted to the study of platinum supported carbon black as PEM fuel cell catalysts. The main core of the experiments focuses on the mass transport properties of the electrosprayed layers and their influence in water distribution in the cell. Mass transport properties of the electrosprayed catalyst layers were studied in a short stay in Lawrence Berkeley National Laboratory (Berkeley, CA) by means of hydrogen-limiting current and dynamic vapor sorption techniques. The influence of water distribution in the cell by the presence of electrosprayed layers is performed by water collection with dry feed gases. The results are supported by electrochemical characterization in a bench-scale single cell and a characterization study using scanning, transmission and scanning-transmission electron microscopy.

The third and last part presents a brand new application of the electrospray deposition technique: the corrosion protection of metallic substrates. The superhydrophobicty and high macroporosity of the carbon black-Nafion composites are able to render Cassie–Baxter type superhydrophobicity surface in a simple step. The composite layers were subjected to an *ex-situ* electrochemical characterization in a three-cell electrode by linear sweep and cyclic voltammetry, and chronopotenciometric experiments. Additionally, preliminary studies of the behavior of carbon-coated PEM fuel cell flow-field plate channels were also performed as a practical use of corrosion protection.

The results compiled in this thesis were obtained between January 2016 and January 2019 at Fuel Cells group at Centro de Investigaciones Energéticas, Medioambientales y Tecnológicas (CIEMAT) in Madrid. Most of the results had been already published in SCI journals before the dissertation was presented. The articles including results of the dissertation (in order of appearance) are presented below.

- J.J. Conde, A.M. Chaparro, P. Ferreira-Aparicio, Understanding the behavior of electrosprayed carbon black-Nafion composite layers, Fuel Cells. 18 (2018) 627–639.
- J.J. Conde, M.A. Folgado, P. Ferreira-Aparicio, A.M. Chaparro, A. Chowdhury, A. Kusoglu, D. Cullen, A.Z. Weber, Mass-transport properties of electrosprayed Pt/C catalyst layers for polymer-electrolyte fuel cells, J. Power Sources. 427 (2019) 250-259.
- M.A. Folgado, J.J. Conde, P. Ferreira-Aparicio, A.M. Chaparro, Single cell study of water transport in PEMFCs with electrosprayed catalyst layers, Fuel Cells. 18 (2018) 602–612.
- J.J. Conde, P. Ferreira-Aparicio, A.M. Chaparro, Anti-corrosion coating for metal surfaces based on superhydrophobic electrosprayed carbon layers, Appl. Mater. Today. 13 (2018) 100–106.

1.5 References

[1] C.W. Garrett, On global climate change, carbon dioxide, and fossil fuel combustion, Prog. Energy Combust. Sci. 18 (1992) 369–407.

[2] I.M. Kennedy, The health effects of combustion-generated aerosols, Proc. Combust. Inst. 31 (2007) 2757–2770.

[3] T.L. Frölicher, Strong warming at high emissions: Climate response, Nat. Clim. Change. 6 (2016) 823–824.

[4] R. Diercks, J.D. Arndt, S. Freyer, R. Geier, O. Machhammer, J. Schwartze, M. Volland, Raw material changes in the chemical industry, Chem. Eng. Technol. 31 (2008) 631–637.

[5] U.N. Treaty Collection, Paris Agreement, Chapter XXVII.

[6] International Energy Agency, World energy outlook special report: Energy and climate change, 2015.

[7] Directive 2006/32/EC of the European Parliament and of the Council of 5 April 2006 on energy end-use efficiency and energy services.

[8] Directive 2009/28/EC of the European Parliament and of the Council of 23 April 2009 on the promotion of the use of energy from renewable sources.

[9] Directive 2012/27/EU of the European Parliament and of the Council of 25 October 2012 on energy efficiency.

[10] N.L. Panwar, S.C. Kaushik, S. Kothari, Role of renewable energy sources in environmental protection: A review, Renew. Sustain. Energy Rev. 15 (2011) 1513–1524.

[11] H. Ibrahim, A. Ilinca, J. Perron, Energy storage systems - Characteristics and comparisons, Renew. Sustain. Energy Rev. 12 (2008) 1221–1250.

[12] Y. Wang, S. Zhang, Economic assessment of selected hydrogen production methods: A review, Energy Sources Part B Econ. Plan. Policy. 12 (2017) 1022–1029.

[13] J. Garche, L. Jörissen, Applications of fuel cell technology: Status and perspectives, ECS Interface. 24 (2015) 39–43.

[14] F. Barbir, T. Gomez, Efficiency and economics of proton exchange membrane (PEM) fuel cells, Int. J. Hydrog. Energy. 22 (1997) 1027–1037.

[15] J. Larminie, A. Dicks, Fuel cells systems explained, John Wiley & Sons Ltd, 2003.

[16] F. Barbir, PEM Fuel Cells. Theory and Practice, Academic Press, 2012.

[17] J.M. Andújar, F. Segura, Fuel cells: History and updating. A walk along two centuries, Renew. Sustain. Energy Rev. 13 (2009) 2309–2322.

[18] W.R. Grove, On voltaic series and the combination of gases by platinum, Lond. Edinb. Dublin Philos. Mag. J. Sci. Ser. 3. 14 (1839) 127–130.

[19] A.J. Appleby, From Sir William Grove to today: fuel cells and the future, J. Power Sources. 29 (1990) 3–11.

[20] W.W. Jacques, Electricity direct from coal, Harper´s Mag. 94 (1896) 144–150.

[21] H. Kragh, From cosmochemistry to fuel cells: Notes on Emil Baur, physical chemist, Bull. Hist. Chem. (2015) 74–85.

[22] A.M. Adams, F.T. Bacon, R.G.H. Watson, Fuel Cells, Academic Press, 1963.

[23] E.W. Justi, A.W. Winsel, Cold combustion fuel cells, Steiner Verlag, Wiesbaden, 1962.

[24] M.L. Perry, T.F. Fuller, A historical perspective of fuel cell technology in the 20th century, J. Electrochem. Soc. 149 (2002) S59.

[25] W.T. Grubb, L.W. Niedrach, Batteries with solid ion-exchange membrane electrolytes II. Low-temperature hydrogen-oxygen fuel cells, J. Electrochem. Soc. 107 (1960) 131–135.

[26] G.V. Elmore, H.A. Tanner, Intermediate temperature fuel cells, J. Electrochem. Soc. 108 (1961) 669–671.

[27] 4th Energy Wave, Fuel Cell and Hydrogen Annual Review, 2017.

[28] H.-Y. Tang, A. Santamaria, J. Kurniawan, J.W. Park, T.-H. Yang, Y.-J. Sohn, Developing a 3D neutron tomography method for proton exchange membrane fuel cells, J. Power Sources. 195 (2010) 6774–6781.

[29] N. Zamel, X. Li, Effect of contaminants on polymer electrolyte membrane fuel cells, Prog. Energy Combust. Sci. 37 (2011) 292–329.

[30] International Energy Agency (IEA), Prospects for Hydrogen and Fuel Cells, 2005.

[31] P. Ferreira-Aparicio, A.M. Chaparro, Portable Hydrogen Energy Systems, Academic Press, 2018.

[32] C.E. Perles, Propriedades físico-químicas relacionadas ao desenvolvimento de membranas de Nafion para aplicações em células a combustível do tipo PEMFC, Polímeros. 18 (2008) 281–288.

[33] A.D. Jenkins, P. Kratochvíl, R.F. Stepto, U.W. Suter, Glossary of basic terms in polymer science (IUPAC Recommendations 1996), Pure Appl. Chem. 68 (1996) 2287–2311.

[34] C. Heitner-Wirguin, Recent advances in perfluorinated ionomer membranes: structure, properties and applications, J. Membr. Sci. 120 (1996) 1–33.

[35] W. Hsu, T.D. Gierke, Ion-transport and clustering in nafion perfluorinated membranes, J. Membr. Sci. 13 (1983) 307–326.

[36] T. Thampan, S. Malhotra, H. Tang, R. Datta, Modeling of Conductive Transport in Proton-Exchange Membranes for Fuel Cells, J. Electrochem. Soc. 147 (2000) 3242–3250.

[37] W. Hsu, T.D. Gierke, Elastic theory for ionic clustering in perfluorinated ionomers, Macromolecules. 15 (1982) 101–105.

[38] G. Gebel, Structural evolution of water swollen perfluorosulfonated ionomers from dry membrane to solution, Polymer. 41 (2000) 5829–5838.

[39] K.A. Mauritz, R.B. Moore, State of understanding of Nafion, Chem. Rev. 104 (2004) 4535–4585.

[40] P.W. Majsztrik, Mechanical and transport properties of Nafion® for PEM fuel cells; temperature and hydration effects, PhD Thesis, Princeton University (2008).

[41] F. Tian, A.B. Anderson, Effective reversible potential, energy loss, and overpotential on platinum fuel cell cathodes, J. Phys. Chem. C. 115 (2011) 4076–4088.

[42] R. Othman, A.L. Dicks, Z. Zhu, Non precious metal catalysts for the PEM fuel cell cathode, Int. J. Hydrog. Energy. 37 (2012) 357–372.

[43] F. Jaouen, E. Proietti, M. Lefèvre, R. Chenitz, J.P. Dodelet, G. Wu, H.T. Chung, C.M. Johnston, P. Zelenay, Recent advances in non-precious metal catalysis for oxygen-reduction reaction in polymer electrolyte fuel cells, Energy Environ. Sci. 4 (2011) 114–130.

[44] Z. Liu, L. Ma, J. Zhang, K. Hongsirikarn, J.G. Goodwin, Pt alloy electrocatalysts for proton exchange membrane fuel cells: A review, Catal. Rev. 55 (2013) 255–288.

[45] R. Bashyam, P. Zelenay, A class of non-precious metal composite catalysts for fuel cells, Nature. 443 (2006) 63–66.

[46] R. Subbaraman, D. Strmcnik, V. Stamenkovic, N.M. Markovic, Three phase interfaces at electrified metal-solid electrolyte systems 1. Study of the Pt(hkl)-Nafion interface, J. Phys. Chem. C. 114 (2010) 8414–8422.

[47] J. Zhang, PEM Fuel Cell Electrocatalysts and Catalyst Layers, Springer-Verlag, 2008.

[48] S. Litster, G. McLean, PEM fuel cell electrodes, J. Power Sources. 130 (2004) 61–76.

[49] K. Wikander, H. Ekström, A.E. Palmqvist, G. Lindbergh, On the influence of Pt particle size on the PEMFC cathode performance, Electrochimica Acta. 52 (2007) 6848–6855.

[50] S. Park, J.-W. Lee, B.N. Popov, A review of gas diffusion layer in PEM fuel cells: Materials and designs, Int. J. Hydrog. Energy. 37 (2012) 5850–5865.

[51] M. Prasanna, Y.H. Ha, E.A. Cho, S.A. Hong, I. Oh, Influence of cathode gas diffusion media on the performance of the PEMFCs, J. Power Sources. 131 (2004) 147–154.

[52] L.R. Jordan, A.K. Shukla, T. Behrsing, N.R. Avery, B.C. Muddle, M. Forsyth, Diffusion layer parameters influencing optimal fuel cell performance, J. Power Sources. 86 (2000) 250–254.

[53] S. Shimpalee, U. Beuscher, J.W. Van Zee, Analysis of GDL flooding effects on PEMFC performance, Electrochimica Acta. 52 (2007) 6748–6754.

[54] J.H. Nam, K.J. Lee, G.S. Hwang, C.J. Kim, M. Kaviany, Microporous layer for water morphology control in PEMFC, Int. J. Heat Mass Transf. 52 (2009) 2779–2791.

[55] H. Wang, J.A. Turner, Reviewing metallic PEMFC bipolar plates, Fuel Cells. 10 (2010) 510–519.

[56] H. Kahraman, M.F. Orhan, Flow field bipolar plates in a proton exchange membrane fuel cell: Analysis & modeling, Energy Convers. Manag. 133 (2017) 363–384.

[57] X. Li, I. Sabir, Review of bipolar plates in PEM fuel cells: Flow-field designs, Int. J. Hydrog. Energy. 30 (2005) 359–371.

[58] R. Antunes, M.C.L. Oliveira, G. Ett, V. Ett, Carbon materials in composite bipolar plates for polymer electrolyte membrane fuel cells: A review of the main challenges to improve electrical performance, J. Power Sources. 196 (2011) 2945–2961.

[59] E. Planes, L. Flandin, N. Alberola, Polymer composites bipolar plates for PEMFCs, Energy Procedia. 20 (2012) 311–323.

[60] H. Tawfik, Y. Hung, D. Mahajan, Metal bipolar plates for PEM fuel cell - A review, J. Power Sources. 163 (2007) 755–767.

[61] R.A. Antunes, M.C.L. Oliveira, G. Ett, V. Ett, Corrosion of metal bipolar plates for PEM fuel cells: A review, Int. J. Hydrog. Energy. 35 (2010) 3632–3647.

[62] H.A. Gasteiger, J. Garche, Fuel Cells, in: Handbook of Heterogeneous Catalysis, Wiley-VCH Verlag, 2008.

[63] A.J. Bard, L.R. Faulkner, Electrochemical Methods. Fundamentals and Applications, Wiley, 2000.

[64] S.K. Das, A.S. Bansode, Heat and Mass Transport in Proton Exchange Membrane Fuel Cells - A Review, Heat Transf. Eng. 30 (2009) 691–719.

[65] A.L. Dicks, The role of carbon in fuel cells, J. Power Sources. 156 (2006) 128–141.

[66] S. Srinivasan, E.A. Ticianelli, C.R. Derouin, A. Redondo, Advances in solid polymer electrolyte fuel cell technology with low platinum loading electrodes, J. Power Sources. 22 (1988) 359–375.

[67] I. D. Raistrick, Modified gas diffusion electrode for proton exchange membrane fuel cells, in: Diaphragms, Separators, and Ion Exchange Membranes, Electrochemical Society Softbound Proceedings Series (1986).

[68] E.A. Ticianelli, C.R. Derouin, A. Redondo, S. Srinivasan, Methods to advance technology of proton exchange membrane fuel cells, J. Electrochem. Soc. 135 (1988) 2209–2214.

[69] M.S. Wilson, S. Gottesfeld, Thin-film catalyst layers for fuel cell electrodes, J. Appl. Electrochem. 22 (1992) 1–7.

[70] O.J. Murphy, G.D. Hitchens, D.J. Manko, High power density proton-exchange membrane fuel cells, J. Power Sources. 47 (1994) 353–368.

[71] Y.G. Chun, C.S. Kim, D.H. Peck, D.R. Shin, Performance of a polymer electrolyte membrane fuel cell with thin film catalyst electrodes, J. Power Sources. 71 (1988) 174–178.

[72] S.M. Andersen, R. Dhiman, M.J. Larsen, E. Skou, Importance of electrode hot-pressing conditions for the catalyst performance of proton exchange membrane fuel cells, Appl. Catal. B Environ. 172 (2015) 82–90.

[73] J.M. Song, S.Y. Cha, W.M. Lee, Optimal composition of polymer electrolyte fuel cell electrodes determined by the AC impedance method, J. Power Sources. 94 (2001) 78–84.

[74] V.A. Paganin, E.A. Ticianelli, E.R. Gonzalez, Development and electrochemical studies of gas diffusion electrodes for polymer electrolyte fuel cells, J. Appl. Electrochem. 26 (1996) 297–304.

[75] R.N. Bonifácio, J.O. Paschoal, M. Linardi, R. Cuenca, Catalyst layer optimization by surface tension control during ink formulation of membrane electrode assemblies in proton exchange membrane fuel cell, J. Power Sources. 196 (2011) 4680–4685.

[76] I.S. Park, W. Li, A. Manthiram, Fabrication of catalyst-coated membrane-electrode assemblies by doctor blade method and their performance in fuel cells, J. Power Sources. 195 (2010) 7078–7082.

[77] E. Gülzow, M. Schulze, N. Wagner, T. Kaz, R. Reissner, G. Steinhilber, A. Schneider, Dry layer preparation and characterisation of polymer electrolyte fuel cell components, J. Power Sources. 86 (2000) 352–362.

[78] D. Bevers, N. Wagner, M. Von Bradke, Innovative production procedure for low cost PEFC electrodes and electrode/membrane structures, Int. J. Hydrog. Energy. 23 (1998) 57–63.

[79] G.S. Kumar, M. Raja, S. Parthasarathy, High performance electrodes with very low platinum loading for polymer electrolyte fuel cells, Electrochimica Acta. 40 (1995) 285–290.

[80] M.B. Sassin, Y. Garsany, B.D. Gould, K.E. Swider-Lyons, Fabrication method for laboratory-scale high-performance membrane electrode assemblies for fuel cells, Anal. Chem. 88 (2017) 511–518.

[81] K. Takahashi, R. Koda, K. Kakinuma, M. Uchida, Improvement of cell performance in low-Pt-loading PEFC cathode catalyst layers with Pt/Ta-SnO_2 prepared by the electrospray method, J. Electrochem. Soc. 164 (2017) 235–242.

[82] T.H. Huang, H.L. Shen, T.C. Jao, F.B. Weng, A. Su, Ultra-low Pt loading for proton exchange membrane fuel cells by catalyst coating technique with ultrasonic spray coating machine, Int. J. Hydrog. Energy. 37 (2012) 13872–13879.

[83] M. Brodt, T. Han, N. Dale, E. Niangar, R. Wycisk, P. Pintauro, Fabrication, in-situ performance, and durability of nanofiber fuel cell electrodes, J. Electrochem. Soc. 162 (2015) 84–91.

[84] S. Shukla, K. Domican, K. Karan, S. Bhattacharjee, M. Secanell, Analysis of low platinum loading thin polymer electrolyte fuel cell electrodes prepared by inkjet printing, Electrochimica Acta. 156 (2015) 289–300.

[85] O. Antoine, R. Durand, In situ electrochemical deposition of Pt nanoparticles on carbon and inside Nafion, Electrochem. Solid-State Lett. 4 (2001) 55–58.

[86] W. Hawut, M. Hunsom, K. Pruksathorn, Platinum electroless deposition on Nafion membrane for PEM fuel cells, Korean J. Chem. Eng. 23 (2006) 555–559.

[87] R. Liu, W.H. Her, P.S. Fedkiw, In situ electrode formation on a nation membrane by chemical platinization, J. Electrochem. Soc. 139 (1992) 15–23.

[88] M.R. Khan, S.D. Lin, Using Pt sols to prepare low Pt-loading electrodes for polymer electrolyte fuel cells, J. Power Sources. 162 (2006) 186–191.

[89] S.K. Babu, R.W. Atkinson, A.B. Papandrew, S. Lister, Vertically oriented polymer electrolyte nanofiber catalyst support for thin film proton-exchange membrane fuel cell electrodes, ChemElectroChem. 2 (2015) 1752–1759.

[90] D. Gruber, N. Ponath, J. Müller, F. Lindataedt, Sputter-deposited ultra-low catalyst loadings for PEM fuel cells, J. Power Sources. 150 (2005) 65–72.

[91] M.S. Saha, A.F. Gullá, R.J. Allen, S. Mukerjee, High performance polymer electrolyte fuel cells with ultra-low Pt loading electrodes prepared by dual ion-beam assisted deposition, Electrochimica Acta. 51 (2006) 4680–4692.

[92] N. Cunningham, E. Irissou, M.C. Denis, D. Guay, J.P. Dodelet, PEMFC anode with very low Pt loadings using pulsed laser deposition, Electrochem. Solid-State Lett. 6 (2003) 125–128.

[93] J.H. Wee, K.Y. Lee, S.H. Kim, Fabrication methods for low-Pt-loading electrocatalysts in proton exchange membrane fuel cell systems, J. Power Sources. 165 (2007) 667–677.

[94] O.A. Baturina, G.E. Wnek, Characterization of proton exchange membrane fuel cells with catalyst layers obtained by electrospraying, Electrochem. Solid-State Lett. 8 (2005) A267–A269.

[95] O.A. Baturina, G.E. Wnek, Characterization of membrane-electrode assemblies obtained by electrostatic processing, Proceedings of the 204th ECS Meeting (2003).

[96] E.H. Sanders, K.A. McGrady, G.E. Wnek, C.A. Edmondson, J.M. Mueller, J.J. Fontanella, S. Suarez, S.G. Greenbaum, Characterization of electrosprayed Nafion films, J. Power Sources. 129 (2004) 55–61.

[97] M. Umeda, S. Kawaguchi, A. Yamada, I. Uchida, Pt/C electrocatalyst painting on polymer electrolyte membrane by electrostatic spray deposition, Jpn. J. Appl. Phys. 44 (2005) 322–325.

[98] M. Umeda, S. Kawaguchi, I. Uchida, Characterization of membrane electrode assembly for fuel cells prepared by electrostatic spray deposition, Jpn. J. Appl. Phys. 45 (2006) 6049–6054.

[99] R. Benitez, A.M. Chaparro, L. Daza, Electrochemical characterisation of Pt/C suspensions for the reduction of oxygen, J. Power Sources. 151 (2005) 2–10.

[100] R. Benitez, J. Soler, L. Daza, Novel method for preparation of PEMFC electrodes by the electrospray technique, J. Power Sources. 151 (2005) 108–113.

[101] A.M. Chaparro, R. Benitez, L. Gubler, G.G. Scherer, L. Daza, Study of membrane electrode assemblies for PEMFC, with cathodes prepared by the electrospray method, J. Power Sources. 169 (2007) 77–84.

[102] A.M. Chaparro, B. Gallardo, M.A. Folgado, A.J. Martin, L. Daza, PEMFC electrode preparation by electrospray: Optimization of catalyst load and ionomer content, Catal. Today. 143 (2009) 237–241.

[103] A.M. Chaparro, M.A. Folgado, P. Ferreira-Aparicio, A.J. Martin, I. Alonso-Alvarez, L. Daza, Properties of catalyst layers for PEMFC electrodes prepared by electrospray deposition, J. Electrochem. Soc. 157 (2010) 993–999.

[104] A.M. Chaparro, P. Ferreira-Aparicio, M.A. Folgado, A.J. Martin, L. Daza, Catalyst layers for proton exchange membrane fuel cells prepared by electrospray deposition on Nafion membrane, J. Power Sources. 196 (2011) 4200–4208.

[105] E. Burkarter, C.K. Saul, F. Thomazi, N.C. Cruz, L.S. Roman, W.H. Schreiner, Superhydrophobic electrosprayed PTFE, Surf. Coat. Technol. 202 (2007) 194–198.

[106] A.M. Chaparro, P. Ferreira-Aparicio, M.A. Folgado, E. Brightman, G. Hinds, Study of superhydrophobic electrosprayed catalyst layers using a localized reference electrode technique, J. Power Sources. 325 (2016) 609–619.

[107] P. Ferreira-Aparicio, A.M. Chaparro, M.A. Folgado, J.J. Conde, E. Brightman, G. Hinds, Degradation study by start-up/shut-down cycling of superhydrophobic electrosprayed catalyst layers using a localized reference electrode technique, ACS Appl. Mater. Interfaces. 9 (2017) 10626–10636.

[108] S. Martin, P.L. Garcia-Ybarra, J.L. Castillo, Electrospray deposition of catalyst layers with ultra-low Pt loadings for PEM fuel cells cathodes, J. Power Sources. 195 (2010) 2443–2449.

[109] S. Martin, P.L. Garcia-Ybarra, J.L. Castillo, High platinum utilization in ultra-low Pt loaded PEM fuel cell cathodes prepared by electrospraying, Int. J. Hydrog. Energy. 35 (2010) 10446–10451.

[110] S. Martin, B. Martinez-Vazquez, P.L. Garcia-Ybarra, J.L. Castillo, Peak utilization of catalyst with ultra-low Pt loaded PEM fuel cell electrodes prepared by the electrospray method, J. Power Sources. 229 (2013) 179–184.

[111] B. Martinez-Vazquez, D.G. Sanchez, J.L. Castillo, K.A. Friedrich, P.L. Garcia-Ybarra, Scaling-up and characterization of ultralow-loading MEAs made-up by electrospray, Int. J. Hydrog. Energy. 40 (2015) 5384–5389.

[112] S. Martin, P.L. Garcia-Ybarra, J.L. Castillo, Long-term operation of a proton exchange membrane fuel cell without external humidification, Appl. Energy. 205 (2017) 1012–1020.

[113] K. Takahashi, K. Kakinuma, M. Uchida, Improvement of cell performance in low-Pt-loading PEFC cathode catalyst layers prepared by the electrospray method, J. Electrochem. Soc. 163 (2016) 1182–1188.

[114] J.H. Yoo, B.H. Choi, B.S. Koh, C.Y. Jung, X. Wang, S.C. Yi, Fabrication of practical PEMFC electrode with ultralow mass loading of platinum via electro-spray deposition technique, J. Ceram. Process. Res. 18 (2017) 4.

[115] N. Chingthamai, K. Sombatmankhong, Y. Laoonual, Experimental investigation of electrospray coating technique for electrode fabrication in PEMFCs, Energy Procedia. 105 (2017) 1806–1812.

[116] B.S. Koh, J.H. Yoo, E.K. Jang, V.R. Jothi, C.Y. Jung, S.C. Yi, Fabrication of highly effective self-humidifying membrane electrode assembly for proton exchange membrane fuel cells via electrostatic spray deposition, Electrochem. Commun. 93 (2018) 76–80.

[117] S. Okuno, N. Katayama, Gradational structured catalyst layer for proton exchange membrane fuel cells, ECS Trans. 83 (2018) 87–91.

[118] A.S. Hollinger, P.J.A. Kenis, Electrohydrodynamic-jet deposition of Pt-based fuel cell catalysts, ASME 14th International Conference on Fuel Cell Science, Engineering and Technology, (2016).

[119] N. Shan, H. Jung, J.Y. Ahn, J.H. Kim, S.H. Kim, Electrospray-assisted fabrication of porous platinum-carbon composite thin layers for enhancing the electrochemical performance of proton-exchange membrane fuel cells, Curr. Appl. Phys. 18 (2018) 728–739.

[120] X. Wang, F.W. Richey, K.H. Wujcik, Y.A. Elabd, Ultra-low platinum loadings in polymer electrolyte membrane fuel cell electrodes fabricated via simultaneous electrospinning/electrospraying method, J. Power Sources. 264 (2014) 42–48.

[121] X. Wang, F.W. Richey, K.H. Wujcik, R. Ventura, K. Mattson, Y.A. Elabd, Effect of polytetrafluoroethylene on ultra-low platinum loaded electrospun/electrosprayed electrodes in proton exchange membrane fuel cells, Electrochimica Acta. 139 (2014) 217–224.

CHAPTER 2
Understanding electrosprayed carbon black-Nafion composite layers

2.1 Outline of the chapter

Electrospray deposition is a method for the preparation of layers based on the ejection of a solid suspension under the influence of a strong electric field between a conductive needle and a substrate. Electrospray is a suitable technique to fabricate thin films of controlled morphology and homogeneous distribution on the substrate. The properties of a deposit strongly depend on the size of the particles and droplets, electrospray can produce films of excellent quality, reducing the number of voids, flaws and cracks, and ensuring a homogenous thickness throughout the surface of the films. Electrospray is also very appropriate for depositing expensive materials, like platinum-based catalysts, because it allows high deposition efficiency of the target material, with minimal losses compared with regular airbrushing methods. However, it is a complicated physical process, which is not fully understood yet, especially when colloidal suspensions, like Pt/C catalyst inks, are fed. In previous studies, the electrospray deposition technique has been proven to be a very useful tool to prepare catalyst layers with enhanced platinum dispersion, high porosity, superhydrophobicity, homogeneity and low resistivity.

This chapter will firstly review the state of the art of the electrospray technique, and its applications, in particular fuel cell catalyst layers. Then, it will analyze in detail the properties of carbon black-Nafion films prepared by electrospray deposition by applying different techniques in order to gain insight into the interactions between the carbon black surface and the Nafion fluorocarbon chains that finally determine their structure and properties. Nafion dispersions have been analyzed by electrospray ionization coupled to

mass spectrometry. Carbon black-Nafion electrosprayed layers have been examined by SEM, XPS, ATR, water contact angle and thermal stability tests in order to study the effects of the ionization potential during the electrospray process, the modification of the ink composition, the carbon black-Nafion ratio in the inks and its dilution.

2.2 Overview of the electrospray deposition technique

Electrospray is a method of liquid atomization, i.e. breaking it into droplets, solely based on the ejection of a liquid under the influence of a strong electric field. Unlike common spray methods, no mechanical force plays a role in the atomization process, that is why the term electrohydrodynamic (EHD) spray is also commonly used to designate electrospray. This term aims to avoid ambiguity with other techniques in which the application of an electric field has no role in creating the spray but charges the particles after the atomization is performed [1]. However, after the exact meaning is clarified, the term electrospray will be used hereinafter for the sake of simplicity.

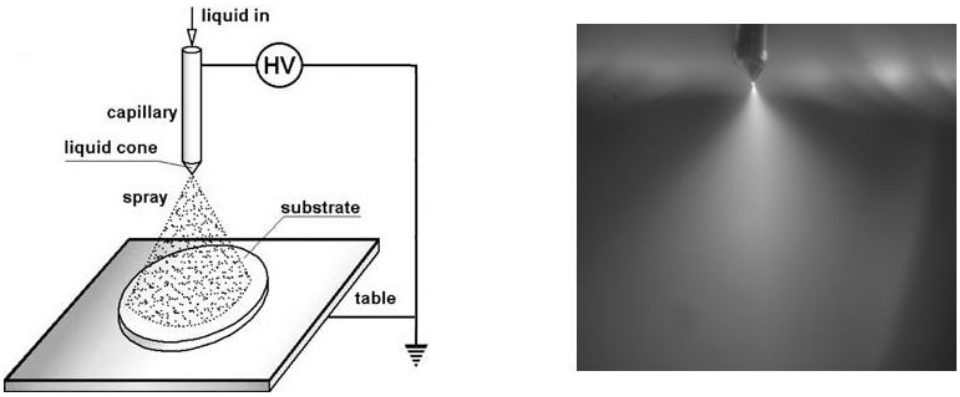

Figure 2-1: Scheme of an electrospray deposition system (Reprinted from reference 3 with permission from Springer Nature, © 2006) and a photograph of the spray used for this study

The electric field imposed between the liquid flowing out of needle and a substrate, gives rise to the formation of a mist of ionized droplets due to charging of the dielectric liquid. A simplified scheme of the electrospray setup is shown in Figure 2-1, where a high voltage is applied between a needle and a facing substrate. Electrospray can produce

charged droplets of a liquid, governed by the electric field between its source and the substrate, with narrow size distributions in the range of micrometers and avoiding droplet coagulation due to the electrostatic repulsion between them [2].

2.2.1 Brief historical review

The first description of an electrospray spraying process dates from 1750, when Jean-Antoine Nollet described that water dripping from a vessel formed an aerosol when the vessel is electrified and placed near electrical ground [4]. However, the first modern report of an electrospray process was not published until 1914, when John Zeleny performed systematic experiments describing how a solvent going through a capillary was break into fine threads disintegrating to small droplets under application of a high electrical potential [5]. A couple of years later, in 1917, Zeleny published another work describing different electrospray modes by using ethanol and glass capillary tubes [6]. In the next decades, studies of the field-dependent deformation of soap films over cylindrical tubes by Wilson and Taylor [7] also detected conical profiles emitting a fine jet that breaks up into a spray of small droplets while Nolan [8] and Macky [9] demonstrated experimentally that similar phenomena occurred with spherical free drops between parallel plates with a potential gradient. The first theoretical description of the cone formation phenomenon in electrospray was published in 1964 by Geoffrey Taylor, which was later named Taylor cone in his honor [10]. During the following years, Taylor continued to his investigation setting the theoretical underpinning of the electrospray process [11, 12]. For more details on evolution of electrospray basic research, a thorough survey of the research in charged particle dynamics, droplets in electric fields, and electrospray ionization can be found on J. N. Smith PhD thesis [13].

By the second half of the 20th century, electrospray emerged as a useful tool for two main practical applications: ion source for mass spectrometry and as a deposition technique. Electrospray as a method to analyze gas phase ions was first introduced in 1968 by Dole et al. in an attempt to determine the mass of polystyrene macromolecules [14]. A couple of decades later, Yamashita and Fenn described for the first time the electrospray

ionization mass spectrometry [15]. J.B. Fenn was later awarded with the Nobel Prize in Chemistry in 2002 ‘for the development of soft desorption ionization methods for mass spectrometric analyses of biological macromolecules’ [16]. Since then, electrospray ionization is a widespread ionization method for mass spectrometry and has become one of the main tools to analyze large biologically macromolecules like proteins and nucleic acids [17].

The first industrial use of the electrospray as a deposition technique was reported by Tilney and Peabody in 1953. They described two different processes called No. 1 and No. 2 used by the Ransburg Company of Indianapolis. No. 1 was an electrostatic-assisted spray painting process using air atomized spray, while No. 2 is defined as a development that ‘represents a fundamental departure from all previous methods of applying coating materials to any surface’, reporting a process only governed electrostatic force with the ability to produce considerably finer particles than can be achieved by other means [18]. The process was developed Ransburg’s housewares factory from 1940 onwards, which manufactured kitchen and other metal goods, to reduce the waste of paint associated with regular handspray painting methods. As a result of their investigation, there was several patents assigned to the Ransburg Electro Coating Corp. describing methods and experimental apparatus for electrostatic atomization during the 1950s [19–23]. A couple of years later, in 1966, Hines described the electrospray painting technique as ‘an accepted industrial process’ and reported the use of a knife edge atomizer with experimental data and some approximate formulas relating fluid properties and the electrical field in the system [24].

2.2.2 Electrospray functioning modes

Electrospray has different functioning modes depending on the physical properties of the liquid (electrical conductivity, surface tension and viscosity), the liquid flow rate, the applied voltage, the geometry of the system and the dielectric strength of the environment. Cloupeau and Prunet-Foch distinguish three main cases: (i) drops are

produced directly at the end of the capillary or the meniscus, (ii) formation of a jet which breaks up into droplets and (iii) the two preceding types occur together [25].

The second mode includes the well-known cone-jet mode, where the meniscus takes the form of a cone extended at its apex by a jet whose breakup produces the droplets. The standard cone-jet and several variants of this mode are depicted in Figure 2-2. For liquids with relatively high conductivities, the jet is produced in the apex of the cone, representing the archetypical form of the cone-jet mode (a). For decreasing conductivities, the acceleration zone is extended towards the base of the cone producing the so-called convergent jet (b). There can also be cases that the cone-jet system can be asymmetrical (c).

Depending on the applied voltage, other variations of the cone-jet mode can be distinguished. The intermittent or pulsed-cone jet (d) appears when the voltage is slightly lower than the required for a single jet, causing an intermittent emission at regular time intervals. On the other hand, when the voltage is higher than the stability point of a single jet, the multi-jet or multi-cone (e) mode can appear [26].

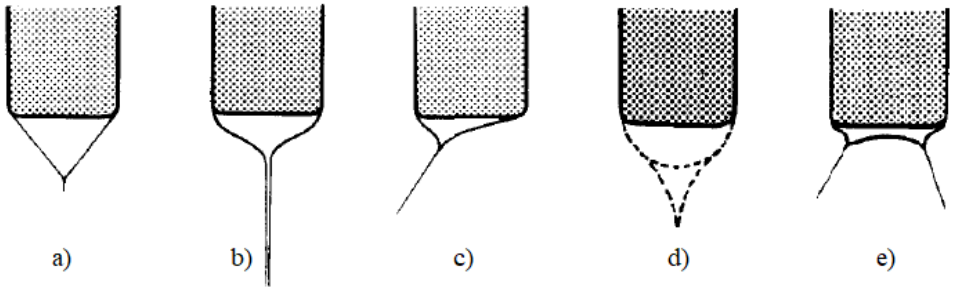

Figure 2-2: Aspects of the meniscus and jet of variants of the cone-jet mode. Reprinted from reference 26 with permission from Elsevier, © 1989

The most appropriate mode for the deposition of thin films is the cone-jet ejection followed by aerosol formation. At the needle end, the meniscus adopts an inverse cone shape (‘Taylor cone’) where particles become ionized. In the apex of the cone, a jet is formed and is ultimately decomposed into a mist of particles and solvent droplets

dispersed in the space over the substrate and deposits under electrostatic interaction. The mechanism of electrospray ionization in the cone-jet mode is usually studied in four different divisions: cone formation and its stability, production of charged droplets, disintegration and evaporation of the charged droplets and deposition of the films. For a review on the fundamental physics of cone-jet mode, one may check the recent review by Rosell-Llompart et al. [27].

2.2.3 Production of the spray

The applied voltage at the electrospray capillary tip produces a separation of positive from negative electrolyte ions in all the volume of the cone liquid. Figure 2-3, depicts the tip of a capillary under positive ionization mode, in which positive ions are dragged to the surface of the liquid converging into a meniscus while negative ions are pushed into of the capillary. The repulsion of the positive ions is able to overcome the surface tension of the liquid and expand the liquid into a Taylor cone, extending into a liquid jet at the least stable point of the meniscus. This charged jet easily breaks up into individual charged droplets proportional to the jet diameter. All those charged droplets are driven away from each other by Coulombic repulsion and spread along the direction of the electric fields forming the spray [28].

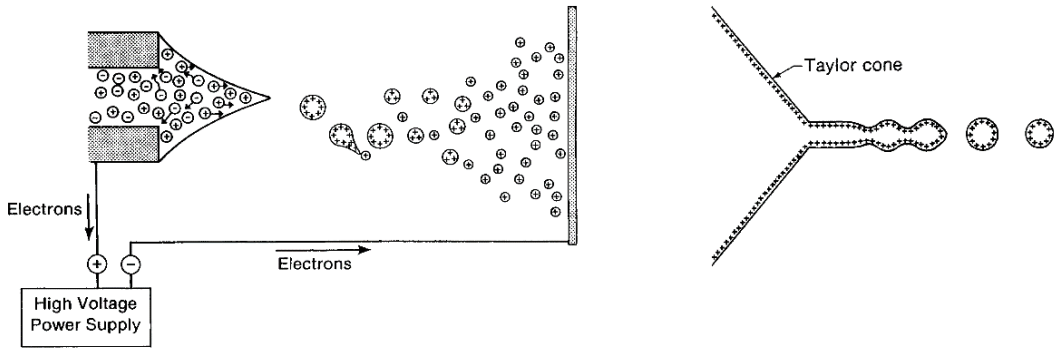

Figure 2-3: Schematic representation of the electrospraying process (left) and detail of the primary drop formation from the charged jet (right). Reprinted from reference 28 with permission from John Wiley and Sons, © 2000

The process of the cone formation has been the subject of theoretical and experimental studies by a number of authors. In the absence of jet emission, Taylor (1964) obtained an exact, infinite electrostatic solution by balancing the surface tension and the electrical normal stress [10]. However, it was not until 1999 when Hartman et al. proposed the first physical model for the liquid cone and jet shape [29]. The appearance of the jet will require the liquid not to be a perfect conductor, to allow the appearance of a component of the electric field tangent to the surface, which, by acting on the surface charges, creates a force driving the liquid and an acceleration of the jet downstream. Two distinct jet behaviors have been observed for the cone-jet mode: the varicose breakup and the whipping jet. In the varicose breakup submode, a straight jet is formed and is subjected to perturbations along its symmetry axis. The main droplets are periodically created from a sequence of swells in the jet. This mode is able to produce homogenous distributions of droplets; although in bimodal distributions (satellite effect) may also be produced depending on the experimental conditions. In the whipping jet submode, the jet is subjected to lateral motions due to the development of lateral perturbations. The formation, on the other hand, present heterogeneous distribution of droplet sizes [27].

The charges of the droplets produced in the jet stream are distributed on droplet surfaces with equidistant spacing to minimize the potential energy [30]. While the droplet is moving to the substrate, it is subjected to two forces acting in opposite directions. One is the surface tension of the droplet, aiming to retain its spherical shape, and the other is the coulombic repulsion between the charges on the surface, trying to break down droplet spheres. As the droplet travels, the thermal energy provided by the ambient gas causes droplet shrinkage due to solvent evaporation, while the charge remains constant and thus increasing the repulsive forces. When the mutual repulsion of charges is high enough to overcome the surface tension of the droplet, the shrinking droplet volume leads to droplet fission, releasing a jet of small, charged progeny droplets. The condition for the instability, also called Coulomb fission, is given by the Rayleigh equation [31]:

$$Q_R = 8\pi(\varepsilon_0 \gamma R^3)^{1/2} \quad (2.1)$$

where Q_R is the charge on the droplet, ε_0 is the permittivity of vacuum, γ is the surface tension of the liquid, and R the radius of the droplet. The shrinkage of the droplets near the Rayleigh limit, releasing of a jet of small, monodisperse charged progeny droplets has been confirmed by a number of experiments [28]. The pattern of the disruption in a droplet is quite similar to the effect at the Taylor cone. Thus, charge density on the droplet is significantly increased in the region of sharper curvature, producing the charged microdroplets emission at ~80 % of the Rayleigh limit [32].

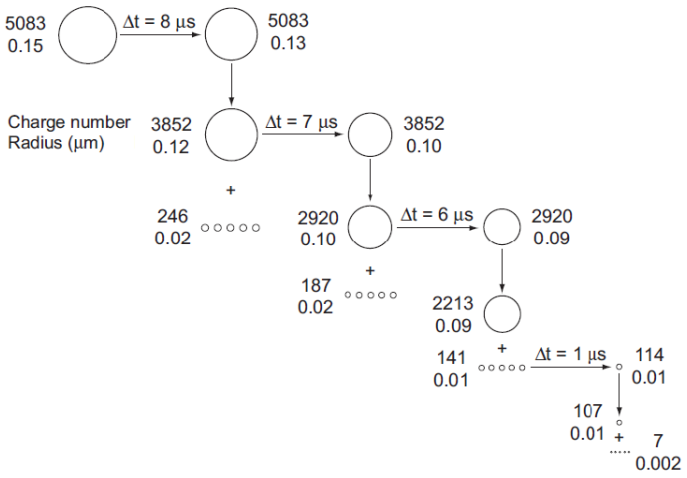

Figure 2-4: History of Coulomb fission of charged water droplets produced by a nanospray device. Reprinted from reference 35 with permission from Springer Nature, © 2014

The droplets produced at low flow rate (below 5 μL/min) have a narrow distribution of sizes with a mean diameter of 3 μm. The parent droplets will eject a couple of smaller offspring droplets, carrying 10-25 % of the total charge, but only about 5 % of the mass of the original droplet [33]. Charged particles, which are preferentially residing at the droplet surface, are reported to preferentially accumulate in the offspring droplets [34]. Figure 2-4 shows the results of droplet evaporation history by Peschke et al. They assumed an initial drop with 0.15 μm radius formed at the Taylor cone of a nanospray capillary with a flow rate of 35 nL/min. The radius and charge of this droplet is followed

in time for three evaporation and fission events. The first generation progeny droplets are shown as well as the fission of one of the progeny droplets that leads to second-generation progeny droplets. These results show that the time between fissions is very short, only some several microseconds, and the times for further fissions of the parent are shorter. The calculations showed that after 15 fissions the droplet has already lost most of the liquid [35]. Continued droplet fission will not only reduce the size of the droplet but also increase charge-to-mass ratio. The process of solvent evaporation and Coulomb fission occurs repeatedly to generate smaller and smaller progeny droplets until the liquid is eliminated and only the charged solid phase remains [32]. Size segregation of primary and secondary droplets was found to occur in some conditions [36]. Special care should be taken with this effect, because it might cause film thickness to vary significantly from the center of the film to its edge and thus degrading the film quality [37].

2.2.4 Electrospray deposition technique

When a colloidal ink is used, the generated droplets may contain nanoparticles in suspension that form deposits after liquid evaporation, or even precursors that can produce chemical reactions either in the deposition or in flight. Thus, electrospray is a suitable technique to fabricate thin films of controlled morphology, as it fulfils the requirements of droplet size, monodispersity and uniform distribution on the substrate. Since thin film properties strongly depend on the size of the particles or the drops forming the layer, electrospray can produce films of excellent quality, reducing the number of voids, flaws and cracks, and ensuring an homogenous thickness and morphology throughout the film [3].

Some authors see the electrospray process as a special kind of electrochemical cell. As in the metal capillary continuous current is delivered, under positive needle polarization, an electrochemical oxidation reaction occurs by creating positive ions or removing negative ions, while an electrochemical reduction reaction removing positive ions takes place at the negative counter electrode. In some cases, it was shown that some compounds, which are normally not ionized in solution, can be ionized by electrochemical oxidation or

reduction [38]. Other authors argued that the presence of ions from the capillary metal tips provides a confirmation of the electrochemical nature of the electrospray process [39]. However, although electrochemical reactions are inherent to the process, there is still controversy between the most prominent researchers in the field, whether or not electrochemistry is a fundamental issue on the understanding of the electrospray process [40]. Overall, the electrospray technique is cheap and easy to handle. It requires relatively low capital investment for a basic set-up, compared to chemical or physical vapor deposition, and the control of the process is governed by means of two fundamental parameters: the liquid flow and the applied voltage. On top of that, the deposition efficiency for charged droplets is much higher than for un-charged droplets methods. The main drawback of this technique is, probably, the low throughput but it .can be overcome by the use of multi-nozzles [41], multi-capillary nozzles [42] or slit-nozzle systems [43].

Electrospray has been reported to be useful for a number of applications that require thin solid films, such as solar cells, fuel cells, lithium batteries, microelectronic devices, piezoelectric actuators, catalyst layers or chemical sensors [44]. A conductive or semi-conductive substrate is usually mandatory for film deposition, however, it is reported that using AC current can be used for film deposition in insulating substrates, possibly due to a reduction in the amount of surface charging [45].

Solvent selection will play a fundamental role on the final layer. The selection of proper solvents to dissolve the particles to deposit will drastically vary the surface morphology of generated particles. In general, using a solvent with low vapor pressure results in particles with smaller size and smoother surface morphology. In contrast, solvents with high vapor pressure, and consequently faster evaporation rate, may result in the formation of highly porous surfaces [46]. An appropriate selection of the solvent and the parameters of the deposition, can secure a deposit with completely dry particles, substantially changing the properties of the resulting deposits in comparison with standard ink-based methods.

In order to gain more insight into the use of the cone-jet mode for deposition of thin films, Rietveld et al. made an exhaustive literature review of the studies of the parameters affecting each of the four sub-processes in cone-jet electrospray deposition. However, with a fixed spray geometry and ink composition, the only parameters that can be modified during electrospray experiments will be the flow rate, current and temperature. These three factors will determine the droplet evolution that will ultimately lead to different film morphologies. In the film formation process, also the surface energies of the compounds and the substrate, namely its structure and temperature, will also have an important role on the final structure of the deposited film [47].

The study of the deposition process is crucial to understand the morphology of the resulting electrosprayed layers. Most of the authors have reported high macroporous structures with dendritic shapes that are probably caused by the control of the electric field in the deposition process due the complete evaporation of the solvents before hitting the substrate. It has been indeed reported that the use of high boiling point solvents result in the deposition of a dense and much less porous layers [48]. Tang and Gomez also confirmed the different properties of the deposits depending on the volatility of the solvents and its ability to achieve a complete evaporation before reaching the substrate [49]. Castillo et al. performed Monte Carlo simulations to predict bulk porosity and surface roughness depending on the approaching velocity to the particles to the substrate [50] and also empirical calculations of experimental parameters to obtain stable cone-jet for two different suspensions; carbon nanoparticles in ethanol with Nafion [51].

2.2.5 Carbon-Nafion based inks in PEM fuel cells

Nafion is a key component for proton exchange membranes and catalytic layers in polymer fuel cells. For instance, Nafion is the industry standard as solid electrolyte in PEM fuel cells and is also incorporated in the catalyst layer to assist in proton and water transport, as explained in the previous chapter. Nafion was thoroughly investigated for decades, but up to this point, some aspects of its behavior have not been yet unraveled. For more information on Nafion research progress and development, Mauritz and Moore

review is recommended for research of Nafion structure and properties up to 2004 [52]. More recently, Kusoglu and Weber published an excellent (and very extensive) review on PFSA ionomers, with a summary of the previous published reviews, where they updated and compiled the latest research trends, such as state-of-the-art in situ characterization techniques as well as multiphysics computation models [53].

While the structures of dry and water-swollen Nafion membranes have been studied extensively, the microstructure of Nafion dispersions in liquid media has not been so thoroughly investigated. The amphiphilic properties of Nafion result in a strong influence of the solvent properties on the Nafion molecular conformation in dilute solutions [54]. Recent studies using small angle neutron scattering and ^{19}F nuclear magnetic resonance techniques have shown that Nafion chains form different types of aggregates depending on the solvent and its concentration (rods, swollen clusters, random-coil network, etc.) [55]. One of the most used solvents for catalyst inks preparation is isopropanol, which is reported to diminish the number of Nafion molecules in a Nafion aggregated particle compared to water [56]. For instance, the effect of isopropanol on Nafion aggregation in water mixtures is reported to enhance hydrophilic interactions over the hydrophobic interactions [57]. A study of the pH of Nafion in isopropanol-water mixtures, proposed that Nafion have less of a preference for sidechain orientation into solution, forming inverted micellar structures, and observed narrow rod-like Nafion aggregates using cryo-TEM [58]. A curious effect is observed when using aliphatic alcohols as solvents, the so-called ‘polyelectrolyte effect’, observed for highly charged ionic polymers in polar solvents. The polyelectrolyte effect causes an abnormally high viscosity, increasing with the dielectric constant for alcohols, but similar in water and in methanol solutions and disappears for high polarity solvents [59]. For example, water/isopropanol mixtures, poorly-defined, highly solvated large particles (> 200 nm) were observed, probably due to a strong polyelectrolyte effect between sulfonated side chains that are solvated by water [60].

While this solvent effect on cast properties has been established, there is still on-going research on effects on Nafion thin films, which are crucial to understand the ionomer properties on the catalyst layer of PEM fuel cells. The structure of ion-conducting polymers when confined to a thin film can be influenced significantly, resulting in drastically different transport characteristics compared to the behavior of bulk membranes [61]. The internal morphology of Nafion thin films has strong effects on water uptake and the substrate/polymer interactions can bias the domain orientation in Nafion thin films [62]. For instance, the hydrophilicity of the substrate was found to enhance interpolymer and polymer/substrate interactions in Nafion thin films [63]. Extensive investigation about molecular dynamics simulation of the substrate effects on the ionomer ultrathin film morphology at different hydration levels have shown that that the affinity of the substrate with the solvent plays a crucial role in the molecular rearrangement of the ionomer film, resulting in completely different morphologies [64].

On top of that, very few studies in literature deal with the adsorption process of Nafion on carbon substrates, although this issue is one of key factors for the optimization and rational design of interfaces in catalyst layers. When carbon black is added to the ink, additional factors must be taken into account for the dispersion of Nafion aggregates in isopropanol. Isopropanol is an excellent solvent for carbon black and is known to form relatively stable dispersions for about 30-40 days [65]. Z potential measurements in carbon black/isopropanol mixtures are close to -70 mV [66], value that is related to the stability of the dispersion. On the other hand, the zeta potential value for the Nafion ionomer in the same dispersion medium has been shown to depend on its concentration [67]. For very diluted dispersions below 0.5 wt%, the zeta potential is close to zero, suggesting that the charge density along the polymer chains is almost negligible [67], but above 1 wt% and up to 5 wt%, the zeta potential values decrease abruptly to a first plateau with values increasing slightly between -8 mV and -12 mV. In this range, there are probably small size aggregates, with high local negative charge density at the polymer-solvent interface. Above that concentration, a dramatic reduction of the zeta potential takes place to reach a second plateau. These new conditions probably

correspond to an increasing number of aggregates negatively charged, whose charge density does not vary. When carbon black aggregates dispersed in isopropanol, which have a highly negative charge, are mixed with those of Nafion, the fluorocarbon chains of Nafion ionomers are probably oriented with the sulfonic groups towards the carbon black surface by repulsion of negative charges. This would finally result in carbon black aggregates covered by negatively charged hydrophobic chains. However, the adsorption will also depend on the hydrophilicity or hydrophobicity of the carbon substrate, as a hydrophilic surface will anchor the sulfonic groups leaving the fluorocarbon skeleton facing outwards, while hydrophobic surfaces will have an opposite effect, with the sulfonic groups facing outwards [68].

When the actual preparation of the catalyst layer come into play, the process gets even more complicated due to the presence of metallic platinum nanoparticles anchored on the carbon surface, and the final Nafion/catalyst structure and property relationship is affected by the processing methods as well as the specific substrate interactions. It is evident that there is a large number of parameters involved in the fabrication process that should be taken into account, which will be explained in the following chapter. Additionally, the presence of platinum nanoparticles on the carbon will also disrupt the previous observations on carbon as sulfonic groups are strongly attracted to Pt surfaces [69]. The situation with the Nafion on the catalyst layer is further complicated by the non-uniform Nafion distribution in the catalyst aggregates [70]. Some approaches managed to homogenize ionomer distribution of carbon surface by NH_x groups. Moreover, they showed that this technique homogenizes also the Nafion distribution through the catalyst layer depth [71]. A better ionomer distribution was also hypothesized in the previous works of our group in electrospray deposition, in which the optimal ionomer content was reduced by half in comparison with traditional ink-based methods [72, 73]. Carbon black-Nafion interactions in electrosprayed films have been scarcely studied, as previous studies in our research group were focused on the performance of electrosprayed catalyst layers as cathodes for PEM fuel cells. In general, the interactions between the catalyst, solvent and the ionomer present in the ink are yet to be fully

understood to control the catalyst layer fabrication process [74]. Along the same lines, this section aims to bring some light on the special properties acquired by the catalyst layers deposited by electrospray.

2.3 Experimental

To analyze the factors influencing the structure and properties of electrosprayed carbon black-Nafion films, the ionization process of Nafion ionomer solutions and the deposits produced by electrospray ionization on carbon black-Nafion inks have been analyzed separately. Additionally, electrosprayed deposits and cast films of these solutions were studied by infrared attenuated total reflection and temperature programmed decomposition under inert atmosphere in a thermobalance.

The resulting surface morphology of carbon black-Nafion films was analyzed by scanning electron microscopy and water contact angle measurements. The interaction of the carbon-Nafion was analyzed by mass spectrometric analysis of the gas phase species resulting during the temperature-programmed decomposition of the ionomer. Additional X-ray photoelectron spectroscopy and attenuated total reflection analysis of the composite layers was performed to complete the characterization.

2.3.1 Electrospray deposition set-up and conditions

Electrospray deposition was performed in a medium laboratory-size setup that allows the deposition on substrates up to 200 cm^2. The Figure 2-5 depicts a schematic of the electrospray deposition setup. The ink suspension was prepared in vials with a volume of 20 cm^3 and immersed in the ultrasonic bath to achieve a better ink homogenization. Afterwards, ink vials were screwed to an adapted head that that is connected to a N_2 inlet on the side and a capillary fitting on its top. The capillary fitting allows removing or modifying the position of the capillary while maintaining the vial gas tight. A flexible borosilicate capillary (VitroCom CV1525) with an approximate length of 35 cm and 150 µm of inner diameter was used in all the experiments. During the deposition process, the catalyst ink was maintained in a thermostatic bath at 22 °C under ultrasonic stirring.

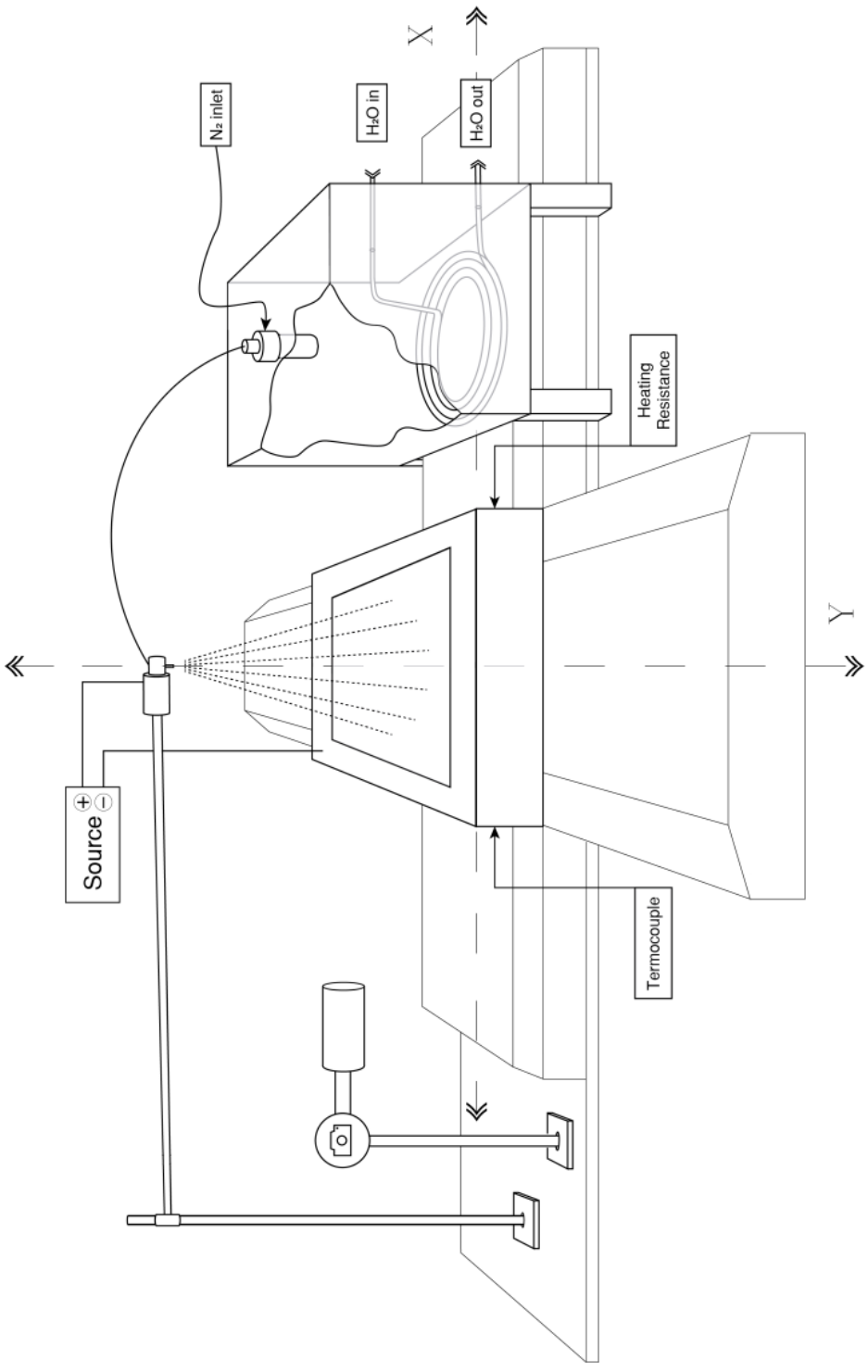

Figure 2-5: Schematic of the electrospray deposition setup

The liquid sample is fed to the tip of the needle through the capillary by applying a small N_2 overpressure inside the vial. Pressure control uses a dead volume of 10 L as buffer controlled by a piezoelectric sensor (Druck PMP-1400) and a high-precision manual pressure regulator with 0-1000 mbar range. The metal needle is embedded in an insulating Teflon support and attached to a metallic arm. This arm is supported in a metallic structure that allows the regulation of the height of the needle distance. A high dc voltage is imposed between the needle (positive pole) and the substrate (negative pole) by means of a high voltage source (Bertran 205B-10R). The application of the voltage originates a spray of very tiny split droplets separated by electrostatic forces when the liquid begins to exit from the capillary. The distance between the needle and the substrate is optimized to allow solvent evaporation and as a consequence, it deposits very fine and dry nanoparticles. Additionally, a digital camera is mounted on a secondary structure allowing an online monitoring of the process.

These charged particles are attracted to the substrate and are deposited according to a pattern, which can be controlled by masks made of insulating material. The substrate base have ceramic heating resistances underneath that can handle temperatures up to 150 °C and mounted on a XY stage (Physik Instrumente M-531) that allow the deposition on large areas.

Different coatings were performed by electrospraying Vulcan XC72 CB-Nafion inks on circular stainless-steel discs of 1 cm diameter length. Before deposition, the stainless-steel substrates were polished with grinding paper (Buehler Grit 180), and washed in sonicated ethanol-acetone solution. Inks were prepared by mixing a commercial solution of Nafion ionomer from Aldrich (5 wt% in water, ethanol and aliphatic alcohols) with Vulcan in isopropanol as dispersion medium. Electrospray conditions were set at 2.5-3.0 cm needle-to-substrate distance, and 0.20-0.40 $mL \cdot h^{-1}$ ink flow rate. During deposition, the substrate temperature was kept at 50 ºC and the vial containing the ink was continuously sonicated at 22ºC. The XY is also used to make much bigger deposits than

the size of the sample to ensure the film homogeneity and eliminate the border effects that can be important due to the small size of the samples.

Several factors were modified in order to analyze their influence on the films structure. To analyze the effect of the ionization voltage on the electrospray deposition process, the applied voltage between the ejector needle and the substrate was varied in the range from -10 to 10 kV. Additionally, ink composition and dilution was also modified from the typical ink composition, which contains 20 wt% Nafion/Vulcan with 1 wt% solid content on isopropanol.

2.3.1 Airbrush deposition

As a reference for comparison, a mechanical spray method was used to coat the same substrates with identical inks and experimental conditions. A commercial airbrush was integrated in the electrospray setup by substituting the ejector needle arm by an arm holder fabricated to operate the airbrush using the capillary as ink feed.

Airbrush is an air-operated tool used to atomize liquid dispersions to produce sprays by the airblast atomization method, using gas at high velocity into a relatively slow-moving stream of liquid [75]. Airbrush systems are based on the Venturi effect, using a stream of compressed air that creates a local reduction in air pressure and thus causing a suction effect to pull the ink from an interconnected reservoir at atmospheric pressure. Atomization occurs through aerodynamic interaction between the liquid and the surrounding gas, leading to unstable wave growth on the liquid jet surface [76]. Turbulence in the liquid, cavitation in the nozzle, and aerodynamic interaction with the surrounding air all are also major contributors to the atomization process. The drops formed in the atomization process in airblast atomization are exclusively dependent on the kinetic energy of the air exhausted through the nozzle. Thus, unlike other atomizers types, airblast aerosols are characterized by the lack of sensitivity of spray geometry characteristics to the physical properties of both the liquid and the surrounding gaseous medium [75].

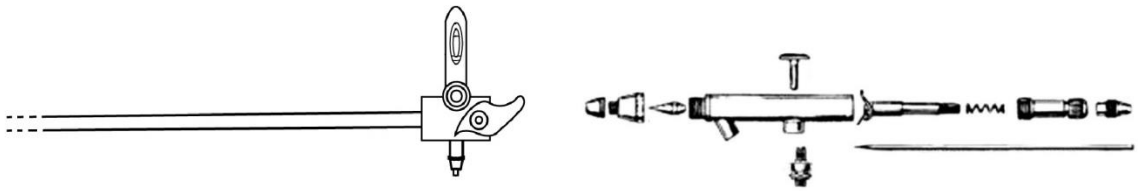

Figure 2-6: Schematic of airbrush support (left) and details of Vega model 2000 (right)

Figure 2-6 depicts a schematic of the Thayer&Chandler Vega 2000 airbrush used in the layer deposition experiments. The compressed air was supplied at a constant pressure of 0.05 barg. Vega 2000 has a self-centering and self-sealing fluid tip with a spring adjuster that customizes lever tension. It also features a dual-action trigger, which enables the simultaneous adjustment of both airflow and ink at the trigger. Trigger depression controls the airflow while the ink flow can be simultaneously adjusted by sliding the trigger back and forth. In the left image shown in Figure 2-6, an arm holder for the commercial Vega 2000 was developed. A homemade Teflon support was attached to the arm, which is interchangeable with the electrospray-needle arm. The Teflon support includes a strapping system for the airbrush with a double-action lever, which can regulate both trigger depression and sliding, and thus improving the reproducibility of the technique. Additionally, the same capillary was used as ink feed by introducing it as close as possible to the nozzle to avoid ink accumulation. The capillary was hold in place by the use of a Teflon tube fabricated for this purpose. The development of the Teflon support allows performing an effective comparison of the electrospray and airbrush process, as the process conditions can be maintained constant until the ink leaves the capillary. The inclusion of a lever in the support also eliminates, the human factor from ink and air regulation, improving the reproducibility and allowing a precise tuning with low ink fluxes with high airflows, reducing drop size and improving solvent evaporation.

2.3.2 Physico-chemical characterization

The **scanning electron microscopy** (SEM) is commonly used to generate high-resolution images of surfaces by analyzing the electron signals produced by a focused beam of electrons on a sample of interest. As the electrons interact with the sample, they can be either 'reflected' (backscattered) from the bulk specimen, in the same way as light in an optical microscope, or analyzed through the secondary electrons released by the incoming (primary) electrons that supply energy to the atomic electrons of the sample [77]. The microscope used in the experiments, belonging to the Microscopy and Surface Analysis Group at CIEMAT, is a Hitachi FE-SEM SU-6600 with a Schottky (thermal) field emission electron source and Everhart-Thornly secondary electron detector for high-resolution images and a low impedance backscattered electron detector. It has and accelerating voltage of 1-30 kV, with imaging resolution of 1.2 nm at 30 kV and 3.0 nm at 1 kV.

X-ray photoelectron spectroscopy (XPS), also referred to as ESCA (electron spectroscopy for chemical analysis), is a technique used to analyze the surface chemistry of materials. X-ray photons have a limited penetrating ability in solid samples, only interacting with the atoms in the outer layers, approximately 1-10 micrometers. Both quantitative elemental and chemical state information can be obtained from XPS analysis, opening the possibility to measure the elemental composition, empirical formula, chemical state and electronic state of the elements within a material [78]. XPS data were acquired using a Perkin-Elmer PHI-5400 spectrometer, belonging to the Microscopy and Surface Analysis Group at CIEMAT. The excitation source was Mg Kα ($h\nu$ = 1253.6 eV) with the aperture lenses set to provide and analysis area of 1 mm diameter. The analyzer was operated at a pass energy of 89.5 eV for general spectra and 35.8 eV for high-resolution spectra. The accelerating voltage was set at 15 kV (20 mA) and the pressure in the analysis chamber was kept below 10^{-9} Torr during acquisition.

Mass spectrometry (MS) is an analytical technique based on the ionization of chemical species and their subsequent analysis according to their mass-to-charge ratio. Mass

spectrometry can provide both qualitative and quantitative information on molecules after their conversion to ions by analyzing the resulting mass spectrum. A mass spectrum is a plot of the ion signal versus mass-to-charge ratio and can be used to determine the elemental signature of a sample, the masses of molecules and particles, and to resolve their chemical structures. The electrospray ionization (ESI) is a soft ionization technique extensively used to obtain gas phase ions, especially in the research field of proteomics, to analyze large biologically macromolecules like proteins and nucleic acids [17]. The design of the electrospray ionization source for mass spectrometry is essentially the same as in the setups used for layer deposition processes [79]. Solutions of Nafion in several solvents were analyzed with an ESI-MS hybrid analyzer (AB Scienx QSTAR-XL), belonging to the Universidad Autónoma de Madrid (SIDI), with ionization voltages in the range between 5 and -5 kV. Ion analysis is performed with a quadrupole time-of-flight (Q-TOF) mass analyzer with a mass range of 20-40000 Da and up to 8000 mass resolution.

Thermogravimetric analysis (TGA) measures the mass of a sample on a controlled atmosphere as a function of temperature [80]. The instrument used for TGA analysis is essentially consisting of an electronic precision balance inside a high temperature oven controlled by temperature program, with a gas inlet system and a data acquisition program. Depending on the selected gas to run the experiment, thermogravimetry may be used to study different processes, such as desorption, absorption, vaporization, oxidation, reduction or decomposition. Evolved gas analysis (EGA) was used to study the gas produced in the decomposition or desorption of the heated sample, allowing qualitative information of the gaseous reaction or decomposition products versus the temperature [81]. Among the different measurement techniques, mass spectrometry is recommended for very low concentrations (ppm level) of small gaseous molecules from samples that are not too complex. The purge gas is transferred from the oven to the spectrometer by a short capillary tube, solely intended for gas transfer, with no separation function [82]. The mass spectra are usually recorded using multiple ion detection (MID) mode, in which specific ion masses are continuously monitored during the entire experiment. The

measurements were carried out in a Mettler-Toledo TGA/SDTA851e with a balance resolution of 1μg and a horizontal oven with a maximum temperature of 1100 ± 0.25 °C. The coupled mass spectrometer is Pfeiffer Vacuum Omnistar GSD-301 with a QMS-200 Prisma quadrupole and a tungsten filament of 70 eV with 1000 V secondary electron multiplier. The spectrometer capillary is embedded in a heated transfer line and inserted into the furnace chamber using a glass tube interface with a secondary outlet to vent the excess gas. The experiments were performed under N_2 atmosphere and heated at 4 $^{o}C \cdot min^{-1}$ up to 600 ºC. The weight loss of the sample and the ion currents for a number of mass-to-charge ratios between 2 and 100 resulting from the analysis of the decomposition products were collected with an interfaced computer. Thermal treatments for some electrosprayed coatings were also carried out in the TG-MS equipment under air flow in order to control and follow in detail the thermal degradation process. The samples were scratched after deposition in planar metallic surfaces and introduced without compaction in TG alumina crucibles. For the sake of simplicity, MS results only show the signals obtained for the mass to charge (m/z) ratios 64 and 69, which can be assigned to the decomposition of sulfonic groups and fluorocarbon chains, respectively.

Attenuated total reflectance (ATR) has been widely used in the recent years to perform solid mid-infrared analyses because it avoids the main drawbacks of standard Fourier-transform infrared spectroscopy (FTIR) analyses, namely sample preparation and spectral reproducibility, by using reflected beams from the sample instead of the transmitted infrared radiation directly through the sample. ATR measurement requires the inclusion of a separate attachment with an optical crystal with a high refractive index. After the sample is intimate contact with the crystal, generally by applying pressure, the source beam is passed through the crystal reflecting at least once in the internal surface in contact with sample forming the evanescent wave of several micrometers, which extends into the sample and is collected by the detector [83]. A Thermo-Fisher Nicolet iS50 spectrometer with a ceramic Polaris™ IR source and a tungsten-halogen white light source was used in the experiments. The spectrometer includes a built-in mid- and far-IR capable diamond ATR (80 to over 5000 cm^{-1}), with a DLaTGS pyroelectric detector and

a pressure device with a down force of 60 lbs. The samples were deposited in thin (200 µm) steel sheets to facilitate the compression and facilitate substrate deformation for an enhanced contact with the sample crystal.

2.3.3 Water contact angle measurements

The contact angle is used quantify the wetting of a solid by a liquid. The contact angle of a liquid droplet on a flat solid surface, θ_0, is defined as the angle formed by the liquid in a three-phase boundary of liquid, gas and solid system at a given pressure and temperature. The balance at the three-phase contact is described by the Young equation:

$$\cos\theta_0 = \frac{\gamma_{SV} - \gamma_{SL}}{\gamma_{LV}} \qquad (2.2)$$

where γ_{SL}, γ_{SV}, and γ_{LV} are the interfacial free energy of the solid-liquid, solid-gas, and liquid-gas interfaces, respectively. When the contact angle with water lies between 0 and 90°, the surface is defined as hydrophilic, and when greater than 90° is defined as hydrophobic. However, the roughness of a surface can modify the wettability of the surface can either enhance its hydrophilicity or its hydrophobicity. Depending on the level of surface roughness, two different states can be distinguished [84].The first one is the Wenzel model, which describes a liquid drop filling the solid asperities. Wenzel proposed a theoretical model, by modifying Young's equation, that describes the contact angle θ at a rough surface [85]:

$$\cos\theta = \frac{r_f(\gamma_{SV} - \gamma_{SL})}{\gamma_{LV}} = \mathrm{r}_f \cos\theta_0 \qquad (2.3)$$

where r_f is the roughness factor, which is defined the area of the actual surface to that of a smooth surface having the same geometric shape and dimensions. Since the roughness factor is always larger than 1, this equation predicts that the surface roughness both enhances the hydrophilicity of hydrophilic surfaces and the hydrophobicity of hydrophobic ones. The other possible model explains the case of the water droplet not

penetrating in the surface asperities. Cassie and Baxter proposed an equation to explain the wettability or water-repellency of porous surfaces. The contact angle of a heterogeneous surface composed of two different materials can be expressed by the following equation [86]:

$$\cos\theta = f_1 \cos\theta_1 + f_2 \cos\theta_2 \quad (2.4)$$

Where f_1 and f_2 are surface area fractions with their corresponding θ_1 and θ_2 contact angles. If f_2 is considered pore area with trapped air, the equation can be modified as follows:

$$\cos\theta = -1 + (1 - \cos\theta_0)\, f \quad (2.5)$$

where f represents the area fraction of liquid-solid interface. Since in the most hydrophobic solids the contact angle on a flat surface never exceeds 120°, this equation is generally used to explain the superhydrophobicity of rough surfaces that entrap air in the hollows of their surface.

Water contact angle (WCA) measurements were performed to test the hydrophobicity of the carbon-based layers, using an optical tensiometer (Theta200 Basic, Biolin Scientific) at ambient temperature (23 °C) and relative humidity (30-35 %). All the measurements were performed using drops of 5-6 µL for 400 s and, before the measurements, a blank experiment of volume evaporation of the water drop is performed with a planar non-porous Teflon piece. Since Nafion is known for its ability to absorb large quantities of water, all WCA measurements have been performed after layer deposition and checked again after a ‘hydrophilic treatment’ that consists in deionized water immersion for 48 h and drying overnight at 80 °C.

2.4 Results and discussion

2.4.1 Electrospray of Nafion

One of the open questions regarding the electrospray process of carbon black inks is the behavior of the Nafion colloidal dispersions under those conditions. The ionization process of Nafion dispersions is analyzed by ESI-MS by modifying the solvent and the ionomer concentration. The ESI-MS analysis has yielded information about the fragmentation patterns obtained under electrospray ionization in high vacuum. In principle, the soft ionization produced by electrospray on large mass molecules allows the formation of desolvated ions to be analyzed by mass spectrometry and determine its mass and/or its structure. It must be taken into account that high-vacuum ESI-MS ionization differs from the conditions on the experimental setup of Figure 2-5, as the ambient conditions, including air humidity, were proven to affect the process to some extent [36].

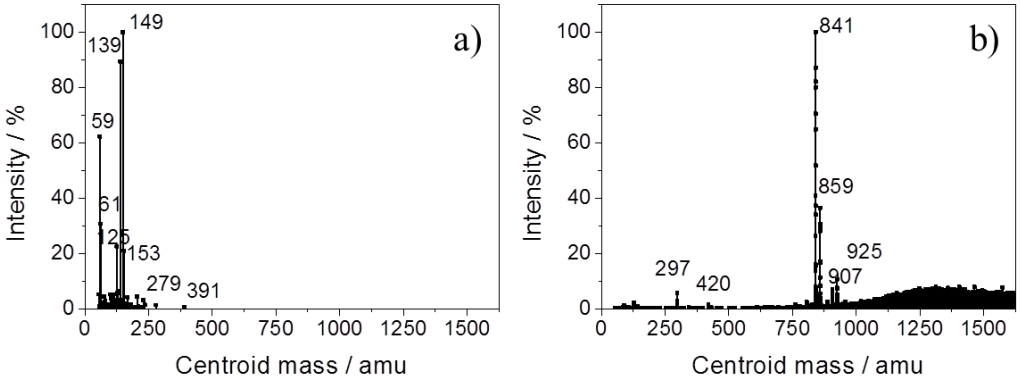

Figure 2-7: Mass spectrometry fragmentation pattern obtained for the as-received Nafion ionomer solution (5 wt%) in a) positive and b) negative ionization modes

Figure 2-7 compiles the fragmentation patterns obtained for the Nafion ionomer solution as received in positive and negative ionization modes. The positive ionization mode yields very small *m/z* fragments (below 391 Da) in the mass scan range from 1-3000 Da.

On the contrary, the application of the negative ionization mode to the same solution yields a very complex and continuous background in the whole range from 1 to 3000 Da.

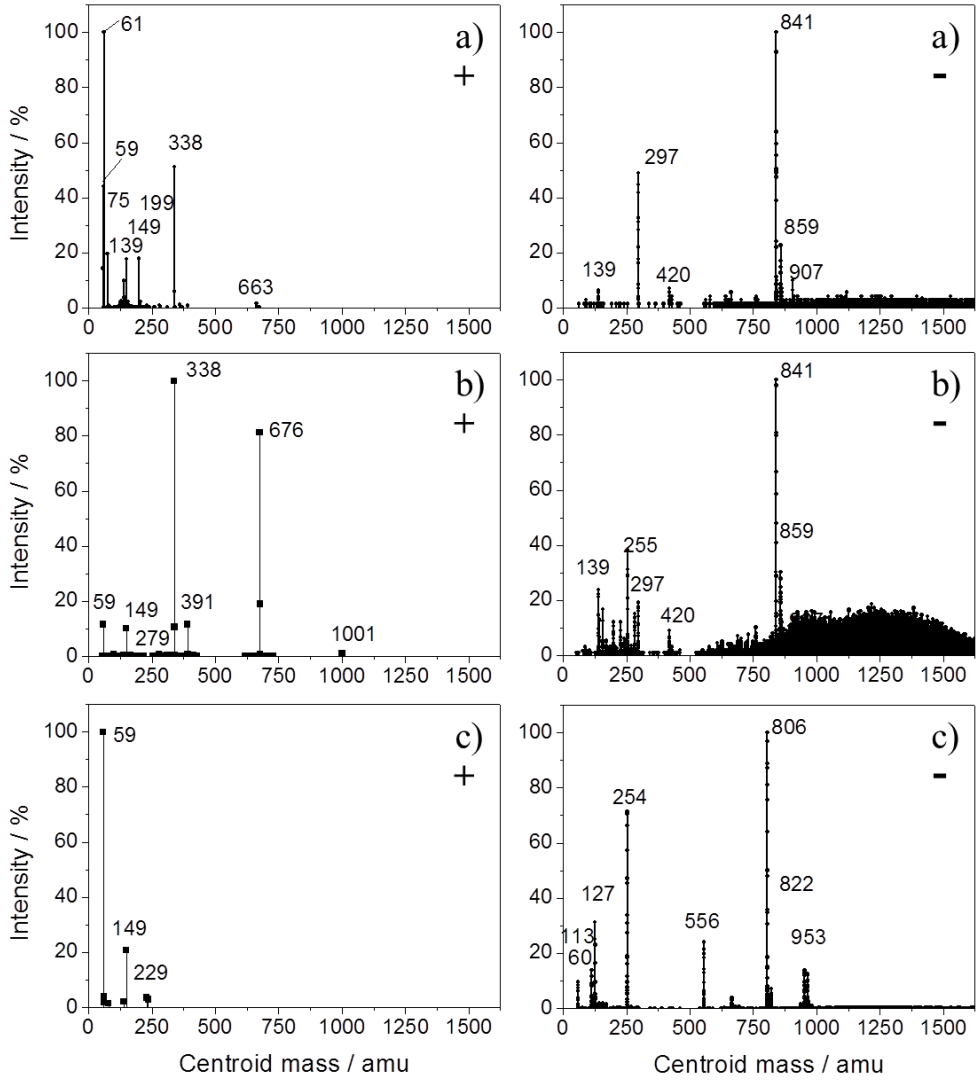

Figure 2-8: Mass spectrometry analyses of Nafion solutions sampled by electrospray ionization in positive mode (+) and in negative mode (-) after dilution at 2wt% with different solvents: a) isopropanol, b) acetone and c) water

The influence of the solvent on electrospray ionization was studied at a Nafion dilution of 2 wt% in isopropanol, acetone and water (Figure 2-8). The fragmentation patterns point out that the Nafion aggregation in solvents strongly affects the ionization process. The

positive and the negative ionization modes follow a similar trend than in more concentrated solutions: smaller fragments are registered for positive ionization, and more complex mass spectra with a continuous background and larger fragments are observed for the negative ionization mode.

In order to obtain more information about the effect of electrospray ionization on the Nafion structure, ATR technique has been used for obtaining infrared absorption spectra. Dry Nafion films prepared by casting from different solutions: as-received (5 wt%), water (2 wt%) and isopropranol (2 wt%); are compared with a electrosprayed layer of the isopropanol-diluted Nafion. The obtained spectra depicted in Figure 2-9 reveal a change in the Nafion structure depending on the solvent for its dispersion.

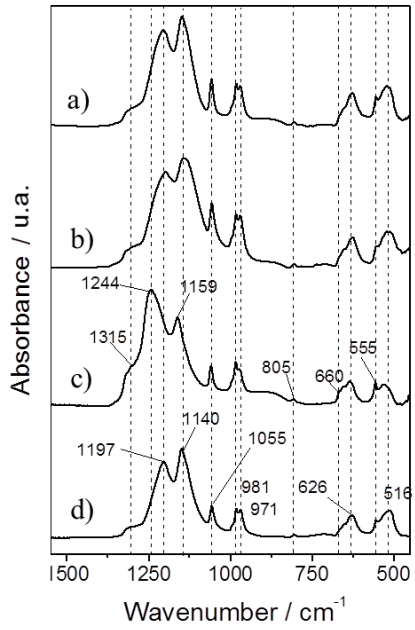

Wavenumber (cm^{-1})	Assignment
~1315	C-C stretching, asymmetric
~1200	CF_2 stretching, asymmetric
~1140	CF_2 stretching, symmetric
~1055	S–O stretching, symmetric
~ 980	C–O–C stretching, asymmetric; intermediate ether bond
~ 970	C–O–C stretching, symmetric; -ether bond closer to SO_3
~ 805	C–S stretching (hydrophilic region)

Figure 2-9: ATR spectra of Nafion films prepared by casting: a) Nafion original solution, b) dilution in water up to 2 wt% and c) dilution of the original solution in isopropanol up to 2 wt%. d) Spectrum of an electrosprayed Nafion film prepared from the isopropanol dilution. The embedded table compiles the assignment for Nafion infrared absorption bands

The main infrared absorption bands of Nafion can be assigned as indicated in the embedded table of Figure 2-9. The results evidence that Nafion films from the isopropanol solution show significant differences with those obtained from the original solution and the water diluted ionomer. The effect of isopropanol on Nafion aggregation is reported to enhance hydrophilic interactions over the hydrophobic interactions [57]. The shifts in CF_2 stretching for isopropanol indicate that hydrophobic moieties could undergo significant interactions with the perfluorinated backbone. However, the blue shift observed in the CF_2 stretching bands disappears when the same solution is electrosprayed. This could be attributed to the fast removal of the solvent during the electrospray ionization process. The blue shift in CF_2 stretching bands has been previously assigned to a higher crystallinity of the Nafion film, mainly favored for thinner films [87].

The ESI-MS and ATR results indicate that solvent election in Nafion colloidal solutions seems to be a key factor for the resulting structure of the polymer after desolvation using electrospray ionization. Isopropanol dilution clearly enhances chain fragmentation, probably because it forms less voluminous Nafion aggregates in solution. This result is in agreement with the reported dispersion or solution behavior of Nafion in different types of solvents. Nafion ionomer is reported to form poorly-defined and highly solvated large particles in water/isopropanol mixtures, while in water is less solvated and even much less solvated in isopropanol [60].

To evaluate the effect of Nafion dilution, different isopropanol solutions with Nafion ionomer concentrations were analyzed in the range between 1 and 4 wt%. As it can be appreciated in Figure 2-10, by reducing progressively the Nafion ionomer concentration from 4 to 1 wt%, the ionized fragments obtained under positive ionization are closer to the polymer equivalent weight.

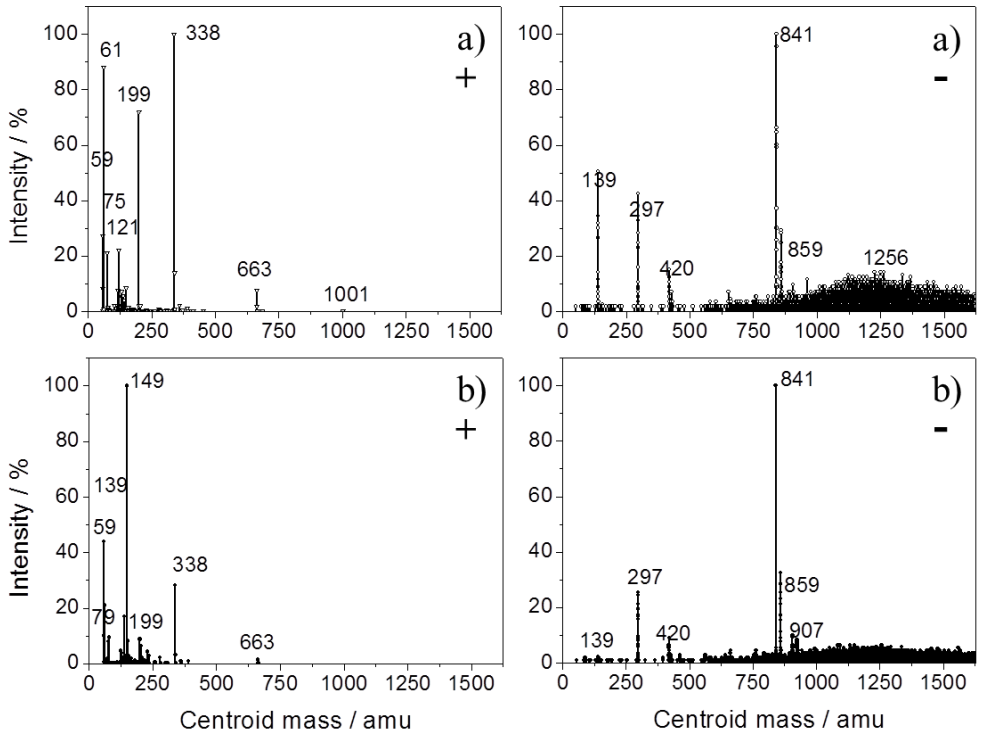

Figure 2-10: Mass spectrometry analysis of isopropanol Nafion solutions by electrospray ionization in positive mode (+) and in negative mode (-) after dilution at a) 1 wt% and b) 4 wt%

For a Nafion ionomer with an equivalent weight of 1000, the general structure of Nafion shown in Figure 1.5 would take the values of x = 5, y = 1 and z = 1, with the general formula of $HC_{17}F_{36}SO_5$. In the positive ionization, the fragment observed in the spectra with *m/z* = 338 at both dilutions could be attributed to perfluorohexane (C_6F_{14}) formed from the fluorocarbon backbone, while its counterpart from a single charged molecule would correspond to $HC_{11}F_{22}SO_5$ (*m/z* = 663) is also observed. With increasing Nafion concentration, the peak corresponding to *m/z*=149, which can be ascribed to trifluoromethanesulfonic acid (CF_3–SO_3H), abruptly increases its intensity. For the negative ionization mode, no significant changes were observed in the fragmentation pattern depending on the Nafion concentration. The main peaks correspond to *m/z* values of 841 and 297, that can be probably assigned to a fluorocarbon backbone that has lost a -CF_2=CF-SO_3 group and to a CO containing perfluoroalkane ($C_6F_{11}O$) respectively. $C_6F_{11}O$ is probably produced from the side-chain cleavage and was previously detected in

degraded Nafion membranes [88]. For more information on the characterization of Nafion mass spectra on may check the investigation of Feng et al. on membrane thermolysis products [89]. Figure 2-11 shows the typical Nafion structure and the expected formation of chain fragments analyzed during the electrospray ionization under positive and negative modes.

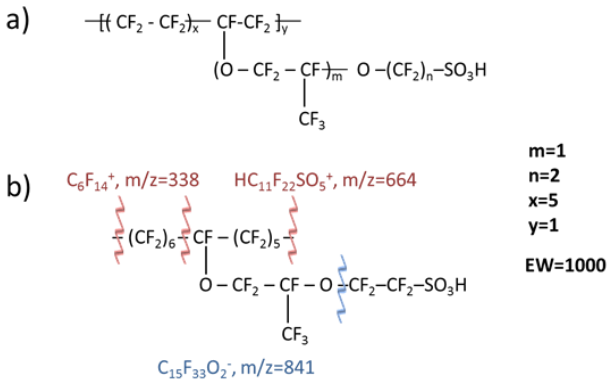

Figure 2-11: a) Nafion (1000 EW) chemical structure and b) structure after ESI-MS analysis

From the spectra in Figure 2-10, it can be assumed as a general trend that diluted solutions favors the ionization of isolated chains of the Nafion polymer is favored. For concentrated solutions, a stronger aggregation of Nafion chains is probably occurring. This presumably produces very heavy mass fragments that cannot be detected and very small fragments with *m/z* values below 300 Da appearing in the spectrum. This is concomitant with zeta potential measurements of Nafion in isopropanol mixtures, in which a change from dispersions with rod-like aggregates to micelles with high local charge density is detected as concentration increases [67].

2.4.2 Electrosprayed carbon black-Nafion inks

Including carbon black powder in a Nafion containing solution to be deposited by electrospray will modify the ionomer behavior during the ionization process of the ink. The interaction of the ionomer with the carbon surface groups may induce the specific adsorption and reduce the amount of free Nafion in solution decreasing its concentration in the micellar phase [90]. Therefore, the previous observations on electrosprayed Nafion

solutions could be not completely transferable to carbon containing inks. By taking this into account, it has been analyzed the effect of the ionization mode and the magnitude of the applied voltage on the electrospray deposit, the effect of the Nafion-carbon black proportion on the resulting film and the influence of the ink dilution. The composition of the ink selected is 20 wt% Nafion with respect to the carbon black, with a total 1 wt% in solid content in the ink dispersed in isopropanol. All the films were deposited with loadings 0.8 $mg \cdot cm^{-2}$ of carbon-Nafion composite. For a complete characterization of the morphology versus carbon loading, one may revise Chapter 4.

Effect of the ionization potential

Inks with 20 wt% Nafion of total solid matter were electrosprayed under positive and negative ionization modes by applying voltages of ±7 and ±10 kV. The deposited films were examined by SEM and the water contact angle with their surface measured. Figure 2-12 compiles surface micrographs of the samples, and compared with airbrushed samples (notice the different magnification) that reveal clear differences regarding the compaction of the aggregates. These differences can be related to both the ionization mode and the applied voltage: the larger the voltage the smaller the size of the aggregates; under negative ionization mode, the repulsion among particles seems to yield a better dispersion of the carbon globules in the aggregates and a more homogeneous surface. The sizes of the aggregates in fractal structures formed by electrospraying the carbon ink are globally thicker, in the range of few micrometers, with larger pores among them than in the case of an airbrushed sample.

The application of positive or negative ionization potentials has an obvious effect on the size of the Nafion/CB aggregates, which reflects a change in the deposition mechanism. The application of negative ionization potentials during the electrospray process probably originates stronger repulsion between the carbon black aggregates, leading to smaller globules that are better dispersed. The effect of electrostatic repulsion could also be the cause of the larger volume of the pores and the bigger size of the aggregates for moderate voltages. The aggregates produced by positive ionization also seem to be more

interconnected, although the orientation of Nafion on the carbon aggregates seems to be unaffected.

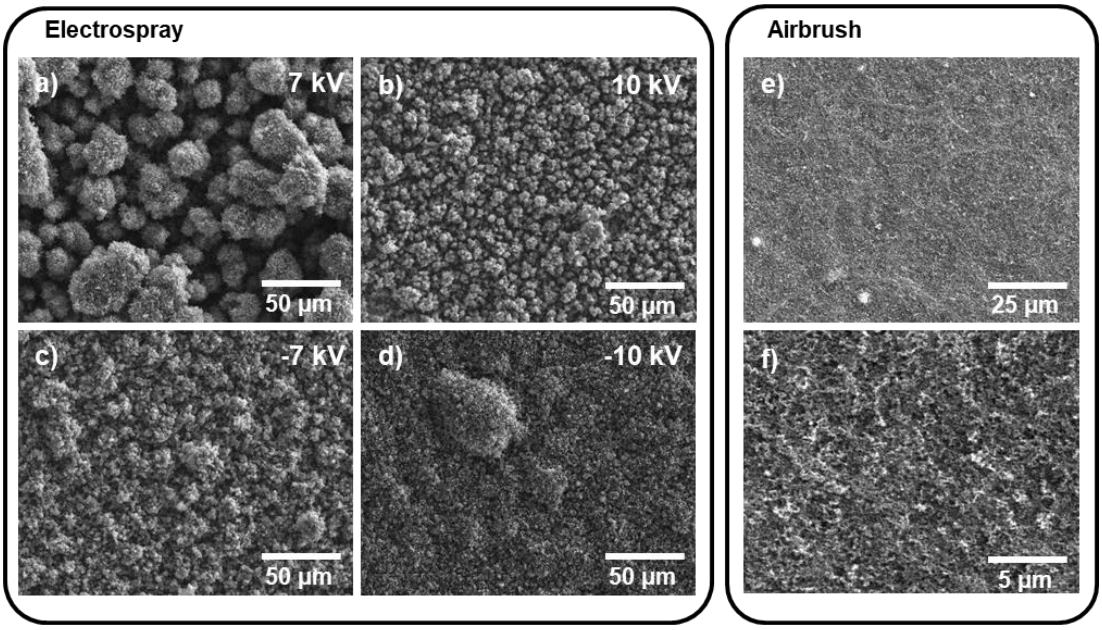

Figure 2-12: SEM images of carbon black-Nafion electrosprayed layers with positive (a and b) and negative (c and d) ionization modes applied at 7 and 10 kV. As comparison, the same ink was also deposited with airbrush (e and f)

The surface of all the electrospray prepared samples is superhydrophobic, as reflected by contact angle measurements with values of $\theta > 160^{o}$. According to these measurements, the differences found in the morphology of electrosprayed layers do not seem to modify their interaction with water. Water contact angle measurements of electrosprayed (7 kV) and airbrushed layers are shown in Figure 2-13. The electrosprayed layers with different voltages are not shown for the sake of simplicity, but similar values are recorded. Electrosprayed layers maintain exactly the same water interaction after the hydrophilic treatment and the constant decrease in angle with time is proven to be caused by drop evaporation after performing a blank experiment (with Teflon). In contrast, the airbrushed layer shows initially certain degree of superhydrophobicity (WCA values close to 150^{o}) that is progressively lost with the hydrophilic treatment. Some larger angle decrease rates as compared with electrosprayed layer also point out to drop imbibition

into the layer. On the airbrushed films, the hydrophilic treatment gives rise to an important change in reducing the contact angle below 120º after its immersion; in contrast, no significant change after hydrophilic treatment was observed for electrosprayed films, reflecting a durable and stable superhydrophobic character.

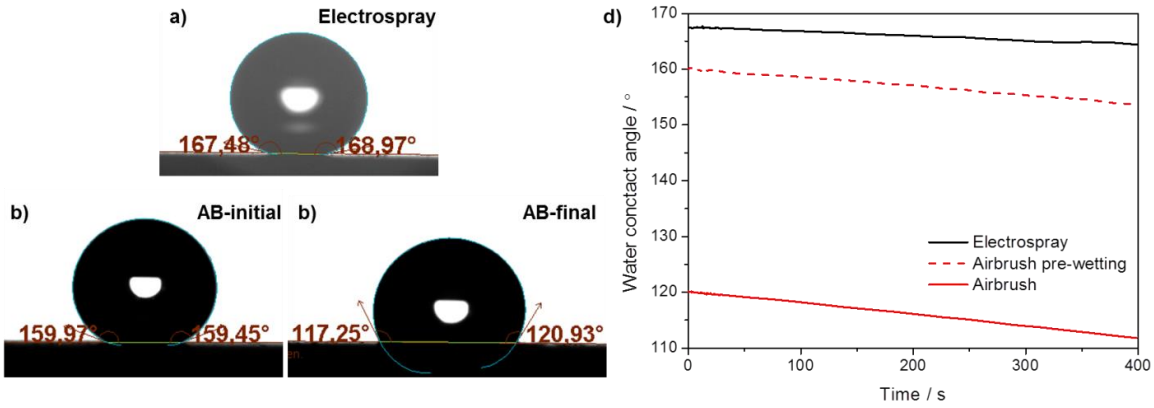

Figure 2-13: Water contact angle measured for the a) electrosprayed (7 kV) and airbrushed layers. Airbrushed layer is shown b) before and c) after hydrophilic treatment

Since chemical modification may increase hydrophobicity to contact angles of up to 120° in planar substrates, but not more, superhydrophobicity must be a main consequence of the surface morphology, the so-called Lotus' effect, when roughness patterns are below the capillary length [84]. Wetting in the Cassie-Baxter's state is a requirement for achieving superhydrophobicity, so the dendritic morphology resulting from the deposition process explains the superhydrophobic ability of the electrosprayed layers that completely avoids water imbibition into the layers as compared with airbrushed layers. The drastic reduction of the contact angle for the airbrushed layers may be caused by a change in Nafion, that cannot be explained by the technique itself.

The addition of Vulcan carbon to the ink originates some changes in the infrared absorption bands. A detailed ATR spectrum is shown in Figure 2-14 for an electrosprayed (at 7 kV) and airbrushed samples of the same ink. These results reveal a slight blue shift for airbrushed films as compared to those prepared by electrospray.

Although it is attenuated, the results have a similar tendency as the observed for dried and electrosprayed Nafion samples. Another particularity for the electrosprayed sample is some attenuation of the band at 1060 cm^{-1}, corresponding to the SO stretching mode.

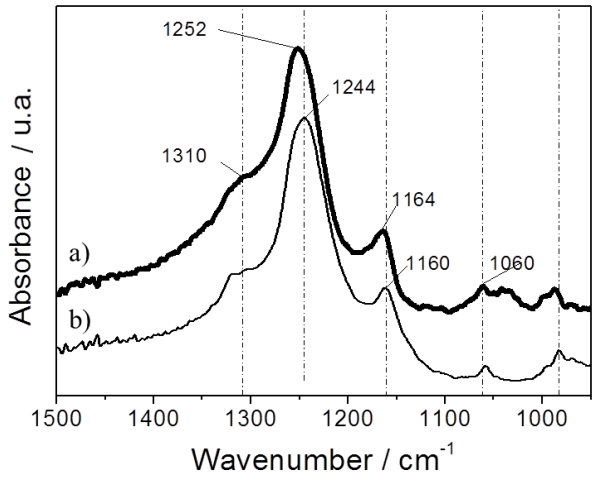

Figure 2-14: ATR-IR spectra obtained for Vulcan XC72-Nafion films prepared from an isopropropanol diluted ink by means of a) airbrush and b) electrospray (7 kV)

However, the infrared absorption measurement of Vulcan-containing samples is problematic, because the presence of carbon black confers the sample a strong black color, which is not appropriated for ATR measurements. Dark materials are difficult to analyze using ATR, because of their strong absorption and scattering of the infrared radiation that can make these type of materials opaque to infrared radiation. A possible solution for this issue could be the use of germanium crystals, which is supposed to give a much cleaner spectrum of dark samples due to a reduced penetration depth in the sample [91]. However, the use of TG and XPS techniques was preferred due to their capability to provide more insights on this particular type of samples.

XPS analyses were carried out to determine if the ionization process originates some differences in the surface of the coatings. The profiles obtained for airbrushed and electrosprayed (±7 and ±10 kV) layers at the *C1s* and *O1s* regions are presented in Figure 2-15. The analysis of the spectra of the electrosprayed layers indicates that there are no

relevant differences on the surface composition among them at different ionization voltages, but there is a clear change in comparison with the surface composition of the airbrushed film. In the *C1s* binding energy region, the proportion between the signals for -CF_2-(291.2 eV) and for C-C (284.3 eV) is higher for all layers prepared by electrospray. Furthermore, in the *O1s* binding energy region, the electrosprayed samples show higher intensities than the airbrushed layers due to the Nafion ether bonds (-CF_2-O-CF_2-) at 534.4 eV with regard to the oxygen bonded to the sulfonic groups (signal at *ca.* 530.7 eV). This observation can be explained as the result of a better distribution of the Nafion ionomer on the surface of the carbon black due to a favored specific interaction (adsorption) of the polymer sulfonic groups with the support surface when electrospray ionization is applied for ink deposition.

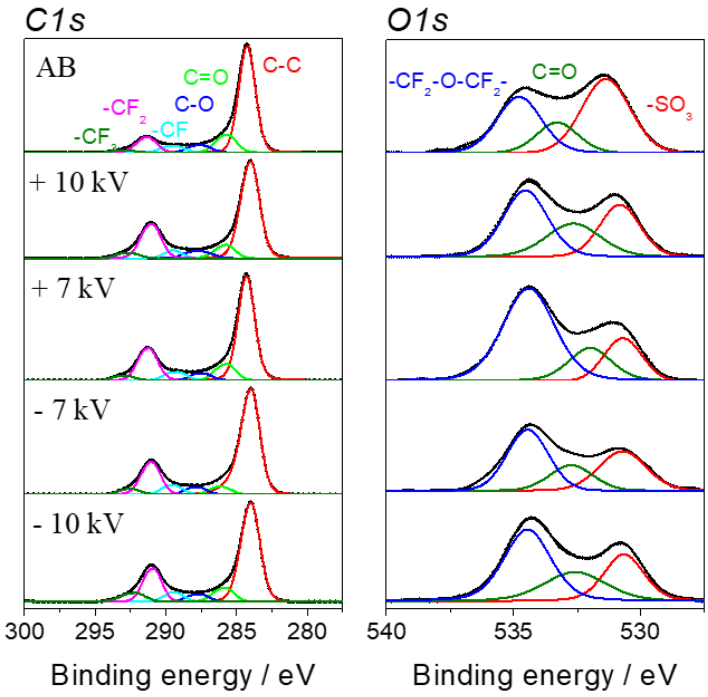

Figure 2-15: XPS analysis in the C1s and O1s binding energy regions of carbon black-Nafion (20 wt%) coatings prepared by airbrush and electrospray with positive and negative ionization and potentials of 7.5 and 10.0 kV

If the deposition process is favoring specific interaction between the ionomer and the carbon, additional information about the deposits could be obtained from the thermal decomposition of these layers. With this aim, samples of Nafion ionomer diluted in isopropanol, and CB-Nafion (20 wt%) deposits prepared by airbrush and electrospray were analyzed by thermogravimetry. Figure 2-16 depicts the mass spectrometer signals for m/z = 64 and m/z = 69, which can be assigned to the decomposition of sulfonic groups and fluorocarbon chains, respectively. In the absence of carbon black, it is clear that for pure Nafion deposits (open symbols), the decomposition of sulfonic groups takes place at lower temperatures (*ca.* 320ºC) independently of the preparation method. However, for carbon black-Nafion inks, the decomposition temperature of sulfonic groups is increased to temperatures over 350ºC. On the other hand, fluorocarbon chains in electrosprayed layers seem to stabilize at least three different fluorocarbon structures with different decomposition temperatures, in contrast with the airbrushed sample that has an invariable fluorocarbon decomposition temperature, whether or not there is carbon on the ink.

The electrospray process seems to stabilize homogeneously the sulfonic groups in the presence of carbon black, leading to a main decomposition peak at *ca.* 350ºC. Additionally, the decomposition process of the fluorocarbon backbone is more homogeneous and takes place in two steps with peaks at *ca.* 350 and 400 ºC. However, airbrushed samples have labile sulfonic groups (approximately one-half) decomposing below 350 ºC, while the rest of the sulfonic decomposition is mainly associated to that of the fluorocarbon backbone, yielding a single peak at *ca.* 400ºC.

Additional thermogravimetric measurements were performed for the electrosprayed layers (7 kV) under oxidative conditions. The temperature of complete Nafion oxidation under air flow was previously narrowed down to the range between 320-330 ºC. Electrosprayed layers deposited on the metallic substrates (not powder, as in the previous TG experiments) were thermally treated under isothermal conditions in the range between 300 and 340 ºC, while registering the *m/z* ratios for sulfonic and fluorocarbon

fragments during the heating up to the temperature of the isothermal treatment. Additionally, WCA measurements were performed to the layers after the thermal treatment. It was found that layers heated up to 320ºC do not lose their hydrophobicity, but heating over 330ºC completely destroys this property, and the layers become completely hydrophilic.

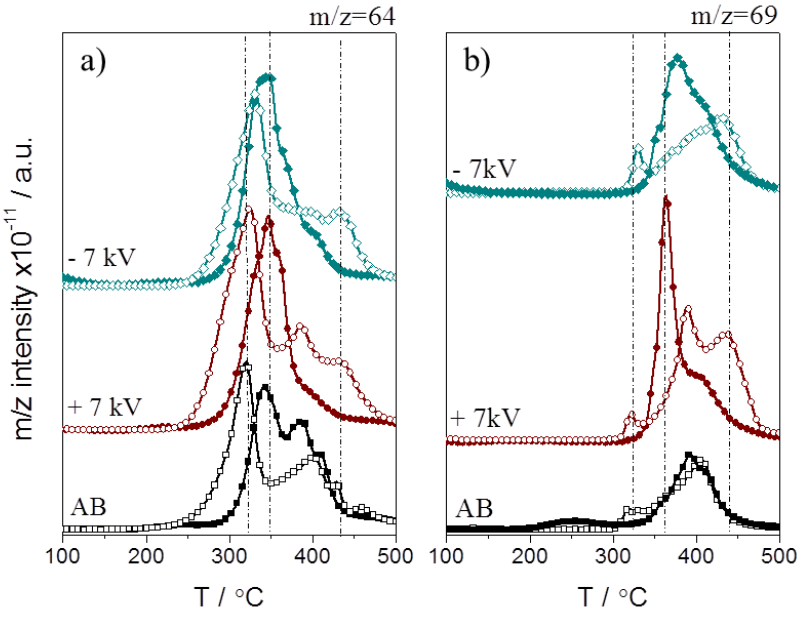

Figure 2-16: Mass spectrometer signals for m/z = 64 and m/z = 69 registered during the thermal decomposition under inert atmosphere of the Nafion (open symbols) and CB-Nafion (20 wt%) (solid symbols) films prepared by electrospray under positive and negative ionization modes and by airbrush

Although the thermal treatment contributes to the partial decomposition of the Nafion sulfonic groups, as depicted in Figure 2-17a, this process does not change the superhydrophobicity of the surface at temperatures as high as 320 ºC. Above this temperature, the decomposition of the fluorocarbon backbone is accompanied by the transformation of the water contact angle to hydrophilic layers. In order to check if the thermal treatment had modified the porous structure of the sample, one the samples was examined by SEM before and after its thermal treatment at 340ºC (Figure 2-17b), where no significant structural differences were found. Therefore, it can be concluded that the superhydrophobicity of electrosprayed layers cannot be completely attributed to the

surface morphology of the carbon, at least to the resolution observed by SEM. The particular arrangement of Nafion and carbon black, induced by the electrospray ionization, combined with the highly porous structure of the carbon aggregates are both the key factors behind the superhydrophobic character to the surface.

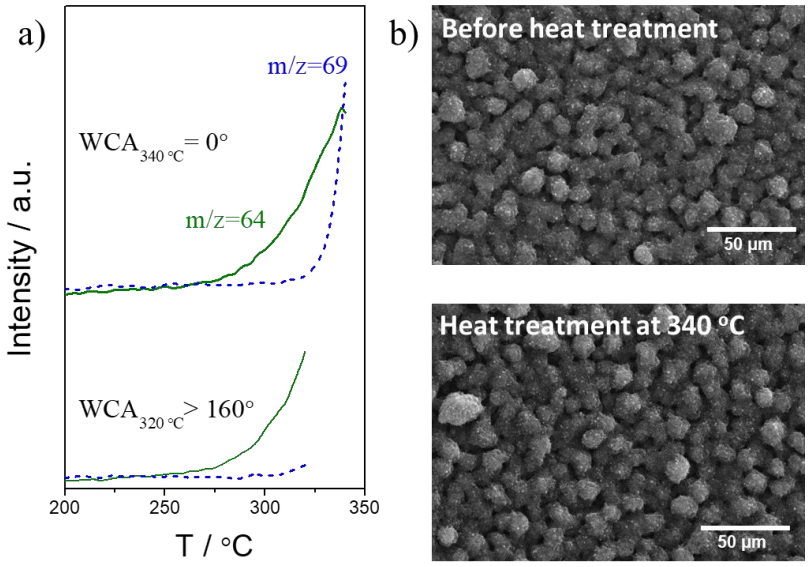

Figure 2-17: a) Intensity of the m/z = 64 and m/z = 69 signals as a function of the temperature during thermal treatments up to 320 and 340 °C under air flow. b) SEM micrographs of the surface of the CB-Nafion electrosprayed sample before and after heat treatments

The differences between airbrushed and electrospray deposited films can be discussed on the basis of key differences in the deposition mechanism. Even though the formation of carbon aggregates surrounded by Nafion chains in isopropanol dispersion medium is an intrinsic property of the ink, as discussed in the introduction, from the opposing results between electrosprayed and airbrushed deposition, it is clear that this aggregation state could be modified by the ink drying process during deposition, which is different in each method. For the airbrushing process, the drying occurs on the surface of the substrate after the deposition process, and is much slower than for electrospray deposition, for which the solvent is removed before the carbon black-Nafion composite hits the target substrate. As a result of the different drying process, the interaction of Nafion and carbon black has shown to be experimentally much weaker in the airbrushed deposits. Although

initially showing a superhydrophobic behavior, the ionomer orientation or distribution seems to change by interaction with water, which is probably causing a reorganization of the polymeric component. On the contrary, electrosprayed layers maintain intact their superhydrophobic behavior even after very long periods of water immersion indicating the high stability of its structure. The hydrophobic behavior of the electrosprayed layers, supported by the surface chemical composition observed by XPS and the increase of the thermal stability of the Nafion points out to a stable arrangement of Nafion on the carbon particles, probably with the sulfonic groups anchored to the carbon and leaving the fluorocarbon backbone facing the voids of the porous layer.

The hypothesis of an enhanced order in electrosprayed layers seems to be concomitant with the results reported in the literature. Superhydrophobic behavior in composite surfaces for a given Nafion /CB ratio and its subsequent transformation in hydrophilic after contact with liquid water was also observed. Vulcan CB/Nafion composites with Nafion-rich surfaces produced by conventional deposition methods have initially a hydrophobic behavior, but water exposure causes the surface to become hydrophilic by the reorientation of the sulfonate groups towards the water droplet. The poorer order in the Nafion/CB aggregates obtained by the more conventional airbrushing methods of deposition leads to reorientation of Nafion chains during extended water exposure [92]. In consequence, the permanent hydrophobicity can only be explained by the enhancement of the Nafion interaction with the carbon surface.

Effect of the carbon black-Nafion proportion

The effect of carbon black-Nafion proportion on the properties of the deposits has also been explored. Different quantities in weight percent of Nafion ranging from 0 to 40 % were prepared with a voltage of 7 kV and loadings of 0.8 $mg \cdot cm^{-2}$ of carbon-Nafion composite. The morphology of the layers is shown in Figure 2-18, where very similar dendritic formations are observed. It can be concluded that the amount of Nafion does not play a critical role on the morphology of the layers, since even bare carbon deposits have similar shapes.

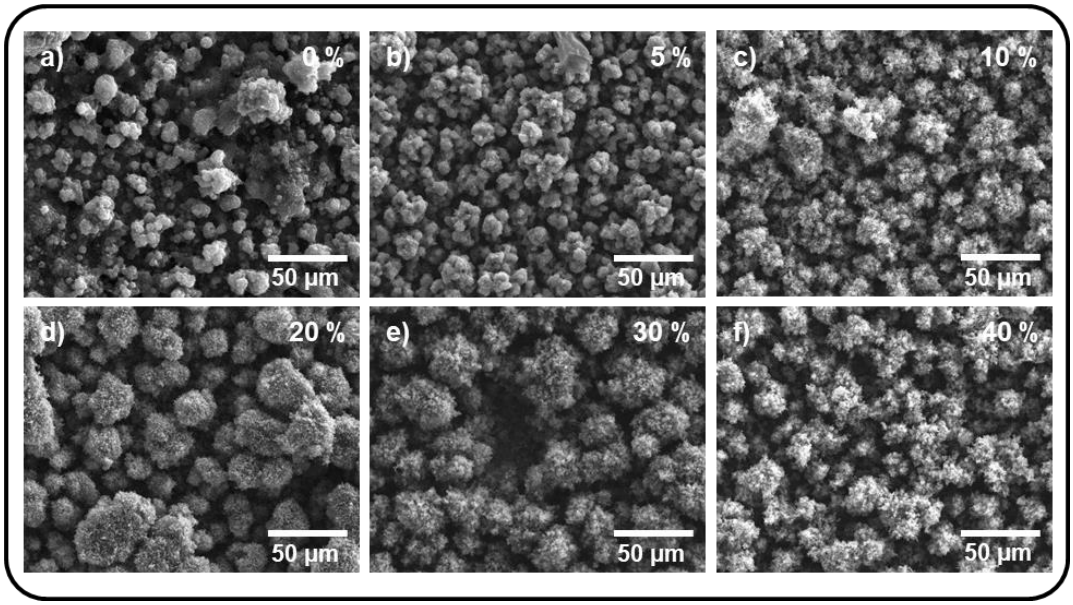

Figure 2-18: SEM images of carbon black electrosprayed layers with a) 0 %, b) 5 %, c) 10 %, d) 20 %, e) 30 % and f) 40 % in weight of Nafion

The water contact angles of these samples were measured, as shown in Figure 2-19, where some differences between the layers can be appreciated. The layer without Nafion, although presenting a similar morphology compared to the rest of Nafion-containing layers, is clearly less hydrophobic. It seems that the water contact angle has a maximum value between 10-20 wt% of Nafion. At 5 wt%, the contact angle is slightly lower probably because the amount of Nafion is below the amount required to form a monolayer on carbon black [90]. However, the contact angle is still above 160°. At 30 wt% and above, the rate of the water contact angle decrease increases, presumably indicating that either the porous structure or the excess Nafion are absorbing water. After finishing the experiment, the layer did not show a water mark, as it was observed with hydrophilic layers. The last point, 40 wt%, could not be well measured because of the low integrity of the layer, as the sole presence of a water drop resulted in a delamination of aggregates that remained on drop surface impeding the measurement of the angles by the software. However, from the images of the drops, the hydrophobicity of the layer can be assumed to be similar to the other samples, despite of the lack of integrity of sample produced by the excess of Nafion.

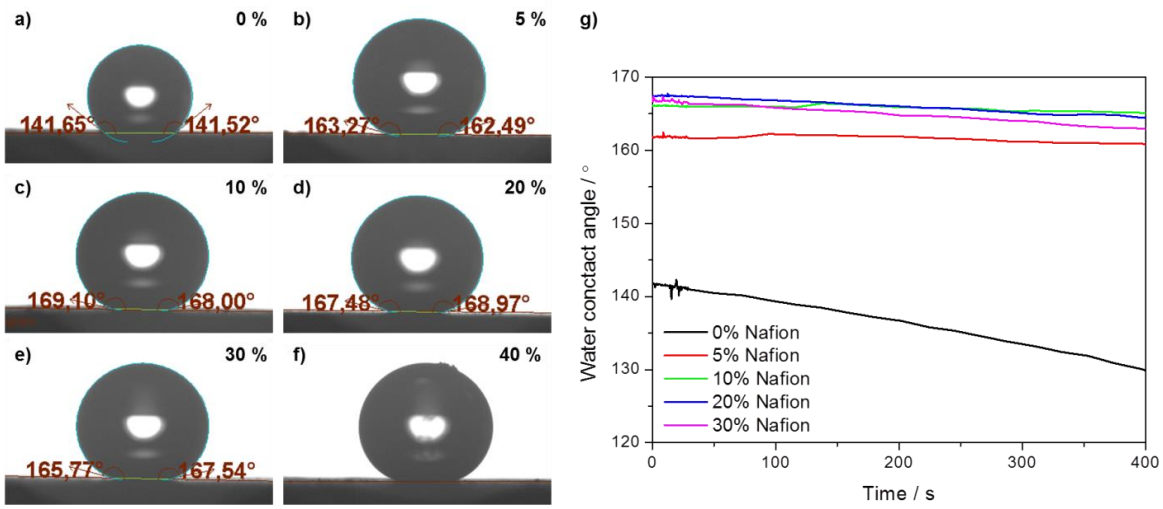

Figure 2-19: Water contact angle measured for the layer shown in Figure 2-18 and its evolution with time

XPS analyses on a series of electrosprayed films with increasing Nafion proportions are shown in Figure 2-20a. In the *C1s* binding energy region, the signal corresponding to -CF_2 bonds increases progressively with the Nafion content in the film, while for the *O1s* binding energy region, the contributions due to surface ether (534.4 eV) and sulfonic groups (530.7 eV), which are due to the presence of Nafion, are balanced for low Nafion contents. However, for ionomer percentages above 10 wt%, ether groups become predominant accounting for almost 50 % of the area of the *O1s* signal. These proportions are presented in Figure 2-20b as a function of Nafion loading. Nafion adsorption on Vulcan carbon black in water solution is reported to reach the monolayer coverage with loadings close to 9 wt% Nafion on Vulcan [90]. This estimation agrees with the XPS results, as certain change in the surface composition appears above 20 wt% Nafion in the electrosprayed films. Nafion loadings above that amount seem to be distributed on the surface in a different way.

Additionally, electrosprayed CB-Nafion samples with increasing Nafion content in comparison with a pure Nafion have been studied by temperature programmed decomposition coupled to mass spectrometry, as shown in Figure 2-21. The decomposition profile for sulfonic species above 20 wt% decreases to lower values,

closer to those found for decomposition of pure electrosprayed Nafion (cf. Figure 2-21, 100 wt%).

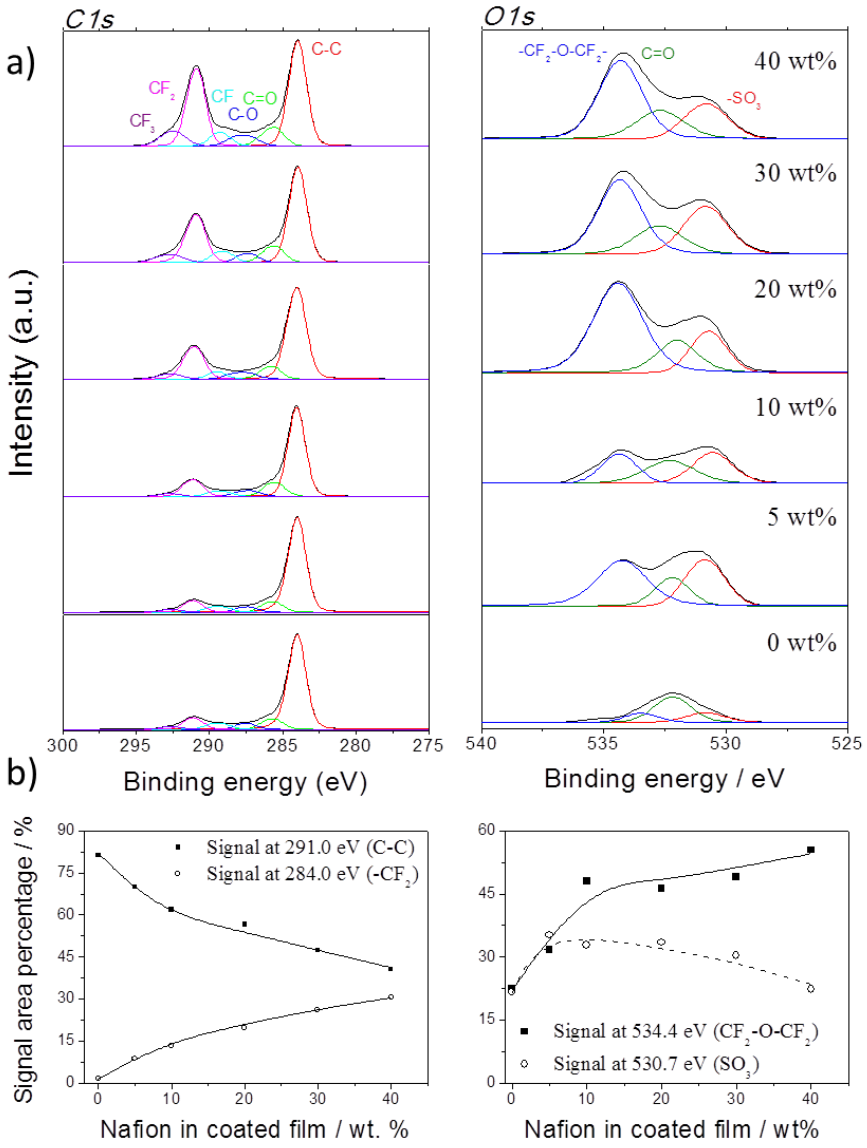

Figure 2-20: a) XPS signals in the *C1s* and *O1s* binding energy regions for deposits containing increasing amounts of Nafion b) Contribution of -CF_2 groups and C-C bonds to the *C1s* signal (left), and ether and sulfonic groups to the *O1s* signal (right)

However, fluorocarbon profiles remain in the same temperature range despite the Nafion content. For the samples up to 10 wt%, Nafion content, two clear peaks can be differentiated for CF_3^+ fragments, that progressively disappear due to convolution with

some other intermediate contribution appears in the CF_3^+ assigned profile as the Nafion loading is increased.

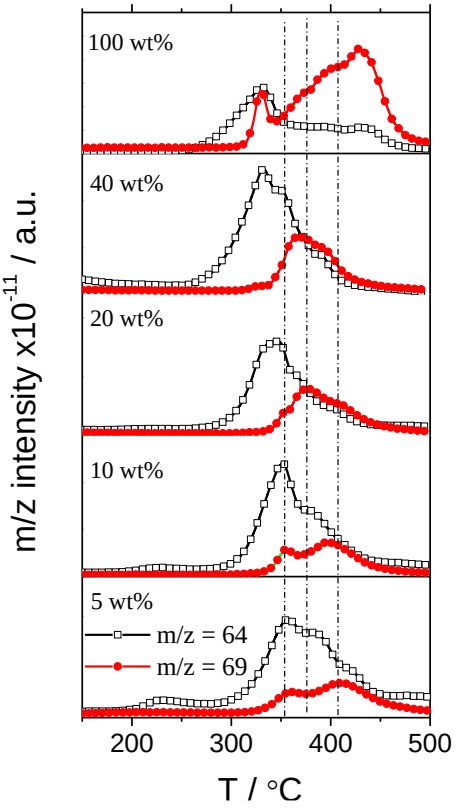

Figure 2-21: Intensity of the *m/z* 64 (open symbol) and 69 (solid symbol) signals during the thermal decomposition under inert atmosphere of the CB-Nafion electrosprayed layers with increasing Nafion proportions. A sample of pure Nafion deposited by electrospray is presented for comparison

A possible interpretation for these results relies on the fast desolvation process occurring in the electrospray deposition that could possibly maintain the strong specific interaction between Nafion sulfonic groups and the carbon black surface present on isopropanol dispersion. In other words, a strong interaction between the Nafion sulfonic groups and the carbon black surface takes place in isopropanol solution and it is maintained during electrospray ionization. This situation could be modified due to a slower drying process of the solvent. For instance, in the airbrushed layers, the resulting Nafion-carbon interaction is not strong enough to anchor the fluorocarbon chains and the coverage of the carbon surface is most likely not homogeneous. However, when the Nafion content

excess 20 wt% in electrosprayed layers, a different CB-Nafion interaction is detected, in which the average strength of the CB-Nafion interaction decreases as the Nafion content increases. This might be caused by different arrangement for the polymer fluorocarbon chains in the isopropanol dispersion medium due to the Nafion concentration increament.

Effect of the ink dilution

The effect of ink dilution on the properties of the electrosprayed layers has also been evaluated. The effect of dilution was studied in three different inks with dry solid content adjusted to 0.2, 2.0 and 5.0 wt%. The inks have a fixed Nafion/Vulcan weight ratio of 20/80 and were prepared with a voltage of 7 kV and loadings of 0.8 $mg \cdot cm^{-2}$. The morphology of the layers is shown in Figure 2-22, where huge differences in morphology are observed in the micrometric range. The most diluted ink (0.2 %) present a complete shift in the morphology previously reported, a dense layer with no appreciable porosity, even with higher magnifications (see Figure 2-22d and Figure 2-22e). On the contrary, the concentrated ink (5 %) exhibits similar morphology as the base dilution (2 wt%), with smaller aggregates and a slight reduction in the porosity.

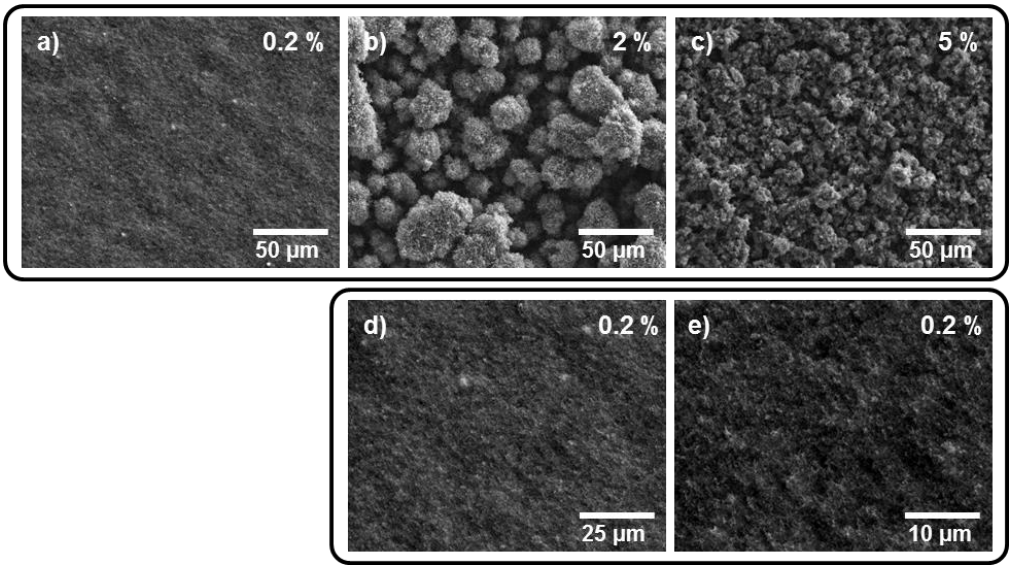

Figure 2-22: SEM images of carbon black electrosprayed layers with a) 0.2 %, b) 2 % and c) 5 % of adjusted dry solid content in isopropanol. Magnification of a) are shown in d) and e) micrographs

Surprisingly, the drastic change in morphology in the diluted ink, to the resolution here observed, does not affect to the superhydrophobicity of the layer, as it can be seen in Figure 2-23. For the sake of simplicity, only 0.2 and 5 % dilutions are depicted. The samples showed identical results, exhibiting a superhydrophobic behavior with contact angles above 160º with no water imbibition into the layer. The water contact angles did not change after the hydrophilization process. Observation of the morphological features that contribute to superhydrophobicity of these layers would require higher resolution images, although, being related with the ionomer phase, they will not easily endure the intense energy of the SEM electron beam.

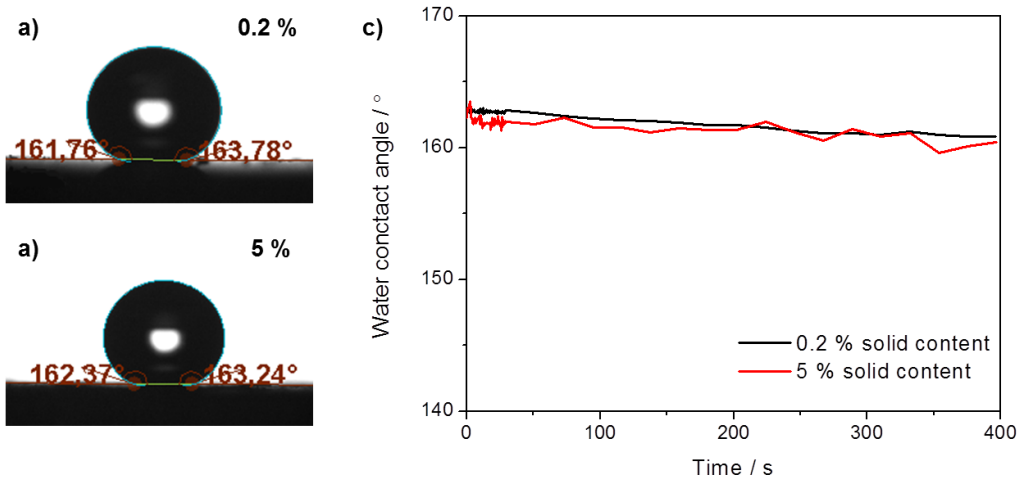

Figure 2-23: Images of WCA of electrosprayed layers with a) 0.2 %, b) 5 % of adjusted dry solid content in isopropanol and c) its evolution with time

Figure 2-24 shows the XPS analysis of the surface composition of the layers with different dilutions. Some differences can be appreciated in the most diluted sample in comparison with those with higher solid content. In the *C1s* region, the percentage of the signal due to the -CF_2 groups (291.2 eV) is stabilized at higher values (close to 20 %) for 1 and 5 wt% content of solid matter, whereas in the most diluted ink this value is almost reduced to a half. In agreement with this result, the intensity of the signal due to the sulfonic groups (530.7 eV) in the *O1s* region is more intense for the most diluted sample

in comparison with that due to the ether bonds (-CF_2-O-CF_2-) in the fluorocarbon chain (534.4 eV).

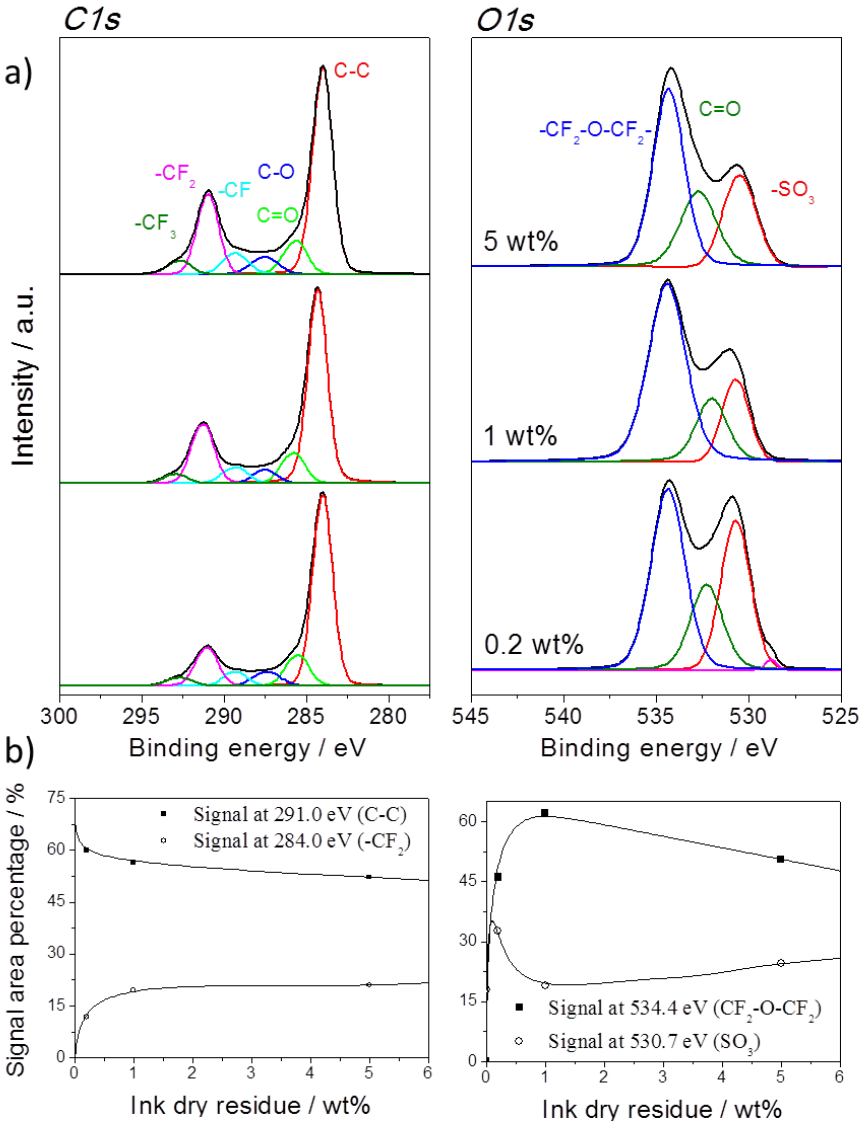

Figure 2-24: a) XPS signals in the *C1s* and *O1s* binding energy regions for inks with increasing amount of diluent for the solid residue. b) Contribution of -CF_2 groups and C-C bonds to the *C1s* signal (left), and ether and sulfonic groups to the *O1s* signal (right)

This may be indicative of the poorer orientation of sulfonic groups in this diluted sample. According to these results, it can be inferred that the orientation of sulfonic groups is partially lost for diluted inks. This effect could explain the drastic change in the

morphology of the layer, and appears to indicate no relation with the superhydrophobic character.

Ink dilution has shown a great potential for the morphology tuning of electrosprayed layers at a micrometric range, in comparison with the potential or carbon/Nafion variation. Although 0.2 % showed poorer orientation of sulfonic groups, it maintains the characteristic superhydrophobicity of the electrosprayed layers, even after long times in contact with water. The ability to create dense electrosprayed layers could open the possibility to use this technique for the fabrication of microporous layers, which are the layers in PEMFCs placed between the catalyst layer and the gas diffusion layer. The fabrication of MPLs with carbon black/Nafion composites was proven to be viable for fuel cell operation using traditional ink-based methods to produce hydrophilic MPLs [93]. Compared to state-of-the-art MPLs, which are fabricated with carbon black and high Teflon contents, electrospray would allow a better distribution of the fluorocarbon chains over the carbon, homogenizing the inner hydrophobicity of the layer, and could substantially reduce the organic content, from 23 wt% content of Teflon [94] to 10-20 % of Nafion and thus improving electrical conductivity of the layer.

2.5 Conclusions

The interaction between Vulcan XC72 carbon black and Nafion in electrosprayed deposits has been analyzed. It has been found that the electrospray ionization of Nafion ionomer solutions depends at least on variables such as the nature of the solvent, the dilution of the ionomer and the ionization mode. Electrospray deposition of suspensions of carbon black and Nafion gives rise to porous films with properties of interest for PEMFC electrodes preparation and catalyst coatings, which are a consequence of the disposition of Nafion onto the carbon phase.

A strong and stable interaction between the sulfonic groups of the Nafion and the carbon surface is observed for electrosprayed composite deposits, which is probably the result of the fast desolvation of the adsorbed ionomer during the ionization process. This

interaction favors a better coverage of the carbon surface with the polymer chains and leads to a particular arrangement of the Nafion, probably with fluorocarbon backbones oriented towards the outer part of the aggregates. This is presumably the origin of the superhydrophobicity of these layers and their high stability even after immersion in acidic solutions. For Nafion percentages above 20 wt% in the composite layers, the strength of the interaction of Nafion with the carbon surface decreases progressively, although the preferential arrangement remains in the samples.

References

[1] M. Cloupeau, B. Prunet-Foch, Electrohydrodynamic spraying functioning modes: A critical review, J. Aerosol Sci. 25 (1994) 1021–1036.

[2] J. Fernandez de la Mora, J. Navascues, F. Fernandez, J. Rosell-Llomprat, Generation of submicron monodisperse aerosols in electrosprays, J. Aerosol Sci. 21 (1990) 673–676.

[3] A. Jaworek, Electrospray droplet sources for thin film deposition, J. Mater. Sci. 42 (2007) 266–297.

[4] Applying inverse electrostatic spraying, Oak Ridge National Laboratory Reviews 29 (1996) 34-35.

[5] J. Zeleny, The electrical discharge from liquid points, and a hydrostatic method of measuring the electric intensity at their surfaces, Phys. Rev. 3 (1914) 69–91.

[6] J. Zeleny, Instability of electrified liquid surfaces, Phys. Rev. 10 (1917) 1–6.

[7] C.T. Wilson, G.I. Taylor, The bursting of soap-bubbles in a uniform electric field, Math. Proc. Camb. Philos. Soc. 22 (1925) 728–730.

[8] J.J. Nolan, The breaking of water-drops by electric fields, Proc. R. Ir. Acad. A. 37 (1926) 28–39.

[9] W.A. Macky, Some investigations on the deformation and breaking of water drops in strong electric fields, Proc. R. Soc. A. 133 (1931) 565–587.

[10] G. Taylor, Disintegration of water drops in an electric field, Proc. R. Soc. A. 280 (1964) 383–397.

[11] G. Taylor, The force exerted by an electric field on a long cylindrical conductor, Proc. R. Soc. A. 291 (1966) 145–158.

[12] G. Taylor, Electrically driven jets, Proc. R. Soc. A. 313 (1969) 453–475.

[13] J.N. Smith, Fundamental studies of droplet evaporation and discharge dynamics in electrospray ionization, PhD Thesis, California Institute of Technology (2000).

[14] M. Dole, L.L. Mach, R.L. Hines, R.C. Mobley, L.D. Ferguson, M.B. Alice, Molecular beams of macroions, J. Chem. Phys. 49 (1968) 2240–2247.

[15] M. Yamashita, J.B. Fenn, Electrospray ion source. Another variation on the free-jet theme, J. Phys. Chem. 88 (1984) 4451–4459.

[16] K. Markides, A. Gräslund, Advanced information on the Nobel Prize in Chemistry 2002, Royal Swedish Academy of Sciences.

[17] S. Banerjee, S. Mazumdar, Electrospray ionization mass spectrometry: A technique to access the information beyond the molecular weight of the analyte, Int. J. Anal. Chem. (2012) 282574.

[18] R. Tilney, H.W. Peabody, Electrostatic coating processes, Br. J. Appl. Phys. 4 (1953) 51–54.

[19] M.R. Miller, Electrostatic atomizer of liquids, US2695002A.

[20] E.M. Ransburg, E.P. Miller, Apparatus for electrostatic atomization, US2706964A.

[21] E.M. Ransburg, Apparatus for electrostatic atomization and coating, US2723646A.

[22] E.P. Miller, Method and apparatus for electrostatic atomization, US2718477A.

[23] M.R. Miller, Electrostatic method and apparatus for atomizing and for coating, US2809128A.

[24] R.L. Hines, Electrostatic atomization and spray painting, J. Appl. Phys. 37 (1966) 2730–2736.

[25] M. Cloupeau, B. Prunet-Foch, Electrostatic spraying of liquids: Main functioning modes, J. Electrost. 25 (1990) 165–184.

[26] M. Cloupeau, B. Prunet-Foch, Electrostatic spraying of liquids in cone-jet mode, J. Electrost. 22 (1989) 135–159.

[27] J. Rosell-Llompart, B. Grifoll, I.G. Loscertales, Electrosprays in the cone-jet mode: From Taylor cone formation to spray development, J. Aerosol Sci. 125 (2018) 2–31.

[28] P. Kebarle, A brief overview of the present status of the mechanisms involved in electrospray mass spectrometry, J. Mass Spectrom. 35 (2000) 804–817.

[29] R.P. Hartman, D.J. Brunner, D.M. Camelot, J.C. Marijnissen, B. Scarlett, Electrohydrodynamic atomization in the cone-jet mode physical modeling of the liquid cone and jet, J. Aerosol Sci. 30 (1999) 823–849.

[30] J.B. Fenn, Ion formation from charged droplets: Roles of geometry, energy and time, J. Am. Soc. Mass Spectrom. 4 (1993) 524–535.

[31] L. Rayleigh, On the equilibrium of liquid conducting masses charged with electricity, Lond. Edinb. Dublin Philos. Mag. J. Sci. Ser. 5. 14 (1882) 184–186.

[32] P. Kebarle, L. Tang, From ions in solution to ions in the gas phase: the mechanism of electrospray mass spectrometry, Anal. Chem. 65 (1993) 972–986.

[33] K. Tang, A. Gomez, On the structure of an electrostatic spray of monodisperse droplets, Phys. Fluids. 6 (1994) 2317–2332.

[34] K. Tang, R.D. Smith, Physical/chemical separations in the break-up of highly charged droplets from electrosprays, J. Am. Soc. Mass Spectrom. 12 (2001) 343–347.

[35] M. Peschke, U.H. Verkerk, P. Kebarle, Features of the ESI mechanism that affect the observation of multiply charged noncovalent protein complexes and the determination of the association constant by the titration method, J. Am. Soc. Mass Spectrom. 15 (2004) 1424–1434.

[36] E. Bodnár, J. Rosell-Llompart, Growth dynamics of granular films produced by electrospray, J. Colloid Interface Sci. 407 (2013) 536–545.

[37] O. Wilhelm, L. Mädler, S.E. Pratsinis, Electrospray evaporation and deposition, J. Aerosol Sci. 34 (2003) 815–836.

[38] G.J. Van Berkel, F. Zhou, Electrospray as a controlled-current electrolytic cell: Electrochemical ionization of neutral analytes for detection by electrospray mass spectrometry, Anal. Chem. 67 (1995) 3958–3964.

[39] A.T. Blades, M.G. Ikonomou, P. Kebarle, Mechanism of electrospray mass spectrometry. Electrospray as an electrolysis cell, Anal. Chem. 63 (1991) 2109–2114.

[40] J. Fernandez de la Mora, G.J. Van Berkel, C.G. Enke, R.B. Cole, M. Martinez-Sanchez, J.B. Fenn, Electrochemical processes in electrospray ionization mass spectrometry, J. Mass Spectrom. 35 (2000) 939–952.

[41] A. Jaworek, W. Balachandran, M. Lackowski, J. Kulon, A. Krupa, Multi-nozzle electrospray system for gas cleaning processes, J. Electrost. 64 (2006) 194–202.

[42] Y. Tatemoto, R. Ishikawa, M. Takeuchi, T. Takeshita, K. Noda, T. Okazaki, An electrospray method using a multi-capillary nozzle emitter, Chem. Eng. Technol. 30 (2007) 1274–1279.

[43] H. Kim, S.S. Kim, Development and characterization of saw-tooth type slit nozzle for electrospray, Aerosol Sci. Technol. 49 (2015) 11–15.

[44] A. Jaworek, A.T. Sobczyk, Electrospraying route to nanotechnology: An overwiew, J. Electrost. 66 (2008) 197–219.

[45] R. Kessick, J. Fenn, G. Tepper, The use of AC potentials in electrospraying and electrospinning processes, Polymer. 45 (2004) 2981–2984.

[46] N. Bock, T.R. Dargaville, M.A. Woodruff, Electrospraying of polymers with therapeutic molecules: State of the art, Prog. Polym. Sci. 37 (2012) 1510–1551.

[47] I.B. Rietveld, K. Kobayashi, H. Yamada, K. Matsushige, Electrospray deposition, model, and experiment: Toward general control of film morphology, J. Phys. Chem. B. 110 (2006) 23351–23364.

[48] B.S. Koh, S.C. Yi, Effect of organic solvents on catalyst structure of PEM fuel cell electrode fabricated via electrospray deposition, J. Ceram. Process. Res. 18 (2017) 810–814.

[49] J. Tang, A. Gomez, Controlled mesoporous film formation from the deposition of electrosprayed nanoparticles, Aerosol Sci. Technol. 51 (2017) 755–765.

[50] J.L. Castillo, S. Martin, D. Rodriguez-Perez, A. Perea, P.L. Garcia-Ybarra, Morphology and nanostructure of granular materials built from nanoparticles, KONA Powder Part. J. 31 (2014) 214–233.

[51] J.L. Castillo, S. Martin, D. Rodriguez-Perez, F.J. Higuera, P.L. Garcia-Ybarra, Nanostructured porous coatings via electrospray atomization and deposition of nanoparticle suspensions, J. Aerosol Sci. 125 (2018) 148–163.

[52] K.A. Mauritz, R.B. Moore, State of understanding of Nafion, Chem. Rev. 104 (2004) 4535–4585.

[53] A. Kusoglu, A.Z. Weber, New insights into perfluorinated sulfonic-acid ionomers, Chem. Rev. 117 (2017) 987–1104.

[54] C.H. Ma, T.L. Yu, H.L. Lin, Y.T. Huang, Y.L. Chen, U.S. Jeng, Y.H. Lai, Y.S. Sun, Morphology and properties of Nafion membranes prepared by solution casting, Polymer. 50 (2009) 1764–1777.

[55] S. Jiang, K.Q. Xia, G. Xu, Effect of additives on self-assembling behavior of nafion in aqueous media, Macromolecules. 34 (2001) 7783–7788.

[56] T.T. Ngo, P.H. Su, T.L. Yu, Conformation of Nafion molecules in dilute isopropyl alcohol/water mixture solutions, Proceedings of the 3rd International Workshop on Nanotechnology and Application (2011).

[57] K.S. Kumar, K.P. Vijayalakshmi, S. Sivanath, T. Jayalatha, S. Mohanty, M. Shaneeth, Interaction of nafion ionomers toward various solvents, J. Appl. Polym. Sci. 128 (2013) 3710–3719.

[58] S.A. Berlinger, B.D. McCloskey, A.Z. Weber, Inherent acidity of perfluorosulfonic acid ionomer dispersions and implications for ink aggregation, J. Phys. Chem. B. 122 (2018) 7790–7796.

[59] P. Aldebert, G. Gebel, B. Loppinet, N. Nakamura, Polyelectrolyte effect in perfluorosulfonated ionomer solutions, Polymer. 36 (1995) 431–434.

[60] C. Welch, A. Labouriau, R. Hjelm, B. Orler, C. Johnston, Y.S. Kim, Nafion in dilute solvent systems: Dispersion or solution?, ACS Macro Lett. 1 (2012) 1403–1407.

[61] A. Kusoglu, D. Kushner, D.K. Paul, K. Karan, M.A. Hickner, A.Z. Weber, Impact of substrate and processing on confinement of Nafion thin films, Adv. Funct. Mater. 24 (2014) 4763–4774.

[62] M.A. Modestino, A. Kusoglu, A. Hexemer, A.Z. Weber, R.A. Segal, Controlling nafion structure and properties via wetting interactions, Macromolecules. 45 (2012) 4681–4688.

[63] Z. Zhang, M. Davies, K. Karan, Probing interfacial interactions of nafion ionomer: Thermal expansion of nafion thin films on substrates of different hydrophilicity/hydrophobicity, J. Polym. Sci. Polym. Phys. 57 (2019) 343–352.

[64] D.D. Borges, G. Gebel, A.A. Franco, K. Malek, S. Mossa, Morphology of supported polymer electrolyte ultrathin films: A numerical study, J. Phys. Chem. B. 119 (2015) 1201–1216.

[65] S. Shukla, S. Bhattacharjee, A.Z. Weber, M. Secanell, Experimental and theoretical analysis of ink dispersion stability for polymer electrolyte fuel cell applications, J. Electrochem. Soc. 164 (2017) 600–609.

[66] R. Xu, C. Wu, H. Xu, Particle size and zeta potential of carbon black in liquid media, Carbon. 45 (2007) 2806–2809.

[67] H. Zhang, J. Pan, H. He, M. Pan, Zeta potential of Nafion molecules in isopropanol-water mixture solvent, J. Appl. Polym. Sci. 107 (2008) 3306–3309.

[68] S.M. Andersen, M. Borghei, R. Dhiman, V. Ruiz, E. Kauppinen, E. Skou, Adsorption behavior of perfluorinated sulfonic acid ionomer on highly graphitized carbon nanofibers and their thermal stabilities, J. Phys. Chem. C. 118 (2014) 10814–10823.

[69] A. Ohira, S. Kuroda, H.F. Mohamed, B. Tavernier, Effect of interface on surface morphology and proton conduction of polymer electrolyte thin films, Phys. Chem. Chem. Phys. 15 (2013) 11494–11500.

[70] M. Lopez-Haro, L. Guetaz, T. Printemps, A. Morin, S. Escribano, P.H. Jouneau, P. Bayle-Guillemaud, F. Chandezon, G. Gebel, Three-dimensional analysis of Nafion layers in fuel cell electrodes, Nat. Commun. 5 (2014) 5229.

[71] A. Orfanidi, P. Madkikar, H.A. El-Sayed, G.S. Harzer, T. Kratky, H.A. Gasteiger, The key to high performance low Pt loaded electrodes, J. Electrochem. Soc. 164 (2017) 418–426.

[72] A.M. Chaparro, B. Gallardo, M.A. Folgado, A.J. Martin, L. Daza, PEMFC electrode preparation by electrospray: Optimization of catalyst load and ionomer content, Catal. Today. 143 (2009) 237–241.

[73] F. Yang, L. Xin, A. Uzunoglu, Y. Qiu, L. Stanciu, J. Ilavsky, W. Li, J. Xie, Investigation of the interaction between Nafion ionomer and surface functionalized carbon black using both ultrasmall angle X-ray scattering and cryo-TEM, ACS Appl. Mater. Interfaces. 9 (2017) 6530–6538.

[74] K.B. Hatzell, M.B. Dixit, S.A. Berlinger, A.Z. Weber, Understanding inks for porous-electrode formation, J. Mater. Chem. A. 5 (2017) 20527–20533.

[75] A.H. Lefebvre, Properties of sprays, Part. Part. Syst. Charact. 6 (1989) 176–186.

[76] R.A. Castleman, The mechanism of atomization accompanying solid injection, NACA Technical Report 440 (1933).

[77] R.F. Egerton, Physical Principles of Electron Microscopy: An Introduction to TEM, SEM, and AEM, Springer-Verlag US, 2005.

[78] J.F. Moulder, W.F. Stickle, P.E. Sobol, K.D. Bomben, Handbook of X-ray Photoelectron Spectroscopy, Perkin-Elmer Corporation, 1992.

[79] J.B. Fenn, M. Mann, C.K. Meng, S.F. Wong, C.M. Whitehouse, Electrospray ionization for mass spectrometry of large biomolecules, Science. 246 (1989) 64–71.

[80] D.A. Skoog, F.J. Holler, S.R. Crouch, Principles of Instrumental Analysis, Brooks Cole, 2006.

[81] M. Schubnell, Thermogravimetry and gas analysis. Part 1: Basic principles and overview, Thermal Analysis UserCom. 45 (2017) 1–9.

[82] A. Hammer, Thermogravimetry and gas analysis. Part 2: TGA-MS, Thermal Analysis UserCom. 46 (2017) 1–5.

[83] G. Ramer, B. Lendl, Attenuated total reflection Fourier transform infrared spectroscopy, in: Encyclopedia of Analytical Chemistry: Applications, Theory and Instrumentation, Wiley, 2013.

[84] D. Quéré, Wetting and roughness, Annu. Rev. Mater. Res. 38 (2008) 71–99.

[85] R.N. Wenzel, Surface roughness and contact angle, J. Phys. Chem. (1949) 1466–1467.

[86] A.B.D. Cassie, S. Baxter, Wettability of porous surfaces, Trans. Faraday Soc. 40 (1944) 546–551.

[87] T.J. Zimudzi, M.A. Hickner, Signal enhanced FTIR analysis of alignment in Nafion thin films at SiO_2 and Au interfaces, ACS Macro Lett. 5 (2016) 83–87.

[88] S. Takeda, Z. Siroma, K. Yasuda, Investigation of ionic components in the solution of treated fuel cell membrane by capillary electrophoresis/mass spectrometry, Bunseki Kagaku. 55 (2006) 263–267.

[89] M. Feng, R. Qu, Z. Wei, L. Wang, P. Sun, Z. Wang, Characterization of the thermolysis products of Nafion membrane: A potential source of perfluorinated compounds in the environment, Sci. Rep. 5 (2015) 9859.

[90] S. Ma, Q. Chen, F. Jogensen, P. Stein, E. Skou, 19F NMR studies of Nafion™ ionomer adsorption on PEMFC catalysts and supporting carbons, Solid State Ion. 178 (2007) 1568–1575.

[91] M. Bradley, F. Izzia, Carbon black analysis using FT-IR with germanium and diamond ATR, Thermo Scientific Application Note 50829 (2008).

[92] X. Li, F. Feng, K. Zhang, S. Ye, D.Y. Kwok, V. Birss, Wettability of nafion and nafion/vulcan carbon composite films, Langmuir. 28 (2012) 6698–6705.

[93] N. Ahn, Y. Cho, Y.H. Cho, J. Kim, N. Jung, Y.E. Sung, Influence of hydrophilicity in micro-porous layer for polymer electrolyte membrane fuel cells, Electrochimica Acta. 56 (2011) 2450–2454.

[94] R. Schweiss, C. Meiser, T. Damjanovic, I. Galbiati, N. Haak, SIGRACET® gas diffusion fayers for PEM fuel cells, electrolyzers and batteries, White Paper SGL Group (2016).

CHAPTER 3

Superhydrophobic carbon black-supported platinum catalyst layers in PEM fuel cells

3.1 Outline of the chapter

The main objective in PEM fuel cell electrode fabrication studies is the reduction of the platinum loading that requires the use of appropriate techniques to deposit conveniently the catalyst particles to maximize their exposition to the electrochemical reactions. The optimal utilization of the catalyst material also relies in a balanced optimization of reactant diffusivity, ionic and electrical conductivity, and the level of hydrophobicity of the electrode. Pursuing to accomplish these objectives, the Low Temperature Fuel Cells group of CIEMAT has been working for several years in the electrospray deposition technique, which enables the production of catalyst layers with particular morphology, transport properties, and wettability. In previous works, PEM fuel cells with cathodic electrosprayed layers have shown improved performance with respect to conventional layers, especially under high current densities, leading to peak power densities 20 % larger. The electrosprayed layers were proven to favor highly homogeneous current distribution through the electrode and increase cell durability under cyclic start-up/shut-down operation.

In this chapter, the mass transport properties and water distribution effects of electrosprayed layers have been analyzed. An introduction to mass transport and water management in PEM fuel cell catalyst is presented as a prelude of the experimental results. The experimental part comprises three distinct analysis approaches of the electrosprayed catalyst layers. The first one comprises a morphological characterization of the layers by means of electron microscopy techniques and water contact angle

measurements. The second part focuses on the analysis of mass-transport of the catalyst layers by means of hydrogen-limiting current and dynamic water vapor sorption techniques supported by single cell characterization. The third part, which study the effect of electrosprayed catalyst layers on water transport using water collection experiments, includes two sections. The first one analyzes the effects of electrosprayed layers on the anodic and/or cathodic sides on water distribution and durability, while the second part focuses on the influence of the properties of the layer on cathodic side affecting water distribution.

The study of mass-transport properties of superhydrophobic electrosprayed catalyst layers may help to a better understanding of their behavior as catalyst layers, and in particular, to clarify the impact of their superhydrophobicity and related ionomer properties on their performance. The electrosprayed layers showed improved mass-transport properties and an excellent water vapor absorption capabilities compared with layers prepared using regular methods. Water collection experiments have been conducted to explain the origin of the positive effects of electrosprayed catalyst layers on the performance, water transport, and stability of PEM fuel cell. The results in this chapter showed an enhancement of the liquid-water back-transport process, i.e. water flux from the cathode through the membrane towards the anode, keeping optimal humidification conditions in the whole cell during operation, so an additional effort was made to understand the origin of such effect. Precise knowledge of the effects of hydrophobicity gradients inside MEAs may open up the possibility of a passive water control in a PEM fuel cell, which is a highly desirable objective from the technological point of view, to minimize fuel cell system complexity.

3.2 Introduction to mass-transport and water management in PEM fuel cell catalysts

3.2.1 Structural parameters of Pt/CB catalyst layers

Catalyst layers are key components of PEM fuel cells, especially in the cathodic electrode where the oxygen reduction occurs. The reaction rate will depend on catalyst layer components, i.e. the platinum nanoparticles supported on carbon and the ionomer phase, their concentration and ratio, and on structural parameters and fabrication method, which will determine the distribution of the catalyst layer materials. The structure of the catalyst layer determines the utilization of the catalyst, the ionic and electric conductivities, mass transport, and water management properties, all of them crucial for an optimum performance in the cell. Cathodic catalyst layers are complex heterogeneous systems where the electrochemical reaction occurs in three-phase boundaries, so researchers are putting a lot of effort in modeling studies to gain a better insight of the system. In these studies, catalyst layers are usually divided in four different phases: ionomer, conductive support, catalyst particles and void spaces [1]. The different phases can be tuned by controlling the structural parameters of the layer, such as ionomer concentration, thickness, porosity, catalyst loading, platinum/carbon ratio, water rejection and material selection. It is important to note that the research described below is focused on ink-based methods. Optimization approaches for platinum deposition methods can be found elsewhere [2].

The **ionomer** in the catalyst layer provides ionic conductivity and improve the contact of the electrolyte with the catalyst layer, in order to minimize ohmic and mass transport overpotentials. Optimum ionomer content in the catalyst layer is necessary for an appropriate performance, since low concentrations of ionomer decrease the ionic conductivity of the layer limiting the performance, while high concentrations could cause catalyst sites blocking and a reduction of gas permeability and electrical conductivity. The optimal ionomer concentration reported by different research groups falls in the

range 30-40 wt%, for electrodes prepared by spraying and casting methods [3, 4]. On the other hand, it was found that the electrosprayed electrodes have an optimum value at 15 wt% [5]. The optimal concentration is also correlated to the platinum loading [6] and the platinum weight percent in the electrocatalyst powder [7]. Optimal thickness of the ionomer film onto platinum surfaces determined from a rotating disk electrode study is around 200 nm [8]. It is also important to note that the effect of the operation conditions should be taken into account, as optimal ionomer concentration was proven to be heavily affected by the water content of the feed gases [9].

Porosity is the key parameter affecting the mass transport of catalyst layers, which is determined by its composition and deposition method. In general, Pt/CB catalyst layers have two distinct pore distributions called primary and secondary pores. Primary pores, in the 1-10 nm range, correspond to carbon particles porosity and small pores in the space between the particles that form agglomerates; while secondary pores (100-1000 nm) correspond to the space between the agglomerates. Porosity measurements have shown that the ionomer incorporates into the secondary pores leaving primary porosity unchanged [10]. The porosity decreases slightly when the ionomer content ranges from 10 to 30 wt%, whereas it starts to decrease dramatically with contents over 30 % [11]. Porosity significantly affects the transport of the reactants and products at the catalyst layers, regulating the flows between the oxygen feed gas and the water leaving the electrode [12]. Specifically, the increase of secondary pore volume is believed to improve the performance [13]. The porosity can be controlled by an adequate tuning of the fabrication method, but there has also been an extensive research on the use of volatile pore formers to obtain higher electrode porosities [14].

Water rejection will be of utter importance on the cathodic catalyst optimization. An adequate balance of the porosity with the hydrophobicity, allows oxygen to pass through the pores, even when water is exiting in the opposite direction. The most common approach to modify water rejection consists on the use of hydrophobic substances to increase the hydrophobicity of the layers [15]. However, this approach is problematic,

since the addition of an extra substance can block catalytic sites and thus reduce the performance of the catalyst. Nonetheless, results in Chapter 2 point out that Nafion interaction with the carbon support is a parameter that can be used to tune water rejection without the addition of extra substances by the use of electrospray deposition. One problematic issue is the quantitative characterization of hydrophobicity in a porous layer like the catalyst layer. A first approach is the measurement of the water contact angle on the surface of the layer, but this value may not be characteristic of the internal hydrophobicity of the layer. More convenient would be using measurements of the capillary pressure that is related with the bulk hydrophobic contact angle by means of the Young's equation (Equation 2.3), as it is usually made for gas diffusion layers [16]. However, the lower thickness of the catalyst layer compared to the carbon backings results in an experimental limitation and gives mediocre results [17].

Thickness of the catalyst layers affects the mass transport overpotential, as thicker layers increase the transport distance for protons, contributing ohmic losses, oxygen diffusion limitations and increasing the resistance to electron circulation. However, too thin catalyst layers also show mass transport limitations, as explained in the next section. Thickness shows, therefore, an optimal value. During electrode preparation, thickness can be either controlled by parameters of the fabrication method, the reduction of the platinum loading or the variation of platinum-carbon ratio of the catalyst. The optimization of the **platinum loading** is a major factor in the quest to reduce the overall cost of the PEM fuel cell systems. Platinum loading can be reduced by improving the catalyst utilization. Literature data shows that platinum utilization, in Pt/C based catalyst layers, may fall in a range between 10 and 30 % of the available platinum on the surface [18], which shows significant underutilization. The main reason is the lack of accessibility to reactant gases and/or water protons. Improper catalyst layer morphology, low porosity, and/or uneven ionomer distribution are some of the reasons for low utilization. Platinum loading should also be carefully balanced to match operation requirements. Even though platinum loading does not affect to oxygen transport

resistance at the platinum surface, the impact due to higher local flux at low loading is magnified as the platinum loading decreases [19].

Carbon loading, including the **platinum/carbon ratio**, is another key structural parameter of the catalyst layer. The platinum-carbon ratio determines the density of platinum nanoparticles distributed on the carbon support and is directly connected to the inter-particle distance. A positive effect of the platinum-carbon ratio on the mass activity of the catalyst was observed due to improved potential distribution of nanoparticles cause by a proximity effect [20], but an optimum value of the ratio has to be reached to avoid the loss of platinum particle surface area [21]. However, an increase of the platinum-carbon ratio was proven to accelerate the catalyst degradation using start-stop conditions, reducing the lifetime of the cell [22]. Besides platinum/carbon ratio, **material selection** is another key factor to control the structural parameters of the catalyst layer. Optimization of platinum nanoparticles [23], type of carbon support [24], type of ionomer [25] and organic solvent [26] will also affect the thickness, porosity and water rejection of the layers. Careful attention on the fabrication of the Pt/CB catalyst is critical to ensure its stability on fuel cell operation [27].

3.2.2 Mass transport limitations in catalyst layers

Mass transport in PEM fuel cell catalyst layers has a significant impact on cell performance and durability. Within the catalyst layer, mass transport of feed gases and water takes place near the catalyst sites, resulting in local transport resistances that affect polarization behavior. In addition, the transport of liquid water in the catalyst layer controls the membrane and electrodes humidification states that determine key parameters for fuel cell performance, like the internal resistance and the catalyst activity. The catalyst layer must allow for facile transport of gas and liquid water, high proton conductivity, and easy accessibility to catalytic sites, keeping at the same time optimal membrane humidification.

The cathode catalyst layer is a key component in the management of water transport. Under steady-state conditions, water transport takes place in both liquid and vapor phases through a porous structure with mixed wettability [28]. The transport within the catalyst layer depends on parameters fixed by the morphology of the layer, such as diffusivity, permeability, and liquid/vapor interfacial area [29]. Morphology and pore size distribution, together with the liquid pore saturation, control the vapor diffusion mode (that can be either Knudsen or molecular diffusion), whereas liquid water is transported by capillary forces and the gradients towards the gas diffusion layer and the polymeric membrane. On the other hand, limitations in the anode caused by water transport are rare, although under some specific operation conditions it may accumulate causing local hydrogen starvation and enhance cell degradation [30].

In addition to water management and transport through the porous matrix, oxygen transport is also crucial for the optimum performance of the cell. The oxygen transport resistance can be separated in three components, i.e. the gas-phase diffusion across the porous media, the permeation into the ionomer film covering the agglomerates, and diffusion through the ionomer film surrounding agglomerates, as shown in Figure 3-1. The so-called agglomerates are believed to be a homogeneous mixture of ionomer, micropores, and Pt supported on carbon particles. It is proven that oxygen permeation through the ionomer film over the catalyst particles can be the limiting process of oxygen transport process in catalyst layers, increasing as the platinum loading decreases [31]. Studies with the rotating electrode technique give 200 nm as the optimal thickness of the ionomer film onto platinum surfaces [8]. However, manufactured electrodes have strong non-uniformities on the distribution of the ionomer, so a practical value is difficult to determine. It is also reported that, depending on the operation conditions, transport losses due to flooded pores can be as significant as the local resistance at the catalyst layer surfaces [32]. As the platinum loading is reduced, the catalyst layer diminishes its active surface area, so higher reactant and proton fluxes are needed at the available active sites. It is believed that the increased transport losses for low-loaded catalyst layers are due to insufficient transport to the active catalytic sites [19].

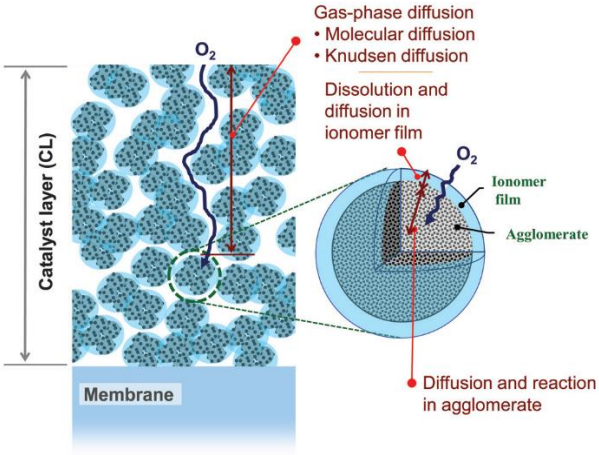

Figure 3-1: Schematic of oxygen diffusion pathway in the cathodic catalyst layer in a PEM fuel cell. Reprinted from reference 31 with permission from The Electrochemical Society, © 2011

On the quest for reducing the amount of cathodic catalyst loading, several problems usually appear, impeding the reduction of platinum in practical applications. As the electrode structure becomes thinner, the water management during transients can limit the performance of the cells [33]. The local current density at the catalyst surface increases with decreasing loading, thus reducing the cell voltage, so the oxygen reduction reaction becomes potential-dependent and stops following simple Tafel kinetics [34]. Additionally, unexplained transport resistances popped up for loadings below 0.1 $mg_{Pt} \cdot cm^{-2}$, due to the increased local flux through the layer to the reaction site and consequentially limiting the minimal Pt loading. This unknown resistance is not related to the turnover frequency of the catalyst, but the local effects at the catalytic site, because it is related to the platinum surface-area specific current density [35]. Weber et al. believe that these unexplained resistances are related to the ionomer film surrounding the catalyst, reporting evidences that the ionomer in the catalyst layer strongly differs from the bulk Nafion due to confinement effects [36]. However, the exact nature of the resistance remains unknown. A comprehensive review on the state-of-the-art discussing the latest results on mass transport studies of low-loaded catalyst layers can be found in a recent article of Weber's group, in which they are able to isolate and quantify various sub-resistances of the catalyst layer resistance [37].

3.2.3 Water management in PEM fuel cells

Water management remains one of the main challenges to maximize the efficiency of PEM fuel cells. The presence of water is essential to keep the membrane and the catalyst layers with high ionic conductivity, to maintain an optimal ionic conductivity through the membrane and maximize the kinetics of the electrochemical reactions [38]. Once optimal hydration is attained, water produced must be evacuated to avoid flooding of the porous media, i.e. the catalyst and gas diffusion layers, which impacts on the mass transport of the gaseous reactants. Ideally, the water produced at the cathodic catalyst layer would diffuse throughout the electrolyte maintaining a suitable state of hydration and the excess water would be expelled through the gas exhausts, however; the processes involving water transport are way more complex.

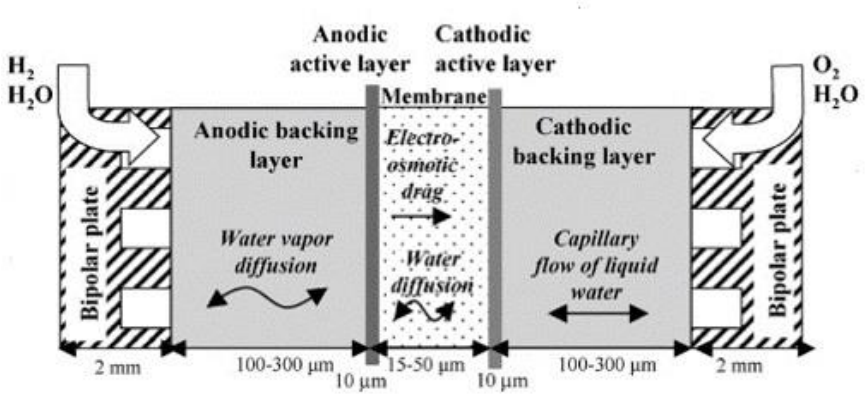

Figure 3-2: Schematic of water transport mechanisms in PEM fuel cells

Water transport in polymeric membranes during fuel cell operation occurs by three different processes, as it can be seen in Figure 3-2, namely, by diffusion due to the water activity gradient across the membrane, by electro-osmotic drag due to proton migration, and by hydraulic permeation due to the a differential pressure across the membrane. Electro-osmotic drag is caused by the movement of protons from the anode to the cathode that requires water molecules as carriers. It is reported that each proton can carry up to five molecules of water [39, 40]. At high current demands, water transported by electro-osmotic drag may be higher than the water transported by back diffusion causing the

depletion of water in the anodic side, and ultimately the dehydration of the anodic side and flooding of the cathodic side [41]. Part of the water fraction returning to the cathode can be by other physical processes, such as thermo-osmosis, as observed and measured experimentally, which can be significant compared to electro-osmosis under high current [42]. The anodic dehydration due to electro-osmotic drag together with the drying effect of the feed gases will require humidifying the feed gases before entering the fuel cell, especially at high temperatures. Although the addition of a by-product of the reaction might seem counterintuitive, it is reported to greatly increase the performance of the fuel cells [43].

Apart from the humidification of the feed gases, the other components of the cell must be carefully designed for an effective water management in order to meet fast response to the power demand required in a system. Water flow and diffusion in catalyst layers, gas diffusion layers and flow fields and its thermal management, i.e. the transformation of water and heat via evaporation and condensation, must be addressed to optimize the performance of the cells. After leaving the catalyst layer, a fraction of water must be transported through the gas diffusion layers to the flow field channels, while the other fraction is transported in opposite direction through the membrane. To avoid flooding the porous interstitial spaces of the GDL with accumulated water, a treatment with hydrophobic materials is often applied. Water management of the two-phase flow in the gas diffusion layers is governed by capillary force, shear force and evaporation; and it can be tuned by modifying porosity, wettability, pore size, thickness and fluid permeability [44]. The introduction of a hydrophobic microporous layer, as described in Chapter 1, can enhance cell performance by speeding up the removal of water from the electrode layer. Flow-field channels also need to be optimized to ensure proper conduction of the liquid water to the gas exhaust. Flow field design is reported to play a fundamental role in the water elimination process [45]. Geometry and hydrophobicity of the channels also have to be optimized to ensure water removal and avoid channel blockage, that prevent a proper feed gas distribution and creating local pressure gradients [46]. The interface between the gas diffusion layer and the ribs of the flow-field channels

has been found to be critical and prone to severe water accumulation [47] and an optimization of landing-to-channel to channel ratio is also recommended [45].

Summarizing, water management is a complex issue that involves an adequate tuning of all the PEM fuel cell components to ensure a proper performance of the cell. The final application and characteristics of the cell will also define the water management requirements; thus, the optimization of the components should be adapted according to the cell specifications. For instance, different cell configurations (i.e. standard, air-breathing, dead-end anode) will require different optimizations. Size will also be a major issue as thermal management become critical as PEM fuel cell stacks grow bigger [48].

Water management control approaches

Given the crucial challenge of maintaining equilibrium between humidification and water rejection, different active and passive approaches to properly manage water in the cell are being studied. **Active water management** strategies use pressure differentials to transport liquid water out or into the cell [49]. The most common active approach is the purge, which consist in periodically flushing the channels with an increased gas flow [50, 51]. More complex approaches have been studied, such as the implementation of an electroosmotic pump for active removal of water from the cathode side of the fuel cell [52], the supply of pressurized water using wicks integrated into the MEA [53], the use of strong cathode-to-anode pressure differentials to force the water to pass through the membrane [54]. The downside of these techniques is the requirement of additional components often with extra energy consumption.

Passive water management is based on the modification of cell components, and/or addition of new ones, in order to actively modify liquid water interaction and its flow within the cell without the use of externally added forces. The primary approach of **passive water managing** consists in the optimization of the existing components as described in the previous section, i.e. by means of a better understanding of the impact of the characteristics of the porous structure of the MEA and the gas flow channels on water

management and its optimization to maximize the performance in accordance with the required utility. Together with the optimization of the components, a proper adjustment of gas feed stoichiometry and humidification will be crucial for a correct water regulation [55].

An alternate approach consists in the integration (or addition) of new materials in the MEA or the flow-field plates. The best example of this approach is the hydrophobic microporous layer added to the gas diffusion layer to facilitate water removal from the electrodes, which, nowadays, is included as an essential part of the porous structure of the MEA. Other less successful approaches have studied polyperflourosulfonic membranes with self-humidifying characteristics [56], membranes with nanocracks to physically capture the water [57], the integration of hygroscopic particles in the catalyst layer [58] or in the polymeric membrane [59] and the fabrication of multi-layered electrodes [60]. The use of porous bipolar [61] and flow-field plates [62] has been studied by several groups. Changing the material of the plates is not invasive, since water expelling only relies on the hydraulic permeation and capillary gradients, without affecting or modifying the MEA composition. Using this same line of action, wicking components have been integrated in the flow field to absorb excess water and humidify dry feed gases [63,64]. The use of low thermal conductivity materials for the cell fabrication have led to higher cell temperatures and has been proven to delay water condensation, resulting in a performance increase of air-breathing fuel cells [65].

A very interesting approach to passively modify the water transport has lately got some attention, which consists in the introduction of asymmetries in MEAs (‘symmetric MEAs’ are those where anode and cathode are identical, with the membrane as symmetry plane). The water transport in porous materials subjected to temperature gradients has been studied, observing a temperature-gradient-driven water flow from the hot to the cold side on catalyst layers and gas diffusion layers [66]. The enhancement of back flux of water to the anode was studied by using an asymmetric microporous layer configuration with controlled thermal and mass transport properties [67, 68]. The use of asymmetric

gas diffusion media was proven to enhance the performance of the cells, but it lacked of a water transport study [69]. Using the idea of the introduction of asymmetries in the MEA, this chapter will focus on the study of hydrophobic gradients in the MEA by using electrosprayed catalyst layers in combination with conventional catalyst layers.

Water distribution measurements

Water distribution within a PEM fuel cell has been studied experimentally and theoretically. Experimentally, most used are the *in-situ* determination of the local water concentration by means of radiation based techniques (neutron, X-ray), optical visualization in specially designed cells, use of water sensors inside the cell and standard single cell testing recovering of water at the exhaust from the gas channels; theoretical investigation have been based mostly on numerical modelling.

Performing *in-situ* determination experiments of water distribution inside an operating PEM fuel cell is a challenging issue. There have been approaches designing a fuel cell with a transparent methacrylate plate in the cathodic side to observe liquid water flowing in the channels with a digital camera. However, this optical method does not allow either observing the liquid water in the GDL or quantifying its condensation in the porous media [70]. Other approaches tried to measure water vapor in the flow channels by either using relative humidity sensors [71] or on-line gas chromatography [72]. The downside of these techniques is the inability to detect liquid water, which is the main cause of cell performance losses through catalyst and flow blockage. The most popular methods to obtain information about water distribution in a working cell are in-operando imaging using X-ray [73, 74] and neutron imaging [75, 76]. These methods have the capability to show in-plane water distribution and profiles with spatial resolution of up to a few microns, and with the possibility to study transient phenomena. They require expensive equipment and special cell configuration to optimize the incidence of the radiation and collection, in terms of plate materials, cell size, and geometry, which may depart from the conditions in a standard fuel cell.

Modelling is a topic of high interest to gain a better understanding of the effects of the different characteristics of the fuel cell components on water transport. In the literature, there is an extensive production on water content of the membranes the effects of membrane dehydration due to the electro-osmotic drag [77]. There are models describing the effects of the flooding of cathode porous structures on cell performance [78]. A two-phase flow model has been used to investigate the effects of liquid saturation of gas diffusion layers on cell performance [79]. The effect of cathode catalyst properties on the water balance of the cell have been also thoroughly described [29]. An in-depth state of the art on water transport modelling can be found in Y.S. Cheng PhD thesis [80].

Water distribution may also be studied by means of water collection experiments. Water collected from cathode and anode exhausts shows the fate of water produced in the cathode catalyst layer without disturbing normal operation conditions and without the requirement of expensive equipment (except for the fuel cell test bench). However, these experiments exchange its simplicity for the uncertainty of the water distribution inside the individual components of the fuel cell. The measurement can be carried out with the cell operated with an externally added humidification that help to spatially homogenize the conditions and water concentration gradients in the flow field and inside the membrane and electrodes [81]. However, this type of measurements require a precise control of the humidification of the gas feed to keep a correct track of the water produced inside the cell. Measurements may also be done without external humidification, i.e. under self-humidification conditions (raw gases at the gas inlets). This second modality enhances water gradients within the cell, in-plane and through-plane, so water collection results are more dependent on water transport properties of the electrodes and the membrane. Dry gas inlet conditions also have high technological interest, because they open the possibility to decrease the complexity of fuel cell systems [82]. Studies presented here on water distribution are mostly based on this type of measurements.

3.3 Experimental

3.3.1 Catalyst layer fabrication

Catalyst layers were prepared by electrospray deposition on the polymer membrane (Nafion 212, 51mm thickness, Ion-Power Inc.) from suspensions of Pt on Vulcan XC72 carbon black and ionomer. The suspensions were prepared using Pt/CB commercial catalyst powder (E-TEK, 20 wt%), Nafion solution (Aldrich, 5 wt%, EW = 1100), isopropanol (Panreac) as solvent and stirred in an ultrasonic bath during about 2 hours prior to electrospray deposition. The electrospray set-up is described in the experimental section of Chapter 2. The catalyst layers were prepared with 15 cm^2 of active area and different loadings and compositions, depending on the experiments. The same process parameters for membrane deposition were used for all the experiments: a dc voltage of 10 kV, with 2.5–3.0 cm needle-to-substrate distance and 0.20–0.40 $mL \cdot h^{-1}$ ink flow rate. The base was thermostated at 50 °C and placed on a computer controlled x-y stage. Deposition was carried out in successive sweeps, with the suspension under ultrasonic stirring with a constant temperature of 22 °C. Airbrushed layers were prepared on Nafion NRE212 from suspensions of Pt/CB and Nafion, using an airbrush (Vega Systems), in successive sweeps using the same x-y stage and ink conditioning as for the electrospray deposition.

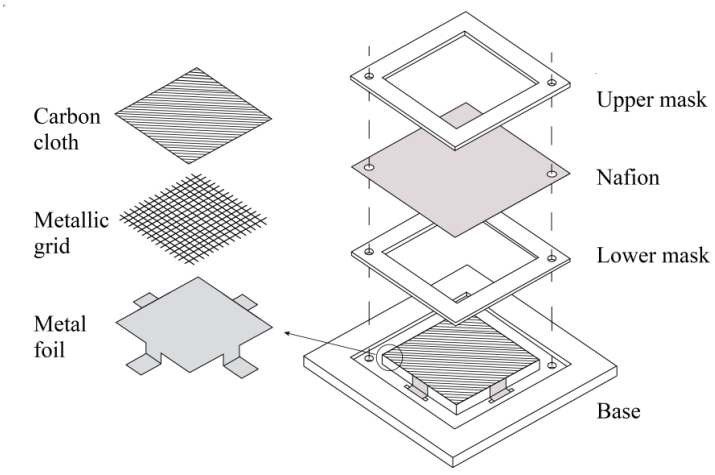

Figure 3-3: Mask setup for electrospray deposition on Nafion membranes

The electrospray deposition on Nafion membranes was performed using a mask setup, depicted in Figure 3-3, designed at Fuel Cells group of CIEMAT. It is designed to facilitate the deposition of ink onto delimited areas of substrates that do not have high electrical conductivity. The setup consists of two square masks with two small holes to hold the Nafion membrane to the base with the help of two bolts. The base has a square area carved to fit the masks and to push the membrane towards the central part. The base and the masks are made of methacrylate, while the central part consists of a thin steel foil glued with a grid and a conductive carbon fiber gas diffusion layer, designed to be conductive and at the same time, allow a certain degree of compression to avoid damage on the thin Nafion membrane. The metal foil is connected to the setup base using four small appendices that go through small holes carved in the base. Using the setup, it is possible to create a well-insulated zone around the area that is destined to be coated, and thus reducing material loss and achieving active areas with well-defined catalyst loadings. Having the membrane trapped between the methacrylate mask also allows for an easy manipulation and the possibility to cover both sides by just flipping the mask on the base. The thermal conductivity of the materials on the center of the base, also allows for the membrane to be heated with the resistances of the base.

Airbrush deposition is also made by holding the membrane with the two masks, but instead of using the plastic base, a square piece of steel is placed between the membrane and the base and to help heat conduction and enhance solvent evaporation. Trapping the membrane with the mask and the bolts was proven to be very useful to hold the membrane in place and avoid deformation upon the small drops of liquid hit the membrane. Using this procedure, we have achieved high deposition efficiency with a one-step procedure to deposit the target loading.

3.3.2 Catalyst layer characterization

Transmission and scanning transmission electron microscopy

Transmission electron microscopy (TEM) provides images of thin specimens down to the nanometric scale by analyzing the electron signals transmitted through the sample of interest, allowing the study of shapes, distribution and location of specific compounds. The technique is based on the interaction of a high-energy electron beam (between 200 and 400 kV) transmitted through thin section of a sample (less than 100 nm). This thickness requirement is the most notable drawback of the technique, as it requires from a careful preparation of the sample. However, if the sample material can be dispersed in solvent, a widespread solution is to directly deposit a drop of the suspension on standard grids coated with holey carbon films to retain the dispersed particles. A scanning transmission electron microscope (STEM) is a type of transmission electron microscope modified by the addition of scanning coils that allow beaming across the sample, combining TEM and SEM technologies to collect a transmission image by the scanning method. The analysis of the X-ray produced by incident electrons also allows qualitatively determination of chemical compositions using energy-dispersive X-ray spectroscopy (EDS).

TEM microscopy was performed on directly deposited electrospray and airbrush catalytic inks onto holey carbon coated copper grids. The deposit was done for very short deposition times to analyze the initial formation of aggregates in each technique. The measurements were carried out in the National Centre for Electronic Microscopy (ICTS) using a JEOL JEM 3000F microscope with an accelerating voltage of 300 kV. STEM microscopy and EDS characterization were performed for cross sectional analysis of morphology and composition of electrosprayed films deposited on top of Nafion membranes. The measurements were carried out in the Center for Nanophase Materials Sciences, Oak Ridge National Laboratory (Oak Ridge, Tennessee) using a FEI Talos F200X microscope. The operating voltage was 200 kV, which is optimized for high X-ray collection efficiency by the integration of four symmetrically arranged 30 mm^2

active-area silicon drift detectors within the microscope column, resulting in a solid angle of 0.9 sr. Cross-section MEAs were embedded in epoxy and cured at 60 °C. The resulting blocks are trimmed and then sectioned into 75 nm thick cross sections by diamond knife ultramicrotomy.

Cross-sectional MEA preparation for SEM microscopy

Cross-sectional analysis studies were performed in collaboration with the Microscopy and Surface Analysis Group at CIEMAT. Three different cross-sectional preparation methods were tested to study the assembled MEAs using SEM microscopy: sharp knife, metallographic and ion-milling preparations. For experimental details on SEM microscopy and microscope specifications, check Chapter 2.

The sharp knife preparation is used as a comparison because it has been the preparation method used by the group so far. The procedure is simple; it just consists in cutting a piece of the MEA with a sharp blade and put it in a sample holder for analysis. The problems associated with this preparation are the lack of reproducibility and the difficulty to perform a planar cut in the macroscopic scale. Due to the heterogeneity of MEA components, material from other layers can be displaced over other layers, impeding a correct visualization. These problems make the sample preparation tedious and not reliable for the analysis of MEA samples.

The metallographic preparation used in the study was adapted from metal sample preparations. Specimens are entrapped using EPOMET® G, a hot compression thermosetting resin, to reduce shrinkage during curing and results in a better mount with edge retention. The samples have been compressed under 80 bar and a temperature of 150 °C. After curing the resin, the specimen was cut in cross-section and the surface of a metallographic specimen was prepared by grinding and polishing. The grinding was performed with successive sweeps with SiC papers (P320, P600, P1200) and water, and finished by polishing with diamond paste (6 microns). The conditions were fixed at a pressure of 6 lb and a disk of 300 rpm for 3 minutes for all the stages of the preparation.

Before introducing the sample in the microscope, carbon coating is applied due to the insulating character of the resin.

The ion milling preparation is performed with an ion milling system, a physical etching technique that uses accelerated ions of an inert gas on substrates to remove material from their surface. This technique is generally used to produce smooth and clean sample surfaces for high-resolution imaging using electron microscopy. However it can also be used as an effective tool for cross-sectional cutting. Cross-section of MEAs were prepared by cutting a small piece of the assembly with a sharp knife followed by sandwiching both sides with adhesive copper tape before mounting onto the sample holder. The ion milling system used is a Hitachi High-Tech IM4000. The system uses an argon ion beam to cut the planar cross section through the specimen along the edge of a titanium mask located between the specimen and ion gun mounted on a removable specimen holder that can be directly introduced on the microscope after the cut. Time and voltage conditions were optimized for MEA assemblies, especially to avoid damage to the Nafion membrane. The optimized conditions for MEAs were an accelerating voltage of 5 kV during 6 h, using 2.3 reciprocation·min^{-1} and a swing angle of ±40 °C. For cross-sectional cuts of catalyst coated membranes, the same conditions were used reducing the time to 3 h.

Dynamic vapor sorption

Dynamic vapor sorption (DVS) is a gravimetric technique that measures the quantity and the kinetics in the absorption of a vapor solvent in a target sample. DVS technique varies the vapor concentration on an inert gas of the surrounding atmosphere of the sample and measures its change in mass. Water vapor is the most commonly used, but it is also possible to use a wide range of organic solvents. This technique was developed to measure water vapor sorption isotherms, i.e. the equilibrium relationship between the water content of a material and the relative humidity. Sorption and desorption isotherms show the water content at a given humidity value, expressed as relative humidity. To determine the isotherms, the technique records the mass change as a function of time

until gravimetric equilibrium is reached for each humidity value, and then generated using the equilibrium mass value at each relative humidity.

Water uptake results were collected at Lawrence Berkeley National Laboratory at Berkeley (California) in Adam Weber research group. A DVS Adventure water vapor sorption analyzer from the company Surface Measurement Systems was used in all the experiments. The equipment is able to generate humidified gas streams within ±0.1 %RH of target humidity up to 60 °C, while the measured mass changes at a resolution of 0.1 µg with peak-to-peak noise of less than or equal to 0.2 µg. Different catalyst layers were deposited by electrospray and airbrush deposition on porous Teflon substrates Whatman® TE-35 PTFE membrane filters, 0.2 µm pore size (Sigma Aldrich). Samples of 0.5-1 cm^2 were cut from the membranes to place it on the balance plate. Before the experiments, the water content of samples was equilibrated with dry nitrogen at 25 °C for two hours, after which the initial dry weight of the sample (M_0) was set. The sample was hydrated using humidified nitrogen stream in steps of 10 % up to 90 % and then to 95 % or 98 %, then dehumidified back to 90 % and to 0 % in the same manner. The weight of the sample was measured at each relative humidity step for at least 1 hour or until the weight change was less than 0.005 %·min^{-1}.

The weight of water absorbed by the sample, M_w, is determined from the measured weight of humidified sample at a given time, $M(t)$, and its initial weight:

$$M_w = \mathrm{M(t)} - M_0 \tag{3.1}$$

Assuming that all the water absorbed is interacting with the ionomer sulfonic groups, then the ionomer water content, λ, which represents the number of water molecules per sulfonic-acid group of ionomer, can be calculated from:

$$\lambda = \frac{M_w / \bar{M}_w}{M_i^{dry} / EW} \tag{3.2}$$

where M_i^{dry} is the dry mass of the ionomer in catalyst layer sample, EW is the equivalent weight of the ionomer (1100 g·mol^{-1} for all samples used in this study) and $\bar{M}_w$ is the molar mass of water (18 g·mol^{-1}).

3.3.3 Single cell characterization

Fuel cell testing equipment

Single cell characterization was carried out with a homemade test bench (PEM3, CIEMAT) that allows the control of parameters of the cell (current, temperature, and backpressure) and gas reactants, which were fed through mass flow controllers, heated pipes, and thermostated humidifiers. A schematic of the bench is shown in Figure 3-4.

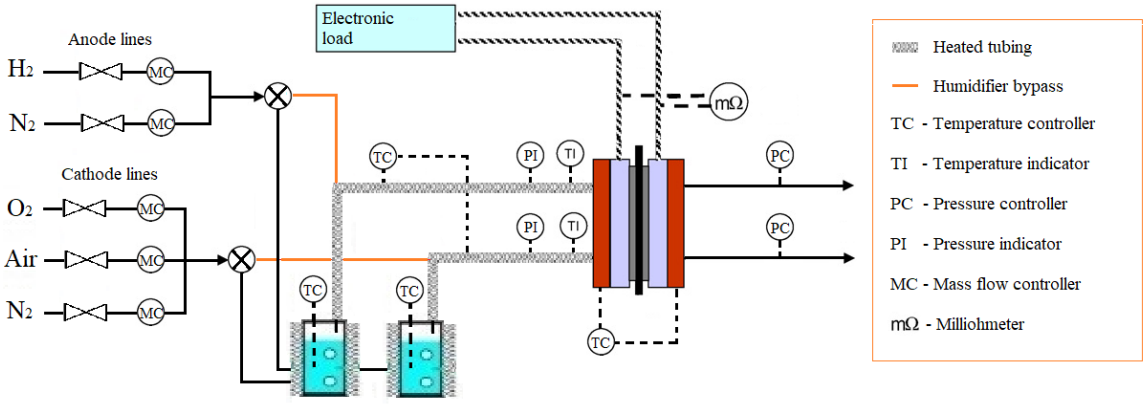

Figure 3-4: Schematic representation of the PEM3 fuel cell test bench of CIEMAT

Cell current was drawn with an electronic load (HP 6060B), while monitoring cell voltage and internal resistance at 1 kHz (HP Agilent 4338A milliohmmeter). Software in Labview allows controlling and data acquisition. Voltammetric and impedance spectroscopy measurements were made by connecting on demand an Autolab 30N (with 10A current booster) and analyzing the results using commercial software (Nova, Autolab).

The single cell hardware is shown in Figure 3-5. It uses stainless steel end plates (8 mm thickness) to clamp the structure with 8 screws tightened to a controlled torque (3 N·m),

that correspond to 20 bar. Gas tightness was accomplished with silicone gaskets. Additionally, both final plates have inserted ceramic resistances to control the temperature of the cell. Anodic and cathodic flow field plates were gold plated stainless steel (Grade 310S, 2 mm thickness) with double serpentine flow channels (1x1 mm section). Current collectors were gold plated brass plates (Udomi).

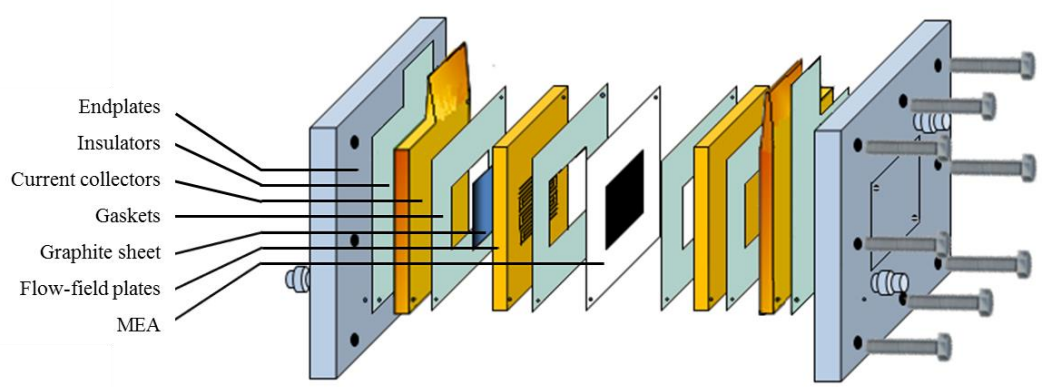

Figure 3-5 Schematic representation of the single cell assembly

After the cell was assembled, it was subjected to leak and crossover tests. Before the characterization, the cell start-up was carried out by a progressive increase of temperature, up to 80 °C, and a demand of current density, up to 60 $mA \cdot cm^{-2}$, with constant gas flow rates of 30 $cm^3 \cdot min^{-1}$ of H_2/O_2. The cell was left in these conditions for no less than 12 h until a steady state response was attained. In general, the characterization protocols are based on own group experience and the technical specification document currently developed by the IEC/TC105 (WG11): IEC/TS 62282-7-1 ‘Single cell test methods for polymer electrolyte fuel cell (PEFC)’.

Polarization curve

The polarization curve is the most accurate representation of the performance of a fuel cell and shows the output voltage of a fuel cell for a given current demand. A theoretical approach is described in Chapter 1.2.2. *I-V* values are obtained by consecutive chronopotenciometric steps at constant experimental conditions. The standard conditions used in all the studies, unless otherwise indicated, for the acquisition of polarization

curves are: 1.5/3.0 H_2/O_2 stoichiometry, 1 barg pressure at both anode and cathode, 80 °C cell temperature and 100 RH% in the gas feeds. Also, the curves were obtained from higher current demands to lower demands, to ensure a proper humidification and avoid electrode dry-out and also maintaining a constant flow below 3 A to avoid mass transport problems due to the low gas flow. No values below 0.4 V were used in order to protect the MEA from unwanted electrochemical deterioration.

The polarization curves were analyzed using the standard expression:

$$V = E' - b \cdot log\frac{j}{r_f j_0} - jR_{dc} \qquad (3.3)$$

where V is the cell voltage, E' is the thermodynamic potential, b is the Tafel slope, j the current density, j_0 the exchange current density per unit platinum area, r_f is the roughness factor calculated from measurement of the active Pt area (described below) and R_{dc} the dc internal resistance. For the fitting, a fixed value of 1.19 V for E' is used (calculated for 80 °C, 1 barg and 100 %RH) and value of $j_0 = 8.5 \cdot 10^{-9}$ $A \cdot cm_{Pt}^{-2}$ determined for platinum nanoparticles supported on Vulcan at 80 °C [83]. The roughness factor ($cm_{Pt}^2 \cdot cm^{-2}$) was obtained from the measured electrochemical area and the platinum loading of the catalyst layer. Using these constant and pairs of I-V values, the parameters b and R_{dc} are obtained from the least squares fitting to Equation 3.3.

Water distribution experiments

In some of the cells, water distribution measurements were carried out. With this aim, water collection experiments were conducted once the start-up process of the MEA was finished. The cell was operated under self-humidification mode (dry H_2 and O_2 feed) under constant load (200 $mA \cdot cm^{-2}$) by bypassing the gas humidifiers. Water collection experiments under self-humidification were carried out at different current densities and cell temperatures, collecting the water produced by the cell from the anode and cathode in deposits (8 cm^3 volume) refrigerated with Peltier cells (5 °C deposit temperature). The

efficiency of water collection experiments tested against Faraday law was normally above 90 % and the data with lower collection efficiency were not considered as valid. Results of water recoveries from anode and cathode (w_i) are given in percentages of the nominal faradaic production:

$$w_i = 100 \cdot m_{H_2O} \frac{nF}{It\,\bar{M}_w} \quad (3.4)$$

where m_{H_2O} is the mass of the water recovered in the deposits, I is the operation current, t is the total time of recollection, while the other parameters $\bar{M}_w$ (= 18.0 g·mol^{-1}), n (= 2) and F (= 96,485 C·mol^{-1}) have their usual meaning. The difference between the nominal faradaic estimation of produced water and the total experimental water collected is taken as the experimental error reported in the figures. The measurements were usually performed from low to high demands to avoid as much as possible the negative effect of residual water in the setup. On this line, to avoid the effect of residual water on the gas lines or dead volume zones of the setup, cell was run on the measurement conditions for several hours before the water collection starts.

The measurements were performed on electrosprayed and airbrushed catalyst layers deposited directly onto Nafion 212 membranes completed with commercial gas diffusion layer BASF ELAT-LT2500W and a commercial gas diffusion electrode BASF ELAT-LT250EWALTSI (0.25 mg·cm^{-2}) on the opposite side. Details on the analyzed catalyst layers are given in the corresponding sections.

Hydrogen-limiting current experiments

Usually, the mass-transport resistance of a catalyst layer is calculated from oxygen-limiting current measurements, using a dilute oxygen feed to reach the mass-transport limit condition [84]. However, in this study, a hydrogen pump is used to analyze mass transport limitations in the catalyst layers using hydrogen. A hydrogen pump does not require any additional set-up other than the regular fuel cell hardware and the regular MEA preparation, the only difference is that hydrogen is fed to both electrodes, so the

reactions occurring inside the cell are hydrogen oxidation at the anode, where mass transport is being tested, and water reduction at the cathode. In consequence, the net result is just the passing ('pumping') of H_2 from the anode to the cathode. The hydrogen-limiting technique presents many advantages compared to the traditional oxygen-limiting technique, such as the elimination of water production of the oxygen reduction reaction, facile reaction kinetics, an oxide-free surface and a minimization of the heat production, thus reducing local environment fluctuations [85]. This approach has been proven to be reliable, demonstrating that the resistances derived from hydrogen-limiting currents match air-breathing PEM fuel cell polarization behavior at low platinum loadings [86].

For hydrogen-limiting measurements, the hydrogen supplied to the cell is highly diluted in an inert gas, slowing down the diffusion and thus magnifying the transport resistances. Under sufficiently high anode overpotential, attained at a low constant voltage demand, it can be assumed that the hydrogen concentration at the catalytic sites of the anode is zero and a limiting current regime is achieved. The total mass-transport resistance of the anodic catalyst layer is directly calculated from the limiting current (i_{lim}) obtained in the potential holds using the following equation [87]:

$$R_{total}^{mt} = \frac{nFC}{i_{lim}} \tag{3.5}$$

where n is the number of electrons exchanged during hydrogen oxidation, F the Faraday constant and C is the averaged reactant feed concentration in the flow channels of the measuring cell. In order to obtain the resistance of the catalyst layer (R_{CL}^{mt}), the total mass-transport resistance can be expressed as the sum of three resistances:

$$R_{total}^{mt} = R_{CL}^{mt} + R_{GDL}^{mt} + R_{foil}^{mt} \tag{3.6}$$

where R_{GDL}^{mt} corresponds to the resistance of the gas diffusion layer and R_{foil}^{mt} corresponds to the copper foil aperture used as current collector. These resistances are

typically below 1 $s \cdot m^{-1}$ (note that mass transport resistance units, $s \cdot m^{-1}$, are different from charge transport resistance units, Ohm) so the measured mass-transport resistance can be almost entirely attributed to the catalyst layer. The resistance of the foil is equal to the binary diffusion coefficient of hydrogen in argon divided by the foil thickness (0.04 mm) and the resistance of the GDL is empirically calculated by stacking experiments. Specifically, for the commercial GDL Sigracet 24BC from SGL Carbon the resistance has been calculated to follow $-0.56 \cdot p$, in which p is the absolute pressure in bar [87]. Mass transport resistance of the catalyst layer is analyzed with a continuum, one-dimensional model that assumes gas-filled pores. According to this model R_{GDL}^{mt} is composed of two contributions: the through-plane resistance due to transport through the porous structure of the catalyst layer in the direction perpendicular to the layer plane; and the local resistance (R_{local}), that accounts for transport limitations close to the reaction site. The following mathematical expression has been obtained for the catalyst layer resistance with the two referred terms [37]:

$$R_{CL}^{mt} = \frac{L}{3D_{CL}} + \frac{R_{local}}{\eta \gamma r_f} \tag{3.7}$$

where L is the catalyst layer thickness, D_{CL} is the effective reactant gas diffusion coefficient in the pores of the inter-agglomerates space, r_f corresponds to the catalyst roughness factor, γ is the fraction of platinum surface in the external surface of agglomerates (active under mass transport limitation) and η is a focusing factor that accounts for the discreteness of Pt surface on the agglomerates. Equation 3.7 is able to explain the observed increase in R_{GDL}^{mt} at very low loading, which is implicit in the second term of the right. The diffusion coefficient D_{CL} is corrected using the following equation:

$$D_{CL} = \frac{\phi}{D\tau} \tag{3.8}$$

where D is the uncorrected diffusion coefficient, while ϕ and τ are the porosity and tortuosity of the catalyst layer respectively. A value of 0.365 is generally taken for the γ fraction when using 20 wt% Pt/CB particles. Additionally, the factor η is considered to be in the range of 2.5-2.9 for ionomer thicknesses between 5 and 10 nm [37].

Another interesting feature of the hydrogen-limiting current method is the ability to obtain information of the nature of gas diffusion through the bulk of the layer by comparing H_2 and D_2 measurements. The typical pore distributions in catalyst layer can be described by molecular and Knudsen diffusion and either of them are dependent on the molecular mass of the diffusing species. Changing the reacting gas from hydrogen to deuterium, with a molecular mass twice as high, the diffusion coefficient should be lowered by a factor of $\sqrt{1.91}$ in the case of molecular diffusion, and by a factor ca. $\sqrt{2}$ for Knudsen diffusion. Considering that non-diffusional processes have no molecular weight dependency, calculating the ratio of deuterium and hydrogen transport can be used to analyze the impact of chemical and diffusional processes on the resistance of the catalyst layers. The principal molecular diffusive processes in the catalyst layer occur for the transport of gases in the pores structure of the catalyst layer and inside the ionomer phase, whereas other relevant processes are the interfacial transport between the different phases present in the pores of the layer (gas, liquid, ionomer, catalyst surface) and surface diffusion over the catalyst particle [87].

The hydrogen-limiting current results were obtained in a short stay on Dr. Adam Weber's group in the Lawrence Berkeley National Laboratory at Berkeley (California). For the measure of the transport resistance at the catalyst layer, a hydrogen-pump cell was used as described by Hwang and Weber [85]. The measurements were performed on electrosprayed and airbrushed catalyst layers deposited directly onto Nafion 212 membranes, covering an area of 15 cm^2. The catalyst coated membranes were cut to leave an exposed electrode area of 0.713 cm^2 and put in contact with a Sigracet 24BC gas diffusion layer as testing electrode (anode), and a commercial gas diffusion electrode BASF ELAT-LT250EWALTSI (0.25 $mg \cdot cm^{-2}$) as counter electrode (cathode). The

MEAs were first conditioned with 25 cyclic voltammetries, from 0.08 to 0.95 V at 50 $mV \cdot s^{-1}$, followed by another 25 cleaning voltammetries at 100 $mV \cdot s^{-1}$ under pure argon flowing through the working electrode while the counter electrode was fed with 200 $cm^3 \cdot min^{-1}$ of 2 % hydrogen diluted in argon for the entire duration of the experiment. Before switching anode gases, a potential hold is applied to calculate the crossover current values. Afterwards, limiting current with hydrogen and deuterium was measured recording the current at 0.3 V after a steady state was reached, feeding the testing electrode with 1000 ppm H_2 (or D_2) diluted in argon with constant flow set at 500 $cm^3 \cdot min^{-1}$.

Electrochemically active surface area measurement

The electrochemically active surface area (ECSA, hereinafter electroactive area) can be defined as the area of an electrode with the capability to promote a certain electrochemical reaction. In PEM fuel cells the electroactive area corresponds to the area of platinum nanoparticles actively promoting oxygen reduction or hydrogen oxidation. Most of the methods for electroactive area determination are based on the charge transfer adsorption or desorption of species with a known adsorption pattern, like hydrogen or carbon monoxide on some metals. The values of the electroactive area are strongly dependent on the method of measurement and there is not a standard measurement method yet [88].

The method used to measure the electroactive area of the cell catalysts in this thesis is the hydrogen underpotential deposition (H_{UPD}). This method has the advantages of being an easy, non-destructive and clean application because it uses the measurement of protons that are already present in the electrolyte and in the ionomer phase surrounding the Pt/CB particles. The value of the electroactive area is related to the amount of surface accessible to hydrogen underpotential deposition in a real electrode, which in acid electrolytes is a fast and reversible process [18]:

$$Pt + H_3O^+ + e^- \leftrightarrow Pt - H_{UPD} + H_2O \qquad (3.9)$$

In equation 3.9, *Pt* denotes an active site for hydrogen adsorption on the platinum surface. The extent of this reaction, or charge passed, is proportional to the number of available *Pt* sites (to which 210 $\mu C \cdot cm^{-2}$ of platinum surface has been assigned), and can be measured by means of cyclic voltammetry using H_2 and N_2 as feed gases in the anode and the cathode respectively, as shown in Figure 3-6. For the experimental determination, fully humidified gases and a cell temperature of 30 °C were maintained overnight before the voltammetric experiments. Microscopically, platinum polycrystalline surfaces have different types of sites with different adsorption energies and, for that reason, the formation of a monolayer of hydrogen does not occur at a fixed potential but in a range approximately between 0 and 0.4 V [89].

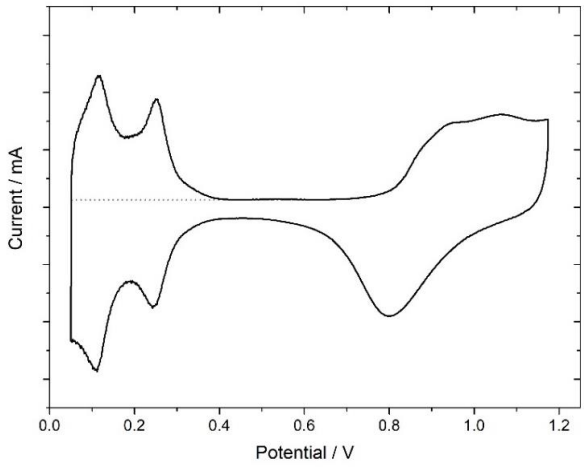

Figure 3-6: Typical voltammogram of carbon black-supported platinum in a PEM fuel cell with H_2/N_2 feed

If the charge under the voltammetric peaks for hydrogen adsorption or desorption is assumed to correspond to adsorption of one hydrogen atom on each metal atom of the surface, the charge associated H-M bond can be calculated on the basis of the distribution of metal atoms on the surface. While this is well defined for the perfect single crystal faces, in the case of polycrystalline platinum the accepted value is 210 $\mu C\ cm^{-2}$, based on the assumption that the density of atoms on the surface is $1.31 \cdot 10^{15}\ cm^{-2}$ [88].

The charge of the hydrogen adsorption/desorption can be obtained from the integration of the intensity on the underpotential potential window:

$$Q_h = \frac{1}{v}\int (I - I_{dl})\,dE \qquad (3.10)$$

where v is the sweep rate, I is the total electric current and I_{dl} is the current of the double layer. The electroactive area is obtained by dividing the charge of hydrogen adsorption/desorption by the theoretical value of the charge per area. The validity of the method relies on the identification of the hydrogen adsorption/desorption potential window and the analysis of the coverage before the rate of hydrogen evolution becomes significant. Additionally, the existence of a three-dimensional layer creates an additional kinetic limitation, compared with a planar electrode. For this reason, it has been reported that the method is strongly dependent on sweep rate and temperature. Moreover, platinum may catalyze the reaction of other species due to carbon support degradation that may interfere in hydrogen adsorption [18].

Electrochemical impedance spectroscopy

Impedance spectroscopy is based on the application of a sinusoidal potential excitation to the electrode $E(\omega)$ using different frequencies, while registering the intensity response, $I(\omega)$, and its phase shift $\theta(\omega)$.

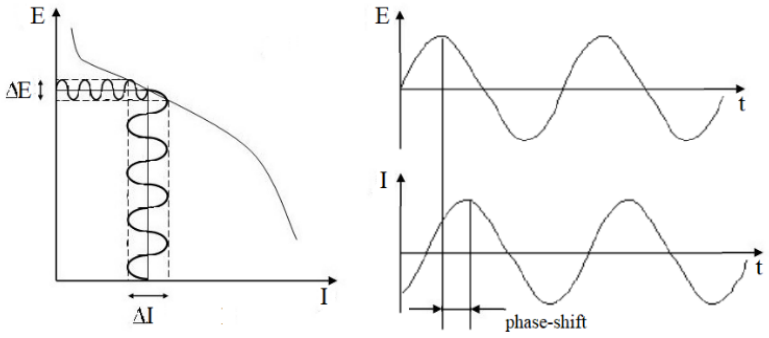

Figure 3-7: EIS excitation signal represented in the working range of a fuel cell (left) and its current response (right)

If the system follows the basic assumptions of linearity, causality, and stability [90], then impedance analysis is reliable, and the intensity response is always a sinusoid at the same frequency of the excitation but shifted in phase, according to the following equations [91]:

$$E(\omega) = E_0 \sin(\omega t) \quad (3.11)$$

$$I(\omega) = I_0 \sin(\omega t + \theta) \quad (3.12)$$

where I_0 and E_0 are the amplitude of the signals, ω is the radial frequency and t corresponds to time. From the relationship of both signals, using an expression analogous to Ohm's Law, the impedance of a certain system can be calculated:

$$Z(\omega) = E(\omega)/I(\omega) \quad (3.13)$$

Combining the previous equations and the Euler relation, impedance can be represented as a complex number:

$$Z(\omega) = Z_0 (\cos\theta + i \cdot sin\ \theta) = Z_r(\omega) + i \cdot Z_i(\omega) \quad (3.14)$$

Where Z_0 is the ratio of E_0 and I_0, i is the imaginary unit, Z_r is the real part of the impedance and Z_i is the imaginary part. This expression leads to the most common representation of the impedance, the Nyquist plot, in which the real part of the impedance is plotted against the imaginary part. A typical Nyquist plot of an electrochemical system is presented in Figure 3-8. Other types of graphics used in the literature are the Bode plots, where the polar coordinates of the impedance are represented against frequency and the Cole–Cole plots, where the squares of the real and imaginary impedances are plotted against each other [92].

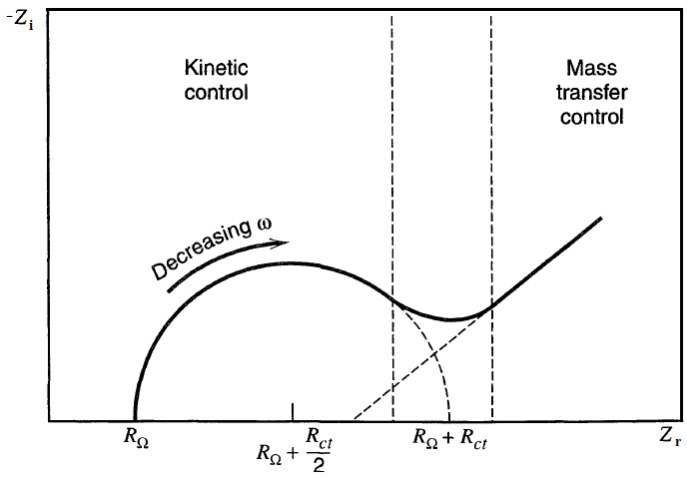

Figure 3-8: Representation of a Nyquist plot for a planar electrode interface. Reprinted from reference 91 with permission from John Wiley and Sons, © 2001

Impedance spectroscopy is one of the most used techniques to characterize the performance of electrical and transport properties. From a set of impedance values obtained at different frequencies, electrical properties of a material and its interfaces can be obtained. The high frequency region (> 100-1000 Hz) reveals the charge transport in the catalyst layer, whereas, below 1 Hz, the impedance spectrum represents the mass transport in the GDL, the catalyst layer and the membrane [92]. These values are obtained by adjusting the experimental data to different equivalent circuits. For fuel cell operation, the Randles circuit (Figure 3-9) is the most common equivalent circuit [93]. It consists of an ohmic resistance (R_Ω) in series with parallel combination of the double layer capacitance (C_d) and the impedance of a faradaic reaction, which consists of a charge transfer resistance (R_{ct}) and the Warburg element (W).

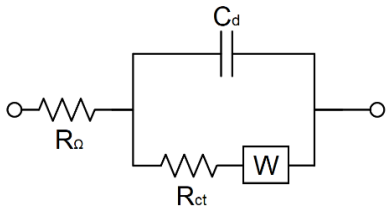

Figure 3-9: Schematic of a Randles circuit

In fuel cells, impedance is generally measured in a **H_2/O_2 gas-feeding mode**. Depending on the operation parameters and the values of the overpotential at which the experiments are conducted, the importance of the various transport process can vary. The simplest impedance spectrum would be a single arc in the Nyquist plot (partially dashed in Figure 3-8), which represents a process controlled by the kinetics of the oxygen reduction reaction. The high frequency intercept of the arc with Z_r represents the ohmic resistance of the system (R_Ω in Figure 3-8) while the diameter of the arc (R_{ct} in Figure 3-8) represents the charge transfer resistance of the reaction [93]. At low frequencies, an additional arc may appear when mass transport and diffusion processes are relevant in the electrode reaction. This is usually modelled using the Warburg element in series with the charge transfer resistance. The Warburg impedance is reserved for the special case of semi-infinite linear diffusion but numerous derivations can be found in the literature [94].

Furthermore, it is also important to remark that in porous electrodes, such as Pt/CB in PEM fuel cells, the frequency dependence of the impedance is slightly different from the ideal case, showing an asymmetric semi-circle due to overlapping loops corresponding to anode and cathode activation processes. In addition, the double layer capacitance, does not match exactly with the behavior of an ideal capacitor, so a correction using an exponent (n) is necessary. This modified capacitor is called constant phase element (CPE) and is an empirical solution for the unevenly distributed electron charges inside the porous electrodes [95].

The majority of the research using impedance in fuel cells is conducted using the H_2/O_2 gas-feeding mode. Given that the global impedance is almost equal to the cathode impedance due to the fast hydrogen oxidation reaction, there is also other possible study modes to eliminate the oxygen limitations on the cathode catalyst in order to analyze transport processes different from oxygen gas transport. For instance, the **H_2/N_2 gas-feeding mode** is used to analyze proton conduction, which is also a significant contribution to performance losses, both in the membrane and in the cathode catalyst

layer [93]. Figure 3-10 shows a typical impedance measurement in H_2/N_2 gas-feeding mode.

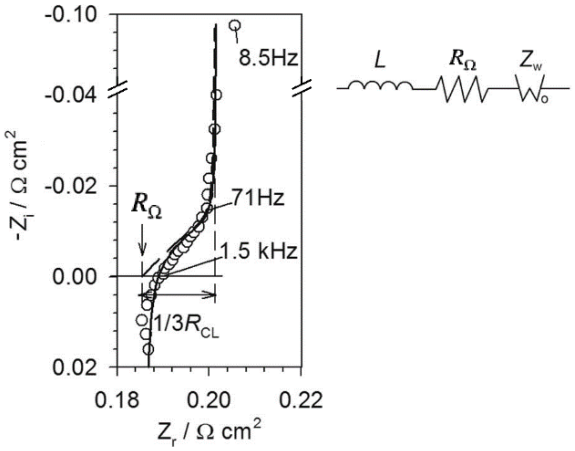

Figure 3-10: Nyquist plot (circles) and fit of the experimental data to the equivalent circuit to the right (solid line) for an impedance experiment with H_2/N_2 gas-feeding mode. Reprinted from reference 96 with permission from The Electrochemical Society, © 2012

From the fit to the circuit shown above, it is possible to extract the catalyst layer resistance (R_{CL}), with calculations based on the finite transmission-line model that is described elsewhere [96]. In this thesis, only a qualitative analysis of the catalyst layer protonic resistance will be performed, as these experiments were proven to be strongly dependent on the water content [97]. Since electrosprayed layers have such special properties on water interaction, a more thorough study is needed to directly correlate the calculations performed with traditional ink-based methods. In any case, to minimize the influence of humidity, the experiments were performed after passing 100 %RH H_2/N_2 gases overnight, ensuring a complete elimination of the oxygen in the system, while trying to maintain the hydration of MEA components.

3.4 Results and discussion

3.4.1 Morphological characterization of electrosprayed catalyst layers

In previous works of the group, cross-sectional SEM images of electrosprayed catalyst layers were obtained by cutting the MEA with a sharp blade. The obtained results were

characterized by irregular thickness and large pores (> 10 μm), in which small globular and dendritic growths could be distinguished in contrast with commercial airbrushed electrodes that presented more compact morphology and lower thickness for a given catalyst loading [98,99]. Micrographs of the surface of electrosprayed layers were also taken, showing a much higher porosity and column-like growth with dendritic shapes [100,101]. The macroporous morphology of electrosprayed layers was also studied in previous works with porosimetry measurements. Mercury porosimetry measurement yielded 12 $cm^3 \cdot g^{-1}$ pore volume for electrosprayed layers, compared with 2.5 $cm^3 \cdot g^{-1}$ carbon of films prepared by airbrushing with the same composition [101]. The total pore volume fraction of the electrosprayed layers is usually above 90 %, compared with 80 % for layers deposited with airbrush and commercial layers [99]. Pore size distribution for electrosprayed and airbrushed films were studied with N_2 adsorption isotherms, showing the micro (below 2 nm) and mesopore contributions (below 50 nm) and mercury porosimetry, yielding the meso and macropores contributions (below 100 μm) [102]. Airbrushed films have typical bimodal pore size distribution with a center at 1–2 nm and another at 70–80 nm. These two contributions are referred to as primary and secondary pores [29]. Electrosprayed layers show an additional large macropore contribution above 10 μm, which depends on Nafion concentration and other deposition parameters [101].

In this section, the previous effort of the group on characterization of the electrosprayed catalyst layers is continued and updated. In collaboration with the Surface and Microscope Analysis Unit of CIEMAT, a methodology has been developed for sample preparation of membrane-electrode assemblies to be studied by SEM microscopy in cross-sectional mode. Additionally, to help to unravel the nature of the electrosprayed films; TEM, STEM and water contact angle measurements were also performed.

MEA cross-sectional analysis

Cross-sectional images allow the analysis of morphology and composition among the different layers of the MEA. Different preparation methods have been employed for MEAs in order to determine optimal conditions for this particular observation mode. All

the MEAs shown in the images have an electrosprayed catalyst layer deposited on top of the membrane looking upwards and a commercial gas diffusion electrode looking downwards, as described in the experimental section. Additionally, the images were taken by the analysis of the backscattered electrons, to enhance the contrast and facilitate the visualization of Pt/CB layers.

In Figure 3-11, there is a selection of the most characteristic images of three methods used to prepare the MEA samples: sharp knife, metallographic and ion-milling preparations. The sharp knife preparation was used in previous characterization studies of the group, with acceptable results [98, 99]. The preparation consists on the use of a sharp knife to cut the MEA, which is directly mounted in a stage for SEM observation.

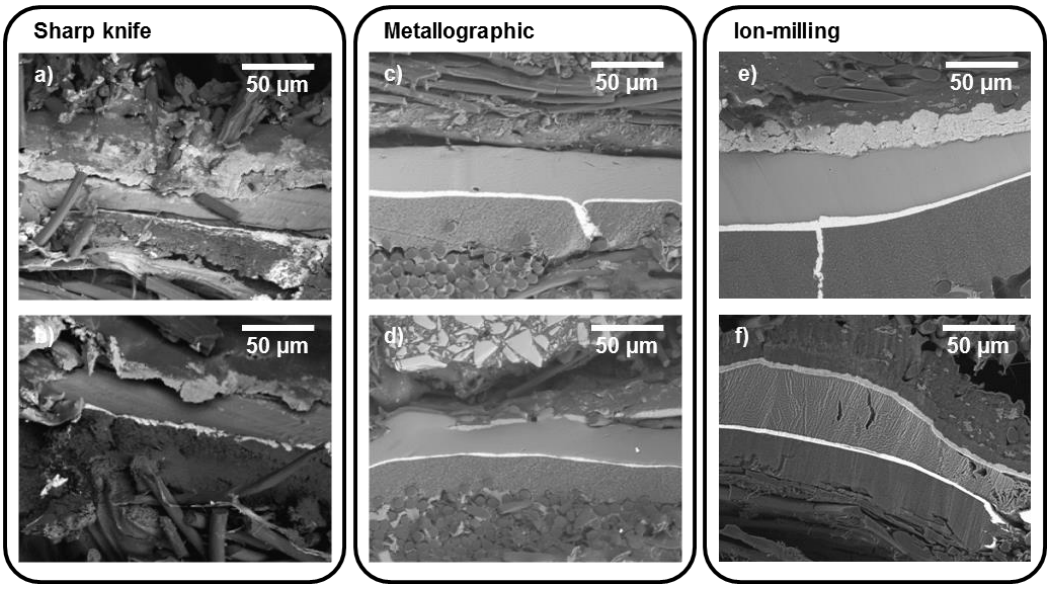

Figure 3-11: Selection of cross-sectional images of sharp knife, metallographic and ion-milling preparations

As shown in Figure 3-11a and Figure 3-11b, the result of the cut may be quite unsatisfactory if not properly done, showing irregularities with different layers displaced, making difficult a proper analysis of the different layers. Finding a proper area to take a clear image of the section with a knife cut is stochastic and not reproducible. The aspect of the section generally looks like in the selected images (Figure 3-11a and Figure

3-11b), and obtain a good image of the MEA cross-section may take several tries. Taking these difficulties in mind, the group established collaboration with the Microscope and Surface Analysis Unit of CIEMAT in order to explore new possibilities to carry out cross sectional analysis of MEAs. The collaboration was possible after the award in 2015 of a national project (E-LIG-E, ENE2015-70417-P), headed by the directors of this thesis, where this task was specifically included.

The metallographic preparation method resulted to be more reproducible and allow a perfect visualization of the different components of the MEA, as shown in Figure 3-11c and Figure 3-11d. Although the commercial catalyst layer is perfectly visible, the electrosprayed layers appear to be missing. It is believed that grinding and polishing processes are too aggressive for the electrosprayed layers, probably due to the fragility under mechanical stress caused by its high macroporosity. In order to avoid the requirement of mechanical methods to obtain a flat surface, ion-milling was considered as possible solution to cut a section of the MEA, as it is a stress-free physical process. Ion-milling preparation gave excellent results for both electrosprayed and commercial catalyst layers as shown in Figure 3-11e and Figure 3-11f, in which electrosprayed layers with different thickness are shown.

Due to the success of the ion-milling preparation method, it was used to characterize the thickness of electrosprayed catalyst layers with different loadings in assembled MEAs. Airbrushed layers were also analyzed to compare the growth of both deposition methods. In Figure 3-12, electrosprayed and airbrushed catalyst layers with loadings in the range of 0.025-0.25 $mg \cdot cm^{-2}$ are shown. The MEAs were submitted to previous electrochemical characterization in single cell, for 50 h under mild conditions, so no component degradation is expected. The downsides of the method are the small cross-section area available to the analysis, which is 1 mm for the ion-milling machine available in the laboratory. The voltage and time have also been carefully optimized for the process, as the polymer membrane is especially sensitive to the process. For instance, Figure 3-12b and Figure 3-12e show the first signals of membrane degradation, although it is not

relevant for the visualization of any of the components, further degradation will result in membrane shrinkage and a modification of the MEA structure.

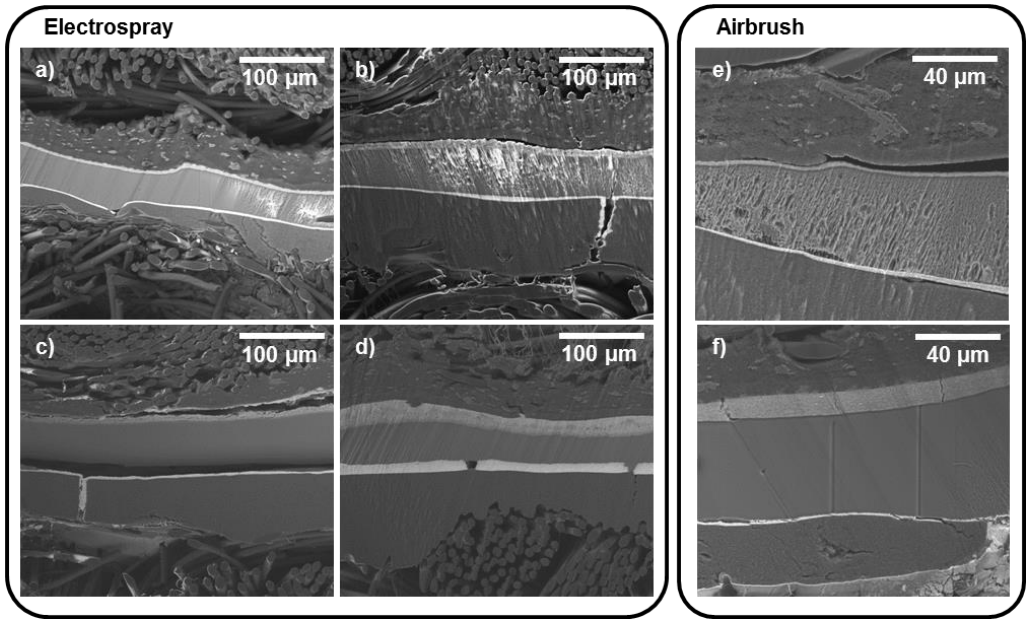

Figure 3-12: Micrographs of MEAs cross-sections prepared by the ion-milling technique on different electrosprayed catalyst coated membranes with loadings of a) 0.025. b) 0.10. c) 0.17 and d) 0.25 mg·cm^{-2} (The electrosprayed layer is on the upper part of the micrograph). Airbrushed catalyst-coated membranes of e) 0.025 and f) 0.25 mg·cm^{-2} are presented for comparison

The values of the catalyst layer thickness versus the platinum loading are depicted in Figure 3-13. In the figure, it is clear that the increased porosity of electrosprayed layers gives rise to a higher thickness compared to airbrushed layers, as the loading increases. Two distinct growth regimes can be deduced for electrospray deposition, a fast growing regime up to 0.17 and a slower growth up to 0.25 mg·cm^{-2}. Electrospray growth regimes will be further analyzed in Chapter 4, as the same tendency is observed for Vulcan-Nafion inks.

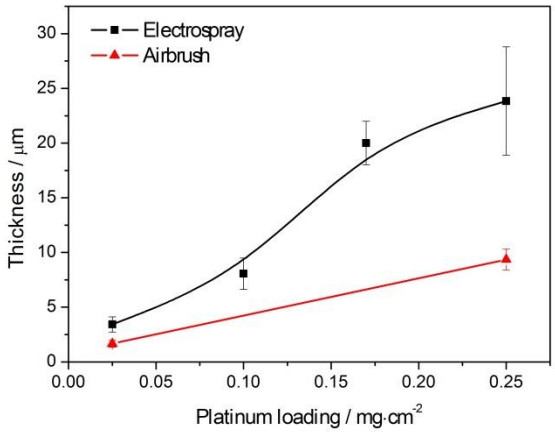

Figure 3-13: Representation of the electrosprayed and airbrushed catalyst layer thickness versus carbon loading after cell assembly

Comparing the ion-milling thickness values with the ones obtained in previous studies there is quite a big discrepancy, as the values for electrosprayed layers with 0.25 mg·cm^{-2} values around 25 µm were measured, in contrast with previous studies, where thickness around 40-50 µm were given for membranes prepared with the exact same procedure [99]. At first, the discrepancy was attributed to the compression of the MEA into the single cell hardware (2 N·m torque with eight bolts), since catalyst layers have a plastic deformation range that was proven to be affected by the hot-pressing pressure, affecting the porous structure and cell performance [103]. It is true that the applied torque pressure is much lower than the pressures applied in hot-pressing processes; however, electrosprayed layers have a much higher macroporosity than other ink-based methods, so the threshold pressure for deformation could also be much lower. To analyze electrosprayed catalyst layers before the compression process, experiments with electrosprayed catalyst coated membranes before MEA assembly were cut with ion-milling. In Figure 3-14, it is compared a photo of a cross-section with a sharp knife and with ion-milling. The thickness of the ion-milling section corresponds to the value obtained in the compressed MEA, while the knife section seems to have a bigger thickness. Comparing images in Figure 3-14b and Figure 3-14e, it can be clearly seen that the ion-milling process clearly define the section plane, in which the microstructure is

changed, in comparison with the sharp knife, that does not clearly define the section plane, and the microstructure below the plane can lead to an erroneous thickness measurement. The shear stress caused by the knife, could drag the outer particles, making the measure even more complicated. Thus, it is concluded that the previous measurements of thickness in electrosprayed layers were overestimated due to the preparation method.

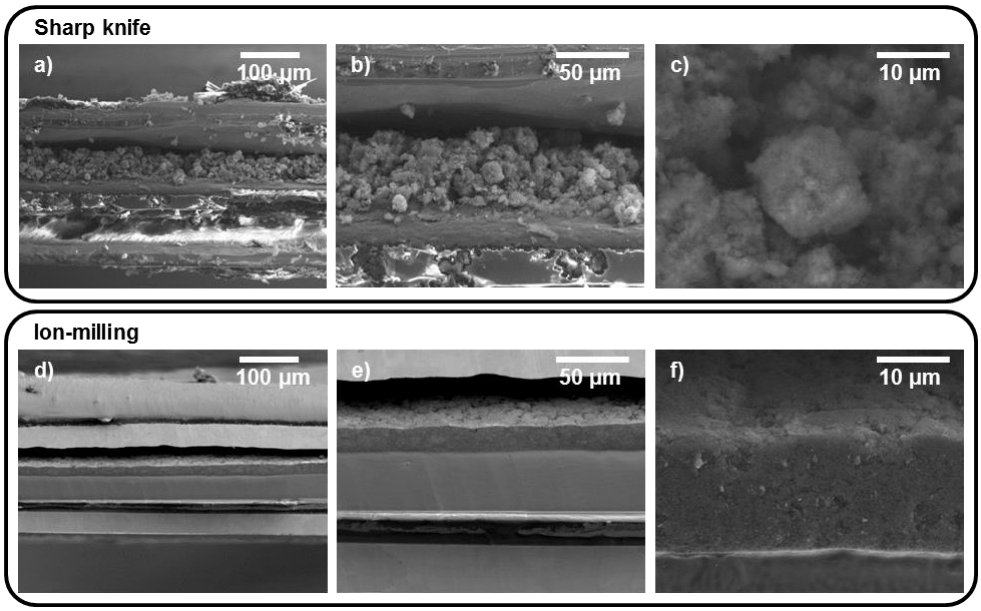

Figure 3-14: Micrographs of cross-sections of electrosprayed catalyst coated membranes with 0.25 $mg_{Pt} \cdot cm^{-2}$ using sharp knife and ion-milling preparation methods at different magnifications

Another drawback of the ion-milling method, as it can be seen by comparing Figure 3-14c and Figure 3-14f, is the modification of the porosity of the catalyst layer, which is probably caused by dust generated in the cutting process. The modification of the porosity eliminates the possibility to characterize the microstructure of porous layer by ion-milling preparation. Further research on an easy and reproducible preparation method for MEAs containing electrosprayed layers is required to enable a proper analysis of the microstructure of the layer. The knife-cut method appears to better preserve the bulk porosity of electrosprayed films, which is important to explain their behavior as catalyst layers in fuel cells.

Additionally, as a side result currently used for other purposes in the research group, metallographic preparation was proven to be useful for regular post-mortem analysis of membrane-electrode assemblies. Using the metallographic preparation, it is possible to analyze MEA cross-sections of several centimeters, allowing the characterization of different areas along the section length, due to the high flatness of the surface, which facilitates an optimal contrast among layers and accurate analysis by means of EDS. Post-mortem characterization includes different analyses such as porous structure characterization, carbon support corrosion, elemental distribution in the catalyst layer and polymeric membrane or changes in size and morphology of the carbon fibers in the gas diffusion layer.

Catalyst layer structure characterization

Pursuing the goal of obtaining more information about the morphology and the component distribution in electrosprayed catalyst layers, STEM and TEM imaging were used to get further insights on this layer preparation method. These methods were assisted by EDS analysis to clarify the interpretation of the results. A part of these measurements were obtained as a result of collaboration with the Oak Ridge National Laboratory and the other in the Microscopy Center of Universidad Complutense de Madrid.

For STEM imaging, the catalyst layers were deposited on Nafion membranes and embedded in epoxy resin for reducing them to thicknesses in the scale of nanometers with ultramicrotomy. Figure 3-15 shows cross-section images of catalyst layers with platinum loadings of 0.025 and 0.25 $mg \cdot cm^{-2}$ and an ionomer loading of 15 wt% deposited on Nafion 212. In these images, the layer shows irregular thickness, 3 to 4 μm, with large macropores (> 50 nm) for the low loaded layer and a thick (around 40 μm) electrode with large gaps between catalyst/support agglomerates for the 0.25 $mg \cdot cm^{-2}$ layer.

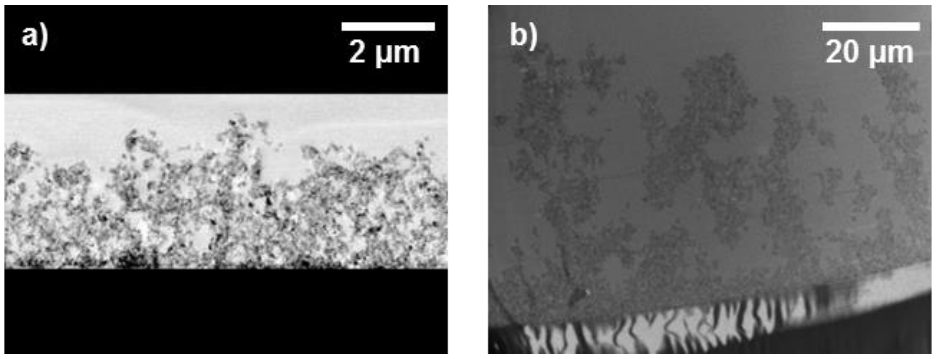

Figure 3-15: STEM images of the cross-section of electrosprayed layers with platinum loadings of a) 0.025 and b) 0.25 mg·cm^{-2}

Figure 3-15 show the micrographs of the entire cross-section of the catalyst layers with loadings of 0.025 and 0.25 mg·cm^{-2}. As the morphology and thickness of the layer were already characterized in the previous subsection, it is clear that the catalytic layer microstructure is negatively affected by the preparation method. This is especially clear in Figure 3-15b, in which the agglomerates are broken and do not have continuity, in contrast with the images taken by SEM microscopy in the previous section. This can be either an effect of the epoxy resin embodiment or the mechanical preparation, which was also not adequate in the metallographic preparation for SEM cross-sectional characterization. Even if STEM is not useful to characterize the microstructure of the layers, it is still an attractive tool for characterizing the distribution of ionomer in Pt/CB layers in combination with EDS [104]. In Figure 3-16, high-angle annular dark-field and the distribution of platinum, fluorine, and carbon in the catalyst layer is shown. At higher magnification (Figure 3-16a), the platinum catalyst nanoparticles appear evenly distributed showing no alteration at this level by the electrospray process. The STEM image shows platinum and carbon black phases (Figure 3-16a) that closely follow the contrasts of the platinum image (Figure 3-16c) and the carbon image (Figure 3-16b), respectively, as expected.

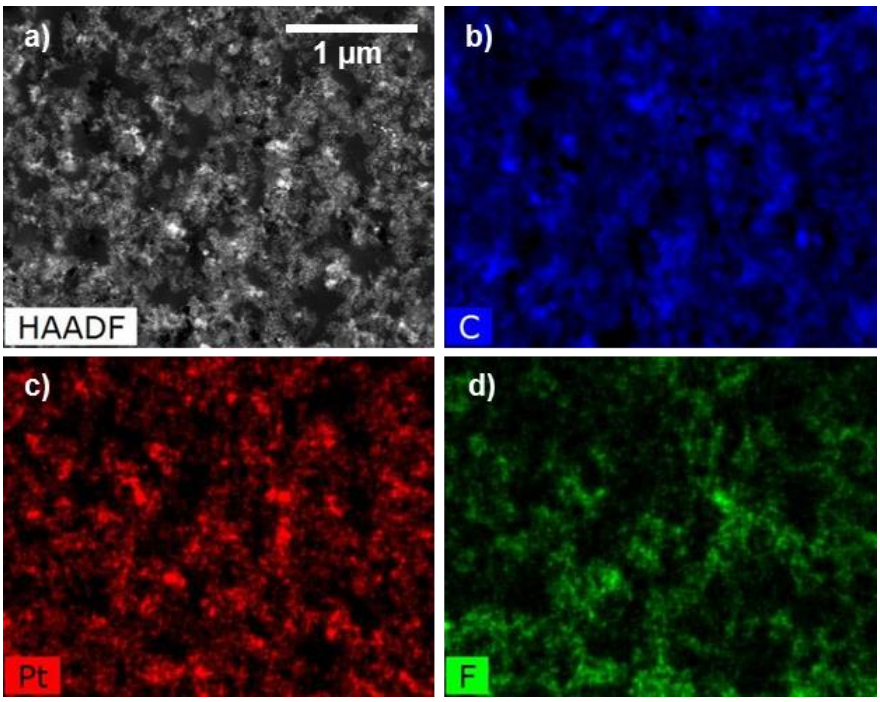

Figure 3-16: High-angle annular dark-field STEM image (a) with images of the distribution of carbon (b), platinum (c) and fluorine (d) of the sample with 0.25 $mg_{Pt} \cdot cm^{-2}$

It is worthy to note the similarity between the distribution of platinum and fluorine (cf. Figs. Figure 3-16c and Figure 3-16d), which reflects a preferential interaction of the Nafion ionomer with platinum nanoparticles, and less with carbon support. Evidences of a specific interaction of the ionomer with platinum in electrosprayed films were obtained from thermogravimetric analysis [105]. STEM images of catalyst particles prepared with a common spray technique show, on the other hand, that the ionomer is unable to uniformly cover the surface of carbon black particles [106]. Electron tomography studies, which allowed 3D analysis of the catalyst agglomerate microstructure, confirmed that Nafion coverage of the catalyst surface is indeed deficient [107].

In order to get further insights on the structure and ionomer distribution, TEM microscopy was used to analyze the initial stages of electrospray and airbrush deposition. The Pt/CB agglomerates were deposited directly onto copper grids as described in the experimental section, to analyze the Pt/CB-Nafion interaction depending on the deposition method. To characterize the ionomer presence, EDS analysis was performed

on selected areas of the samples. However, the EDS characterization results should be only taken as a qualitative indication of the ionomer presence, since ionomer decomposition was reported when catalyst inks are subjected to high-energetic electron beams [108]. A quantitative analysis would require previous optimization to reduce the electron-beam induced damage.

In Figure 3-17, the typical agglomerate formation in electrospray deposition can be observed. The agglomerates tend to present circular shapes and form compact secondary aggregates. Vertical growth can be observed, as the contrast in central areas becomes higher, in the very first initial stages caused by the antenna effect. Figure 3-17a corresponds to an ink with 15 wt% of Nafion ionomer. To the right of the micrograph, EDS analysis of the circled area is presented as a typical spectrum for catalyst aggregates with 15 wt% ionomer, confirming an adequate distribution of Nafion on the surface of the Pt/CB particles. The presence of Nafion in the images is identified by means of F signal at 677 keV in the EDS spectrum.

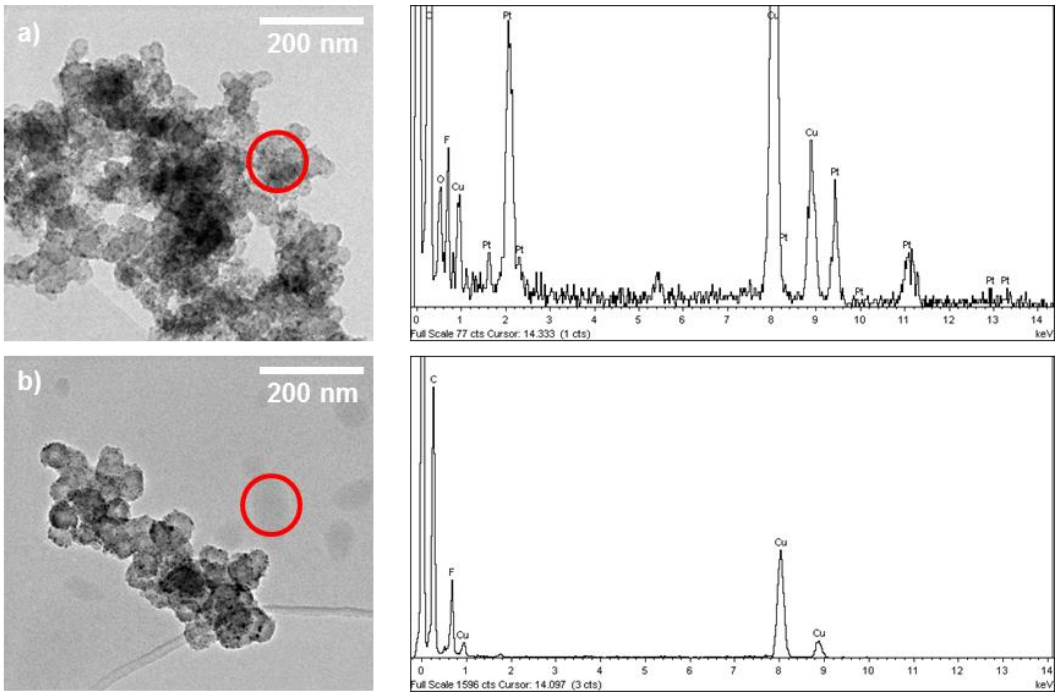

Figure 3-17: TEM micrographs of electrosprayed aggregates with a content of a) 15 % and b) 30 wt% of Nafion ionomer with two selected EDS analyses of the areas marked with a red circle

On the other hand, an ink with 30 wt% of Nafion, gives rise to the formation to segregated Nafion accumulations, as in the red circle in Figure 3-17b. The EDS analysis of the circled area confirms that the drops are indeed formed by pure ionomer. It was also observed that Pt/CB aggregates had much lower fluorine signals or no signal at all (not shown), suggesting that the interaction between Pt/CB particles and the ionomer could be reduced as the concentration of the ionomer grows. These results match with the previous findings of the group, in which the optimum value of Nafion concentration was set around 15 % [5]. These results clearly show that an excess of ionomer will not contribute to Pt/CB coverage, but produce isolated Nafion regions that will probably reduce the electrical conductivity of the catalyst layers.

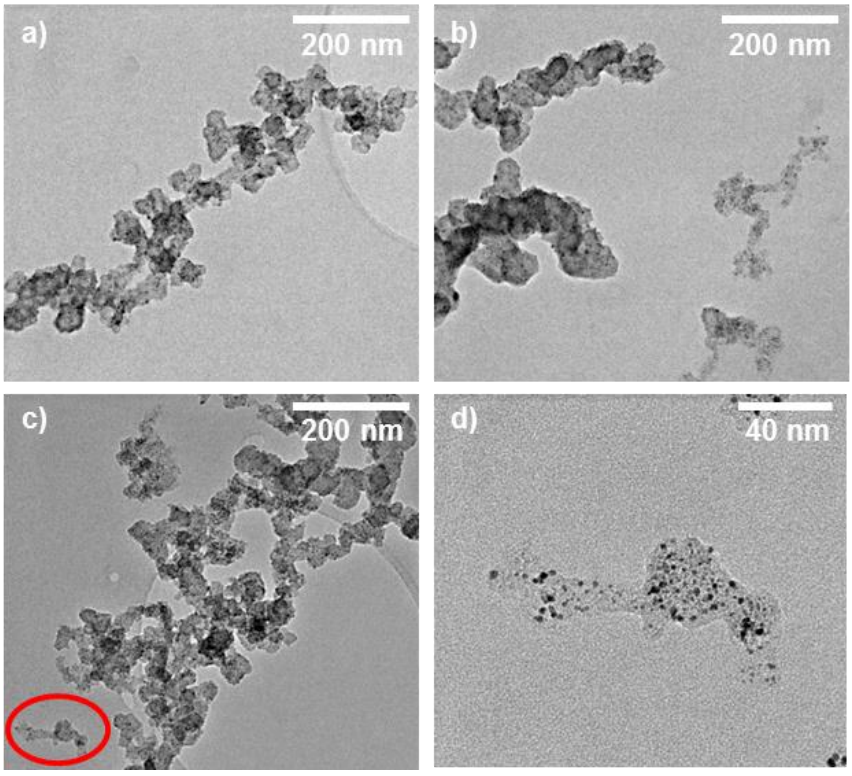

Figure 3-18: TEM micrographs of airbrushed aggregates with a content of 30 % (a and b) and 5 wt% (c and d) of Nafion ionomer

For comparison, typical airbrushed aggregates can be seen in Figure 3-18. They are characterized by less rounded primary aggregates and a loose structure of secondary

aggregates, probably due to the drying process of the ink on top of the substrate. In Figure 3-18a and Figure 3-18b, an ink with 30 wt% of Nafion was selected since it is reported to be the optimum concentration for 'mechanical spraying' processes. EDS spectra (not shown) suggest that less ionomer is present in the surface of the Pt/CB particles. In the micrographs, the presence of an ionomer phase (right area of Figure 3-18b) was observed in multiple samples, indicating a segregation of the Nafion phase on the deposition process. The formation of the ionomer phase was also observed for inks with low ionomer concentration. For instance, an ink with 5 wt% of Nafion can be seen in Figure 3-18c and Figure 3-18d. The red circle detail shown in Figure 3-18d, in which the same ionomer phase observed for 30 wt% is formed.

The Nafion phases present in Figure 3-18, point out that airbrush deposition does not achieve a proper interaction between the catalyst particles and the ionomer regardless of Nafion concentration, unlike electrospray deposition. These results also support the findings in Chapter 2, in which ionomer interaction with the carbon support particles is stronger in electrospray than in airbrush deposition and this strong interaction is progressively lost as the ionomer content is increased in electrospray deposition.

Water contact angle measurements

The hydrophobicity of catalyst layers deposited on Nafion membrane has been probed by means of contact angle measurements of a water drop with the sample surface. Initially, an instant measurement of water contact angle was performed. Then, the water drop contact angle was measured as a function of time on the surface of catalyst layers prepared by electrospray and aerography with 15 and 30 wt% ionomer [99]. After the results in the previous chapter, in which it was seen that the airbrushed layer had an important transition between high contact angles immediately after its preparation and the measurements in acidic water media, it was decided to perform some additional measurements of catalyst layers deposited on Nafion membranes after a 'hydrophilic treatment'. The hydrophilic treatment consisted in immersion during 12 h in H_2SO_4 0.5

M at room temperature, followed by acid wash out in distilled water, and drying in air at 80 °C for 1 h.

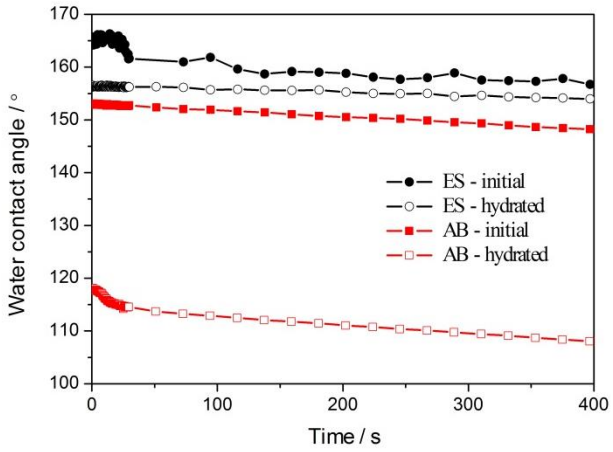

Figure 3-19: Water contact angle measurements Pt/CB layers with 0.25mg$_{Pt}$·cm^{-2} loading and 15 wt% Nafion ionomer, deposited on Nafion 212 membrane by electrospray (ES) and airbrush (AB), before and after hydrophilic treatment

Figure 3-19 shows the contact angle measurements as a function of time. The experiments show an initial stabilization for 30 s, followed by a constant decrease rate. For the electrosprayed film, the angle decrease can be entirely attributed to the reduction of drop volume due to evaporation, as tested with a drop on a non-porous Teflon film (not shown), whereas, for the airbrushed film, the larger decrease rate reflects drop imbibition into the layer. Airbrushed catalyst layers show a high initial contact angle but, as expected, after the hydrophilic treatment they lose their hydrophobicity. Contact angle values show that electrosprayed layers have a superhydrophobic character ($\theta > 150$) that is conferred by their particular morphology and persist after the hydrophilic treatment. It is also relevant that no noticeable wetting is observed even with a fully hydrated Nafion support. Moreover, it was also noted that the superhydrophobicity of the electrosprayed catalyst layers persisted after several hundred-hour operation in a fuel cell, in which water was generated inside the bulk of the layer, reflecting the high stability of the morphology generated by the electrospray deposition process.

3.4.2 Mass-transport properties of electrosprayed layers

Mass transport in the catalyst layer of PEM fuel cells has a significant impact on fuel cell performance and durability. Within the catalyst layer, mass transport of reactants and product water takes place near the catalyst sites, resulting in local transport resistances that affect polarization behavior. In addition, the transport of liquid water in the catalyst layer controls the membrane and electrodes humidification states that determine key parameters for fuel cell performance, like the internal resistance and the catalyst activity. The catalyst layer must allow for facile transport of gas and liquid water, high proton conductivity, and easy accessibility of catalytic sites, keeping at the same time optimal membrane humidification. The mass transport measurements shown in this thesis were obtained during a predoctoral stay in the National Berkeley Laboratory (USA).

Catalyst layer mass-transport resistance

The mass-transport resistance (R_{CL}^{mt}) of electrosprayed catalyst layers deposited on Nafion membranes was measured using the hydrogen-limiting current technique at different Pt/CB loadings and ionomer concentrations. Additionally, the resistance effect of cell operation parameters is analyzed at different feed gas humidities and cell temperatures. The mass-transport resistance is calculated from the limiting-current experiments using hydrogen, while molecular-weight specific resistances ratio (R_{CL}^{D2}/R_{CL}^{H2}) determination is carried out by an additional limiting-current measurement using deuterium.

The effect of platinum loading on mass-transport resistance of electrosprayed catalyst layers is depicted in Figure 3-20a. The measurements were performed in catalyst layers with ionomer content of 15 wt% at 80 °C and 80 %RH. The reduction of the platinum loading in electrosprayed layers resulted, as expected, in a steady increase of mass-transport resistance, but most importantly, the unexplained resistance increase at low loadings is much lower using electrospray than on catalyst layers prepared by other deposition techniques. Spingler et al. registered an increase from 22.5 to 52.3 $m \cdot s^{-1}$ when

decreasing loading from 0.24 mg·cm^{-2} to 0.028 mg·cm^{-2} for a conventional catalyst layer [87].

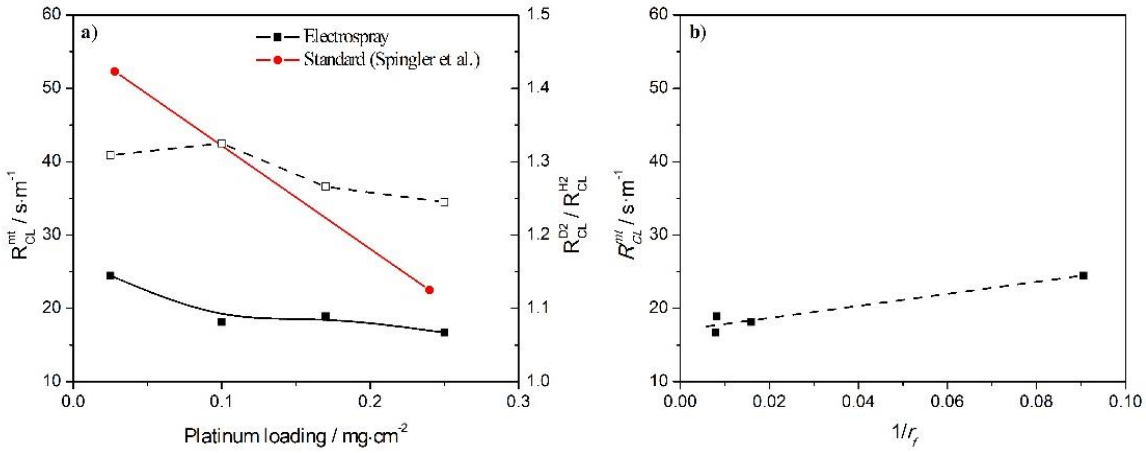

Figure 3-20: a) Mass-transport resistance and molecular-weight specific resistances ratio (dashed) as a function of platinum loading for electrosprayed (black) and airbrushed (red) catalyst layers. b) Mass-transport resistance of the electrosprayed layers versus catalyst roughness factor

These results clearly show that electrospray mitigates the inherent mass-transport losses in catalyst layers at low platinum loadings. Such losses are mostly attributed to the local mass-transport resistance, i.e. transport losses very close to the reaction site, represented by the term $R_{local}/\eta\gamma$ in equation 3.7. An estimation of this term can be obtained from the slope of the linear relation R_{CL}^{mt} vs. $1/r_f$, as shown in Figure 3-20b. The value obtained, 82 s·m^{-1}, is 20 times lower than that measured for a conventional catalyst layer [37], showing improved local mass transport in electrosprayed catalyst layers. This beneficial effect could be caused by the better distribution of the ionomer over the catalyst surface, and opens the possibility to improve the performance of the cells when using low-loaded catalyst layers.

Figure 3-20a also shows the ratio of resistances using deuterium and hydrogen as gas probes. This ratio can be used to acquire more insights on the character of the transport process. When the ratio of the resistances approaches 1.4, the mass transport resistance is closer to that corresponding to a pure diffusive process. For catalyst layers, this value was

found to be smaller (between 1.30-1.35), indicating a contribution of non-diffusional transport, ascribed to the local diffusion within the ionomer film. For low loading catalyst layers prepared using standard ink-based methods, the effect of non-diffusive transport phenomena is increased and the value of the ratio is reduced to 1.2 [87]. Electrosprayed layers show an increasing limitation caused by diffusive processes at low loadings due to local diffusion within the ionomer film. On the other hand, non-diffusive transport phenomena increase limitation at high catalyst loadings, ascribed to transport processes through ionomer/pore and ionomer/Pt interfaces [37]. This effect on electrosprayed layers is the opposite as compared with the previously reported data, indicating once more that the ionomer interaction with the catalyst agglomerate is more optimal in comparison with traditional ink-based methods.

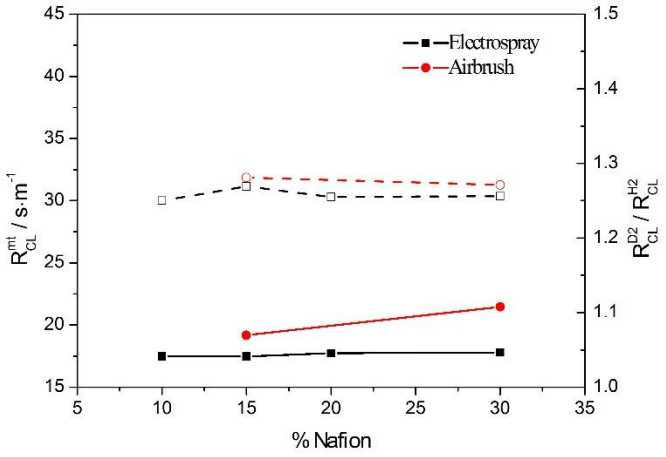

Figure 3-21: Mass-transport resistance and molecular-weight specific resistances ratio (dashed) as a function of ionomer concentration for electrosprayed (black) and airbrushed (red) catalyst layers

As previous studies of the group hypothesized that the electrospray deposition method contributes to a better ionomer distribution onto the catalyst layer [5], the effect of ionomer content on mass-transport resistance were also studied. For this study, a Pt/CB loading of 0.25 mg·cm^{-2} was selected and measured at 80 °C and 80 %RH. Figure 3-21 shows that the ionomer concentration has minor influence on the mass-transport resistance of electrosprayed layers, as the resistance remains unchanged between 10-30 wt% of ionomer content, whereas for airbrushed layers R_{CL}^{mt} increases significantly with

ionomer loading. Such result confirms that the electrospray deposition accommodates better larger amounts of the ionomer, having a minor impact on the transport properties of the films. The same conclusion was attained in Chapter 2 by thermogravimetric and XPS analysis, and from porosity measurements in a previous work [101], and reflects an optimized distribution of the ionomer phase around the catalyst particles as determined herein.

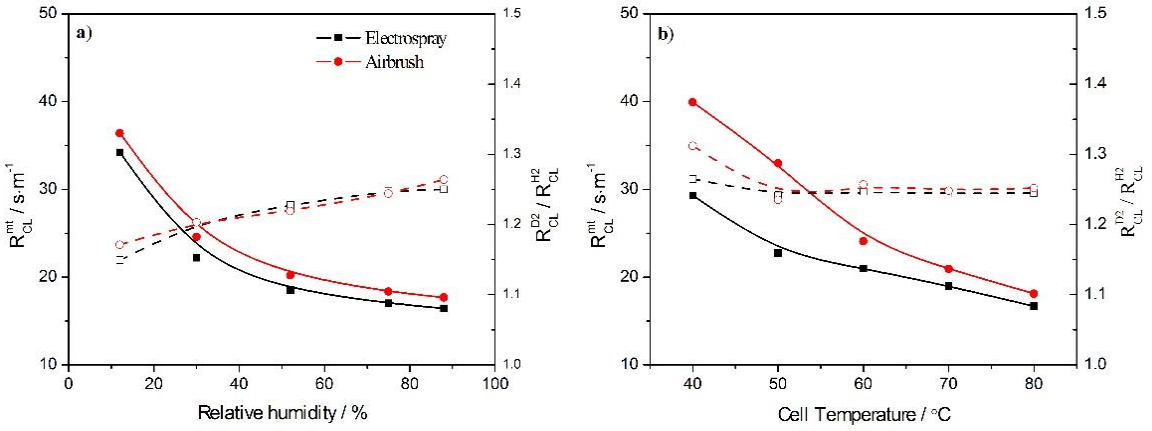

Figure 3-22: Mass-transport resistance and molecular-weight specific resistances ratio (dashed) as a function of gas relative humidity (a) and cell temperature (b) for electrosprayed (black) and airbrushed (red) catalyst layers

In order to analyze the effect of the operation conditions on mass transport, electrosprayed and airbrushed catalyst layers with 0.25 $mg_{Pt}\cdot cm^{-2}$ and 15 wt% Nafion were studied at different cell temperatures and relative humidities. Gas humidification has almost the same effect on both film types (Figure 3-22a), showing a decay with humidity that is consistent with transport through the ionomer film being the most determining transport process. The decreasing resistance ratio at low relative humidities reflects more difficulties with interfacial transport. However, limiting-current measurements at low RH could also be affected by drying of the cell membrane. Cell temperature exhibits, on the other hand, a different effect on transport properties for the two catalyst layers, as shown in Figure 3-22b. The airbrushed film presents a larger slope when decreasing temperatures that reflects larger thermal activation of transport than in electrosprayed films, especially at low temperature (< 50 °C). Similar resistance ratio in

both layer types demonstrates that the controlling transport processes must be qualitatively similar in both catalyst-layer types, with some more differences at the lowest temperature (40 °C). The larger thermal activation of the airbrushed layer may be a consequence of its lower water-vapor-uptake capability (see next section), which determines the hydrogen transport rate within the ionomer film.

Water uptake of catalyst layers

Water-vapor uptake measurements on catalyst layers prepared by electrospray and airbrush are shown in Figure 3-23. In these experiments, an inert gas with a controlled pressure of water vapor enters the structure of the catalyst layer leading to a mass increase upon absorption (or adsorption) into the layer [17]. From Figure 3-23a, it is clear that electrospray layers are characterized by larger water-vapor-uptake compared to airbrushed layers in the whole range of relative humidities. Such a result may explain the good behavior that they show during fuel-cell operation under low humidification conditions (see Chapter 3.5). Assuming that all water vapor absorbs into the ionomer, water content λ can be calculated from equation 3.2, which is an indication of the absorbed water molecules per sulfonic group.

Results in Figure 3-23b show that the ionomer deposited through the electrospray process is able to absorb more water vapor, leading to higher λ values, which may be due to its specific morphology as derived from the fabrication process. The decrease in λ with increasing Nafion content may reflect a change in the interaction of the ionomer film with the catalyst aggregates, from a specific adsorption on the catalyst surface, with high water-absorption capability, to a bulky phase with less absorption capability. The second state occurs upon exceeding 15 % weight percent, as reflected by XPS and thermogravimetric analyses on Chapter 2 and the TEM characterization in the previous section. High λ values (over 15-20), however, may indicate that not all the water-vapor is interacting with the ionomer sulfonic groups, but subjected to different interactions with the platinum surfaces or capillary condensation inside the pores. However, the trend of

the increased water-uptake for the electrosprayed layers is in qualitative agreement with their increased performance.

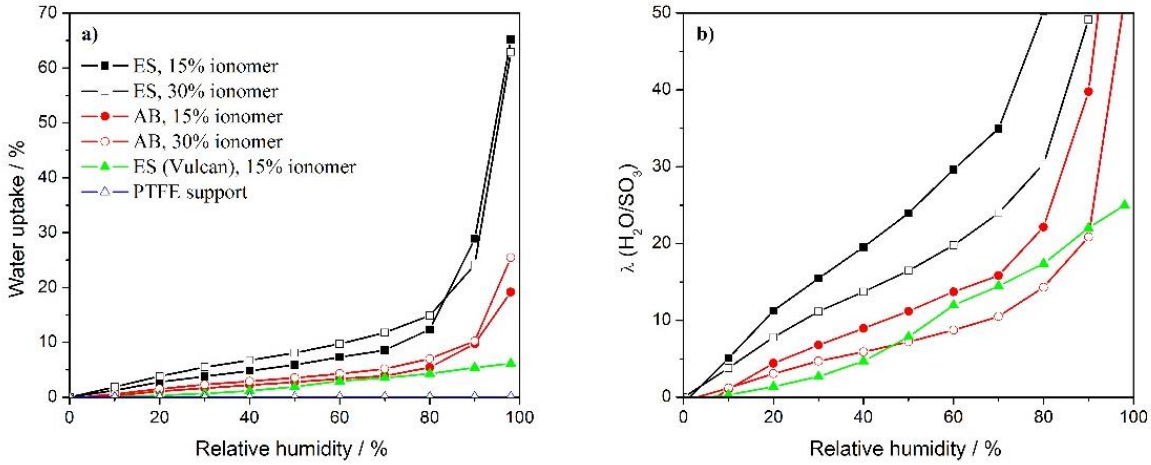

Figure 3-23: a) Water-vapor uptake absorption curves and b) calculated water molecules per sulfonic acid group as a function of relative humidity, for catalyst layers deposited by electrospray and airbrushing

The rate of absorption of water, depicted in Figure 3-24, is normalized by the amount of ionomer of each layer to facilitate the comparison between samples with different ionomer contents. The absorption rate of the electrosprayed layers with 15 wt% ionomer content is faster than that in the layer with 30 wt%. This is clearly another indication of the different interaction of the ionomer and Pt/CB for the optimal value of 15 wt%, in which not only the amount of absorbed water is higher, but also the absorption kinetics is favored, being faster at any RH range compared to the other samples. The water absorption rate for airbrushed layers is similar in all the ranges, indicating that the state of Nafion is independent on the concentration. The shape of the rate of absorption curves of electrosprayed layers with 30 wt% ionomer almost matches perfectly to with its airbrushed counterparts, thereby gives another proof that an excess of Nafion in the electrospray process does not favor the special properties obtained with the deposition method at lower ionomer contents.

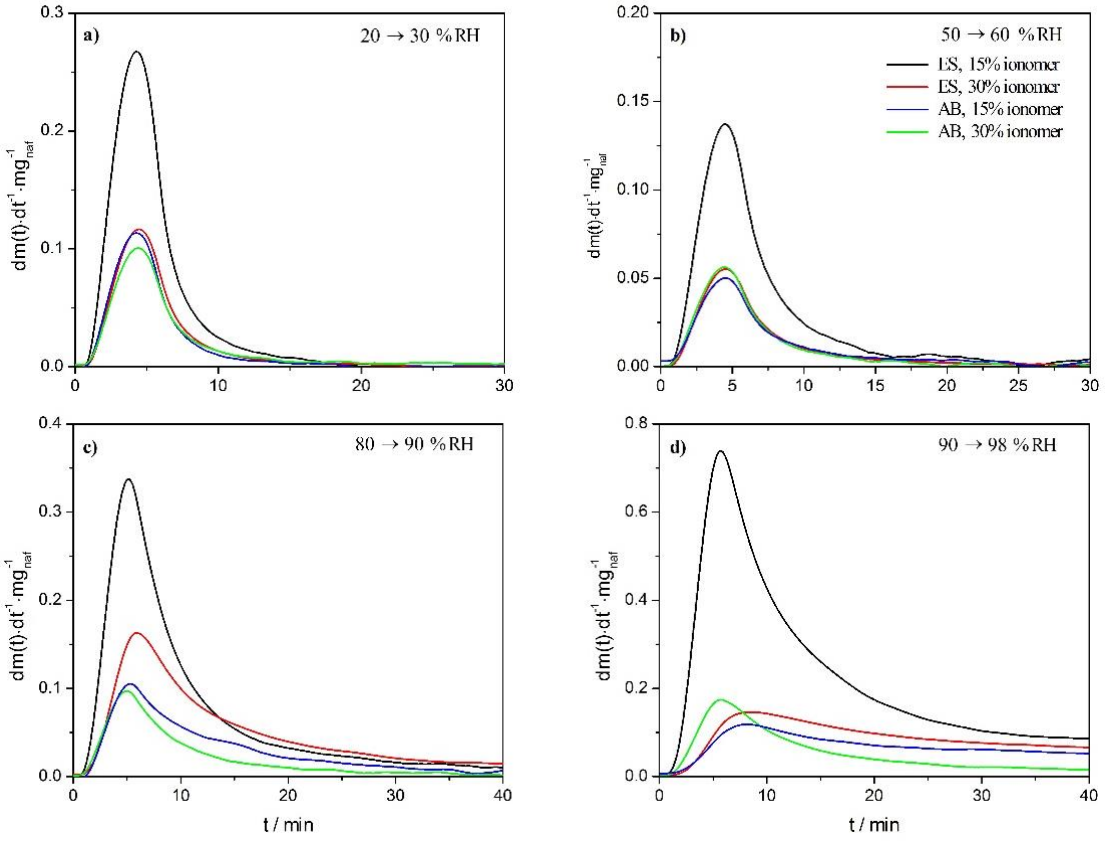

Figure 3-24: Rate of normalized water absorption as a function of time for a) 20 to 30 %, b) 50 to 60 %, c) 80 to 90 % and d) 90 to 98 % relative humidity steps for electrosprayed and airbrushed catalyst layers with different ionomer content

The data in Figure 3-23 also confirm that platinum plays a critical role in water absorption capabilities. Bare carbon electrosprayed layers resulted in a much lower water uptake for compared to Pt/CB, which is consistent with prior studies with traditional ink-based methods [17]. Figure 3-25 presents the comparison between the normalized water absorption rates of an electrosprayed Pt/CB and a Vulcan CB layer with 15 wt% of ionomer content. These results prove that the presence of platinum enhance the absorption kinetics of water on the carbon-ionomer composite at all RH ranges. From these results, it can also be deduced that platinum is critical to enhance water absorption in the initial stages, when the ionomer is dry and also at high relative humidities, to increase the total amount of absorption. From the Figure 3-23, it can be seen that

platinum has a critical effect on the amount of water absorbed up to 90 %RH despite of the fabrication method. It is probable that the inherent hydrophilicity of metallic platinum surfaces helps water absorption and interaction with the porous layer.

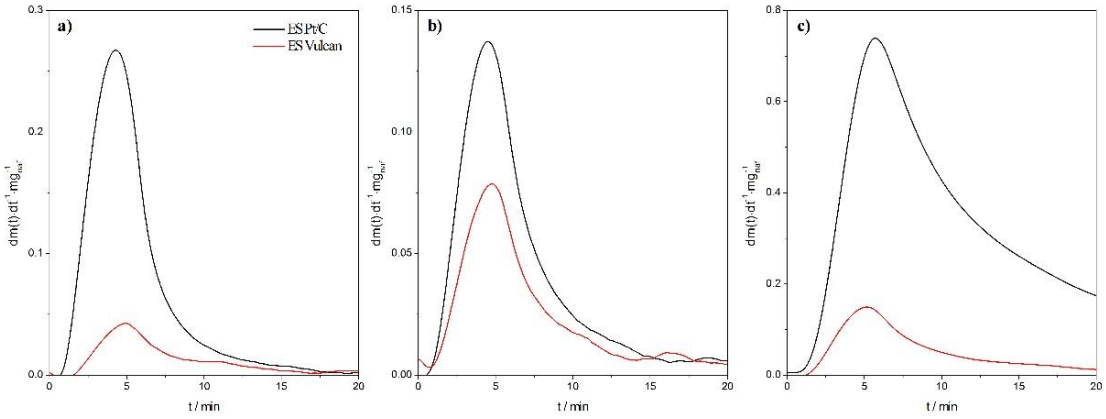

Figure 3-25: Rate of normalized water absorption as a function of time for a) 20 to 30 %, b) 50 to 60 %, c) 90 to 98 % relative humidity steps for electrosprayed Pt/CB and Vulcan carbon black with 15 wt% of Nafion

It must be noted that the enhanced water-vapor uptake of the electrosprayed layers is accompanied by very low wettability and superhydrophobic character (cf. Figure 3-19). Such apparently opposite behavior is a consequence of the amphiphilic properties of the ionomer, combined with its specific interaction and distribution within the porous structure of the layer. They also explain the capability for fast water transport while retaining high ionic conductivity, which is more appropriate for catalyst layer requirements in a PEM fuel cell.

Single cell testing

Single cells were mounted for standard characterization with electrosprayed catalyst layers in the cathodic electrode. Polarization and power density curves are shown in Figure 3-26 for four MEAs with different catalyst loadings at the cathode.

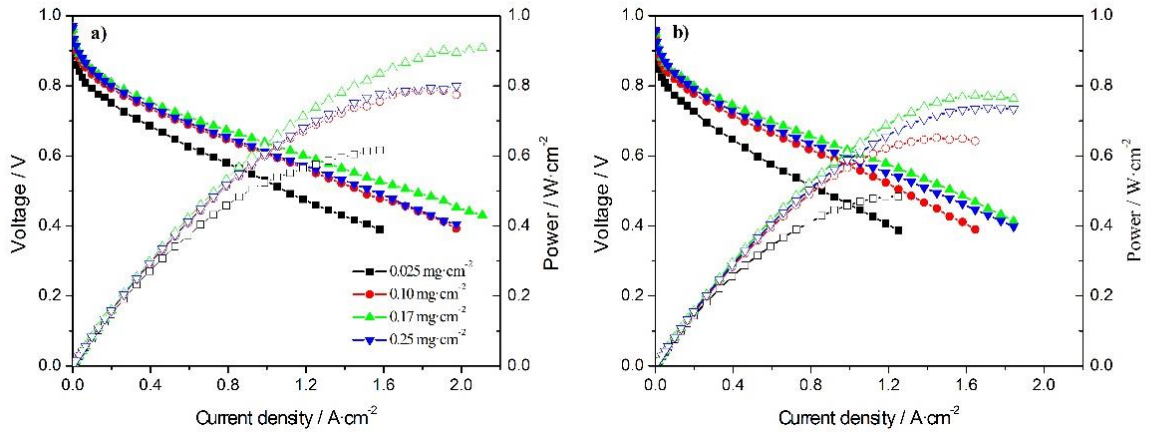

Figure 3-26: Polarization and power density curves of single PEMFCs with electrosprayed catalyst layers of variable Pt loading in the cathode. Cells were tested at 80 °C, 1 barg, and a) 100 % and b) O %RH conditions, using H2/O2 (1.5/3.0 stoichiometry)

An optimal cell response is attained at a cathode loading of 0.17 $mg_{Pt} \cdot cm^{-2}$ in accordance with previous results [5]. The roughness factor (r_f) and platinum electrochemical area are plotted in Figure 3-27a as a function of platinum loading. Additionally, the Tafel slope and the dc resistance values estimated from the fitting of the previous polarization curves are presented in Figure 3-27b.

A peak in the mass-specific platinum area is encountered at 0.17 $mg_{Pt} \cdot cm^{-2}$, which reflects the conditions for the maximum accessibility of the platinum surface to reactants, which agrees with performance peak in the polarization curves of Figure 3-26. The plateau in roughness factor at larger loadings is consistent with a reduction of platinum accessibility, probably due to the thickness of the layers at high loadings (over 20 μm). The increase in the Tafel slope with catalyst loading must be attributed to ohmic losses occurring by the increasing thickness of the catalyst layer. This effect was previously reported for spray-coated membranes with variable Pt/CB ratio [109] and coated membranes blending Pt/CB particles with bare carbon black [110]. The larger values of *b* registered with dry gases (denoting a decrease in cell performance) could be caused by either a decrease in catalyst performance and/or additional mass transport losses at low humidification and shifting of the reaction distribution next to the membrane. However,

the evolution of R_{dc} in Figure 3-27b seems to be more determining for cell performance. As opposed to values of Tafel slopes, the internal resistance shows almost no differences between fully humidified or dry gas operations except at the lowest loading. Increased performance of electrosprayed catalyst layers on the cathode under dry operation will be discussed in the following chapter. Again, a minimum value of the resistance is found at 0.17 $mg_{Pt} \cdot cm^{-2}$. At this loading, conditions are optimal for the transport of gases, ionic conduction and platinum utilization in the electrosprayed cathodic catalyst layer, which are a consequence of its high water-vapor uptake capability and superhydrophobic character.

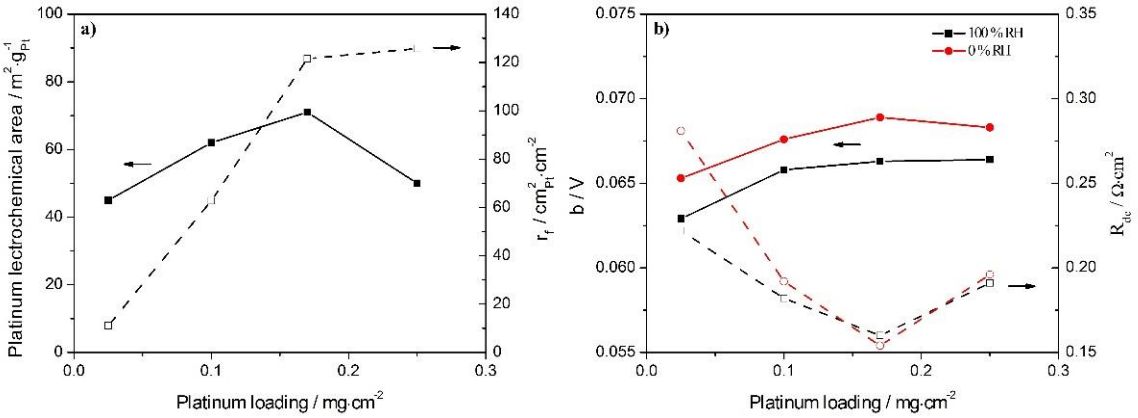

Figure 3-27: a) Mass specific electrochemical area and roughness factor (r_f) and of the electrosprayed catalyst layers of Figure 3-26 as a function of Pt loading. b) Tafel slope (b) and dc internal resistance (R_{dc}) at 100 %RH and 0 %RH, obtained from the least square fitting of the polarization curves

Impedance spectroscopy was carried out on the cells with electrosprayed cathode catalyst layer. Nyquist plots exhibit one unique semicircle response at cell voltages between 0.8 and 0.6V that is entirely ascribed to the cathodic catalyst layer impedance [55]. A second semicircle at low frequencies, reflecting transport losses in other parts of the cell, like the gas diffusion layers or the flow fields, is not observed at these operating conditions. A simple electrical circuit consisting in a resistance element in series with the parallel combination of a constant phase element for the capacitive processes and the impedance of the faradaic reaction has been used for the fitting. Series resistance (R_Ω) accounts for the fast ohmic losses due to ionic conduction in the membrane and electronic conduction

in the electrodes and contacts, while charge transfer resistance (R_{ct}) accounts for transport and charge transfer losses in the cathodic catalyst layer and the constant phase element (Y_{CL}, n) is related with the pseudo-capacitive character of this same layer.

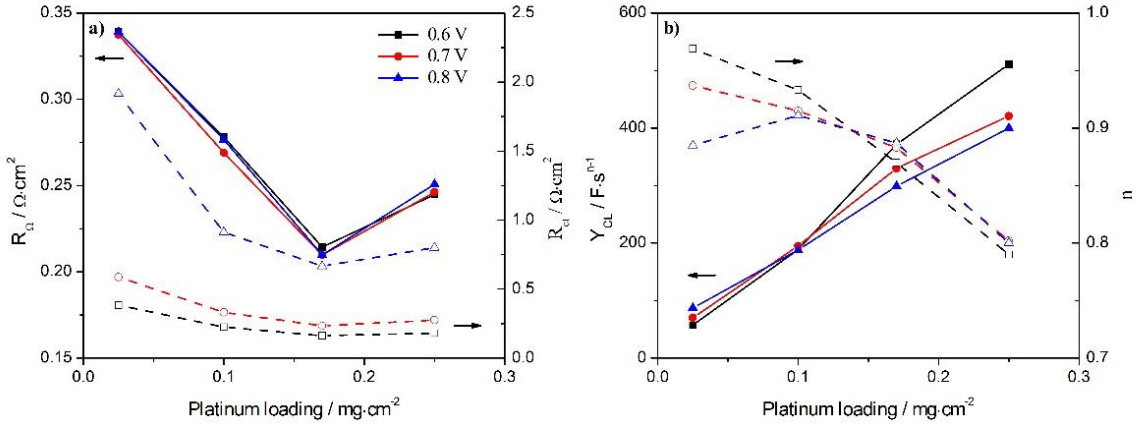

Figure 3-28: a) Series resistance (R_{Ω}, full symbols) and charge transfer resistance (R_{ct}, open symbols) as a function of Pt loading in the electrosprayed catalyst layer, at three cell voltages. b) Constant phase element parameters, Y_{CL} (full symbols) and the exponent n (open symbols), as a function of catalyst loading, at three cell voltages

Cell series and charge transfer resistances are plotted in Figure 3-28a as a function of catalyst loading for three cell voltages. At 0.17 mg·cm^{-2}, the appearance of a minimum of series resistance is concomitant with the better cell performance and the local minimum values found in dc resistance and the maximum platinum active area values. In this case, it can be assumed that the ionic conduction in the cell is optimal at this loading. Following the same trend, there is also a minimum of the charge transfer resistance at 0.17 mg·cm^{-2}, which is more pronounced at low overpotentials, when the cathode catalyst-layer properties govern the cell response. Such minimum reflects the optimization of the electrochemical kinetics and mass transport in the cathodic catalyst layer. The analysis of the constant-phase-element parameters in Figure 3-28b provides some more useful information about the behavior of the electrosprayed catalyst layers. The exponent n reflects the dispersion of time constants frequently encountered in porous electrodes, with $n = 1$ for the case of a single time constant, and decreasing ($0 < n < 1$) by increasing dispersion [111]. For a catalyst layer, dispersion may be larger by increasing

the layer thickness because of larger heterogeneities in all parameters affecting its response, e.g., temperature, pressure, potential, current, concentration of reactants, water, etc. Consequently, results in Figure 3-28b show that *n* decreases with catalyst loading (film thickness). On the other hand, Y_{CL} shows a continuous increase with the platinum loading, with increasing slope by decreasing cell voltage (increasing the current). The information of interest from this parameter resides in its pseudo-capacitive character, which is related to the charge storage in the catalyst layer. The electrical capacitance of the cathodic catalyst layer can be determined from Y_{CL} using the following relationship [112]:

$$C_{CL} = Y_{CL}^{1/n} R_{ct}^{1/n-1} \qquad (3.15)$$

where C_{CL} is the electrical capacitance of the cathodic catalyst layer. The capacitance of the catalyst layer is plotted in Figure 3-29 versus the platinum and the carbon loading.

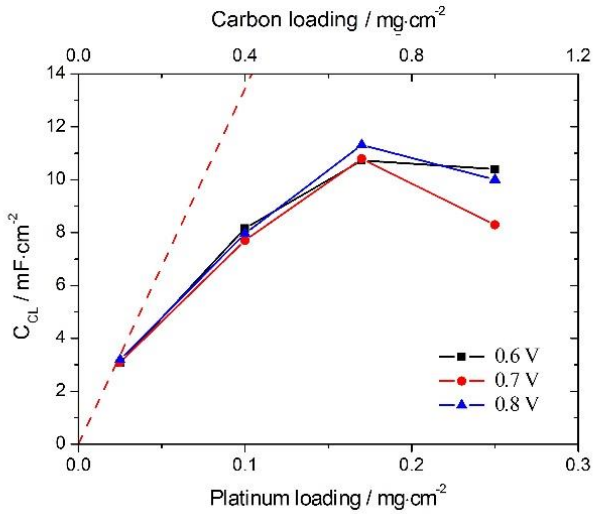

Figure 3-29: Electrical capacitance of the cathodic catalyst layer as a function of catalyst loading. Dashed red line indicates the estimated nominal capacitance of the carbon black phase

A maximum in capacitance is found with loading at 0.17 mg·cm^{-2} (corresponding to 0.68 mg$_C$·cm^{-2}), which shows similar dependence as the electrochemical active platinum area. The capacitance must be related to the total electrochemical active area of the catalyst layer, including platinum and carbon surfaces. For comparison, the figure includes the

nominal capacitance expected for the carbon black surface, using a specific area of 210 $m^2 \cdot g_c^{-1}$ and a specific capacitance 16 $\mu F \cdot cm^{-2}$ [113], that match the experimental curves only at low loadings. The presence of a maximum in charge storage indicates that above 0.17 $mg \cdot cm^{-2}$, the additional catalyst is electrochemically inactive. Such result may be a consequence of the greater layer thicknesses compared with other methods and/or the enhanced wetting properties and hydrophobicity of the layers.

3.4.3 Impact of electrosprayed catalyst layers on water distribution

The increased performance and improved catalyst corrosion resistance reported in previous works of the group for electrosprayed layers in the cathodic side of the MEA, were attributed to its inherent superhydrophobicity, which is believed to favor fast removal of the water generated in the cathode [98, 99]. In order to gain further insights on water transport by electrosprayed cathodic catalysts layers, studies of water distribution were performed within the cell. Five single cells with different catalyst layers configuration have been prepared, namely the cells with electrosprayed catalyst layer in cathode (EScat), in anode (ESan), in both electrodes (ESboth), together with a cell with a cathodic airbrushed catalyst layer (AEcat) and a cell with commercial electrodes (STD). The catalyst layers were deposited directly onto membranes using loadings of 0.25 $mg \cdot cm^{-2}$ as explained in the experimental section. For these cells, water collection experiments on the different cells were carried out under self-humidification conditions by condensing the water carried by the exhaust gases exiting the cell as a function of current density and temperature.

Performance results

Polarization and power density curves are shown in Figure 3-30 under standard conditions (80 °C, 100 %RH and 1 barg). Figure 3-30a and Figure 3-30b show the curves obtained after the start-up and initial stabilization of the cells, whereas Figure 3-30c and Figure 3-30d show end-of-life results, after water collection measurements and operation in-between measurements at constant load (I = 3 A) with dry gases. Except for EScat, which showed minimal degradation, the end-of-life for the other cells was caused by

membrane failure. Figure 3-30c shows the last curves taken before the failure, at the time indicated in the figures, except for EScat which showed no failure.

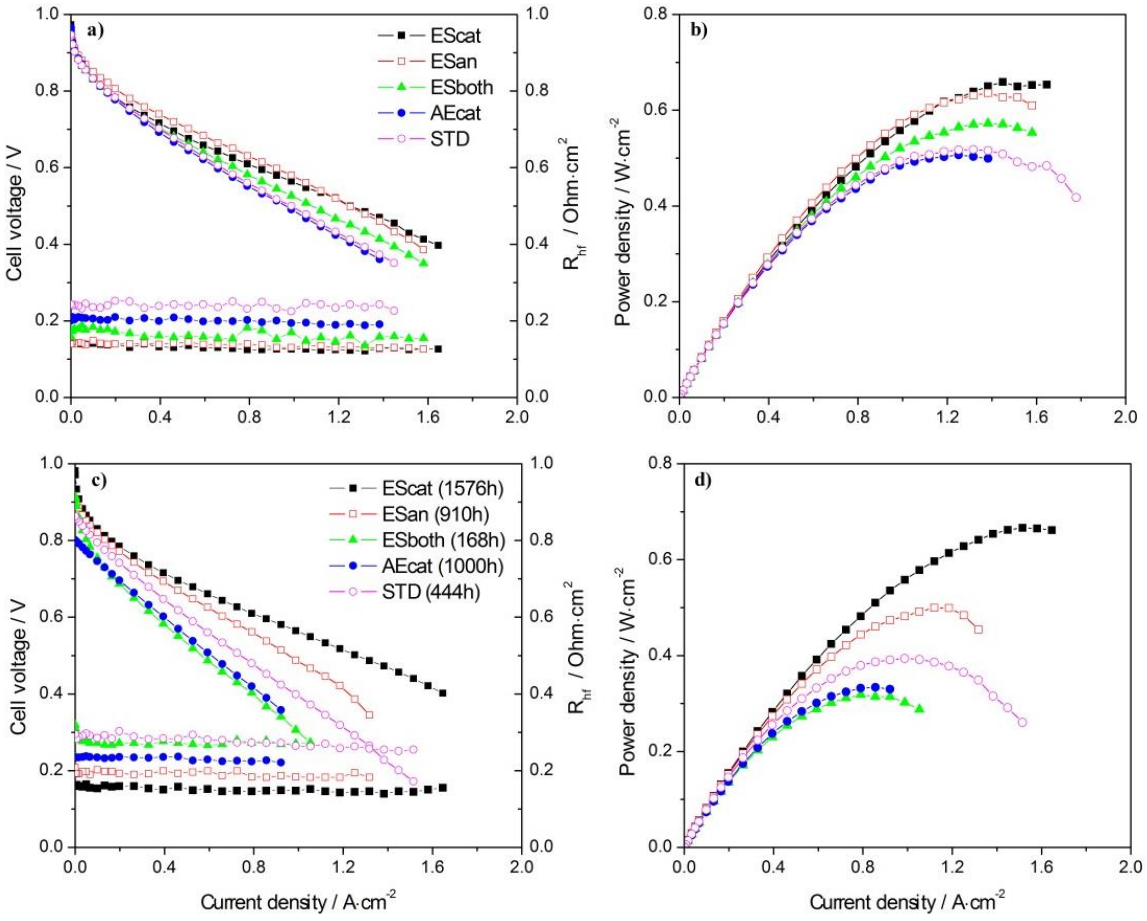

Figure 3-30: a) Polarization curves, R_{hf} and b) power density curves after the activation procedure. c) Polarization curves, R_{hf} and d) power density curves after dry gas inlet operation, and operation at constant load (I = 3 A) for the time indicated

The results of the fitting of the polarization curves (*b* and R_{dc}) are given in Table 3-1, together with the internal resistance measured on-line at each point of the curve at 1 kHz (R_{hf}), the difference between both resistances (R_{dc}–R_{hf}) and the maximum power density achieved by the cell (W_{max}). For polarization curve fitting, an estimated value of the platinum electrochemical area of 40 $m^2 \cdot g^{-1}$ was used, as the area could not be measured at the end of life of the cells due to membrane failure.

Table 3-1: Tafel slope (b), dc resistance (R_{dc}), 1 kHz resistance (R_{hf}), difference (R_{dc}–R_{hf}), and maximum power density (W_{max}) obtained from polarization curves in Figure 3-30. Percentages with respect to the STD values are given in parenthesis

Cell	Anode	Cathode	*b* mV	R_{dc} Ω·cm^2	R_{hf} Ω·cm^2	R_{dc} - R_{hf} Ω·cm^2	W_{max} W·cm^{-2}
EScat	Comm.[a]	ES[b]	67	0.224 (83)	0.15 (58)	0.074 (239)	0.66 (127)
ESan	ES	Comm.	64	0.202 (75)	0.20 (77)	0.002 (6)	0.64 (123)
ESboth	ES	ES	66	0.257 (95)	0.16 (62)	0.097 (313)	0.57 (110)
AEcat	Comm.	AE[c]	66	0.297 (110)	0.22 (85)	0.077 (248)	0.51 (98)
STD	Comm.	Comm.	66	0.271 (100)	0.24 (100)	0.031 (100)	0.52 (100)

Abbreviations stand for: [a] commercial, [b] electrospray and [c] airbrush. For more details of the preparation, see experimental section. All the electrodes have a loading of 0.25 mg·cm^{-2}

According to Table 3-1, performance differences among the cells must be almost entirely attributed to dc and high-frequency internal resistances, whereas electrocatalysis processes (implicit in parameters *b* and R_{dc}–R_{hf}) do not appear to be determinant for the observed differences. The initial polarization curves show superior performance for both EScat and ESan, with maximum power densities above 20 % compared with the STD cell, in accordance with previous works for cathodic layers [98], while the improvement with the ESan configuration is here reported for the first time. The differences among both cells can be inferred from the tabulated data. The origin of the high performance of EScat could be originated from the low values R_{hf}, whereas for ESan it appears to be a consequence of low R_{dc} and R_{dc}–R_{hf}. The performance increase of EScat must be attributed to positive effects on transport phenomena by the presence of the superhydrophobic electrosprayed catalyst layer in the cathode. For instance, these results agree with the reduction of mass-transport resistance reported in the previous section, and additionally, low R_{hf} indicates better proton conductivity in the MEA. The high performance of ESan, on the other hand, is probably a consequence of an increase of the electrocatalytic activity of the commercial catalyst layer together enhanced by accelerated water transport in the anode towards the cathode. Using electrosprayed layers simultaneously in cathode and anode (ESboth) causes a decrease of the performance,

eliminating the positive transport effects observed for the asymmetrical cells, probably because of water flux forced in opposite directions by the two layers.

The analysis of stability of the cells under dry operation conditions shows different degradation effects depending on the catalyst layers configuration. All the measured configurations, except EScat, suffer significant decay in performance and an increase in the internal resistance, ultimately causing gas crossover due to membrane breakage. Membrane failure was more frequent during operation at high current densities with dry gas inlet, and could be attributed to the intense drying of the anode side by the unbalanced flow of water by electroosmotic drag (from anode to cathode) and back diffusion (from cathode to anode). These conditions cause local increase of the ionic resistance, heat generation, mechanical stress, and membrane breaking [114]. The high performance of EScat is maintained almost constant after more than 1,000 h of operation under self-humidification, reflecting the improvement in water management and membrane humidification with the electrosprayed layer in the cathode. More insight into the effect of the electrosprayed layers on water transport in the cell can be obtained from the water collection experiments.

Water collection experiments

Water recovered from anode and cathode for the five cell configurations is plotted as a function of current density in Figure 3-31. Measurements were carried out after cell stabilization at constant demand for several hours using a 1.5/3.0 H_2/O_2 stoichiometry and different temperatures (40, 60 and 80 °C). The values of the internal resistance of the cell measured at 1 kHz during water collection are also plotted, for additional information of the process. Larger proportion of water collected from the cathode (over 80 % in most of the cases) is observed for all configurations, with the exception of EScat. Larger cathodic water proportion is expected as a consequence of the higher permeability of the gas diffusion layer compared with the polymeric membrane [115]. At increasing temperature, the amount of water recovered from the anode increases reflecting thermal

activation of the back diffusion of water from cathode to anode. Water collection ratios show large dependence on cell temperature, and lower dependence on cell current [81].

However, the presence of electrosprayed catalyst layers in the cathode introduces significant differences in water distribution. The most astonishing results are obtained for EScat configuration operated at 80 °C, where the recovered fraction of water in the cathode is around 60 % at high current densities, while at low current densities (< 0.3 $A \cdot cm^{-2}$), anodic water proportion (up to 60 %) increases significantly and surpasses cathodic fraction. This effect can also be appreciated to a lesser extent for EScat at 60 °C, where the anode water is around 20 % at high current densities, while in the rest of the configurations is below 10 %. Water collection results indicate that EScat operates under enhanced water back diffusion. It is also noticeable that the anodic water recovery from EScat increases upon decreasing current density, as a difference from the other cells where the anodic fraction slightly increases with current density. In addition, the internal resistance for EScat cell is lower at any temperature and current density.

These results can be rationalized by considering the hydrophobicity of electrosprayed films, which is a result of large macropores and dendritic growths covering the catalyst agglomerates. If we assume that in electrosprayed layers, the external film surface and the internal macropores surface are morphologically and chemically similar, then the external and internal contact angles should also be similar. In conclusion, the inner morphology of the agglomerates should confer the same superhydrophobic character to the bulk of the layer, which shows to be resistant to hydrophilic treatments and electrochemical aging in the fuel cell. This assumption would be confirmed if the capillary pressure of the catalyst layer were measured, as it was done with gas diffusion layers [16]. However, this measurement is difficult to be performed in layers in the range of micrometers due to the technical limitations of the method and the results in the literature are scarce [17, 116].

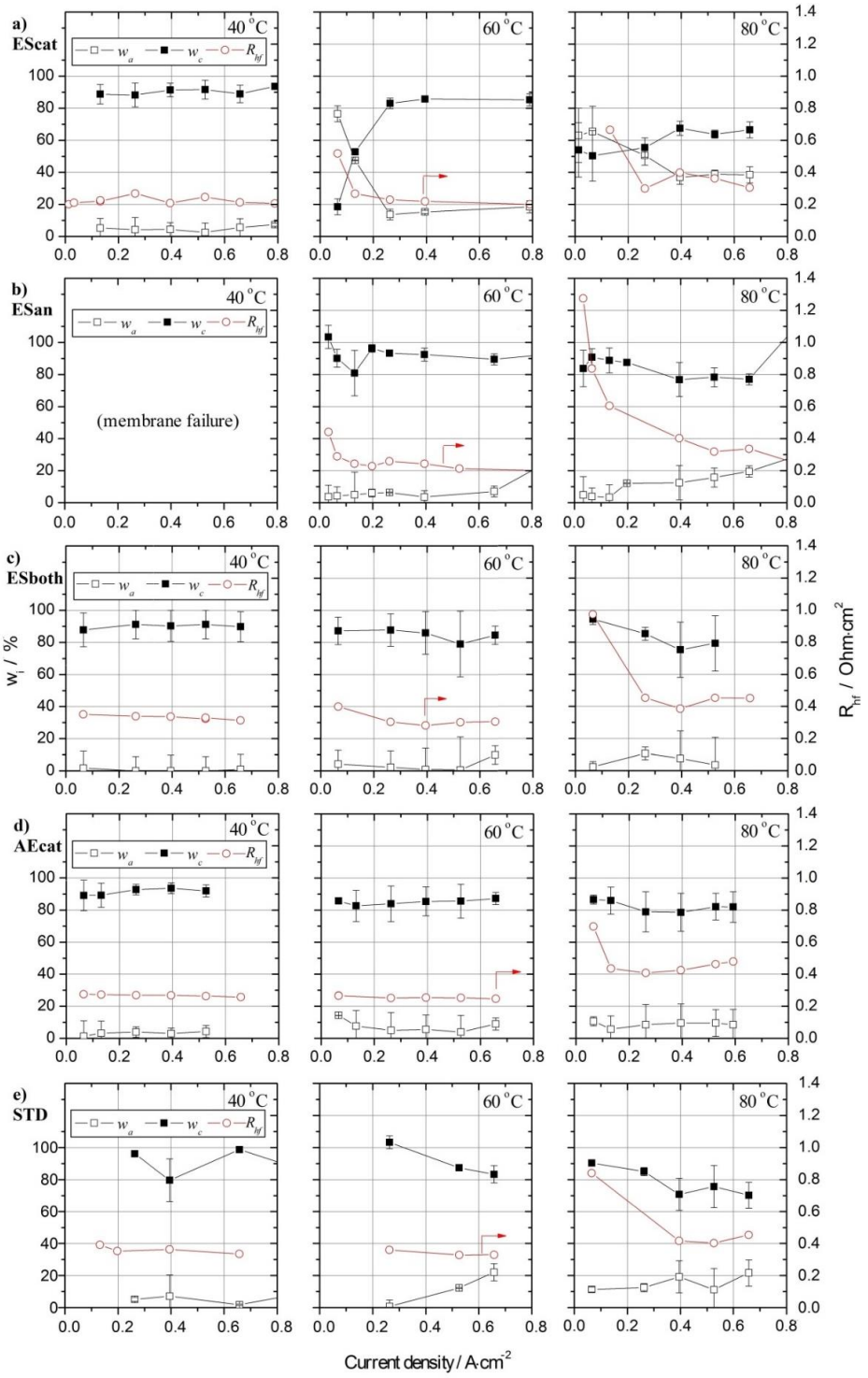

Figure 3-31: Water fractions recovered from the cathode and the anode of a) EScat, b) Esan, c) ESboth, d) AEcat and e) STD cells, as a function of current density and R_{hf} at three temperatures

In a much bigger scale, for example in soil science experiments, it is well known that bulk hydrophobicity of the porous films changes liquid water interactions inside them. As the hydrophobicity of a film is increased, the interactions within its pores favors the existence of isolated water drops (‘insular saturation’) and thus reduces the water content in the pores, i.e. water saturation [117]. In contrast, inside a hydrophilic film, liquid water forms a continuous phase (‘funicular saturation’), which is the situation prevailing in a conventional catalyst layer. It is also proven that low water saturation in a porous medium decreases its permeability [117], so if the electrosprayed layers present this insular saturation state, it would hinder the transport towards the gas diffusion layer in favor of the back diffusion through the membrane. This effect would also explain the increased water push to the anode at lower current densities, since under these conditions a larger proportion of water is generated closer to the anode, so the water has to travel through a greater part of the thickness of a low saturated layer, and, thus, the water conduction to the gas diffusion layer is more hindered.

3.4.4 Influence of the thickness of a hydrophobic catalyst layer on water transport

In the previous sections, it has been proven that the introduction of asymmetries on the hydrophobicity of the catalyst layer can influence water distribution inside a PEM fuel cell. Among all the studied configurations, the best results were obtained using a superhydrophobic electrosprayed layer in the cathode confronting a commercial catalyst layer in the anode. This MEA configuration showed that back diffusion towards the anode was increased, resulting in a 25 % enhancement in cell performance and improved stability. Based on these results, the influence on water distribution on the thickness of electrosprayed catalyst layers in the cathode of MEAs has been studied. The interest is not only fundamental understanding, but also practical since it could provide a passive control method of the water distribution inside the cell.

In order to vary the thickness of the catalyst layer, the platinum-supported carbon black is blended with Vulcan carbon support (XC-72R), which is the same carrier of Pt in the catalyst used in the experiments. The addition of carbon black to the catalyst layer is an

approach that has been already used in literature with different objectives. For instance, Suzuki et al. blended carbon black and standard Pt/CB to analyze the effect of thickness and platinum loading in cell operation [110]. Owejan et al. also used carbon to maintain a constant catalyst layer thickness to analyze the platinum dispersion (varying the %Pt of the catalyst) and study the parameters affecting the local transport performance by the use of limiting-current methods [118]. Lee et al., on the other hand, used carbon dilution to vary the overall Pt content of the catalyst layer trying to develop a method to measure the effectiveness of the catalyst, i.e. the effective platinum utilization by measuring the mass activity [109].

For the analysis of these measurements, different **assumptions** will be taken i) the added Vulcan carbon black is identical to the carbon supporting the catalyst, so it can be added to the corresponding weight of carbon in Pt/Vulcan catalyst, ii) the ionomer interaction with the carbon support is the same for Pt-containing CB and the extra Vulcan, iii) the formation of an homogeneous ink, iv) the substitution of the catalyzed carbon black for regular carbon black does not affect the electrospray deposition process, v) the resulting microstructure and thickness is not affected by carbon dilution. Many of these assumptions can be discussed attending to the results already shown in this thesis. Assumptions *i* and *iii* are reasonable, since similar morphology and chemical surface are observed by the results presented here, and there are no special differences reported to the author knowledge, for pure Vulcan and Pt-supported Vulcan; in addition, ink homogeneity appears not to be affected in pure and mixed compositions, probably thanks to the continuous ultrasonic stirring. The assumptions *ii*, *iv* and *v* may be more controversial according to the results presented in previous sections. For instance, water-vapor absorption in Figure 3-23 show significant differences in ionomer interaction with Vulcan and Pt/Vulcan. Additionally, changes in electrospray deposition conditions can be expected from both particles types in microstructure and thickness, as observed, for instance, by comparing Figure 3-13 and Figure 4-8 of next chapter.

Summary of the experimental samples

This section will discuss the analysis of more than 15 samples of catalyst-coated membranes in the cathodic side. Therefore, in order to facilitate the interpretation of the results, it has been considered necessary to graphically explain and summarize the rationale of the prepared samples. A graphic summary of the different cathodic catalyst layers that were characterized in the experiments is depicted in Figure 3-32. Surrounded with a black-dashed line, the experiments that analyze the variation of platinum loading of electrosprayed layers are depicted, showing the subsequent thickness variation, and including airbrushed layers with the same loading. Thickness values are taken from those determined from cross-sectional analysis in Figure 3-13. The green-dashed line highlights the experiments performed using layers with constant thickness, varying the Vulcan-Pt/Vulcan ratio. In contrast, the experiments within the red-dashed line analyze the variation of thickness by the addition of bare Vulcan with a fixed catalyst loading. In addition, a couple of samples were studied with sequential deposition (blue-dashed line) to compare the effect on carbon mixing and sequential deposition of the layers.

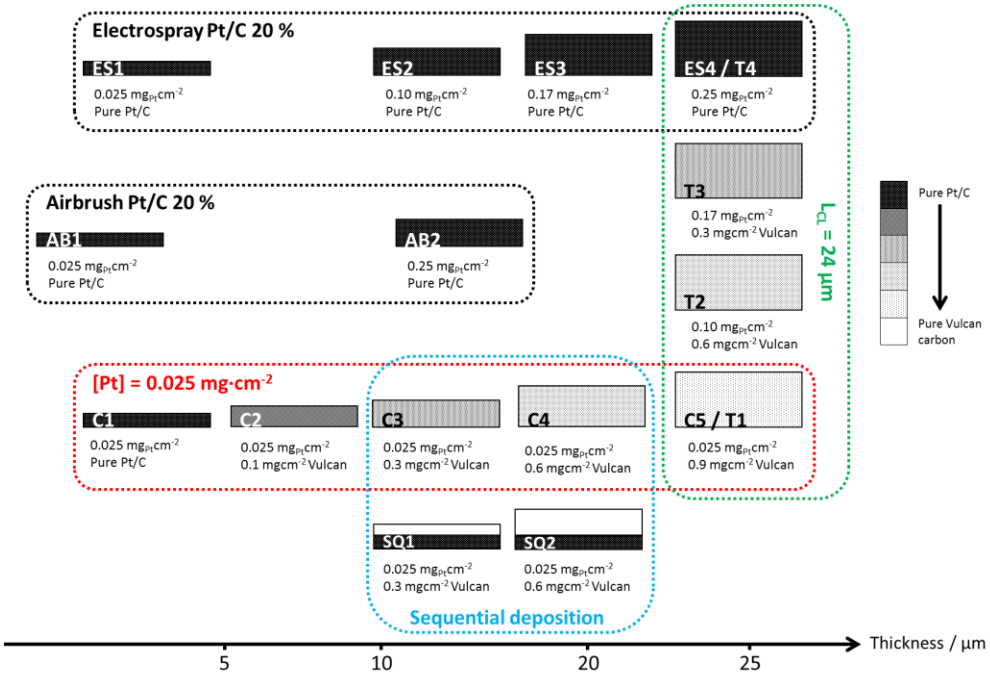

Figure 3-32: Graphic summary of cathodic catalyst layers studied in this section

Table 3-2 summarizes the data of the previous figure, aiming to facilitate the comparison of the characteristics of the different samples. In the last column, carbon dilution represents the percentage of Vulcan carbon black addition with respect of the total weight of the catalyst layer. The ionomer concentration was fixed at 15 wt% with respect to the total catalyst layer weight, which is the optimum concentration for electrosprayed layers [5].

Table 3-2: Summary of the characteristics of cathodic catalyst layers studied in this section

Sample	Thickness µm	Platinum loading mg·cm^{-2}	Added Vulcan mg·cm^{-2}	Carbon dilution %
Electrospray				
ES1	3.4	0.025	-	-
ES2	8.1	0.10	-	-
ES3	20.0	0.17	-	-
ES4	23.8	0.25	-	-
Airbrush				
AB1	1.7	0.025	-	-
AB2	9.4	0.25	-	-
Constant catalyst loading				
C1[a]	3.4[c]	0.025	-	0
C2	5.8[d]	0.025	0.1	44
C3	8.1[c]	0.025	0.3	71
C4	20.0[c]	0.025	0.6	83
C5[b]	23.8[c]	0.025	0.9	88
Constant catalyst loading / Sequential addition				
SQ1	8.1[c]	0.025	0.3	-
SQ2	20.0[c]	0.025	0.6	-
Constant catalyst layer thickness				
T1[b]	23.8[c]	0.025	0.9	88
T2	23.8[c]	0.10	0.6	55
T3	23.8[c]	0.17	0.3	26
T4[a]	23.8[c]	0.25	-	0

[a] Repeated samples (control experiments), [b] T1 and C5 are the same sample, [c] estimated and [d] interpolated thicknesses

The ionomer concentration of the carbon-diluted samples is calculated by maintaining a constant (18 wt%) carbon black/ionomer ratio, that match the optimum value for the pure Pt/CB layers. For details on the rest of the MEA elements, one may check the experimental section. The thickness on the second column is taken from the characterization experiments in section 3.4.1, while the rest of the thickness values are estimated assuming that Vulcan carbon addition contribution to the thickness of the layer is the same as platinum supported Vulcan.

For each group of experiments, a complete characterization of the MEAs is performed, with polarization curves and impedance analysis on fuel cell operation at 80 °C. The operation conditions slightly differ from the previous section, because it was observed that the low-loaded catalyst layers suffered from excessive drying during water collection experiments, so the cathodic stoichiometry was diminished from λ = 3.0 to 1.5. In consequence with this decision, all the characterization experiments were performed using this same stoichiometry (1.5/1.5 H_2/O_2). Additionally, cyclic voltammetries and impedance analysis with H_2/N_2 feed gases at 30 °C were performed to calculate the electrochemical active area and gain more insights on the proton conductivity of the catalyst layers, respectively. The measurements with H_2/N_2 were performed at the beginning of the life of the MEA, to avoid changes by degradation or membrane failure problems, as in the last section. All the data are collected in one figure for each group of layers to facilitate the interpretation of the results. For full characterization of samples ES1 through ES4 one may check section 3.2.3.

Effect of catalyst loading on water distribution

Water management behavior of the different catalyst loadings used in the mass transport experiments of section 3.2.3 is analyzed with water collection experiments in order to further understand the effect of hydrophobic gradients inside the MEAs. Two airbrushed layers were prepared with the minimum and the maximum loadings used in the experiments to compare the effect of electrosprayed layers with those produced by this standard method. Figure 3-33 shows the results of water collection in the anodic exhaust

represented as a function of catalyst layer thickness, at low and medium current densities. The thickness of the catalyst layer is here varied by changing catalyst loading, so it corresponds to the samples ES1-4 in Table 3-2. Note that the results cannot be quantitatively related to the previous section, since these experiments were conducted with a lower cathode stoichiometry, as explained in the experimental section.

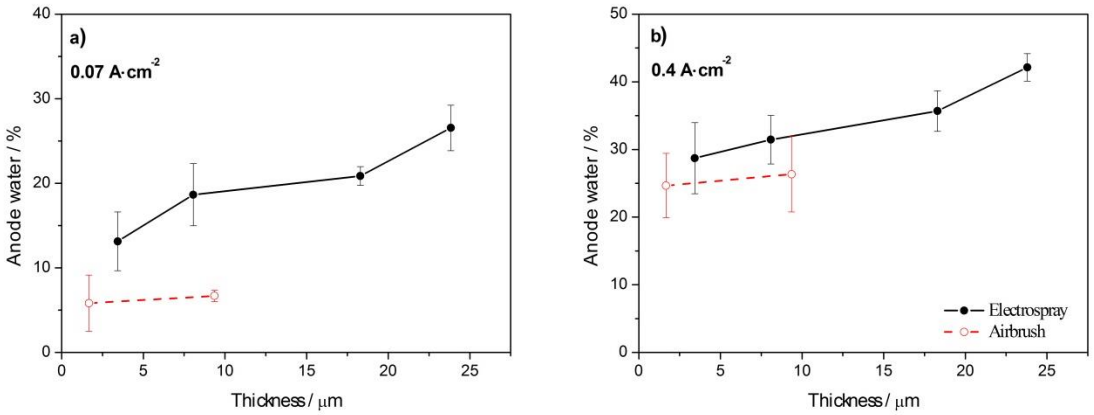

Figure 3-33: Percentage of total water collection in the anode of electrosprayed and airbrushed cathode thickness at low (a) and medium (b) current densities. Thickness was varied by changing Pt load in the catalyst layer (samples ES1 through ES4 in Table 3-2)

As expected, the percentage of water recovered in the anodic side is much higher for electrosprayed layers in comparison with airbrushed layers for low current densities, although it is not as high as the values observed with the experimental conditions in the previous section. Additionally, the use of a lower stoichiometry in the cathode also seems to increase the water back-diffusion towards the anode at medium current densities, unlike the results obtained in the previous section. It is interesting to note the linearity of the water recovered in the anode with the cathodic layer thickness in the electrosprayed layers. On the other hand, the thickness effect in more hydrophilic airbrushed layers seems to be less relevant than in the electrosprayed layers, although this method has lower dependence on thickness with catalyst loading, as can be inferred from Figure 3-13. These results show higher amount of water recovered in the anode at medium and low current densities, from 10 to 25 % of the total produced water in the cell, using superhydrophobic layers. This effect improves the performance of the cell, as explained

in previous sections of this Chapter, and opens up the possibility to tune the water distribution in the MEA with the use of the electrospray deposition technique.

Effect of thickness on water distribution

The effect of the thickness of a hydrophobic catalyst layer on water distribution inside a fuel cell without changing catalyst loading was also analyzed. Films were prepared with a fixed catalyst loading and un-catalyzed support to obtain catalyst layers with constant platinum loading and variable thickness. The lowest catalyst loading, 0.025 $mg_{Pt}·cm^{-2}$, was selected as the most appropriate for carbon dilution due to the possibility to experiment with a wide range of thicknesses. Various quantities of Vulcan carbon black were added to simulate the thickness obtained with the different pure Pt/CB catalyst layers until 24 µm (corresponding to 0.25 $mg_{Pt}·cm^{-2}$).

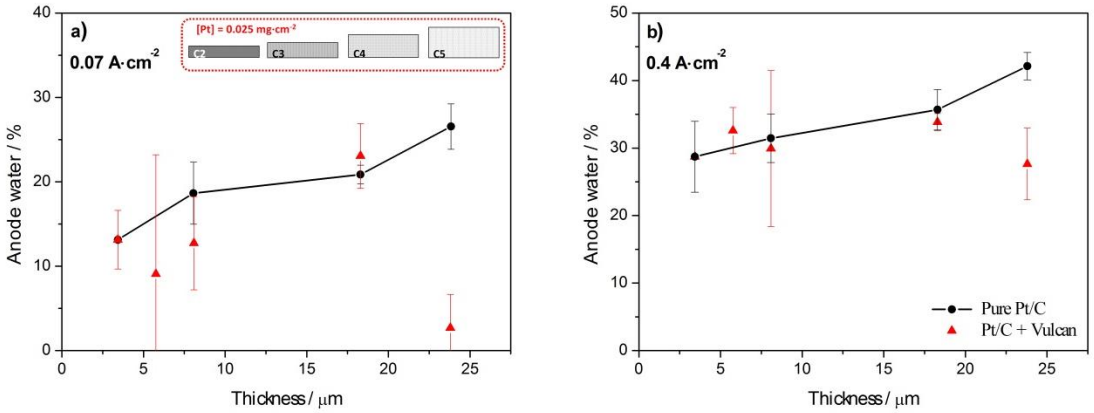

Figure 3-34: Percentage of total water collection in the anode versus cathodic layer thickness with 'pure' catalyst layer and diluted catalyst layers at low (a) and medium (b) current densities. As a difference from Figure 3-33, thickness was varied by preparing inks with variable addition of Vulcan carbon to the same Pt/Vulcan amount (Samples C1 through C5 in Table 3-2).

Figure 3-34 shows the percentage of water recovered in the anode of the cell for different thicknesses and constant loading, which is comparable with previous results of 'pure' catalyst layers in Figure 3-33. Carbon-diluted catalyst layers appear to follow a similar tendency as pure Pt/CB layers, increasing water anode fraction as thickness increases, except for the thicker layer, sample C5, corresponding to 0.9 $mg·cm^{-2}$ of added Vulcan (88 % of carbon dilution). This point may be affected by the low cell operation

performance (Table 3-3) which changes water transport conditions in the cell, so cannot be considered in the same conditions as the others. Although the increase of water pushed to the anode can be debatable at medium current densities when the last point is disregarded (Figure 3-34b), water push becomes evident when comparing the same points at low current densities (Figure 3-34a).

In Figure 3-35a, the polarization curves of the MEAs shows that the addition up to 0.3 $mg \cdot cm^{-2}$ of Vulcan support in samples C2 and C3 (up to three times the quantity of the carbon support in 0.025 $mg \cdot cm^{-2}$) does not have a great effect on cell performance under standard conditions. Negative effects on cell performance are clearly observed in samples C4 and C5. Since it is not until 0.6 $mg \cdot cm^{-2}$ (C4) of added Vulcan when the effect on the water push is significant, thickness increase by carbon dilution in catalyst layers of low loadings has no practical application for modifying water distribution within the cell. The results of the cyclic voltammetries in Figure 3-35b show a slight increase of the platinum electrochemical area for C2 and C3 samples together with a decrease of the mass specific double layer capacitance of the carbon phase. It means that a reduction of the electrochemically active carbon area occurs upon addition of bare carbon black. This effect could be responsible for the increase of the electrode performance due to the enhancement of oxygen accessibility, as described by Lee at al. [109]. The positive effect of the carbon addition up to 0.3 $mg \cdot cm^{-2}$ can also be observed in the reduction of the charge-transfer resistances in the impedance measurements in Figure 3-35c and Figure 3-35d. This effect implies that a slight thickness increase on low-loaded catalyst layers appears to improve the mass transport for the oxygen reduction reaction. From the H_2/N_2 impedance results in Figure 3-35f, on the other hand, it can be clearly seen that the protonic resistance progressively increases as more un-catalyzed support is added, probably due to the thickness increase that results in longer path for the protons to reach the membrane.

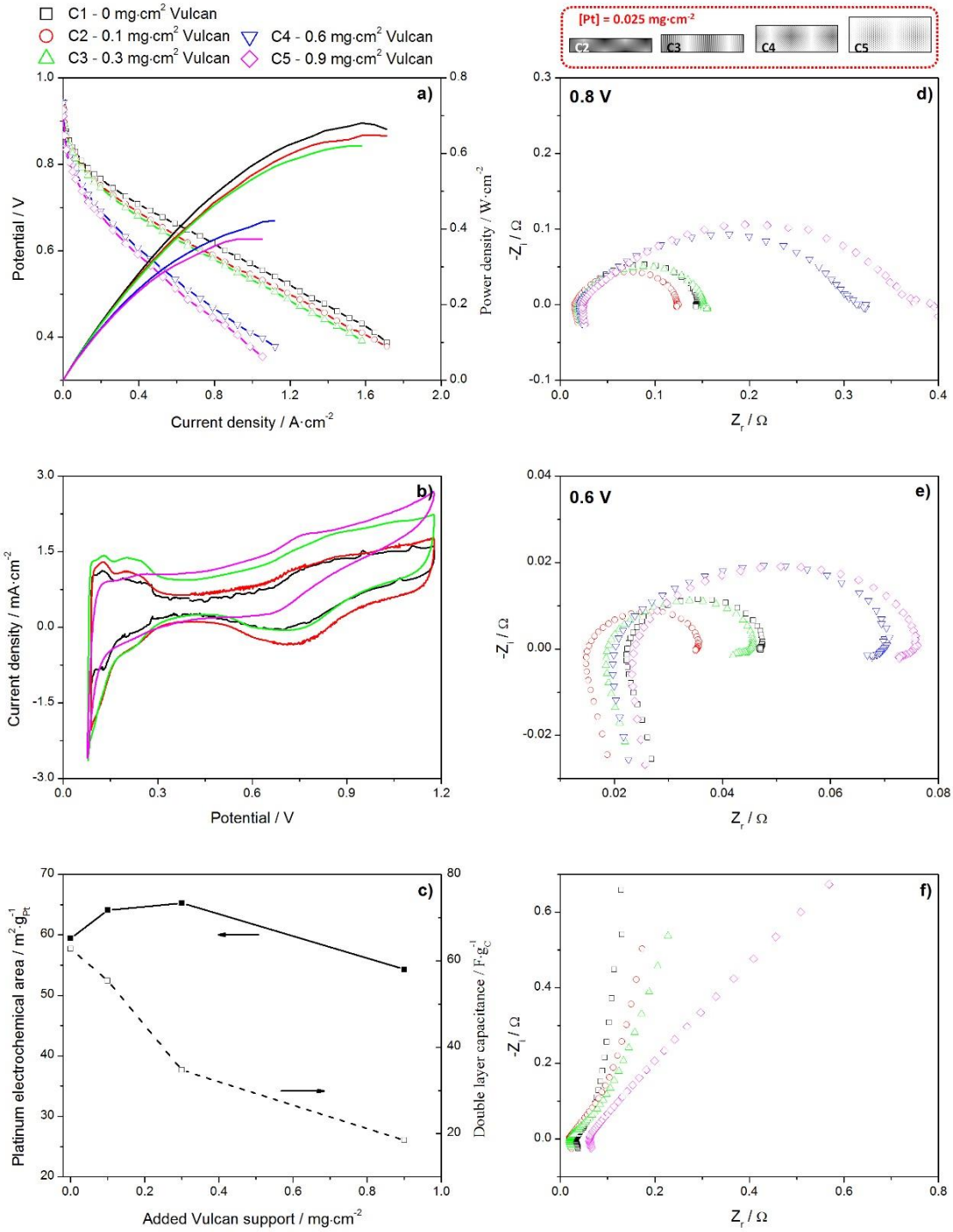

Figure 3-35: Characterization of the layers with constant catalyst loading and variable thickness: a) Polarization curves (1.5/1.5 H_2/O_2, 80 °C, 100 %RH and 1 atm). b) Cyclic voltammetries at 0.025 $V \cdot s^{-1}$ and 30 °C. c) Electrochemical active area calculated from the H_2 desorption region and double layer capacitance. d) Impedance measurement (1.5/1.5 H_2/O_2, 80 °C, 100 %RH and P_{atm}) at 0.8 V. e) Impedance measurement at 0.6 V. f) Nyquist plot of H_2/N_2 impedance at 100 %RH and 30 °C

As an additional backing to the results, Table 3-3 presents the value of the cathodic Tafel slopes and the dc internal resistance by fitting the polarization curves and the values of the potential in the water collection experiments at 0.4 $A \cdot cm^{-2}$. Tafel and dc resistance also show a steady increase as more bare carbon black is added to the catalyst layers, meaning that carbon addition has a negative effect on oxygen reduction reaction kinetics.

Table 3-3: Operation parameters of the cathodic of the carbon-diluted catalyst layers studied in this section

Sample	**Added Vulcan** $mg \cdot cm^{-2}$	**V @ 0.4** $A \cdot cm^{-2}$ **(0 atm)** **V**	**V @ 0.4** $A \cdot cm^{-2}$ **(1 atm)** **V**	**b (1 atm)** $mV \cdot dec^{-1}$	R_{dc} **(1 atm)** $\Omega \cdot cm^2$
C1	-	0.63	0.71	61.8	0.196
C2	0.1	0.56	0.69	63.5	0.225
C3	0.3	0.49	0.68	64.4	0.230
C4	0.6	0.46	0.61	68.4	0.343
C5	0.9	0.28	0.59	69.8	0.356

As the thickness of the layer becomes higher and thus the carbon dilution, the cell performance is progressively damaged, until sample C5, for which a huge drop in performance occurs at water collection conditions (zero gauge pressure). In this layer, water transport conditions cannot be assumed to be the same as for the other catalyst layers, because potential difference can modify the water production profile inside a catalyst layer, so this result can be disregarded as commented above in Figure 3-34. It is surprising, that the low performance of C5 at zero gauge pressure is greatly improved under standard conditions (1 atm) for the polarization curve measurement. It is also observed that the performance losses of C2 and C3 are also attenuated in the pressurized measurements, although the potential losses at zero gauge pressure are much more significant. Gas pressure is known to affect slightly to the reaction kinetics, but has a deeper effect on transport processes in the electrodes [119]. This fact explains the significant increase in the low frequency impedance with cathodic catalyst layer dilution (Figure 3-35d and Figure 3-35e). Therefore, the large change in performance observed in

more dilute catalyst layers is a clear indication of higher oxygen transport losses in these catalyst layers.

Effect of sequential deposition of Pt/CB and CB phases on water distribution

In addition to the simultaneous deposition of mixtures of both phases, sequential deposition of Pt/CB and CB phases was also performed to provide further understanding of the effect of catalyst layer thickness on water distribution. In this case, the active catalyst will be confined to an area close to the polymeric membrane with an inert Vulcan carbon layer on top grown with the same experimental conditions.

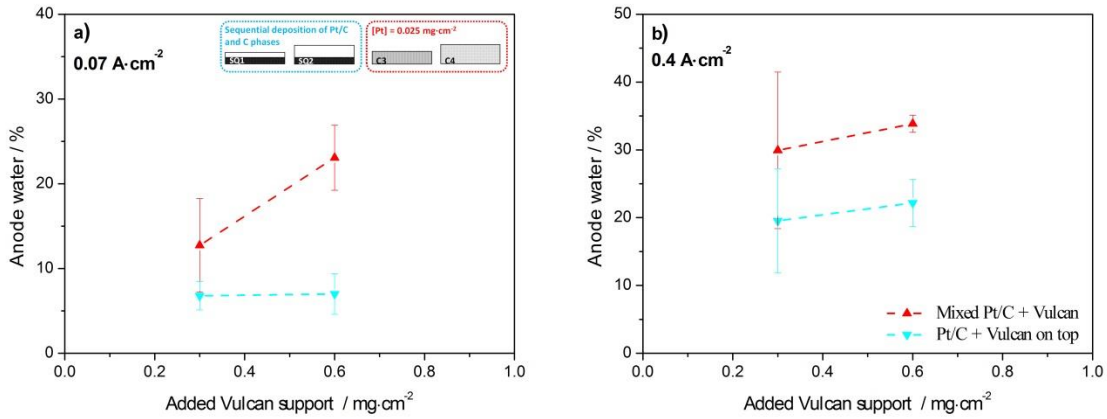

Figure 3-36: Percentage of total water collection in the anode versus cathodic layer thickness manufactured with sequential deposition of Pt/C and C phases compared with their counterparts with a mixed ink at (a) low and (b) medium current densities

Figure 3-36 depicts the percentage of total water collection in the anode of catalyst layers manufactured with sequential deposition of Pt/CB and CB phases, and compared with diluted carbon layers of similar thickness prepared in the previous section. These experiments yielded baffling results, as the addition of a thick hydrophobic layer on top of the catalyst layer does not appear to contribute to push water towards the anode, but to reduce of the water collected in the anodic side is observed even below the quantities obtained with airbrushed layers.

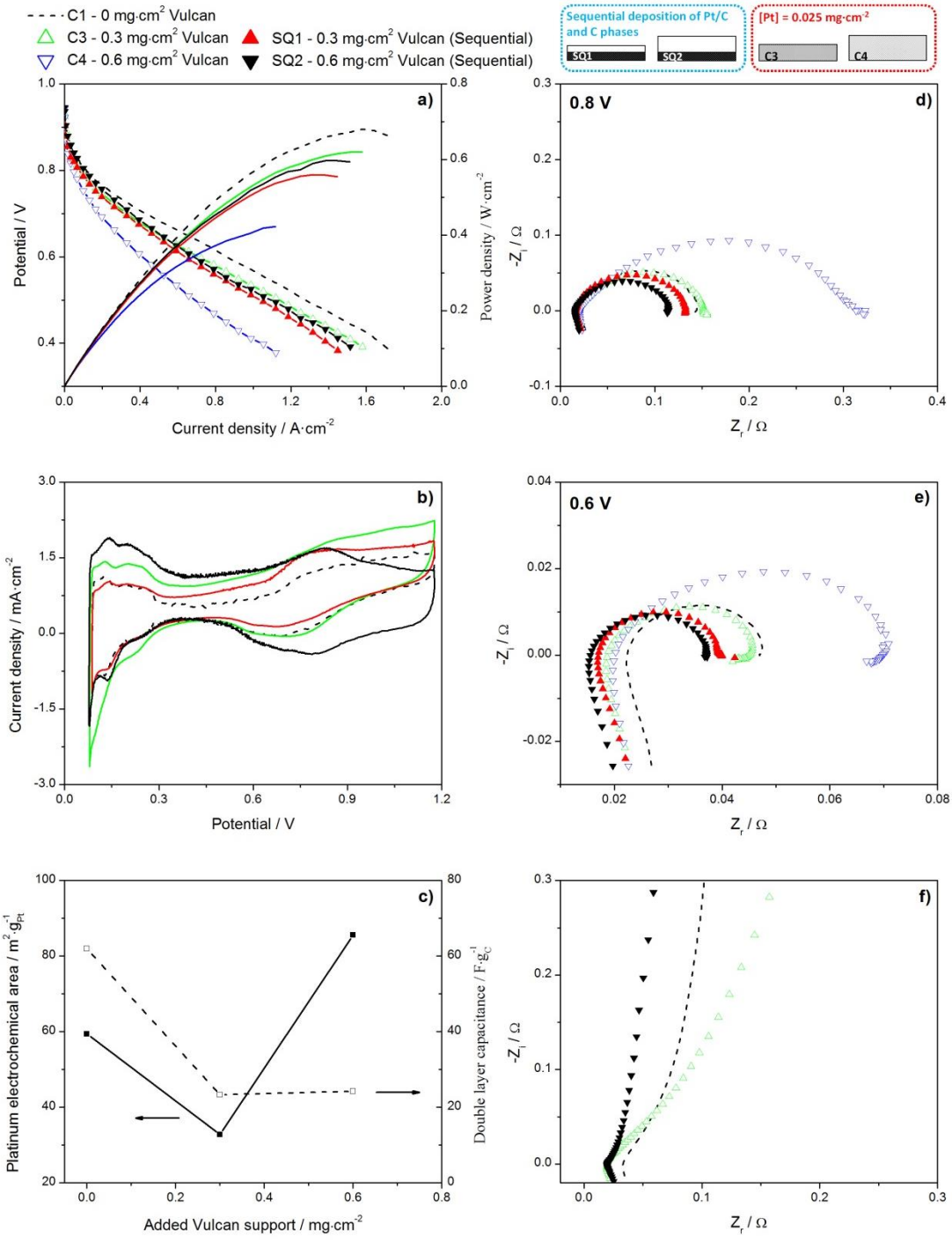

Figure 3-37: Characterization of the catalyst layers with sequential deposition of Pt/CB and CB layers compared with their counterparts with a mixed ink: a) Polarization curves (1.5/1.5 H_2/O_2, 80 °C, 100 %RH and 1 atm). b) Cyclic voltammetries at 0.025 $V \cdot s^{-1}$ and 30 °C. c) Electrochemical active area calculated from the H_2 desorption region and double layer capacitance. d) Impedance measurement (1.5/1.5 H_2/O_2, 80 °C, 100 %RH and Patm) at 0.8 V. e) Impedance measurement at 0.6 V. f) Nyquist plot of H_2/N_2 impedance at 100 %RH and 30 °C

Okuno et al. performed very similar experiments varying the position of the sequentially deposited layers. However, in their work there is no available comparison with a pure Pt/CB layer with the same platinum loading [120]. This effect have yet to be explained, as other author reported that the presence of a hydrophobic microporous layer on the cathode neither enhances back-diffusion nor increases water removal from the cathode catalyst layer to the gas diffusion layer [121].

Figure 3-37 compiles the electrochemical characterization in single cell of the sequential-deposited, and compared with the carbon-mixed catalyst layers. Also the sample with 0.025 $mg_{Pt} \cdot cm^{-2}$ and no extra carbon (C1) is depicted with a black-dashed line. In Figure 3-37a, it can be seen that there is a slight performance reduction because of the addition of the carbon layer on top of the Pt/CB layer, although it is not increased as the carbon layer thickness increases. Impedance results (Figure 3-37d and Figure 3-37e) show a reduction of the charge transfer resistance and the protonic resistance of the sequential deposition samples compared to the pure and mixed carbon samples. Surprisingly enough, sequential deposited layers also show a decreased ohmic (high-frequency) resistance values. Protonic resistance measurements (Figure 3-37f), although incomplete due to experimental problems, show the beneficial effect on proton transport of sequential deposition over the mixed and pure carbon sample. The decrease of the protonic resistance in sample SQ2 is accompanied by the increment of active sites in the Pt/CB layer, reflected in the increase of platinum electrochemical area in Figure 3-37c.

Effect of Pt/CB and carbon phases proportion on water distribution

Considering the huge performance losses of sample C5, in which a catalyst loading of 0.025 $mg \cdot cm^{-2}$ of platinum is mixed with 0.9 $mg \cdot cm^{-2}$ of Vulcan carbon black, and the change in the trend in water distribution, samples of the same thickness (24 µm) were prepared by varying the proportions of catalyst and Vulcan loadings to analyze the behavior of catalyst layer with constant thickness.

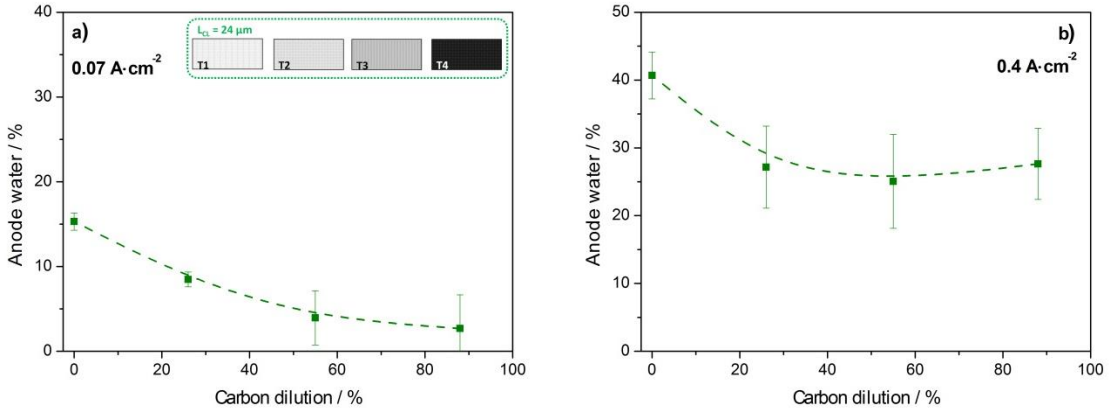

Figure 3-38: Percentage of total water collection in the anode versus cathodic layer thickness with variable catalyst loading and constant thickness at low and medium current densities

By analyzing the water collection in the anode of MEAs with cathode layers with the same thickness, depicted in Figure 3-38, it becomes evident that the water distribution is not only controlled by the thickness of the hydrophobic catalyst layers, but also by the amount of platinum. This fact is not surprising provided the important effect of the platinum phase on water interaction and absorption as shown in previous section (Figure 3-25). As thickness appears to be one of the factors affecting water distribution, current density profile of the electrode may also have an important role governing the direction of water during cell operation. It is reported that high overpotentials for a given current density, results in more water produced close to the GDL [122], thus facilitating the water drag by the oxygen gas stream and reducing the water in the anodic exhaust.

Figure 3-39 shows polarization curves, impedance analysis, and active area measurements. Unlike the layers with low catalyst loading, carbon dilution has no positive effect, even at the lowest dilution, as it can be seen from the polarization curves (Figure 3-39a), where the performance decreases steadily as the dilution percentage is increased. Impedance spectroscopy analysis of fuel cell operation (Figure 3-39d and Figure 3-39e) and proton conductivity measurements (Figure 3-39f) clearly show that both mass transport and proton conductivity are negatively affected by the addition of carbon.

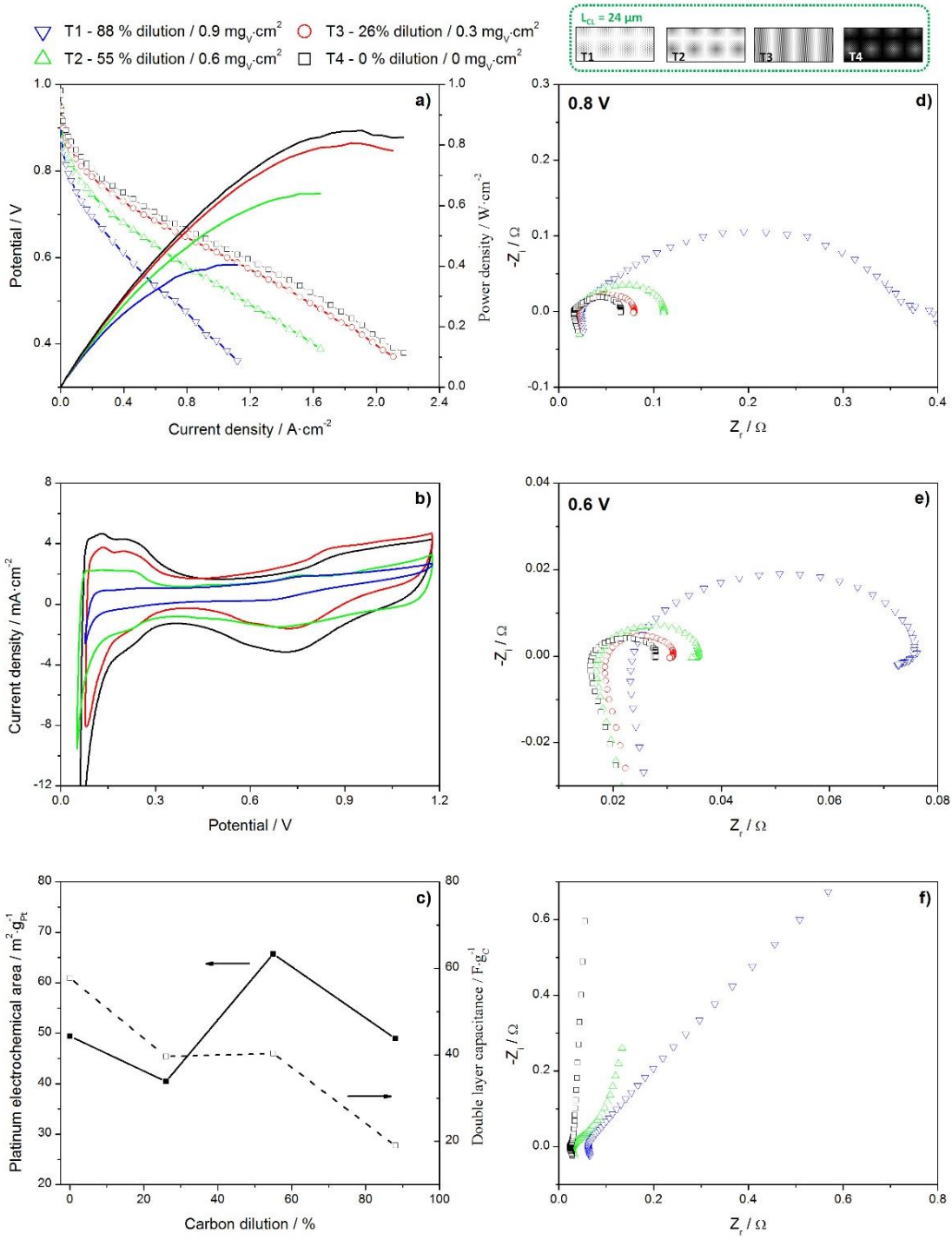

Figure 3-39: Characterization of the catalyst layers with variable catalyst loading and constant thickness: a) Polarization curves (1.5/1.5 H_2/O_2, 80 °C, 100 %RH and 1 atm). b) Cyclic voltammetries at 0.025 V·s^{-1} and 30 °C. c) Electrochemical active area calculated from the H_2 desorption region and double layer capacitance. d) Impedance measurement (1.5/1.5 H_2/O_2, 80 °C, 100 %RH and Patm) at 0.8 V. e) Impedance measurement at 0.6 V. f) Nyquist plot of H_2/N_2 impedance at 100 %RH and 30 °C

The platinum electrochemical area (Figure 3-39c), on the other hand, seems to remain in the same range of values, but the double layer capacitance decreases by more than a half, indicating an effective decrease of the carbon charged area and, consequently, the amount of catalyst that is active.

3.5 Conclusions

From this part of the thesis, the following conclusions can be extracted.

The **morphologic characterization** studies show results of a new characterization procedure for the cross-sectional analysis of MEAs by using metallographic methods and the application of the ion-milling technique. The ion-milling procedure shows to be a precise and reproducible method of catalyst layer thickness measurement for conventional and electrosprayed layers. Additionally, STEM and TEM microscopies have confirmed the ability of electrosprayed layers to achieve a better distribution of the ionomer on the catalyst layer aggregates when the ionomer concentration is optimal.

The study of the **mass-transport properties** of the catalyst layer reveals improved transport properties of electrosprayed samples compared with conventional ones. Additionally, the mass-transport losses usually observed for catalyst layers with low loadings that limit the reduction of catalyst amounts for traditional ink-based methods were halved using electrospray. The water-uptake capability of the electrosprayed layers is enhanced due to their particular morphology and distribution of the ionomer phase. The enhanced water-vapor uptake of electrosprayed layers combined with their very low wettability and superhydrophobic character, allow for an optimal catalyst layer with low mass transport resistance and high ionic conductivity.

The **impact on water distribution** of the use of electrosprayed layers showed a new behavior. Electrosprayed layers in the cathode of a PEM fuel cell in combination with a standard more hydrophilic anode, enhance the back diffusion of water from the cathode to the anode. The behavior is explained by the superhydrophobic character of the

electrosprayed layer, which gives rise to operation under lower saturation conditions and lower water permeability compared with conventional layers. Larger water back diffusion towards the anode improves membrane and anode humidification, decreases the internal resistance of the cell, and, as a result, improves the performance (above 20 % in maximum power density) and stability of the PEM fuel cell.

Aiming to attain a passive control the water distribution in PEM fuel cells, the **influence of the thickness of a hydrophobic catalyst layer** on water transport was studied by using blended catalyst layers with the catalyst and the bare carbon black support. The variation of the catalyst loading, with its subsequent variation of thickness, was proven to alter up to 15 % of the total water distribution between anode and cathode. Although it was proven that the catalyst layer thickness can control water distribution, the loss of performance in the cells, made these approach less useful for practical application. However, it has been found that the deposition of a bare carbon layer on top of the catalyst layer, reverses the effect of the water push to the anode of catalyst layers with low loadings. Although these findings need more investigation, it opens up the possibility to preferentially push water to the anode by using electrosprayed catalyst layers, or to the cathode, by using an additional bare carbon black layer on top of the previously electrosprayed layer.

References

[1] D. Harvey, J. Pharoah, K. Karan, A comparison of different approaches to modelling the PEMFC catalyst layer, J. Power Sources. 179 (2008) 209–219.

[2] S. Litster, G. McLean, PEM fuel cell electrodes, J. Power Sources. 130 (2004) 61–76.

[3] E.A. Ticianelli, C.R. Derouin, A. Redondo, S. Srinivasan, Methods to advance technology of proton exchange membrane fuel cells, J. Electrochem. Soc. 135 (1988) 2209–2214.

[4] E. Antolini, L. Giorgi, A. Pozio, E. Passalacqua, Influence of Nafion loading in the catalyst layer of gas-diffusion electrodes for PEFC, J. Power Sources. 77 (1999) 136–142.

[5] A.M. Chaparro, B. Gallardo, M.A. Folgado, A.J. Martin, L. Daza, PEMFC electrode preparation by electrospray: Optimization of catalyst load and ionomer content, Catal. Today. 143 (2009) 237–241.

[6] G. Sasikumar, J.W. Ihm, H. Ryu, Optimum Nafion content in PEM fuel cell electrodes, Electrochimica Acta. 50 (2004) 601–605.

[7] Z. Qi, A. Kaufman, Low Pt loading high performance cathodes for PEM fuel cells, J. Power Sources. 113 (2003) 37–43.

[8] M. Watanabe, H. Igarashi, K. Yosioka, An experimental prediction of the preparation condition of Nafion-coated catalyst layers for PEFCs, Electrochimica Acta. 40 (1995) 329–334.

[9] S. Jeon, J. Lee, G.M. Rios, H.J. Kim, S.Y. Lee, E. Cho, T.H. Lim, J.H. Jang, Effect of ionomer content and relative humidity on polymer electrolyte membrane fuel cell (PEMFC) performance of membrane-electrode assemblies (MEAs) prepared by decal transfer method, Int. J. Hydrog. Energy. 35 (2010) 9678–9686.

[10] M. Uchida, Y. Aoyama, N. Eda, A. Ohta, Investigation of the microstructure in the catalyst layer and effects of both perfluorosulfonate ionomer and PTFE-loaded carbon on the catalyst layer of polymer electrolyte fuel cells, J. Electrochem. Soc. 142 (1995) 4113–4119.

[11] P. Gode, F. Jaouen, G. Lindbergh, A. Lundblad, G. Sundholm, Influence of the composition on the structure and electrochemical characteristics of the PEFC cathode, Electrochimica Acta. 48 (2003) 4175–4187.

[12] Y.G. Yoon, G.G. Park, T.H. Yang, J.N. Han, W.Y. Lee, C.S. Kim, Effect of pore structure of catalyst layer in a PEMFC on its performance, Int. J. Hydrog. Energy. 28 (2003) 657–662.

[13] H.S. Park, Y.H. Cho, Y.H. Cho, C.R. Jung, J.H. Jang, Y.E. Sung, Performance enhancement of PEMFC through temperature control in catalyst layer fabrication, Electrochimica Acta. 53 (2007) 763–767.

[14] A. Fischer, J. Jindra, H. Wendt, Porosity and catalyst utilization of thin layer cathodes in air operated PEM-fuel cells, J. Appl. Electrochem. 28 (1998) 277–282.

[15] G.S. Avcioglu, B. Ficicilar, I. Eroglu, Improved PEM fuel cell performance with hydrophobic catalyst layers, Int. J. Hydrog. Energy. 43 (2018) 18632–18641.

[16] J.T. Gostick, M.W. Fowler, M.A. Ioannidis, M.D. Pritzker, Y.M. Volfkovich, A. Sakars, Capillary pressure and hydrophilic porosity in gas diffusion layers for polymer electrolyte fuel cells, J. Power Sources. 156 (2006) 375–387.

[17] A. Kusoglu, A. Kwong, K.T. Clark, H.P. Gunterman, A.Z. Weber, Water uptake of fuel-cell catalyst layers, J. Electrochem. Soc. 159 (2012) 530–535.

[18] A.M. Chaparro, A.J. Martin, M.A. Folgado, B. Gallardo, L. Daza, Comparative analysis of the electroactive area of Pt/C PEMFC electrodes in liquid and solid polymer contact by underpotential hydrogen adsorption/desorption, Int. J. Hydrog. Energy. 34 (2009) 4838–484.

[19] T.A. Greszler, D. Caulk, P. Sinha, The impact of platinum loading on oxygen transport resistance, J. Electrochem. Soc. 159 (2012) 831–840.

[20] M. Nesselberger, M. Roefzaad, R.F. Hamou, P.U. Biedermann, F.F. Schweinberger, S. Kunz, K. Schloegl, G.K. Wiberg, S. Ashton, U. Heiz, K.J. Mayrhofer, M. Arenz, The effect of particle proximity on the oxygen reduction rate of size-selected platinum clusters, Nat. Mater. 12 (2013) 919–924.

[21] T.F. Yang, L.W. Hourng, T.L. Yu, P.H. Chi, A. Su, High performance proton exchange membrane fuel cell electrode assemblies, J. Power Sources. 195 (2010) 7359–7369.

[22] J. Speder, A. Zana, I. Spanos, J.K. Kirkensgaard, K. Mortensen, M. Hanzlik, M. Arenz, Comparative degradation study of carbon supported proton exchange membrane fuel cell electrocatalysts – The influence of the platinum to carbon ratio on the degradation rate, J. Power Sources. 261 (2014) 14–22.

[23] E. Antolini, Structural parameters of supported fuel cell catalysts: The effect of particle size, inter-particle distance and metal loading on catalytic activity and fuel cell performance, Appl. Catal. B Environ. 181 (2013) 298–313.

[24] A.L. Dicks, The role of carbon in fuel cells, J. Power Sources. 156 (2006) 128–141.

[25] Y. Liu, C. Ji, W. Gu, D.R. Baker, J. Jorne, H.A. Gasteiger, Proton conduction in PEM fuel cell cathodes: Effects of electrode thickness and ionomer equivalent weight, J. Electrochem. Soc. 157 (2010) 1154–1162.

[26] M. Chisaka, E. Matsuoka, H. Daiguji, Effect of organic solvents on the pore structure of catalyst layers in polymer electrolyte membrane fuel cells, J. Electrochem. Soc. 157 (2010) 1218–1221.

[27] J.C. Meier, C. Galeano, I. Katsounaros, J. Witte, H.J. Bongard, A.A. Topalov, C. Baldizzone, S. Mezzavilla, F. Schüth, K.J. Mayrhofer, Design criteria for stable Pt/C fuel cell catalysts, Beilstein J. Nanotechnol. 5 (2014) 44–67.

[28] V. Mulone, K. Karan, Analysis of capillary flow driven model for water transport in PEFC cathode catalyst layer: Consideration of mixed wettability and pore size distribution, Int. J. Hydrog. Energy. 2013 (2013) 558–569.

[29] M. Eikerling, Water management in cathode catalyst layers of PEM fuel cells: A structure-based model, J. Electrochem. Soc. 153 (2006) 58–70.

[30] T.W. Patterson, R.M. Darling, Damage to the cathode catalyst of a PEM fuel cell caused by localized fuel starvation, Electrochem. Solid-State Lett. 9 (2006) 183–185.

[31] N. Nonoyama, S. Okazaki, A.Z. Weber, Y. Ikogi, T. Yoshida, Analysis of oxygen-transport diffusion resistance in proton-exchange-membrane fuel cells, J. Electrochem. Soc. 158 (2011) 416–423.

[32] F.C. Cetinbas, X. Wang, R.K. Ahluwalia, N.N. Kariuki, R.P. Winarski, Z. Yang, J. Sharman, D.J. Myers, Microstructural analysis and transport resistances of low-platinum-loaded PEFC electrodes, J. Electrochem. Soc. 164 (2017) 1596–1607.

[33] A. Kongkanand, P.K. Sinha, Load transients of nanostructured thin film electrodes in polymer electrolyte fuel cells, J. Electrochem. Soc. 158 (2011) 703–711.

[34] N.P. Subramanian, T.A. Greszler, J. Zhang, W. Gu, R. Makharia, Pt-oxide coverage-dependent oxygen reduction reaction (ORR) kinetics, J. Electrochem. Soc. 159 (2012) 531–540.

[35] A.Z. Weber, A. Kusoglu, Unexplained transport resistances for low-loaded fuel-cell catalyst layers, J Mater Chem A. 2 (2014) 17207–17211.

[36] A. Kusoglu, D. Kushner, D.K. Paul, K. Karan, M.A. Hickner, A.Z. Weber, Impact of substrate and processing on confinement of Nafion thin films, Adv. Funct. Mater. 24 (2014) 4763–4774.

[37] T. Schuler, A. Chowdhury, A.T. Freiberg, B. Sneed, F.B. Spingler, M.C. Tucker, M.L. More, C.J. Radke, A.Z. Weber, Fuel-cell catalyst-layer resistance via hydrogen limiting-current measurements, J. Electrochem. Soc. 166 (2019) 3020–3031.

[38] F.A. Uribe, T.E. Springer, S. Gottesfeld, A microelectrode study of oxygen reduction at the platinum/recast-Nafion film interface, J. Electrochem. Soc. 139 (1992) 765–773.

[39] T.A. Zawodzinski, C. Derouin, S. Radzinski, R.J. Sherman, V.T. Smith, T.E. Springer, S. Gottesfeld, Water uptake by and transport through Nafion® 117 membranes, J. Electrochem. Soc. 140 (1993) 1041–1047.

[40] X. Ren, S. Gottesfeld, Electro-osmotic drag of water in poly(perfluorosulfonic acid) membranes, J. Electrochem. Soc. 148 (2001) 87–93.

[41] T.V. Nguyen, A gas distributor design for proton-exchange-membrane fuel cells, J. Electrochem. Soc. 143 (1996) 103–105.

[42] L.J. Zheng, A.K. Srouji, R. Dross, A. Turhan, M.M. Mench, Computational engineering of porous flow field PEFCs to enable high temperature high power density operation, J. Electrochem. Soc. 160 (2013) 119–128.

[43] J. Larminie, A. Dicks, Fuel cells systems explained, John Wiley & Sons, 2003.

[44] H. Li, Y. Tang, Z. Wang, Z. Shi, S. Wu, D. Song, J. Zhang, K. Fatih, J. Zhang, H. Wang, Z. Liu, R. Abouatallah, A. Mazza, A review of water flooding issues in the proton exchange membrane fuel cell, J. Power Sources. 178 (2008) 103–117.

[45] A. Turhan, K. Heller, J.S. Brenizer, M.M. Mench, Passive control of liquid water storage and distribution in a PEFC through flow-field design, J. Power Sources. 180 (2008) 773–783.

[46] J.P. Owejan, T.A. Trabold, D.L. Jacobson, M. Arif, S.G. Kandlikar, Effects of flow field and diffusion layer properties on water accumulation in a PEM fuel cell, Int. J. Hydrog. Energy. 32 (2007) 4489–4502.

[47] Y.S. Chen, H. Peng, D.S. Hussey, D.L. Jacobson, D.T. Tran, T. Abdel-Baset, M. Biernacki, Water distribution measurement for a PEMFC through neutron radiography, J. Power Sources. 170 (2007) 376–386.

[48] S.G. Kandlikar, Z. Lu, Thermal management issues in a PEMFC stack – A brief review of current status, Appl. Therm. Eng. 29 (2009) 1276–1280.

[49] S. Litster, C.R. Buie, T. Fabian, J.K. Eaton, J.G. Santiago, Active water management for PEM fuel cells, J. Electrochem. Soc. 154 (2007) 1049–1058.

[50] M.W. Knobbe, W. He, P.Y. Chong, T.V. Nguyen, Active gas management for PEM fuel cell stacks, J. Power Sources. 138 (2004) 94–100.

[51] Z. Hu, Y. Yu, G. Wang, X. Chen, P. Chen, J. Chen, S. Zhou, Anode purge strategy optimization of the polymer electrode membrane fuel cell system under the dead-end anode operation, J. Power Sources. 320 (2016) 68–77.

[52] C.R. Buie, J.D. Posner, T. Fabian, S.W. Cha, D. Kim, F.B. Prinz, J.K. Eaton, J.G. Santiago, Water management in proton exchange membrane fuel cells using integrated electroosmotic pumping, J. Power Sources. 161 (2006) 191–202.

[53] M. Watanabe, Y. Satoh, C. Shimura, Management of the water content in polymer electrolyte membranes with porous fiber wicks, J. Electrochem. Soc. 190 (1993) 3190–3193.

[54] D.P. Wilkinson, H.H. Voss, K. Prater, Water management and stack design for solid polymer fuel cells, J. Power Sources. 49 (1994) 117–127.

[55] T.E. Springer, T.A. Zawodzinski, M.S. Wilson, S. Gottesfeld, Characterization of polymer electrolyte fuel cells using AC impedance spectroscopy, J. Electrochem. Soc. 143 (1999) 587–589.

[56] M. Watanabe, H. Uchida, Y. Seki, M. Emori, P. Stonehart, Self-humidifying polymer electrolyte membranes for fuel cell, J. Electrochem. Soc. 143 (1996) 3847–3852.

[57] C.H. Park, S.Y. Lee, D.S. Hwang, D.W. Shin, D.H. Cho, K.H. Lee, T.W. Kim, M. Lee, D.S. Kim, C.M. Doherty, A.W. Thornton, A.J. Hill, M.D. Guiver, Y.M. Lee, Nanocrack-regulated self-humidifying membranes, Nature. 532 (2016) 480–483.

[58] A. Uzunoglu, F. Dundar, A. Ata, C-SiO_2 supported catalysts for durability and performance improvement in PEM fuel cells, ECS Trans. 41 (2011) 1257–1267.

[59] Y. Tominaga, I.C. Hong, S. Asai, M. Sumita, Proton conduction in Nafion composite membranes filled with mesoporous silica, J. Power Sources. 171 (2007) 530–534.

[60] B.S. Koh, J.H. Yoo, E.K. Jang, V.R. Jothi, C.Y. Jung, S.C. Yi, Fabrication of highly effective self-humidifying membrane electrode assembly for proton exchange membrane fuel cells via electrostatic spray deposition, Electrochem. Commun. 93 (2018) 76–80.

[61] J.S. Yi, J.D. Yang, C. King, Water management along the flow channels of PEM fuel cells, AIChE J. 50 (2004) 2594–2603.

[62] X. Guo, Y. Zeng, Z. Wang, Z. Shao, B. Yi, Investigation of porous water transport plates used for the humidification of a membrane electrode assembly, J. Power Sources. 302 (2016) 84–91.

[63] T. Fabian, R. O'Hayre, S. Litster, F.B. Prinz, J.G. Santiago, Passive water management at the cathode of a planar air-breathing proton exchange membrane fuel cell, J. Power Sources. 195 (2010) 3201–3206.

[64] S.H. Ge, X.G. Li, I.M. Hsing, Water management in PEMFCs using absorbent wicks, J. Electrochem. Soc. 151 (2004) 523–528.

[65] P.M. Kumar, V. Parthasarathy, A passive method of water management for an air-breathing proton exchange membrane fuel cell, Energy. 51 (2013) 457–461.

[66] S. Kim, M.M. Mench, Investigation of temperature-driven water transport in polymer electrolyte fuel cell: phase-change-induced flow, J. Electrochem. Soc. 156 (2009) 353–362.

[67] Y.A. Gandomi, M.M. Mench, Assessing the limits of water management using asymmetric micro-porous layer configurations, ECS Trans. 58 (2013) 1375–1382.

[68] Y.A. Gandomi, M.D. Edmundson, F.C. Busby, M.M. Mench, Water management in polymer electrolyte fuel cells through asymmetric thermal and mass transport engineering of the micro-porous layers, J. Electrochem. Soc. 163 (2016) 933–944.

[69] R. Schweiss, Benefits of membrane electrode assemblies with asymmetrical GDL configurations for PEM fuel cells, Fuel Cells. 16 (2016) 100–106.

[70] K. Tüber, D. Pócza, C. Hebling, Visualization of water buildup in the cathode of a transparent PEM fuel cell, J. Power Sources. 124 (2003) 403–414.

[71] H. Nishikawa, R. Kurihara, S. Sukemori, T. Sugawara, H. Kobayasi, S. Abe, T. Aoki, Y. Ogami, A. Matsunaga, Measurements of humidity and current distribution in a PEFC, J. Power Sources. 155 (2006) 213–218.

[72] M.M. Mench, Q.L. Dong, C.Y. Wang, In situ water distribution measurements in a polymer electrolyte fuel cell, J. Power Sources. 124 (2003) 90–98.

[73] C. Hartnig, I. Manke, R. Kuhn, S. Kleinau, J. Goebbels, J. Banhart, High-resolution in-plane investigation of the water evolution and transport in PEM fuel cells, J. Power Sources. 188 (2009) 468–474.

[74] R. Banerjee, N. Ge, J. Lee, M.G. George, S. Chevalier, H. Liu, P. Shrestha, D. Muirhead, A. Bazylak, Transient liquid water distributions in polymer electrolyte membrane fuel cell gas diffusion layers observed through in-operando synchrotron X-ray radiography, J. Electrochem. Soc. 164 (2017) 154–162.

[75] A.Z. Weber, M.A. Hickner, Modeling and high-resolution-imaging studies of water-content profiles in a polymer-electrolyte-fuel-cell membrane-electrode assembly, Electrochimica Acta. 53 (2008) 7668–7674.

[76] P. Oberholzer, P. Boillat, Local characterization of PEFCs by differential cells: systematic variations of current and asymmetric relative humidity, J. Electrochem. Soc. 161 (2014) 139–152.

[77] T.E. Springer, T.A. Zawodzinski, S. Gottesfeld, Polymer electrolyte fuel cell model, J. Electrochem. Soc. 138 (1991) 2334–2342.

[78] J.J. Baschuk, X. Li, Modelling of polymer electrolyte membrane fuel cells with variable degrees of water flooding, J. Power Sources. 86 (2000) 181–196.

[79] U. Pasaogullari, C.Y. Wang, Liquid water transport in gas diffusion layer of polymer electrolyte fuel cells, J. Electrochem. Soc. 151 (2004) 339–406.

[80] Y.S. Chen, A segmented model for studying water transport in a PEM fuel cell, PhD Thesis, University of Michigan (2009).

[81] T. Colinart, A. Chenu, S. Didierjean, O. Lottin, S. Besse, Experimental study on water transport coefficient in proton exchange membrane fuel cell, J. Power Sources. 190 (2009) 230–240.

[82] F.N. Büchi, S. Srinivasan, Operating proton exchange membrane fuel cells without external humidification of the reactant gases, J. Electrochem. Soc. 144 (1997) 2767–2772.

[83] K.C. Neyerlin, W. Gu, J. Jorne, H.A. Gasteiger, Determination of catalyst unique parameters for the oxygen reduction reaction in a PEMFC, J. Electrochem. Soc. 153 (2006) 1955–1963.

[84] D.R. Baker, D.A. Caulk, K.C. Neyerlin, M.W. Murphy, Measurement of oxygen transport resistance in PEM fuel cells by limiting current methods, J. Electrochem. Soc. 156 (2009) 991–1003.

[85] G.S. Hwang, A.Z. Weber, Effective-diffusivity measurement of partially-saturated fuel-cell gas-diffusion layers, J. Electrochem. Soc. 159 (2012) 683–692.

[86] A.T. Freiberg, M.C. Tucker, A.Z. Weber, Polarization loss correction derived from hydrogen local-resistance measurement in low Pt-loaded polymer-electrolyte fuel cells, Electrochem. Commun. 79 (2017) 14–17.

[87] F.B. Spingler, A. Phillips, T. Schuler, M.C. Tucker, A.Z. Weber, Investigating fuel-cell transport limitations using hydrogen limiting current, Int. J. Hydrog. Energy. 42 (2017) 13960–13969.

[88] S. Trasatti, O.A. Petri, Real surface area measurements in electrochemistry, J. Electroanal. Chem. 327 (1992) 353–376.

[89] P.N. Ross, Structure sensitivity in the electrocatalytic properties of Pt: Hydrogen adsorption on low index single crystals and the role of steps, J. Electrochem. Soc. 126 (1979) 67–77.

[90] E. Barsoukov, J.R. Macdonald, Impedance Spectroscopy: Theory, Experiment, and Applications, Wiley-Interscience, 2005.

[91] A.J. Bard, L.R. Faulkner, Electrochemical Methods. Fundamentals and Applications, Wiley, 2000.

[92] P.M. Gomadam, J.W. Weidner, Analysis of electrochemical impedance spectroscopy in proton exchange membrane fuel cells, Int. J. Energy Res. 29 (2005) 1133–1151.

[93] X. Yuan, H. Wang, J. Colinsun, J. Zhang, AC impedance technique in PEM fuel cell diagnosis - A review, Int. J. Hydrog. Energy. 32 (2007) 4365–4380.

[94] S.R. Taylor, E. Gileadi, Physical Interpretation of the Warburg Impedance, Corrosion. 51 (1995) 664–671.

[95] A.M. Dhirde, N.V. Dale, H. Salehfar, M.D. Mann, T.H. Han, Equivalent electric circuit modeling and performance analysis of a PEM fuel cell stack using impedance spectroscopy, IEEE Trans. Energy Convers. 25 (2010) 778–786.

[96] D. Malevich, B.R. Jayasankar, E. Halliop, J.G. Pharoah, B.A. Peppley, K. Karan, On the determination of PEM fuel cell catalyst layer resistance from impedance measurement in H_2/N_2 cells, J. Electrochem. Soc. 159 (2012) 888–895.

[97] J.H. Jang, S. Jeon, J.H. Cho, S.K. Kim, S.Y. Lee, E. Cho, H.J. Kim, J. Han, T.H. Lim, Complex capacitance analysis of ionic resistance and interfacial capacitance in PEMFC and DMFC catalyst layers, J. Electrochem. Soc. 156 (2009) 1293–1300.

[98] A.M. Chaparro, P. Ferreira-Aparicio, M.A. Folgado, E. Brightman, G. Hinds, Study of superhydrophobic electrosprayed catalyst layers using a localized reference electrode technique, J. Power Sources. 325 (2016) 609–619.

[99] P. Ferreira-Aparicio, A.M. Chaparro, M.A. Folgado, J.J. Conde, E. Brightman, G. Hinds, Degradation study by start-up/shut-down cycling of superhydrophobic electrosprayed catalyst layers using a localized reference electrode technique, ACS Appl. Mater. Interfaces. 9 (2017) 10626–10636.

[100] A.M. Chaparro, P. Ferreira-Aparicio, M.A. Folgado, A.J. Martin, L. Daza, Catalyst layers for proton exchange membrane fuel cells prepared by electrospray deposition on Nafion membrane, J. Power Sources. 196 (2011) 4200–4208.

[101] A.M. Chaparro, M.A. Folgado, P. Ferreira-Aparicio, A.J. Martin, I. Alonso-Alvarez, L. Daza, Properties of catalyst layers for PEMFC electrodes prepared by electrospray deposition, J. Electrochem. Soc. 157 (2010) 993–999.

[102] J. Rouquerol, D. Avnir, C.W. Fairbridge, D.H. Everett, J.H. Haynes, N. Pernicone, J.D. Ramsay, K.S. Sing, K.K. Unger, Recomendations for the characterization of porous solids, Pure Appl. Chem. 66 (1994) 1739–1758.

[103] T. Suzuki, S. Tsushima, S. Hirai, Pore structure and cell performance analysis of PEMFC catalyst layers fabricated by decal transfer method with variation of hot pressing pressure, ECS Trans. 41 (2011) 909–914.

[104] L. Guétaz, M. Lopez-Haro, S. Escribano, A. Morin, G. Gebel, D. Cullen, K. More, R. Borup, Catalyst-layer ionomer imaging of fuel cells, ECS Trans. 69 (2015) 455–464.

[105] A.M. Chaparro, R. Benitez, L. Gubler, G.G. Scherer, L. Daza, Study of membrane electrode assemblies for PEMFC, with cathodes prepared by the electrospray method, J. Power Sources. 169 (2007) 77–84.

[106] Y. Park, H. Tokiwa, K. Kakinuma, M. Watanabe, M. Uchida, Effects of carbon supports on Pt distribution, ionomer coverage and cathode performance for polymer electrolyte fuel cells, J. Power Sources. 315 (2016) 179–191.

[107] M. Lopez-Haro, L. Gue´taz, T. Printemps, A. Morin, S. Escribano, P.H. Jouneau, P. Bayle-Guillemaud, F. Chandezon, G. Gebel, Three-dimensional analysis of Nafion layers in fuel cell electrodes, Nat. Commun. 5 (2014) 5229.

[108] D.A. Cullen, R. Koestner, R.S. Kukreja, Z.Y. Liu, S. Minko, O. Trotsenko, A. Tokarev, L. Guetaz, H.M. Meyer III, C.M. Parish, K.L. More, Imaging and microanalysis of thin ionomer layers by scanning transmission electron microscopy, J. Electrochem. Soc. 161 (2014) 1111–1117.

[109] M. Lee, M. Uchida, D.A. Tryk, H. Uchida, M. Watanabe, The effectiveness of platinum/carbon electrocatalysts: Dependence on catalyst layer thickness and Pt alloy catalytic effects, Electrochimica Acta. 56 (2011) 4783–4790.

[110] T. Suzuki, S. Tsushima, S. Hirai, Fabrication and performance evaluation of structurally-controlled PEMFC catalyst layers by blending platinum-supported and stand-alone carbon black, J. Power Sources. 233 (2013) 269–276.

[111] A. Lasia, Impedance of porous electrodes, J. Electroanal. Chem. 397 (1996) 587–599.

[112] W.G. Pell, A. Zolfaghari, B.E. Conway, Capacitance of the double-layer at polycrystalline Pt electrodes bearing a surface-oxide film, J. Electroanal. Chem. 532 (2002) 12–23.

[113] F. Beck, M. Dolata, E. Grivei, N. Probst, Electrochemical supercapacitors based on industrial carbon blacks in aqueous H_2SO_4, J. Appl. Electrochem. 31 (2001) 845–853.

[114] C. Lim, L. Ghassemzadeh, F. Van Hove, M. Lauritzen, J. Kolodziej, G.G. Wang, S. Holdcroft, E. Kjeang, Membrane degradation during combined chemical and mechanical accelerated stress testing of polymer electrolyte fuel cells, J. Power Sources. 257 (2014) 102–110.

[115] Q. Duan, H. Wang, J. Benziger, Transport of liquid water through Nafion membranes, J. Membr. Sci. 392 (2012) 88–94.

[116] X. Wang, T.V. Nguyen, Modeling the effects of capillary property of porous media on the performance of the cathode of a PEMFC, J. Electrochem. Soc. 155 (2008) 1085–1092.

[117] J. Bear, Dynamics of Fluids in Porous Media, Dover Publications, 1988.

[118] J.P. Owejan, J.E. Owejan, W. Gu, Impact of platinum loading and catalyst layer structure on PEMFC performance, J. Electrochem. Soc. 160 (2013) 824–833.

[119] J. Zhang, H. Zhang, J. Wu, J. Zhang, Pressure Effects on PEM Fuel Cell Performance, in: PEM Fuel Cell Testing and Diagnosis. Elsevier, 2013: pp. 225-241.

[120] S. Okuno, N. Katayama, Gradational structured catalyst layer for proton exchange membrane fuel cells, ECS Trans. 83 (2018) 87–91.

[121] H.K. Atiyeh, K. Karan, B. Peppley, A. Phoenix, E. Halliop, J. Pharoah, Experimental investigation of the role of a microporous layer on the water transport and performance of a PEM fuel cell, J. Power Sources. 170 (2007) 111–121.

[122] M. Eikerling, A.A. Kornyshev, Modelling the performance of the cathode catalyst layer of polymer electrolyte fuel cells, J. Electroanal. Chem. 453 (1998) 89–106.

CHAPTER 4

Application of electrosprayed carbon-based deposits as metallic substrate coating

4.1 Outline of the chapter

The development of protective coatings for metallic surfaces is an issue of major interest for the reliability and durability of metallic components in PEM fuel cells. For instance, flow-field plates are key components for fuel cell efficient performance as they are used to separate individual MEAs in fuel cell stacks, transport the generated current, and distribute the feed gases, while carrying out the water produced in the electrochemical reaction. However, as the vast majority of plates are made of stainless steel, the strong acidic media of the cells can cause major corrosion problems.

The electrosprayed carbon coatings described in Chapter 2 are believed to be a proper candidate to fulfill all the requirements as a coating layer for the internal metallic components of PEMFC, by combining the good electronic conductivity of the carbon and the hydrophobicity acquired by the use of electrospray deposition technique as a solution for corrosion protection. In addition, the presence of a hydrophobic coating might be useful to enhance the water removal through the plate channels.

In this chapter, an *ex-situ* study of the protective behavior of the electrosprayed carbon layers on stainless steel metallic surfaces is carried out by means of electrochemical analysis in a three-electrode cell. Conventional airbrushing was used as a control method for deposition of carbon porous layers with the same loading and composition. The resulting electrosprayed films are shown to be structurally stable and provide a protective coating for metals against corrosion, in contrast with those prepared by airbrushing. Additionally, single cell tests using a cathodic flow-field plate with coated channels were

performed to study the removal effect of water in the presence of hydrophobic surfaces. The cell with coated channel plates presents a better performance and a reduction of the transport overpotential under high water production conditions.

4.2 State of the art of corrosion protection of flow-field plates

4.2.1 Corrosion protection of metallic flow-field plates

Stainless steel is the preferred material for the fabrication of flow-field plates due to its high strength, no brittleness, no permeability to reactant gases, and especially for the possibility of low-cost mass production [1]. The main drawback of stainless steel is the poor corrosion resistance in acidic media, causing the growth of oxide layers and the production of cationic ions. Stainless steel forms passive oxide layers under PEM fuel cell operating conditions, significantly increasing the ohmic resistance of the cells. However, the formation of a passive layer does not completely avoid the dissolution of metal cations that lead to membrane degradation, affecting water flux and proton conductivity inside the membrane [2], as well as catalyst layer degradation, affecting the rate of the electrochemical reactions [3].

In other to improve the corrosion resistance of flow-field plates, there are two possible approaches: the use of special alloys (Ni-based and Ti-based alloys) or the surface modification of stainless-steel [4]. The coating materials are usually classified as metal- or carbon-based coatings. On the one hand, metal-based coatings comprise metal carbide, transition metal nitride films and noble metal films [5]. Thermal nitrification of stainless steel is a well-known method to avoid corrosion [6, 7], but the high temperature of the process (>1000 °C) can modify and damage the steel structure, and thus the physical deposition of metal nitrides could be a better choice. Physical deposition of chromium nitride [8], titanium nitride [9], tantalum nitride [10], and zirconium nitride films [11] have been investigated in recent years with positive results as protective coatings in an operating environment of PEM fuel cells. Carburization of stainless steel can also be used to enhance the corrosion resistance and electrical conductance [12], but it is also a high

temperature process. Low temperature carburization processes [13] and physical deposition methods [14, 15] are also potential attractive options for PEM flow-field plates.

Noble metals such as gold and platinum-group metals and alloys have been also tested as stainless steel coatings. Gold coatings have been widely used to avoid the formation of the oxide layer on stainless steel reporting excellent resistance values [16–18]. However, some studies point out that the long-term corrosion protection could be compromised by a high concentration of Fe ions detected in the MEA after a post-mortem analysis [19]. Nonetheless, as it can be seen in Chapter 3, our stainless steel flow-field plates are gold coated for single cell PEM characterization, since gold sputtering offers a simple and reliable method for laboratory scale experiments. However, this coating procedure is only valid for small surfaces and is not adequate for mass production due to the high price of the noble metals.

4.2.2 Carbon-based coatings for PEM fuel cell flow-field plates

The use of metallic plates is widespread in order to avoid the brittleness and high mechanization costs of graphite plates. The use of carbon coating layers on metallic plates aims to take advantage of the chemical inertness and the electric conductivity of the carbon-based materials and thus combine the advantages of carbon and metallic plates.

The vast majority of carbon-based coatings relies on the deposition of amorphous carbon or graphitic materials. Lately, following the growing interest in the search for graphene practical applications, it has also been tried as corrosion protection layer in fuel cells [20, 21]. Additionally, some researchers also investigated the viability of conductive polymer coatings, such as polyaniline and polypyrrole [22, 23] or the use of polymers as part of composite films [24].

Chemical vapor deposition (CVD) was tried by several research groups to study the feasibility of carbon deposits. Sone et al. studied the carbon deposition on stainless steel reporting fibrous deposits [25]. Fukutsuka et al. reported the deposition of sp^2 conductive carbonaceous layers on 304-SS with reduced interfacial resistance and improved corrosion resistance produced via plasma assisted CVD [26, 27], while Show et al. deposited amorphous carbon on titanium flow-field plates reducing the contact resistance [28], and resulting in a 30 % increase of the power output in a single cell [29]. However, the best results so far were reported by Chung et al. depositing carbon layers on 304-SS plates with a thin intermediate nickel layer to catalyze the graphitization reaction. The results showed a chemical stability as compared with commercial graphite, without increasing the electrical resistance of the metal, and a good response in single cell testing at low operation temperatures [30, 31].

Physical deposition methods were also tested for carbon deposition via magnetron sputtering, arc ion plating and electron cyclotron resonance sputtering. Feng et al. used magnetron sputtering to deposit amorphous carbon on 316L-SS showing a great reduction of the interfacial resistance of the steel and enhanced chemical resistance [32–34]. The use of electron cyclotron resonance reportedly improved the cell performance, comparable to that using conventional graphite separators [35]. The arc ion plating deposition, on the other hand, showed a poor enhancement of the chemical resistance after the deposition of pure carbon and carbon-chromium composite films [36].

Novel approaches are using carbon-metal interlayer deposition [37–39] to avoid corrosive liquid infiltration through pinholes under long working hours and improve the adhesion between the substrate [40]. Some examples of polymeric [41] and ceramic [42] intermediate layers can also be found in the literature. Also, metallic doped carbons, are currently being studied for its possibilities in modifying the microstructure and electric conductivity of the carbon layers [43–46].

However, both physical and CVD deposition methods require a high capital investment and having low deposition areas, so they are not adequate for industrial production. The

main problem on coating an electric conductive carbon or graphite thin film without the use of these methods is that the formation of a carbonaceous thin-film is often too loose to serve as a barrier layer from acidic solution. Although there is some published research, other simpler, cheaper and more scalable methods have yet to be explored. Wang et al. studied sol-gel and spin-coating techniques to deposit mesoporous carbon-silica composite layers, showing an increase of the corrosion protection [47]. Husby et al. combined a mixture of carbon, graphite and epoxy resin, applied with spraying technique and followed by a hot-pressing step, but the substrates were found to not be sufficiently protected at long exposure times from the electrolyte due to the high porosity of the layer [48].

4.2.3 Hydrophobic protection against corrosion processes

The hydrophobicity of the protective coatings can be a crucial issue to ensure a proper protection for a metallic material working in aqueous environment, like in a hydrogen fuel cell. The presence of a hydrophobic surface can enhance the corrosion protection of coatings by reducing the contact surface between liquid water and the substrates and thus reducing the area for corrosion processes to occur. Highly porous silica thin films (around 0.5µm) with hydrophobic fluoroalkyl ligands have been proven to prevent water infiltration into porous films, due to the mix of trapped air and surface roughness. The resulting films had water contact angles over 160°, allowing a low water penetration, measured with neutron reflectivity, to a depth of hundreds of ångströms, comprising about 5 % of the deposited layer [49]. The limited exposure of the aluminum substrates to corrosive media due to a hierarchical fractal surface decorated with hydrophobic ligands was reported to decrease the rate of corrosion roughly tenfold compared to the unprotected aluminum [50]. Other common approach consists on generating porous layers of native oxide in the surface of the metal using laser or plasma methods followed by the addition of a hydrophobic agent to cover the pretreated metal [51].

The use of organic–inorganic hybrid coatings, most specifically sol-gel coatings composed of hydrophilic oxides and hydrophobic organic molecules, have been recently

compiled in a review, in which more examples of corrosion protection using hydrophobic layers can be checked out [52]. Electrosprayed carbon-Nafion composites, that are proposed in this thesis for the first time, resemble these organic-inorganic hybrid coatings, so they could have similar protective properties as such hybrid coatings if combining hydrophobic and hydrophilic properties in the same way.

4.2.4 Effect of the hydrophobicity of flow-field plates on fuel cell performance

In a standard configuration, generated water drops in the catalyst layer and arriving at the back of the porous media enter the flow-field plate, where they are dragged by the gas stream towards the outlet. The rate of water elimination from the channels of flow-field plates may limit the efficiency of PEM fuel cells, especially at high current densities. Formation of liquid water droplets on the surface of the gas diffusion layers and its accumulation in the gas channels has been reported to have a strong effect on cell performance [53] while creating significant pressure drops inside gas channels [54].

The use of hydrophobic coatings opens the possibility to accelerate liquid water flow in the gas channels. Owejan et al. reported smaller and more distributed water slugs in PTFE-coated channels. At medium and low current densities, hydrophobic channels tend to accumulate more liquid water, but it does not cause channel obstructions due to better water distribution. However, for high current densities, water accumulation within the hydrophobic channels is reduced and is lower in comparison with the operation with hydrophilic channels. Polarization curves also show an improvement of the cell performance due to the hydrophobization of the channels [55]. Turhan et al. confirmed the increase of water accumulation in channels coated with PTFE. In their study, hydrophobic channels are reported to form discrete droplets with high removal efficiency, whereas hydrophilic channels form film layers around the channel walls promoting a steadier cell operation but increasing the difficulty to purge the excess water [56].

However, under certain conditions, water detachment from the surface of the GDL in the present of hydrophobic channels is not favored, and droplet merging to form large water

waves along the GDL of the cathode is reported [57]. The hydrophobicity of the flow-field plate channels will not be beneficial in every circumstance; ambient conditions and cell operation mode will also be significant to decide the desired degree of interaction of the flow-field plate surface with water. Since hydrophilic surfaces favor the water entrapment between the GDL/land area interface [58], this effect could favor the operation with dry gases or air-breathing configurations. For instance, in the start-up at sub-zero temperatures, required for automotive applications, hydrophilic treatment of flow-field plates is reported to prevent complete reactant channel blockage under sub-freezing temperatures [59].

4.3 Experimental

4.3.1 Layer preparation

Carbon black-ionomer (20 wt%) composite films were prepared from inks of carbon black (Vulcan XC-72R, Cabot), Nafion® perfluorinated ion exchange resin (5 wt% in lower aliphatic alcohols and water, Aldrich), and isopropanol (Panreac), with 1 % solid content.

The metal substrate used to deposit the layers is SS-310S, the same stainless steel used in the bipolar plates of the single cell used in the previous chapter. The substrate is a 1.5 cm diameter and 0.1 cm thick disk. Before deposition, the substrate was polished with grinding paper (Buehler Grit 180) and sonicated in ethanol-acetone (1:1) solution. Electrospray and airbrush deposits were carried out using the set-up described in Chapter 2. Electrosprayed layers were deposited by applying 7.5-8 kV, with 2.5-3.0 cm needle-to-substrate distance, and 0.20-0.40 $mL \cdot h^{-1}$ ink flow rate. During deposition, substrate temperature was kept at 50 °C, and ink temperature at 22 °C under ultrasonic stirring. As described in Chapter 2, the XY axis was also used to extend the deposited layer sufficiently beyond the substrate limits, ensuring film homogeneity by eliminating the border effects that can be important due to the small size of the samples.

4.3.2 Layer characterization

Hydrophobicity of the carbon layers was tested by means of water contact angle measurements, as explained in Chapter 2, using an optical tensiometer (Theta 200 Basic, Biolin Scientific) at ambient temperature (23 °C) and relative humidity (30−35 %). The angle measurements were taken after 400 s water drop contact. Some hydrophobicity measurements, were carried out after subjecting the films to a 'hydrophilic treatment', consisting in the immersion in H_2SO_4 0.5 M for at least 24 h, in order to stabilize their interaction with water. Before the contact angle measurements, deposits were left overnight in a stove to remove the soaked electrolyte during the process.

SEM images of the films surface were obtained with scanning electron microscope used in Chapter 2 (Hitachi FE-SEM SU-6600) using a secondary electron detector and accelerating voltage of 10 kV. Optical images of the substrate surface before and after corrosion were taken with a Leica DM4M upright light microscope. The microscope has an objective turret of 6x M32 thread with magnifications between 25x and 1000x. It uses LED ilumination and five different contrast modes: brightfield, high dynamic darkfield, differential interference contrast, fluorescence and polarization mode.

4.3.3 Electrochemical characterization

The protective character of the carbon layers on the substrate was tested using electrochemical methods. Cyclic voltammetry and chronoamperometric experiments were performed using a commercial three-electrode cell (Radiometer Analytical, Model C145/170), with the carbon coated disk as working electrode, using a sample holder that adjusts the exposed geometric area to 1 cm^2, and a platinum counter electrode. The electrolyte was H_2SO_4 0.5 M at ambient temperature (21 $^{\circ}$C), deaerated by bubbling N_2 for ½ h before measurements, and cell blanketing with the same gas during measurements.

Additionally, linear sweep voltammetry tests were performed in order to estimate the corrosion potential and the corrosion current density using the Tafel slope extrapolation method and the Stern-Geary method.

Three-electrode cell

The three-electrode cell is the most common tool in electrochemistry to investigate electrode processes out of the equilibrium. The cell setup consists in a closed vessel that contains a conductive electrolyte and generally has five connections and a double wall to allow thermostatization. As shown in the Figure 4-1, three of the connections are for the different electrodes, while the other two correspond to a gas feed and a gas outlet. In general, tests are performed in the absence of oxygen, due to its electroactive properties. To avoid the interferences of oxygen, the electrolyte is saturated with an inert gas by bubbling it into the solution before the test and blanketing is carried out during measurements by feeding the gas on top of the electrolyte to avoid convection [60].

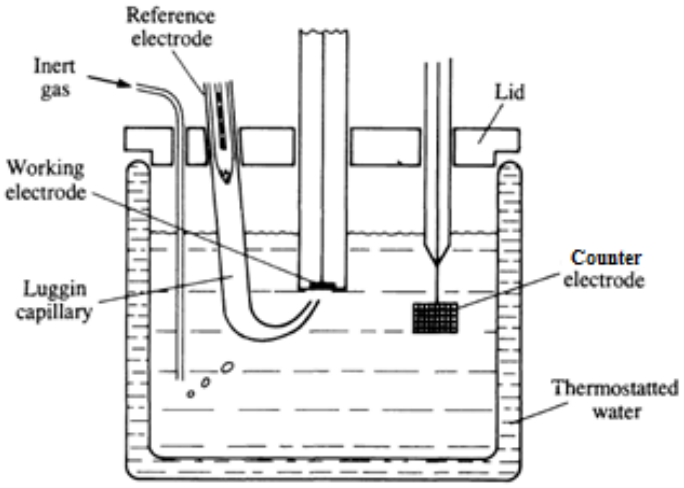

Figure 4-1: Electrochemical cell for measurements in a three-electrode cell scheme at a planar electrode. Reprinted from reference 60 with permission from Oxford University press, © 1993

The working electrode is studied by the control of the electrical perturbations (potential or current), which lead to charge transfer processes, while a counter electrode closes the circuit. A reference electrode is added to serve purely as a reference potential while all

the current passes from the working electrode to the counter electrode. The counter electrode must be inert and have larger area than the working electrode to avoid polarization.

The mercury/mercurous sulphate reference electrode was home-made and its potential was tested versus a commercial calomel electrode. The electrode consists on a single drop of mercury on a small tube covered with mercurous sulphate and in contact with sulphuric acid (or potassium sulphate) solution with a constant activity. For the experiments, 1 M concentration of H_2SO_4 was used, which gives a potential (vs SHE) of 615.15 mV at 25 °C [61]. The potential of the reference electrode was periodically checked against a commercial calomel electrode. Another important feature in this setup is the Luggin capillary, which is used to control the working electrode potential accurately by reducing the resistance, i.e. diminishing the distance as much as possible, between the working and the reference electrodes. Since no current is flowing through the reference electrode, there is no potential loss between the tip capillary tube and the electrode; the only potential loss is due to the distance between the tip of the Luggin and the surface of the working electrode [62].

Linear sweep and cyclic voltammetry

Linear sweep voltammetry (LSV) and cyclic voltammetry (CV) are potentiodynamic electrochemical techniques based on the application of a linear time-dependent potential sweep on a working electrode. Typically, the plot of the current response versus the applied potential is known as voltammogram and, by convention, the current has positive values for the oxidation processes (anodic sweep) and negative values for reduction processes (cathodic sweep) [63]. When a cyclic sweep is applied, the oxidized species in the anodic sweep can be reduced in the next cathodic sweep if they are dissolved and remain close to the electrode surface, so the species that are generated in the forward sweep can be corroborated by the reverse sweep, giving this technique a great power for the study and diagnosis of electrodic reactions.

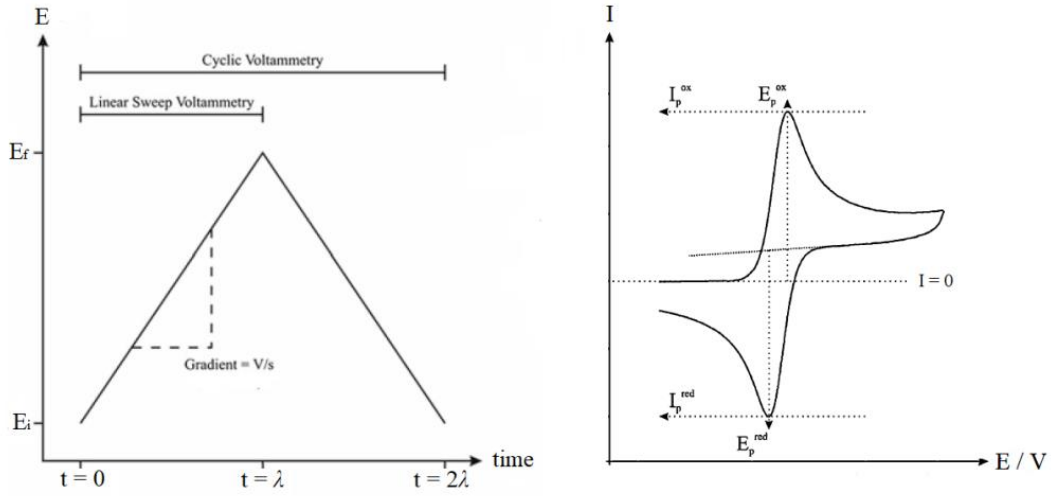

Figure 4-2: Representation of the potential signal of linear sweep and cyclic voltammetry (left) and intensity response of cyclic voltammetry for a reversible redox couple (right). Reprinted from reference 63 with permission from Springer Nature, © 2014

In a voltammogram, two different types of current are recorded: the faradaic and the capacitive current. The faradaic contribution is the current generated by the reduction or oxidation of the electrochemical species, while the capacitive one is caused by the rearrangement of the ions in the double layer and does not involve any chemical reactions. The double layer current can be used to calculate the area of the working electrodes in contact with the electrolyte, and, in order to obtain it from the voltammograms, a procedure was followed to extract it from the superposed faradaic signals, as explained in the Figure 4-3.

The double layer calculation was made following five single steps: (i) find a flat zone in the oxidation process with capacity contribution (points A and B), (ii) draw a line between points A and B, (iii) find a point C with no contribution of faradaic current, (iv) draw a parallel line crossing point C and (v) divide the current value by half to obtain the double layer current.

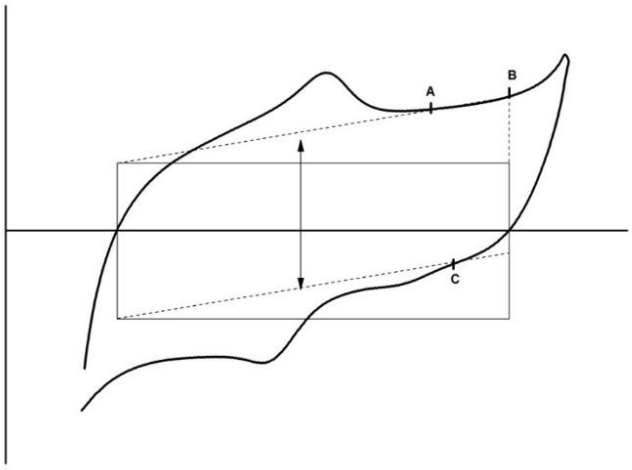

Figure 4-3: Schematic of the determination of the double layer in a tilted cyclic voltammetry with superimposed faradaic processes.

Estimation of the corrosion parameters

Since most corrosion processes consist of electrochemical reactions on the surface of a metal in contact with an aqueous electrolyte, electrochemical tests methods can provide an alternative to traditional methods used to determine the rate of corrosion, such as weight loss measurements, that require long term exposure of the samples and present several problems in the extrapolation of the results. Among them, linear sweep voltammetry allows a direct and quantitative determination of corrosion rates [64].

Electrochemical corrosion processes consist in two reactions: the oxidation of the metal and the reduction of other species donating electrons to the metal, thus corrosion rate will be determined by the equilibrium between the opposing electrochemical reactions.

An *I-V* semilogarithmic plot for an electrochemical reaction under activation control is shown in Figure 4-4, in which both processes are simplified using Tafel equation (dashed lines) as described in Equation 1.11 at Section 1.2.2. This analysis, known as Tafel slope analysis, uses the extrapolated intercept of the two linear segment of the predicted Tafel slope to estimate a value of the corrosion potential (E_{corr}) and corrosion current (I_{corr}).

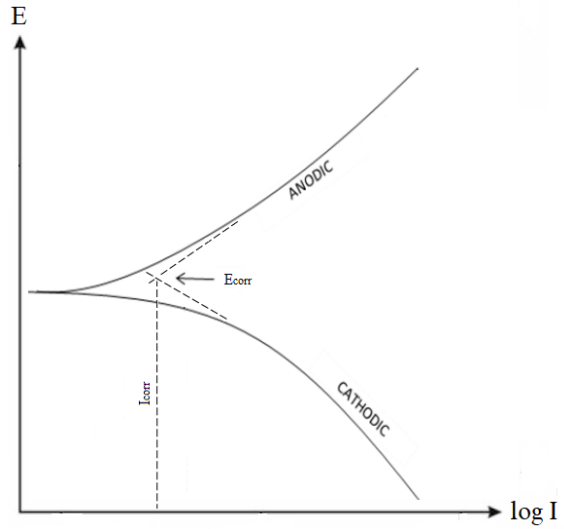

Figure 4-4: Representation of Tafel plot

Alternatively, corrosion rates can be calculated by Stern-Geary method, using the region of linear dependence of potential on applied current by treating it in a manner analogous to that for a non-corroding electrode. This approach aims to avoid the interfering reactions in the determination of Tafel slopes at higher current densities [65]. Equation 4.1 is derived by relating the slope of this linear region to the corrosion rate and Tafel slopes and assuming that the reduction and oxidation reactions are controlled and the corrosion morphology is uniform [66]:

$$I = \frac{1}{R_p} \frac{b_a|b_c|}{2.3(b_a+|b_c|)} = \frac{B}{R_p} \qquad (4.1)$$

where b_a and b_c are the Tafel coefficients of the anodic and cathodic reactions respectively and R_p is the polarization resistance, that is defined as the slope of the polarization curve at the corrosion potential:

$$R_p = \left.\frac{\Delta E}{\Delta I}\right|_{E=E_{corr}} \qquad (4.2)$$

In Figure 4-5, the dashed line represent the polarization curve of a corrosion system decomposed in the partial anodic and cathodic reactions (solid lines) starting at their respective theoretical reversible potentials (E^{rev}). Additionally, it is also depicted the calculation of the polarization resistance.

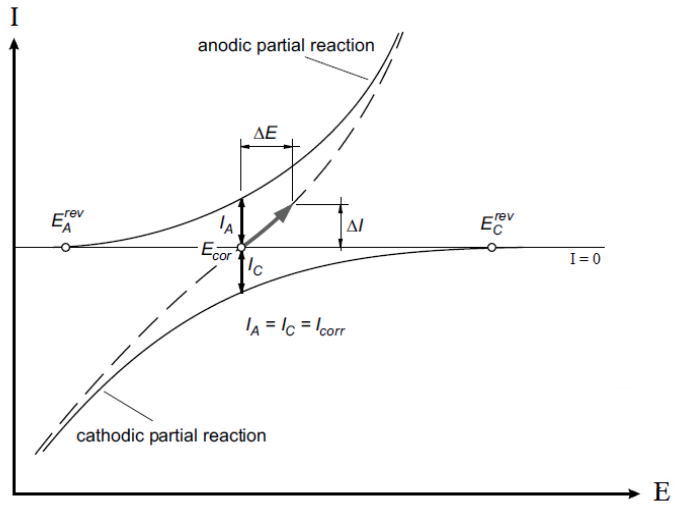

Figure 4-5 Schematic of the *E-I* relationship on a corrosion process subjected to external polarization. Reprinted from reference 66 with permission from John Wiley and Sons, © 2014

Since the value of the polarization resistance is calculated in a potential range close to the corrosion potential and the applied currents are lower than corrosion current, the nature of the surface will not be changed significantly, which is a major advantage for non-destructive calculation of the corrosion rate. However, it is important to note, that the so-called polarization resistance, even though it has resistance units, it is not an ohmic resistance in the usual sense, and the linear dependence is only true when the logarithmic functions of current are of the same order of magnitude [67].

Chronoamperometric methods

Chonoamperometry involves measuring the electrode current with time while stepping the potential of the working electrode, usually from a value at which no faradaic reaction occurs to a potential at which the surface concentration of an electroactive species is effectively zero. In this technique, the mass transport processes are only governed by

diffusion, if an unstirred cell is used, and the current versus time curve reflects the depletion of reactants in the electrode surface. The intensity response of a planar electrode will decrease as a function of square root of time, according to the Cottrell equation [68].

Chronoamperometric experiments are commonly used to measure the diffusion coefficient or the electrode surface area. However, in this thesis, it was used to measure the resistance to corrosion of steel with protective coatings. The application of an active anodic potential is a common technique to test the corrosion of stainless steel in different media [69] and also to study the corrosion protection of stainless steel coatings [70].

4.3.4 Single cell characterization of coated bipolar plate channels

For the single cell characterization experiments, the homemade test bench and protocols described in Chapter 3 were used. The test bench allows the control of the cell parameters: current, voltage, temperature, back pressure, gas reactants composition and humidification and flow rate. The polarization curves were taken at 80 °C and 100 % feed gas humidification. For H_2/O_2 measurements constant stoichiometry was kept at 1.5/3.0, while for H_2/air the stoichiometry was kept at 2.0/6.5.

The test cells were assembled using electrosprayed catalyst-coated membranes on the cathode side (Nafion 212, Chemours) depositing 0.25 $mg_{Pt}\cdot cm^{-2}$, completed with commercial gas diffusion layer (BASF ELAT GDL LT2500W). Commercial electrode (FCETC LLGDE, Pt/C 40 %, 0.3 $mg_{Pt}\cdot cm^{-2}$) was used in the anode.

The gold-coated bipolar plates (see Chapter 3) were covered with Vulcan XC72R carbon black composite layers as described in the Section 4.2.1, with an estimated loading of 1.0 $mg_{Pt}\cdot cm^{-2}$. An insulating 4.2x4.2 mask was used to limit the deposited surface of the plate and allow a better control of the coated surface. After deposition, the deposited carbon on the flat outer surface of the plate was carefully removed leaving the carbon coating on the inner walls of the flow-field channels.

4.4 Results and discussion

4.4.1 *Ex-situ* analysis of the carbon based layers

The *ex-situ* experiments were focused on the study of the required thickness of an electrosprayed layer to attain proper protection ability. Moreover, as a control experiment, airbrushed layers were studied to compare the properties of the electrosprayed layer with layers with the same chemical composition and deposited using a different method. The study comprises a morphological characterization of the coating, an analysis of its surface hydrophobicity and the electrochemical characterization of the carbon layers. The substrate corrosion and the stability of the carbon layers at ambient temperature will also be evaluated.

Morphology and surface hydrophobicity of carbon black layers

A morphological study of both electrosprayed and airbrushed layer deposited on stainless steel was conducted on samples with three different carbon loadings: 0.17 $mg \cdot cm^{-2}$, 0.4 $mg \cdot cm^{-2}$ and 0.8 $mg \cdot cm^{-2}$. The surface of the porous carbon layers applying a loading of 0.4 $mg_C \cdot cm^{-2}$ on the substrate is shown in SEM images of Figure 4-6. As previously seen in Chapter 2, electrospray deposited films (Figure 4-6a) are highly macroporous with pores of micrometric size in comparison with the airbrushed films (Figure 4-6b).

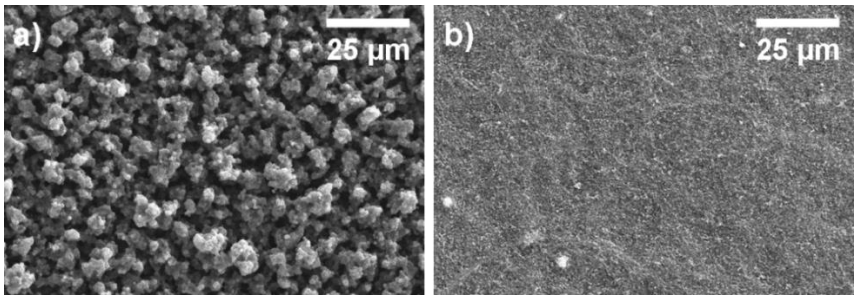

Figure 4-6: SEM images of the surface of carbon black composite layers deposited on a stainless-steel substrate by a) electrospray and b) airbrushing

In order to obtain a better approach on the morphology and film thickness, a closer view of the layers is presented in Figure 4-7. For the observation of the cross-sectional profile,

a groove was made with a sharp blade and the angle of the sample in microscope was set to 40º with respect to the perpendicular plane of the electron beam. The tilting of the stage allows having a detailed insight of the inner structure of the layers which provides information of changes in the growing mechanisms, and also an estimation of the film thickness.

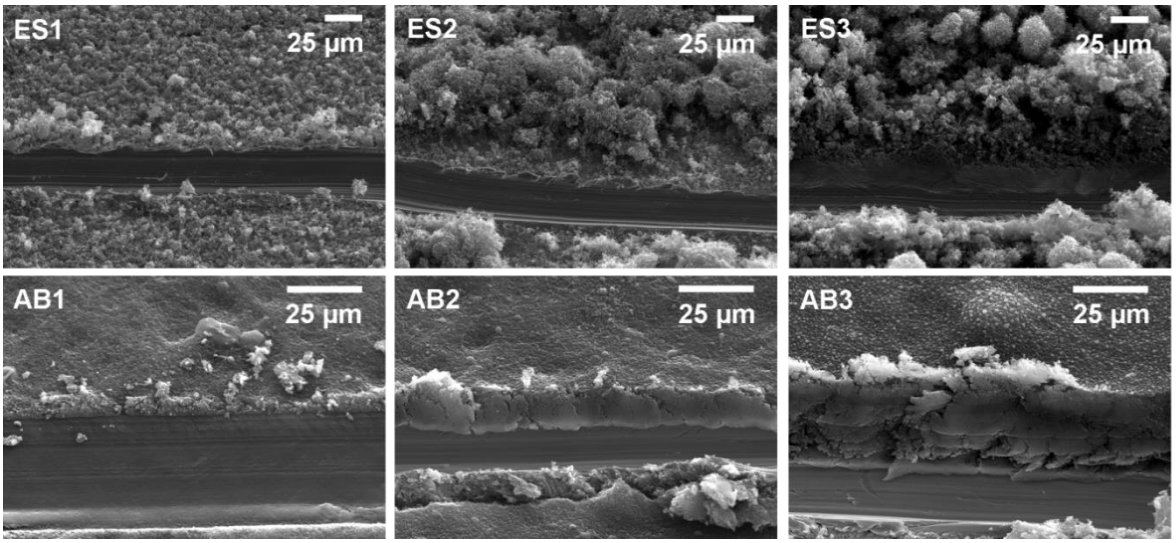

Figure 4-7: SEM images of carbon black layers deposited on stainless-steel substrate by electrospray with different carbon loads. ES stands for electrospray and AB for airbrush: 1) 0.17 mg·cm^{-2}, 2) 0.40 mg·cm^{-2}, 3) 0.8 mg·cm^{-2}

The groove on the films reveals changes in the morphology of the electrosprayed film. At the lowest carbon loading, 0.17 mg·cm^{-2} (Figure 4-7-ES1), the first stage of layer growth presents a characteristic morphology with small agglomerates (below 10µm) together with submicrometer dendritic formations. As the carbon load increases, the growth of larger globular agglomerates (>20-30 µm) can be observed on top of the previous ones (Figure 4-7-ES2 and ES3). The structure of the film resembles the surface structure made of islands separated by deep crevices, as predicted by numerical calculations [71]. The evolution of the morphology and the growing size of agglomerates might be caused by a change in the conditions for the electrospray film growth process. Initial growth stages are probably mostly controlled by the electric field between the needle and the substrate and, thus, inducing the transport of the particles over the film surface by electrostatic

forces. However, as the film thickness is increased, the evolution to more globular structures points to a change of particle-particle interactions predominance over the electrostatic forces. This effect might be caused by the electric-field-induced diffusion-limited aggregation due to the relaxation of electrostatic forces by the dielectric properties of the growing film [72].

On the other hand, airbrushed films (Figure 4-7-AB1, AB2 and AB3) show a great reduction of the porosity, homogenous growth with increasing carbon loading, and no appreciable morphological changes with the increasing film thickness.

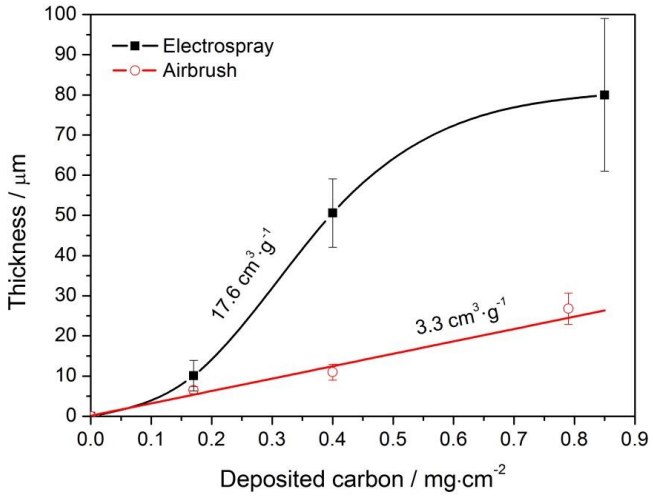

Figure 4-8: Thickness of electrosprayed and airbrushed carbon films as a function of the carbon load

The film thickness is estimated from the previous SEM images and plotted in Figure 4-8 as a function of the carbon load of the coating. Electrosprayed layers appear to present three distinct growth regimes, showing an initial low rate below 0.2 $mg_C \cdot cm^{-2}$, followed by a period of faster growth rate and volume of 17.6 $cm^3 \cdot g^{-1}$ in the 0.2-0.6 $mg_C \cdot cm^{-2}$ region. The last region, corresponding to values over 0.6 $mg \cdot cm^{-2}$ of carbon loading, corresponds to the morphology change from dendritic to globular shape observed with SEM images. On the contrary, the airbrushed film thickness creates more compact deposits that have a clear linear dependence with carbon concentration in the studied range. For instance, the specific volume determined for the airbrushed layers (3.3 $cm^3 \cdot g^{-}$

[1]), reflect a density of 0.30 g·cm^{-3} that is only slightly superior to the nominal density of Vulcan XC72R (0.264 g·cm^{-3}).

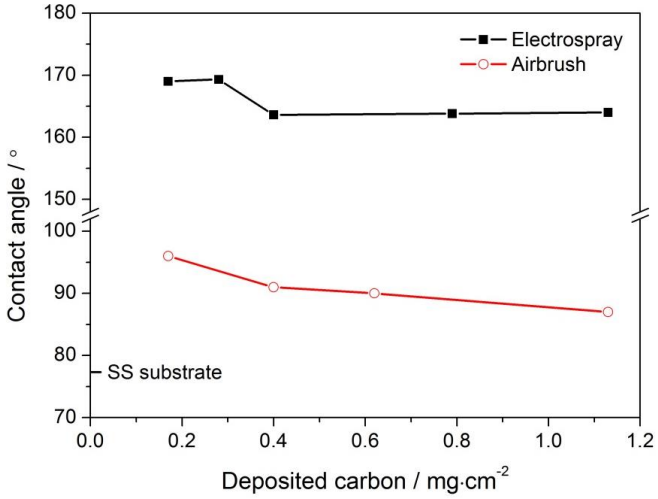

Figure 4-9: Water contact angles on carbon films deposited on a stainless steel plate obtained after hydrophilic stabilization, as a function of the carbon load in the coating

The measurements of surface hydrophobicity were carried out on freshly prepared films, before and after immersion in H_2SO_4 0.5 M for 24 h in order to analyze the stability of their surface after interaction with an aqueous medium. Results shown in Figure 4-9 correspond to the films submitted to the hydrophilic process by immersion in the acidic media. As it was shown in Chapter 2, the hydrophilic treatment of airbrushed films causes the water contact angle to fall from values over around 150^o to values under 100^o after its immersion; in contrast, no significant change was observed for electrosprayed films. Superhydrophobicity of the electrosprayed layers is also reflected by permanent air cushion on top of the deposit, allowing minimal contact of the electrolyte with the surface of the carbon composite layer. This effect was also observed in other types of superhydrophobic surfaces [73, 74]. Figure 4-9 reflects the impact of the change in the morphology of the layer, from dendritic to globular on the hydrophobicity of electrosprayed films. The initial dendritic morphology is characterized by the highest

superhydrophobicity (Θ > 168º), whereas the globular morphology gives rise to some decrease (Θ = 163º).

Electrochemical characterization and bulk film hydrophobicity

The electrochemical characterization of the carbon layers were conducted by means of a cyclic voltammetry analysis between 0.1 and 1.35 V in a deaerated aqueous electrolyte with 0.5 M H_2SO_4. Figure 4-10 shows the voltammetric response of electrosprayed (Figure 4-10a and Figure 4-10b) and airbrushed (Figure 4-10c) coatings with different carbon loads.

The voltammetries present some remarkable features, such as curve tilting and small peaks in the limits of the selected potential window and, in some cases, a reversible signal at 0.55-0.70 V region. Although the ideal capacitance of an electrode material should have a rectangular shape, the voltammetric response of the studied carbon layers resembles previous studies of carbon material voltammetries. The curve tilting and the current increase near the potential limits are attributed to pseudocapacitance properties, as reported in carbon materials studied as electrochemical capacitors [75, 76]. At first glance, airbrushed layers have one order of magnitude above the electrosprayed layers, due to the extreme differences on their wetting properties. This can be directly related to the area of carbon in direct contact with the electrolyte.

Even though, the largest proportion of the current in Figure 4-10 is produced by the double layer charging of the carbon film, two types of faradaic contributions can be observed. The first consist in a reversible signal at 0.55-0.70 V that can be ascribed to reactivity of the metallic substrate corrosion products confined in the carbon layer. The assignation of this faradaic signal was confirmed by voltammetries performed on carbon coatings deposited on a non-corroding carbon substrate.

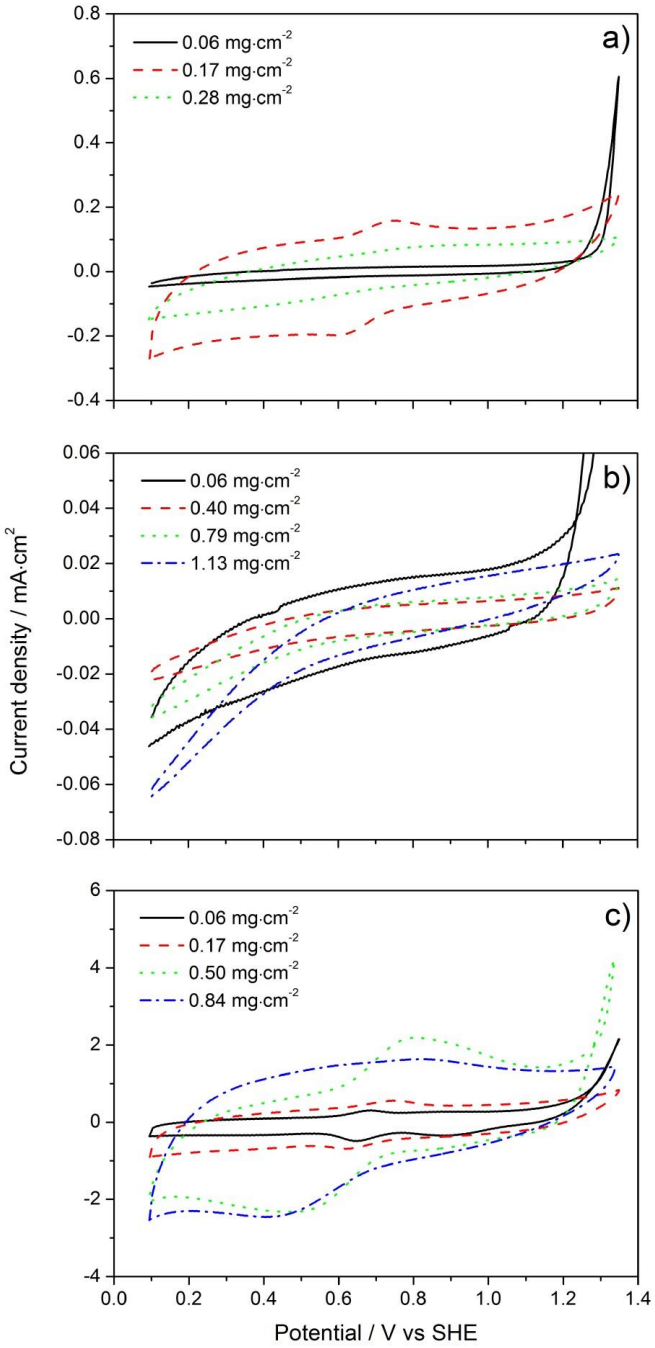

Figure 4-10: Voltammetries of carbon black on stainless steel substrate deposited by electrospray at two different resolutions (a and b) and airbrush (c) at 0.1 $V \cdot s^{-1}$ sweep rate, in H_2SO_4 0.5 M deaerated solution, at room temperature (23 ºC)

In Figure 4-11, a graphite disk was used to deposit a regular carbon-Nafion film and carbon-Nafion film contaminated with Fe^{3+} ions. The impurity source was iron (III) nitrate nonahydrate added to the Nafion solution before the ink preparation. The reversible process appears in artificially contaminated Nafion without the presence of the ion source in the substrate. The growth of the double layer current compared to the non-contaminated layer is caused by the hydrophilic nature of the contaminated layer.

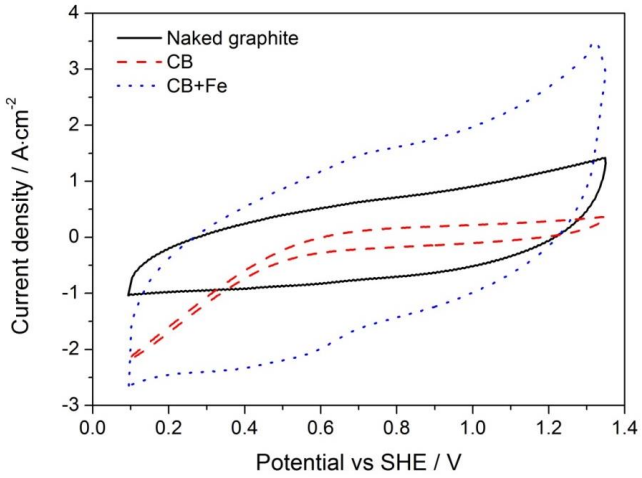

Figure 4-11: Cyclic voltammetries of a graphite substrate and 0.4 mg·cm^{-2} electrosprayed layer with and without Fe ions entrapped in Nafion. CVs were taken at 0.1 V·s^{-1} in 0.5 M H_2SO_4

The second faradaic contribution in the voltammograms is detected in substrates with thinner layers, which experience a steep increase in current above 1.2 V. This effect is caused by an insufficient coverage of the substrate at potentials above the transpassivation point of the stainless steel. This is confirmed by the voltammetry of naked stainless steel in Figure 4-12. In this figure, the stabilized cyclic voltammetry of a bare SS 310S substrate is presented with that of the same substrate with a Nafion 117 membrane on top of it. This effect is an additional proof that Nafion allows the transport of metallic ions from the substrate to the electrolyte solution. A slight decrease of the oxidative current at high potentials is observed together with a slight increase of reduction current, probably due to the Nafion membrane as diffusion hindrance to the corrosion products. It is also important to note that the faradaic signal at 0.55-0.70 V is

absent in naked stainless steel substrates, where corrosion products may diffuse freely to the electrolyte.

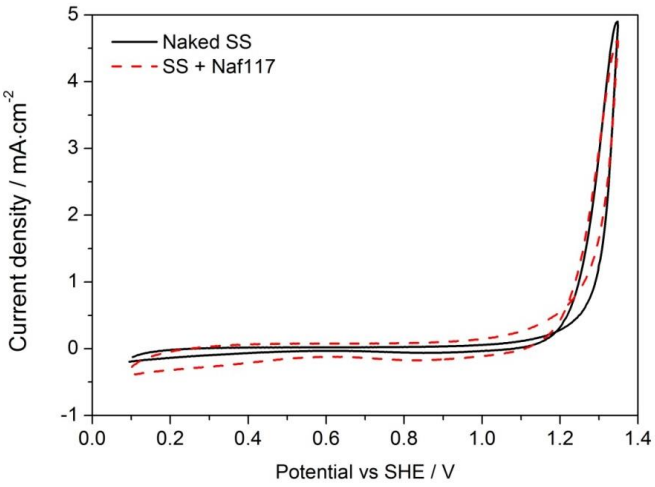

Figure 4-12: Cyclic voltammetries of a graphite substrate and 0.4 mg·cm^{-2} electrosprayed layer with and without Fe ions entrapped in Nafion. CVs were taken at 0.1 V·s^{-1} in 0.5 M H_2SO_4

Since the ferric cations produced at the transpassivation potential, can travel through a dense Nafion membrane and will give a reversible electrochemical response between 0.55-0.70 V when entrapped in the Nafion ionomer, we can conclude that the appearance of the reversible signal is an indication of substrate corrosion. Going back to the voltammetries recorded in Figure 4-10, the oxidation current at transpassivation potentials is attenuated as the thickness of the layers increase for both types of layers, while the reversible signal ascribed to ferric ions is present in all the airbrushed layer voltammetries, while in the electrosprayed layers, it decreases and disappears at loadings above 0.4 $mg_C \cdot cm^{-2}$. This can be the first indication of substrate protection of the electrosprayed layers. All the voltammetries shown in the images are recorded after the current response is stabilized. It is important to note that the 0.55-0.70 V signal is always absent during the first voltammetric cycle, and immediately starts growing on successive cycles up to a steady-state value.

The double layer charging current (j_{DL}) can be used to analyze the area of carbon in contact with the electrolyte, i.e. electrochemical area of the porous carbon, according to:

$$j_{DL} = C_{DL} \cdot v \cdot w_c \cdot A_c \cdot S \quad (4.3)$$

where C_{DL} ($F \cdot m_C^{-2}$) is the specific capacitance, v ($V \cdot s^{-1}$) the voltammetry sweep rate, w_C ($g_C \cdot cm^{-2}$) the carbon load, A_C ($cm^2 \cdot g_C^{-1}$) the mass specific area of carbon, and S corresponds to the fraction of carbon surface in contact with water (S=0 correspond to a completely dry layer while S=1 corresponds to a flooded layer).

The obtained voltammetries with different carbon loads reflect an important dependence on the double layer current. The double layer current density (j_{DL}), calculated as described in the experimental section, and the mass specific current (j_{DL}/w_C) versus the carbon load (w_C) for electrosprayed and airbrushed carbon films are depicted in Figure 4-13.

The evolution of j_{DL} in Figure 4-13a is governed by the wetting properties of the porous carbon layers. The electrosprayed films show low double layer current densities because of the reduced number of contact points between the carbon surface and the electrolyte due to the superhydrophobicity of the layers; in contrast, airbrushed films show much larger current densities reflecting their low hydrophobicity. For the airbrushed films the values before and after hydrophilic treatment are plotted in the same figure. Showing both values is especially relevant, because even though the surface is wet shortly after the immersion in the electrolyte and the hydrophobicity of the layers as prepared is lost, the electrolyte appears to take more time to penetrate into the layer to reach the substrate. On the other hand, for the electrosprayed layers, the hydrophilic treatment has no noticeable effect and the wetting is not enhanced over time in contact with the electrolyte.

The behavior of the double layer current of electrosprayed films shows an unexpected penetration of the electrolyte into the porous electrosprayed film between 0.1-0.2 $mg_C \cdot cm^{-2}$, despite of the superhydrophobicity of the layer. The relative high current

densities at low carbon weights are followed by a reduction of the double layer current to quasi-constant value upon increasing carbon load. Some small increase of the double layer current is also observed for high loading coatings, and is probably caused by the enhancement of the surface contact area as a consequence of the morphological change to larger globular agglomerates. However, this effect is not present when the double layer current is normalized by the amount of carbon in the layer.

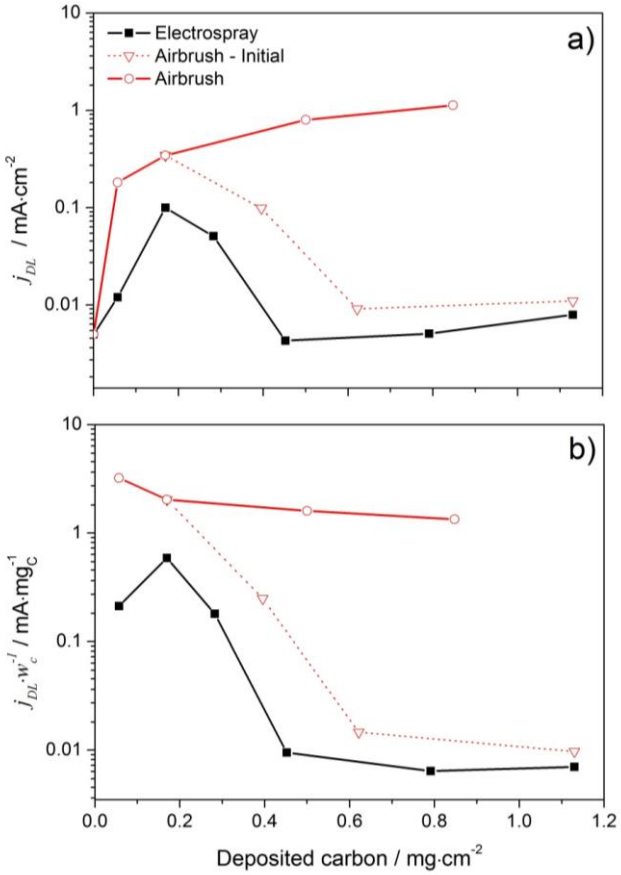

Figure 4-13: Double layer a) charging current density (j_{DL}) and b) mass specific charging current density ($j_{DL}\cdot w_C^{-1}$), for electrosprayed and airbrushed carbon black coatings on stainless steel, as a function of the carbon load (before (dotted) and after (solid) hydrophilic treatment)

For the airbrushed films, the double layer current density always increases with carbon load, and neither the current density nor mass specific current shows a local maximum as in the electrosprayed films. It is important to highlight the slow wetting kinetics of the

airbrushed layers to avoid a wrong assessment of its behavior in contact with an aqueous electrolyte: if not enough time is given for complete wetting, one could mistakenly consider that the airbrushed layers have the same behavior of the electrosprayed layers with more carbon surface in contact with the electrolyte due to its hydrophilicity. In Figure 4-13b, there is a slight reduction of the specific current density for high loading airbrushed layers. This effect is attributed to the presence of a continuous gradient of electrolyte into the film resulting from a stochastic mixture of air-filled and liquid-filled pores for films with contact angles around 100° [49].

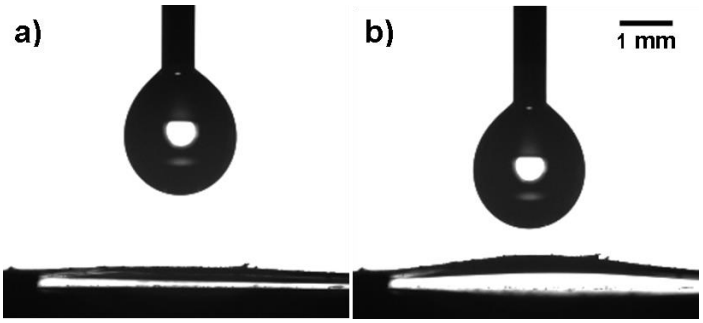

Figure 4-14: Images of carbon layer (0.2 mg·cm^{-2}) on top of a Nafion 212 membrane with a water drop in its surroundings. The images shows: a) the initial state and b) the membrane deformation after 60s

The peaks in j_{DL} and j_{DL}/w_C in electrosprayed films reflects increasing carbon-water contact at low carbon loadings which is suppressed above 0.2 mg·cm^{-2}, that can be explained by a distant interaction of the liquid water from the electrolyte meniscus with the hydrophilic substrate through the macropores of the carbon coating. Distant water interaction is reported to be caused by the vapor atmosphere gradients emitted by liquid surfaces, affecting water drops separated even by a few millimeters [77]. This same effect was believed to be occurring in the water contact angle measurements of thin hydrophobic Pt/CB electrosprayed layer deposited on top of a hydrophilic Nafion membrane [78]. This effect caused a noticeable deformation of the membrane when water drops are placed on top of it; however, this effect could not be explained in that work.

Based on the previous observation on the Nafion membrane, Figure 4-14 shows the distant interaction effect of a water drop above a carbon/Nafion layer deposited on top of a Nafion 212R membrane, where the membrane deformation can be observed while the surface deposit maintains its superhydrophobicity. The interaction between the water drop and the Nafion membrane is quite fast and is noticeable after a couple of seconds. This interaction is suppressed as the films thickness is increased, therefore, we conclude that the superhydrophobicity of the surface of electrosprayed carbon films in combination with the distant interaction of water in thin layers explain the drop on the specific double layer current observed in Figure 4-13.

Characterization of substrate corrosion at ambient temperature

Considering that the disappearance of the reversible signal in Figure 4-10 is an indication of substrate corrosion protection by the porous films, it can be assumed that full protective behavior of carbon coatings is attained for electrosprayed layers at loads above 0.4 $mg_C \cdot cm^{-2}$ (Figure 4-13a). This assertion will be further proven with chronoamperometric and linear sweep voltammetric analysis, together with post-mortem analysis of the layers by XPS and the substrates with optical microscopy.

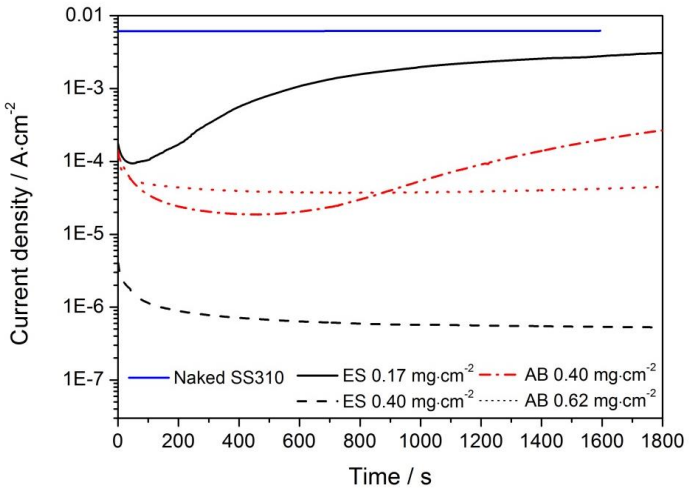

Figure 4-15: Chronoamperograms (1.35 V vs. SHE) of electrosprayed and airbrushed carbon black layers at different carbon loads. ES stands for electrospray and AB for airbrush

Figure 4-15 shows the chronoamperograms of the naked and the coated substrates recorded at 1.35 V versus SHE. In order to avoid the effect of the inherent passive layer in the stainless steel surface, experiments are conducted above the transpassivation potential to promote metal dissolution into the electrolyte. Even though this potential is well above fuel cell working potentials, previous studies have shown that transient local potentials can increase up to 1.4 V during start-up/shut-down events in PEMFC anodes [79] and has been also reported to be appropriate to mimic anode degradation in an accelerated fuel cell test [70].

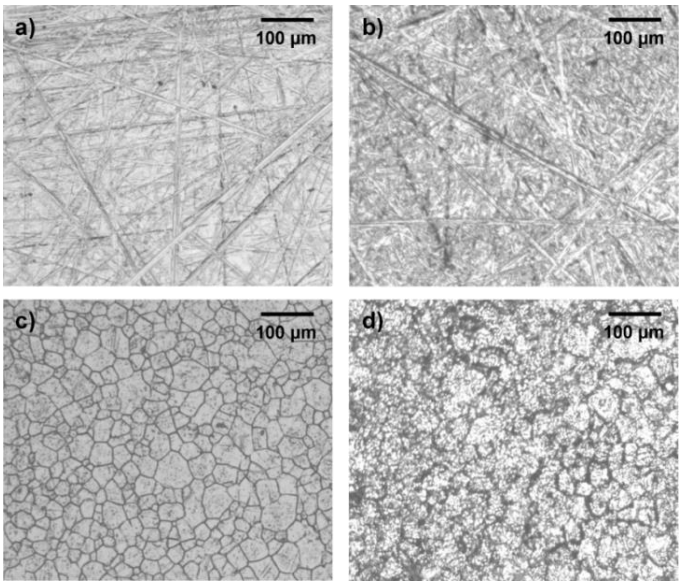

Figure 4-16: Micrographs of the surface of the stainless-steel substrate as prepared for electrochemical tests (a); after chronoamperometric measurements coated with an electrosprayed layer with 0.4 mg·cm^{-2} of carbon black (b), airbrushed layer with 0.4 mg·cm^{-2} of CB (c) and uncoated stainless steel substrate (d)

Non-coated stainless steel shows a severe corrosion process, with values of current densities of several miliamperes per square centimeter and rising current densities upon polarization, which is indicative for the increasing area by roughening of a corroding substrate. As observed for the naked stainless steel, the airbrushed films and the electrospray film below 0.17 mg·cm^{-2} also present the same behavior of rising current densities with a slightly reduced current density due to the partial protection of the layers. Full protection is acquired with electrosprayed layers above 0.40 mg·cm^{-2}; their behavior

upon polarization is characterized by a constant decay to current values below microamperes. The protective behavior of the carbon coatings is further confirmed by observing the stainless steel substrates after removing the 0.40 mg·cm^{-2} coatings (Figure 4-16) using optical micrographs. The electrosprayed coated substrate leaves unmodified the substrate surface, in which only the scratches produced by the grinding paper are visible, whereas the airbrushed layer shows new surface cracks and intense pitting that reflect the strong corrosion of the surface, in the same way as the naked substrate.

Further analysis of corrosion kinetics is carried out from potentiodynamic experiments. Tafel plots obtained for the bare substrate and for airbrushed and electrosprayed coatings with a carbon loading of 0.4 mg·cm^{-2} immediately after chronoamperometric experiments are presented in Figure 4-17. Lower current densities and more positive corrosion potential are qualitative indicators of an incensement on the protective character of a surface. This trend is clear when comparing the electrosprayed layer with the airbrushed layer and the naked substrate. Table 1 presents the values of anodic (b_a) and cathodic (b_c) Tafel slopes, corrosion potential (E_{corr}) and corrosion current density (j_{corr}) extracted from Figure 4-17. Corrosion current density is also calculated with the Stern-Geary relationship using the polarization resistance (R_p).

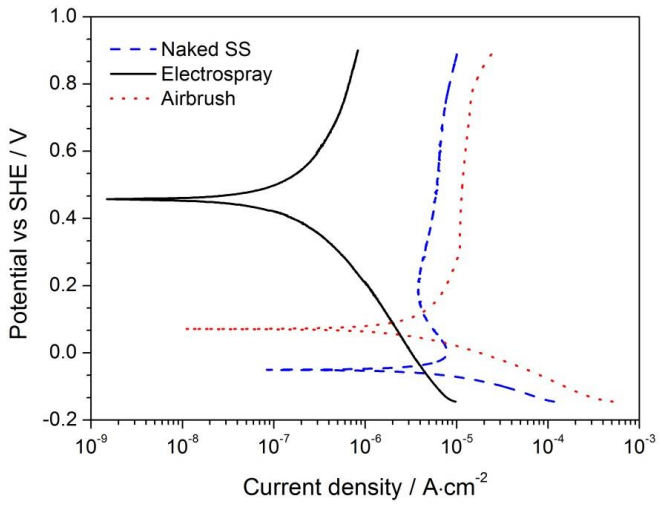

Figure 4-17: Tafel plots for uncovered stainless steel and airbrushed and electrosprayed coated substrates with 0.4 mg·cm^{-2} carbon loading in 0.5 M H_2SO_4 at 0.001 V·s^{-1}

The values in Table 4-1 show an increase of the corrosion potential by 0.4 V and a decrease of two orders of magnitude of the corrosion current in electrosprayed coated stainless steel compared to the bare substrate. As a reference for fuel cell application of these layers, the U.S. DOE recommends a bipolar plate corrosion current (both anodic and cathodic) below 1 $\mu A \cdot cm^{-2}$ for PEM bipolar plates in its technical targets for 2020 [80], which is sufficiently accomplished with the electrosprayed film at ambient temperature conditions.

Table 4-1. Values of Tafel constants, corrosion potential, corrosion current density and polarization resistance for bare and airbrushed and electrospray coated stainless steel in 0.5 M H_2SO_4

	E_{corr} mV vs SHE	**b_a mV·dec^{-1}**	**b_c mV·dec^{-1}**	**j_{corr} (Tafel) µA·cm^{-2}**	**R_p kΩ·cm^2**	**j_{corr} (Stern) µA·cm^{-2}**
SS 310S	- 44	80	426	6.5	2.8	24.0
Airbrush	60	85	423	3.7	8.4	8.3
Electrospray	460	300	428	0.1	326.7	0.5

Stability of the carbon layers

After the tests at constant potential in Figure 4-15, an XPS analysis of the layers was conducted to check for chemical degradation. The results in Figure 4-18, show the XPS signals of the *O1s* region for both airbrushed and electrosprayed layers with 0.4 $mg \cdot cm^{-2}$ before and after the corrosion tests. For a detailed explanation of the XPS experiments, check Chapter 2.

The electrosprayed layer showed no appreciable changes after the chronoamperometric tests, whereas the airbrushed presented an enormous change in the XPS profile with regard to its initial state. As stated in a previous chapter, the signals at a binding energy ca. 530.7 eV are assigned to ether bonds (C=O) and the signals at ca. 534.4 eV to sulfonic groups ($-SO_3$). For the airbrushed sample, the signal assigned to ether groups increases after chronoamperometric measurements and the signal due to sulfonic groups becomes predominant. On the other hand, only slight changes can be observed for the

electrosprayed sample. The ratio of the areas of XPS signals due to ether groups and sulfonic groups at the *O1s* region are included in Table 4-2.

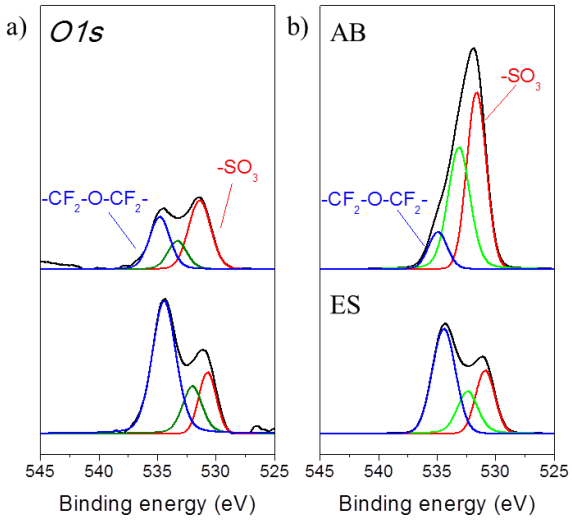

Figure 4-18: XPS signals of the *O1s* region for the airbrushed and electrosprayed stainless steel plates a) before and b) after the corrosion test

Table 4-2. Ratio of the areas of XPS signals for ether and sulfonic groups measured before and after the corrosion tests

Sample	**XPS *O1s* ($A_{ether}/A_{sulfonic}$)**	
	After deposition	**After corrosion test**
Electrospray	3.2	2.0
Airbrush	0.73	0.22

In order to further prove the protection ability of the electrosprayed layers, long-term experiments consisting in continuous cycling between 0.4 and 1.35 V at 0.1 $V \cdot s^{-1}$, with a control test once a day, with cyclic voltammetry between 0.1 and 1.35 V at 0.1 $V \cdot s^{-1}$ together with chronoamperomertry for 1h at 1.35 V were carried out. Figure 4-19 depicts control voltammetries of the electrosprayed layer, with initial response upon immersion and the stabilized response after it was cycled overnight. Once the layer had stabilized its contact points with the electrolyte, electrosprayed samples presented no significant changes in the chronoamperometric response even after a week in corrosive media with

periodic polarization experiments. The only change after a week of continuous cycling can be seen in voltammetric response. A slight growth of the reversible signal at 0.55-0.70 V can be appreciated in the voltammogram indicating entrapped ferric ions. However, this faradaic signal value is below 1 $\mu A \cdot cm^{-2}$ and thus shows the excellent protection ability of the electrosprayed layer even after long periods of continuous cycling at potentials over the transpassivation point of the stainless steel.

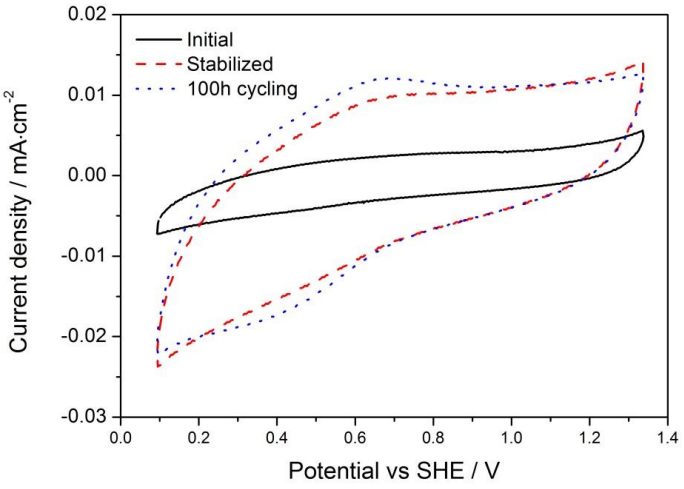

Figure 4-19: Voltammetries of the evolution with time of an electrosprayed substrate with 0.4 $mg \cdot cm^{-2}$ carbon loading in 0.5 M H_2SO_4 at 0.1 $V \cdot s^{-1}$

Airbrushed layers, in contrast, could not overcome the testing procedure for more than one or two days, depending on the sample. Figure 4-20 shows the evolution of an airbrushed layer, from initial values with low capacitive currents after immersion to a full wetting state within a day. However, further chonoamperometric experiments showed zones of preferential corrosion and cracks within the layer, allowing free access for the electrolyte to the surface of the substrate, as shown in the blue voltammogram in the figure. Eventually due to the cracks on the surface, the layer fails and is peeled off from the steel surface.

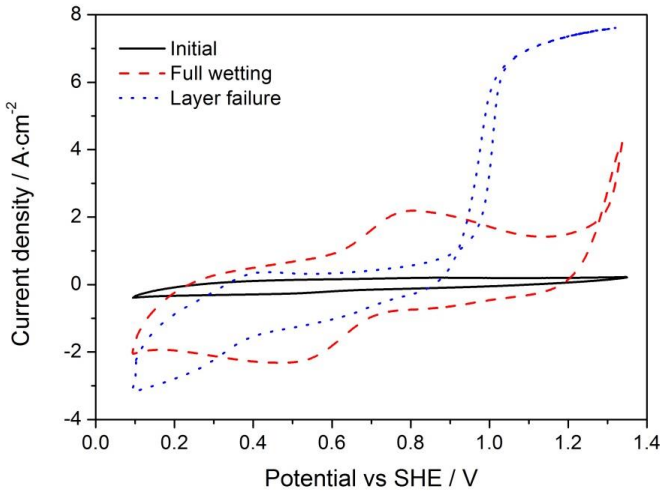

Figure 4-20: Voltammetries of the evolution with time of an airbrushed substrate with 0.4 mg·cm^{-2} carbon loading in 0.5 M H_2SO_4 at 0.1 V·s^{-1}

4.4.2 Hydrophobization of PEM fuel cell bipolar plate channels: Preliminary results

Superhydrophobic carbon black-based layers not only protect the flow-field plates against corrosion, but they may also improve the transport of liquid water through the channels, which becomes a limitation for fuel cell performance at high current densities. In order to test this second property, carbon black was electrosprayed in the gas channels of a stainless steel cathodic bipolar plate to evaluate the impact of a superhydrophobic surface in an operating fuel cell. The carbon black layers were fabricated with the electrospray deposition technique in the same way as the planar substrates in the previous section. In this study, only cathodic gas channels were coated to evaluate water rejection. To our knowledge, this is the first application of a superhydrophobic coating on PEM fuel channels. So far, only hydrophobic (below 150°) surfaces were studied as coatings for fuel cell components.

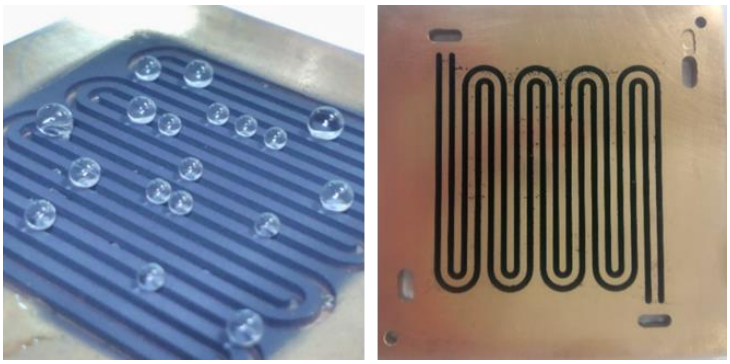

Figure 4-21: Gold-coated bipolar plate with carbon black-based layers before (left) and after (right) cleaning the channels lands

This preliminary study only includes the cell characterization with coated channels in the cathodic bipolar plate, since most of the water produced in the electrochemical reaction is evacuated through the cathodic gas exhaust. Figure 4-21 shows the bipolar plate with the complete GDL-plate contact area covered with the carbon composite layer and the same plate after cleaning the channel lands, with the superhydrophobized channels remaining. Channel lands were not hydrophobized to maintain the same electrical contact interfaces used in a regular single cell characterization analysis and to avoid interferences in the GDL-land interface.

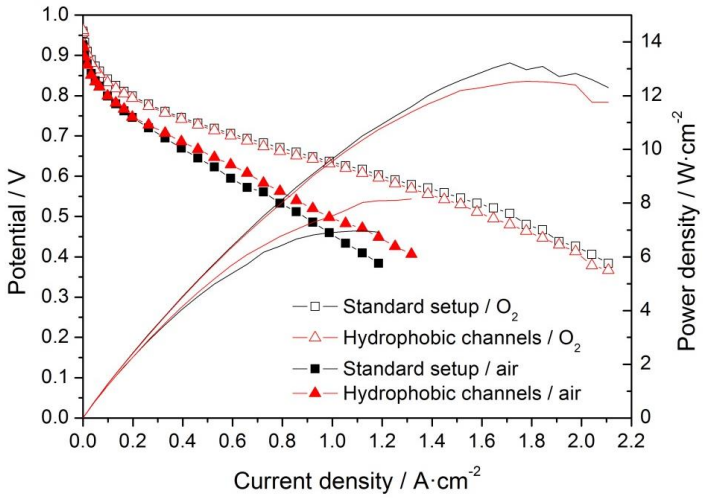

Figure 4-22: Polarization curves (80 °C, 100 %RH) obtained with uncovered (squares) and with hydrophobized cathodic flow-field channels (triangles) for H_2/O_2 (hollow) and H_2/air (solid symbols)

Water saturated gases were used in both anode and cathode performing characterization experiments with H_2/O_2 and H_2/air as feed gases. The use of air in the cathode causes an increase in the total amount of water inside the cell for a given stoichiometry due to the increase in water dragged from the humidifiers by a larger inlet gas flow rate ($N_2 + O_2$), difficulting water management as compared to pure oxygen experiments. The results obtained in single cell experiments under standard testing conditions show that the hydrophobization does not affect the performance of the cell when pure oxygen is fed to the cathode. However, when feeding air, the presence of a hydrophobic layer on the channel walls causes a performance increase up to a 20 % as the demand increases. This effect could be caused by a higher water elimination rate and the water repulsion of the hydrophobized channel walls. To gain more insight into water transport phenomena, impedance spectroscopy analyses were carried out.

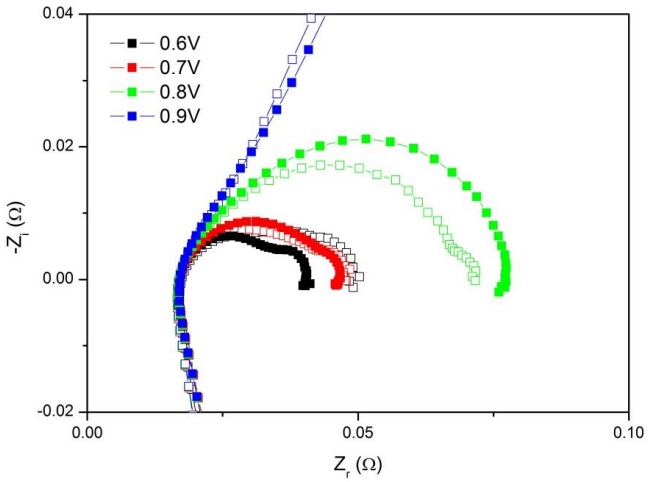

Figure 4-23: Nyquist plots (80 °C, 100 %RH) obtained for the regular bipolar plate (hollow) and with hydrophobized cathodic flow-field channels (solid symbols) with H_2/air feed gases

The Nyquist plots obtained at different operating voltages with saturated H_2/air feed gases are presented in Figure 4-23. The diminution of the low frequency intercept at low cell voltages (i.e. high current densities) confirms the reduction of cell performance losses at higher current demands observed in the polarization curves in these particular experimental conditions.

Despite the promising preliminary results, more insightful understanding of the effect of the hydrophobization of the gas channels and a wider range of experimental conditions remains to be studied to confirm the suitability of these layers for the gas flow channels. Since hydrophobization of channel walls is reported to increase the water in GDL-channel interface [56], the effect of the channel superhydrophobic walls could also make a huge impact on cell operation with dry gases or in air-breathing conditions, improving the water immobilization effect and improving membrane hydration.

4.5 Conclusions

Carbon black composite layers deposited by electrospray are characterized by macroporous morphology and superhydrophobicity, in comparison with standard spray methods. Electrosprayed layer growth is characterized by a characteristic dendritic shape evolving to a globular growth as the thickness of the coating layer is increased. Analyzing double layer current dependence of electrosprayed deposits revealed an interesting feature that allow electrolyte penetration in the superhydrophobic film below a certain thickness. This effect was attributed to the distant interaction of water vapor with the hydrophilic substrate and sets the boundary between protective and non-protective layers versus corrosive liquid electrolytes. In this study, complete and stable protective behavior of electrosprayed carbon layers for coatings above 0.4 $mg_C \cdot cm^{-2}$ has been demonstrated. Hydrophilic layers of identical composition prepared by airbrushing deposition are not able to protect the substrate regardless of their thickness. Corrosion experiments in aqueous acid media show that the electrospray deposited carbon black composite is appropriate for protecting the surface of metal substrates at ambient temperature. Moreover, its ability for expelling produced water in the cathodic gas channel is evaluated, showing promising results with humidified H_2/air as feed gases. To sum up, the results suggest that electrosprayed carbon layers could be good candidates as coatings for metallic flow-field plates and contacts used in low temperature fuel cells due to their inner superhydrophobicity, which confers a good corrosion protection and the ability to avoid water accumulation in the gas channels of the plates.

References

[1] R.A. Antunes, M.C.L. Oliveira, G. Ett, V. Ett, Corrosion of metal bipolar plates for PEM fuel cells: A review, Int. J. Hydrog. Energy. 35 (2010) 3632–3647.

[2] X. Cheng, Z. Shi, N. Glass, L. Zhang, J. Zhang, D. Song, Z.S. Liu, H. Wang, J. Shen, A review of PEM hydrogen fuel cell contamination: Impacts, mechanisms, and mitigation, J. Power Sources. 165 (2007) 739–756.

[3] T. Okada, Y. Ayato, H. Satou, M. Yuasa, I. Sekine, The effect of impurity cations on the oxygen reduction kinetics at platinum electrodes covered with perfluorinated ionomer, J. Phys. Chem. B. 105 (2001) 6980–6986.

[4] H. Wang, J.A. Turner, Reviewing metallic PEMFC bipolar plates, Fuel Cells. 10 (2010) 510–519.

[5] S. Karimi, N. Fraser, B. Roberts, F.R. Foulkes, A review of metallic bipolar plates for proton exchange membrane fuel cells: materials and fabrication methods, Adv. Mater. Sci. Eng. 2012 (2012) 1–22.

[6] I.E. Paulauskas, M.P. Brady, H.M. Meyer III, R.A. Buchanan, L.R. Walker, Corrosion behavior of CrN, Cr_2N and π phase surfaces on nitrided Ni–50Cr for proton exchange membrane fuel cell bipolar plates, Corros. Sci. 48 (2006) 3157–3171.

[7] M.P. Brady, H. Wang, B. Yang, J.A. Turner, M. Bordignon, R. Molins, L. Abd Elhamid, L. Lipp, L.R. Walker, Growth of Cr-Nitrides on commercial Ni-Cr and Fe-Cr base alloys to protect PEMFC bipolar plates, Int. J. Hydrog. Energy. 32 (2007) 3778–3788.

[8] M. Zhang, G. Lin, B. Wu, Z. Shao, Composition optimization of arc ion plated CrN_x films on 316L stainless steel as bipolar plates for polymer electrolyte membrane fuel cells, J. Power Sources. 206 (2012) 318–323.

[9] N.D. Nam, J.G. Kim, W.S. Hwang, Effect of bias voltage on the electrochemical properties of TiN coating for polymer electrolyte membrane fuel cell, Thin Solid Films. 517 (2009) 4772–4776.

[10] C. Choe, H. Choi, W. Hong, J.J. Lee, Tantalum nitride coated AISI 316L as bipolar plate for polymer electrolyte membrane fuel cell, Int. J. Hydrog. Energy. 37 (2012) 409–411.

[11] C. Turan, O.M. Cora, K. Muammer, Investigation of the effects of process sequence on the contact resistance characteristics of coated metallic bipolar plates for polymer electrolyte membrane fuel cells, J. Power Sources. 243 (2013) 925–934.

[12] K. Feng, T. Hu, X. Cai, Z. Li, P.K. Chu, Ex situ and in situ evaluation of carbon ion-implanted stainless steel bipolar plates in polymer electrolyte membrane fuel cells, J. Power Sources. 199 (2012) 207–213.

[13] V.V. Nikam, R.G. Reddy, S.R. Collins, P.C. Willians, G.H. Schiroky, G.W. Henrich, Corrosion resistant low temperature carburized SS 316 as bipolar plate material for PEMFC application, Electrochimica Acta. 53 (2008) 2743–2750.

[14] Y.J. Ren, C.L. Zeng, Corrosion protection of 304 stainless steel bipolar plates using TiC films produced by high-energy micro-arc alloying process, J. Power Sources. 171 (2007) 778–782.

[15] L. Wang, J. Sun, B. Kang, S. Li, S. Ji, Z. Wen, X. Wang, Electrochemical behaviour and surface conductivity of niobium carbide-modified austenitic stainless steel bipolar plate, J. Power Sources. 246 (2014) 775–782.

[16] P.L. Hentall, J.B. Lakeman, G.O. Mepsted, P.L. Adcock, J.M. Moore, New materials for polymer electrolyte membrane fuel cell current collectors, J. Power Sources. 80 (1999) 235–241.

[17] S.H. Wang, J. Peng, W.B. Lui, J.S. Zhang, Performance of the gold-plated titanium bipolar plates for the light weight PEM fuel cells, J. Power Sources. 162 (2006) 486–491.

[18] Y.H. Yun, Deposition of gold–titanium and gold–nickel coatings on electropolished 316L stainless steel bipolar plates for proton exchange membrane fuel cells, Int. J. Hydrog. Energy. 35 (2010) 1713–1718.

[19] J. Wind, R. Späh, W. Kaiser, G. Böhm, Metallic bipolar plates for PEM fuel cells, J. Power Sources. 105 (2002) 256–260.

[20] Y.J. Ran, M.R. Anisur, W. Qiu, J.J. He, S. Al-Saadi, R.K. Singh Raman, Degradation of graphene coated copper in simulated proton exchange membrane fuel cell environment: Electrochemical impedance spectroscopy study, J. Power Sources. 362 (2017) 366–372.

[21] Y.H. Lee, S.T. Noh, J.H. Lee, S.H. Chun, S.W. Cha, I. Chang, Durable graphene-coated bipolar plates for polymer electrolyte fuel cells, Int. J. Hydrog. Energy. 42 (2017) 27350–27353.

[22] S. Joseph, J.C. McClure, R. Chianelli, P. Pich, P.J. Sebastian, Conducting polymer-coated stainless steel bipolar plates for proton exchange membrane fuel cells (PEMFC), Int. J. Hydrog. Energy. 30 (2005) 1339–1344.

[23] M.A. Lucio Garcia, M.A. Smit, Study of electrodeposited polypyrrole coatings for the corrosion protection of stainless steel bipolar plates for the PEM fuel cell, J. Power Sources. 158 (2006) 397–402.

[24] Y. Fu, M. Hou, H. Xu, Z. Hou, P. Ming, Z. Shao, B. Yi, Ag–polytetrafluoroethylene composite coating on stainless steel as bipolar plate of proton exchange membrane fuel cell, J. Power Sources. 182 (2008) 580–584.

[25] Y. Sone, H. Kishida, M. Kobayashi, T. Watanabe, A study of carbon deposition on fuel cell power plants - morphology of deposited carbon and catalytic metal in carbon deposition reactions on stainless steel, J. Power Sources. 86 (2000) 334–339.

[26] T. Fukutsuka, T. Yamaguchi, S.I. Miyano, Y. Matsuo, Y. Sugie, Z. Ogumi, Carbon-coated stainless steel as PEFC bipolar plate material, J. Power Sources. 174 (2007) 199–205.

[27] Y. Matsuo, S.I. Miyano, Y. Sugie, T. Fukutsuka, Factors affecting the formation of carbon film on the stainless steels for the bipolar plate of polymer electrolyte fuel cells, J. Fuel Cell Sci. Technol. 8 (2011) 031008.

[28] Y. Show, Electrically conductive amorphous carbon coating on metal bipolar plates for PEFC, Surf. Coat. Technol. 202 (2007) 1252–1255.

[29] Y. Show, M. Miki, T. Nakamura, Increased in output power from fuel cell used metal bipolar plate coated with a-C film, Diam. Relat. Mater. 16 (2007) 1159–1161.

[30] C.Y. Chung, S.K. Chen, P.J. Chiu, M.H. Chang, T.T. Hung, T.H. Ko, Carbon film-coated 304 stainless steel as PEMFC bipolar plate, J. Power Sources. 176 (2008) 276–281.

[31] C.Y. Chung, S.K. Chen, T.S. Chin, T.H. Ko, S.W. Lin, W.M. Chang, S.N. Hsiao, Catalyst layer-free carbon-coated steel - An easy route to bipolar plates of polymer electrolyte membrane fuel cells: Characterization on structure and electrochemistry, J. Power Sources. 186 (2009) 393–398.

[32] K. Feng, Y. Shen, H. Sun, D. Liu, Q. An, X. Cai, P.K. Chu, Conductive amorphous carbon-coated 316L stainless steel as bipolar plates in polymer electrolyte membrane fuel cells, Int. J. Hydrog. Energy. 34 (2009) 6771–6777.

[33] K. Feng, X. Cai, H. Sun, Z. Li, P.K. Chu, Carbon coated stainless steel bipolar plates in polymer electrolyte membrane fuel cells, Diam. Relat. Mater. 19 (2010) 1354–1361.

[34] W. Jin, K. Feng, Z. Li, X. Cai, L. Yu, D. Zhou, P.K. Chu, Properties of carbon film deposited on stainless steel by close field unbalanced magnetron sputter ion plating, Thin Solid Films. 531 (2013) 320–327.

[35] Y. Mori, M. Ueda, M. Hashimoto, Y. Aoi, S. Tanase, T. Sakai, Amorphous carbon coated stainless separator for PEFCs, Surf. Coat. Technol. 202 (2008) 4094–4101.

[36] Y. Fu, G. Lin, M. Hou, B. Wu, Z. Shao, B. Yi, Carbon-based films coated 316L stainless steel as bipolar plate for proton exchange membrane fuel cells, Int. J. Hydrog. Energy. 34 (2009) 405–409.

[37] Y. Wang, J. Pu, J. Wang, J. Li, J. Chen, Q. Xue, Interlayer design for the graphite-like carbon film with high load-bearing capacity under sliding-friction condition in water, Appl. Surf. Sci. 311 (2014) 816–824.

[38] W. Mingge, L. Congda, H. Tao, C. Guohai, W. Donghui, Z. Haifeng, Z. Dong, W. Aiying, Chromium interlayer amorphous carbon film for 304 stainless steel bipolar plate of proton exchange membrane fuel cell, Surf. Coat. Technol. 307 (2016) 374–381.

[39] F. Bi, L. Peng, P. Yi, X. Lai, Multilayered Zr-C/a-C film on stainless steel 316L as bipolar plates for proton exchange membrane fuel cells, J. Power Sources. 314 (2016) 58–65.

[40] Y.S. Li, Y. Tang, Q. Yang, C. Xiao, A. Hirose, Growth and adhesion failure of diamond thin films deposited on stainless steel with ultra-thin dual metal interlayers, Appl. Surf. Sci. 256 (2010) 7653–7657.

[41] W.L. Wang, S.M. He, C.H. Lan, Protective graphite coating on metallic bipolar plates for PEMFC applications, Electrochimica Acta. 62 (2012) 30–35.

[42] S.H. Lee, S.P. Woo, N. Kakati, Y.N. Lee, Y.S. Yoon, Corrosion and electrical properties of carbon/ceramic multilayer coated on stainless steel bipolar plates, Surf. Coat. Technol. 303 (2016) 162–169.

[43] B. Wu, G. Lin, Y. Fu, M. Hou, B. Yi, Chromium-containing carbon film on stainless steel as bipolar plates for proton exchange membrane fuel cells, Int. J. Hydrog. Energy. 35 (2010) 13255–13261.

[44] H.C. Wang, K.H. Hou, C.E. Lu, M.D. Ger, The study of electroplating trivalent CrC alloy coatings with different current densities on stainless steel 304 as bipolar plate of proton exchange membrane fuel cells, Thin Solid Films. 570 (2014) 209–214.

[45] H.C. Wang, H.H. Sheu, C.E. Lu, K.H. Hou, M.D. Ger, Preparation of corrosion-resistant and conductive trivalent Cr–C coatings on 304 stainless steel for use as bipolar

plates in proton exchange membrane fuel cells by electrodeposition, J. Power Sources. 293 (2015) 475–483.

[46] Z. Wang, K. Feng, Z. Li, F. Lu, J. Huang, Y. Wu, P.K. Chu, Self-passivating carbon film as bipolar plate protective coating in polymer electrolyte membrane fuel cell, Int. J. Hydrog. Energy. 41 (2016) 5783–5792.

[47] T. Wang, J. He, J. Zhou, Y. Guo, X. Ding, S. Wu, J. Zhao, J. Tang, Fabrication of continuous mesoporous organic–inorganic nanocomposite films for corrosion protection of stainless steel in PEM fuel cells, Corros. Sci. 53 (2011) 1498–1504.

[48] H. Husby, O.E. Kongstein, A. Oedegaard, F. Seland, Carbon-polymer composite coatings for PEM fuel cell bipolar plates, Int. J. Hydrog. Energy. 39 (2014) 951–957.

[49] D.A. Doshi, P.B. Shah, S. Singh, E.D. Branson, A.P. Malanoski, E.B. Watkins, J. Majewski, F. van Swol, C.F. Brinker, Investigating the interface of superhydrophobic surfaces in contact with water, Langmuir. 21 (2005) 7805–7811.

[50] P.M. Barkhudarov, P.B. Shah, E.B. Watkins, D.A. Doshi, C.F. Brinker, J. Majewski, Corrosion inhibition using superhydrophobic films, Corros. Sci. 50 (2007) 897–902.

[51] S.V. Gnedenkov, S.L. Sinebryukhov, V.S. Egorkin, D.V. Mashtalyar, A.M. Emelyanenko, L.B. Boinovich, Electrochemical properties of the superhydrophobic coatings on metals and alloys, J. Taiwan Inst. Chem. Eng. 45 (2014) 3075–3080.

[52] R.B. Figueira, C.J. Silva, E.V. Pereira, Organic-inorganic hybrid sol-gel coatings for metal corrosion protection: a review of recent progress, J. Coat. Technol. Res. 12 (2015) 1–35.

[53] K. Tüber, D. Pócza, C. Hebling, Visualization of water buildup in the cathode of a transparent PEM fuel cell, J. Power Sources. 124 (2003) 403–414.

[54] M. Venkatraman, S. Shimpalee, J.W. Van Zee, S.I. Moon, C.W. Extrand, Estimates of pressure gradients in PEMFC gas channels due to blockage by static liquid drops, Int. J. Hydrog. Energy. 34 (2009) 5522–5528.

[55] J.P. Owejan, T.A. Trabold, D.L. Jacobson, M. Arif, S.G. Kandlikar, Effects of flow field and diffusion layer properties on water accumulation in a PEM fuel cell, Int. J. Hydrog. Energy. 32 (2007) 4489–4502.

[56] A. Turhan, S. Kim, M. Hatzell, M.M. Mench, Impact of channel wall hydrophobicity on through-plane water distribution and flooding behavior in a polymer electrolyte fuel cell, Electrochimica Acta. 55 (2010) 2734–2745.

[57] W. Zhu, Z.W. Dunbar, R.I. Masel, MicroCT X-ray imaging of water movement in a PEM fuel cell, ECS Trans. 16 (2008) 995–1000.

[58] A. Bazylak, J. Heinrich, N. Djilali, D. Sinton, Liquid water transport between graphite paper and a solid surface, J. Power Sources. 185 (2008) 1147–1153.

[59] X. Liu, T.A. Trabold, Non-active area water mitigation in PEM fuel cells via bipolar plate surface energy modification, Int. J. Hydrog. Energy. 43 (2018) 908–920.

[60] C.M.A. Brett, A.M. Oliveira Brett, Electrochemistry: Principles, Methods, Applications. Oxford Science Publications, 1993.

[61] H. Kahlert, Reference electrodes, in: Electroanalytical Methods: Guide to Experiments and Applications. Springer-Verlag, 2010: pp. 291–308.

[62] A.J. Bard, L.R. Faulkner, Electrochemical Methods. Fundamentals and Applications. Wiley, 2000.

[63] D.A.C. Brownson, C.E. Banks, Interpreting Electrochemistry, in: The Handbook of Graphene Electrochemistry. Springer London, 2014: pp. 23–77.

[64] J. Genesca, J. Mendoza, R. Duran, E. Garcia, Conventional DC electrochemical techniques in corrosion testing, Proc. 15th Int. Corros. Congr. Granada, 2002: pp. 122–139.

[65] M. Stern, A.L. Geary, Electrochemical polarization: A theoretical analysis of the shape of polarization curves, J. Electrochem. Soc. 104 (1957) 56–63.

[66] U. Angst, M. Büchler, On the applicability of the Stern–Geary relationship to determine instantaneous corrosion rates in macro-cell corrosion, Mater. Corros. 66 (2015) 1017–1028.

[67] M. Stern, A method for determining corrosion rates from linear polarization data, Corrosion. 14 (1958) 440–444.

[68] J. Wang, Analytical Electrochemistry. Wiley-VCH, 2006.

[69] R. Von Wandruszka, S.W. Orchard, A. Greeff, Corrosion measurements by potential-step chronoamperometry, Talanta. 32 (1985) 307–311.

[70] A. Orsi, O.E. Kongstein, P.J. Hamilton, A. Oedegard, I.H. Svenu, K. Cooke, An investigation of the typical corrosion parameters used to test polymer electrolyte fuel cell bipolar plate coatings, with titanium nitride coated stainless steel as a case study, J. Power Sources. 285 (2015) 530–537.

[71] F.J. Higuera, Structure of deposits formed from electrosprayed aggregates of nanoparticles, J. Aerosol Sci. 118 (2018) 45–58.

[72] W. Wen, K. Lu, Electric-field-induced diffusion-limited aggregation, Phys. Rev. E. 55 (1997) 2100–2013.

[73] J. Jia, J. Fan, B. Xu, H. Dong, Microstructure and properties of the super-hydrophobic films fabricated on magnesium alloys, J. Alloys Compd. 554 (2013) 142–146.

[74] W. Wang, S. Liu, S. Wei, Y. Liu, J. Lian, Q. Jiang, Robust superhydrophobic surface on Al substrate with durability, corrosion resistance and ice-phobicity, Sci. Rep. 6 (2016) 20933.

[75] E. Frackowiak, F. Béguin, Carbon materials for the electrochemical storage of energy in capacitors, Carbon. 39 (2001) 937–950.

[76] H.A. Andreas, B.E. Conway, Examination of the double-layer capacitance of an high specific-area C-cloth electrode as titrated from acidic to alkaline pHs, Electrochimica Acta. 51 (2006) 6510–6520.

[77] N.J. Cira, A. Benusiglio, M. Prakash, Vapour-mediated sensing and motility in two-component droplets, Nature. 519 (2015) 446–450.

[78] A.M. Chaparro, P. Ferreira-Aparicio, M.A. Folgado, E. Brightman, G. Hinds, Study of superhydrophobic electrosprayed catalyst layers using a localized reference electrode technique, J. Power Sources. 325 (2016) 609–619.

[79] P. Ferreira-Aparicio, A.M. Chaparro, M.A. Folgado, J.J. Conde, E. Brightman, G. Hinds, Degradation study by start-up/shut-down cycling of superhydrophobic electrosprayed catalyst layers using a localized reference electrode technique, ACS Appl. Mater. Interfaces. 9 (2017) 10626–10636.

[80] DOE Technical Targets for Polymer Electrolyte Membrane Fuel Cell Components. Office of Energy Efficiency & Renewable Energy, U.S. Department of Energy. https://energy.gov/eere/fuelcells/doe-technical-targets-polymer-electrolyte-membrane-fuel-cell-components (Accessed January 2019).

CHAPTER 5
General conclusions

The results compiled in the thesis advance in the state-of-the-art knowledge of electrosprayed carbon-based layers for fuel cell applications. The carbon black-Nafion electrosprayed layers showed improved interaction of Nafion with the carbon black surface, improved mass-transport and water management as catalyst layer and the ability to protect metal substrates in acidic environments. A detailed explanation of the results is given below.

The analysis of carbon black-Nafion composites studied in the first chapter reveals a strong and stable interaction between the sulfonic groups of the Nafion and the carbon black surface. This interaction is attributed to the fast desolvation of the adsorbed ionomer during the electrospray ionization process, favoring a better coverage of the carbon surface, most likely due to sulfonic group anchoring to the carbon black surface that leaves fluorocarbon backbones oriented towards the outer part of the carbon aggregates. The preferred backbone orientation to the outer part of the void space between the aggregates is presumably the origin of the superhydrophobicity of electrosprayed layers.

The study of the of electrosprayed layers of platinum supported carbon black as fuel cell catalysts on the second chapter confirms the ability of electrosprayed layers to achieve a better distribution of the ionomer on the catalyst layer aggregates when the ionomer concentration is optimal by using STEM and TEM microscopies. The study of the mass-transport properties proved that electrosprayed layers limit the mass performance losses of low-loaded catalyst layers. The enhanced water-vapor uptake of electrosprayed layers combined with their very low wettability and superhydrophobic character, allow for an

optimal catalyst layer with low mass transport resistance and high ionic conductivity. Additionally, the use of cathodic electrosprayed layers showed an enhancement of the back diffusion of water from the cathode to the anode, giving rise to operation under lower saturation conditions and lower water permeability, which resulted in enhanced power density and stability of the PEM fuel cell.

The study of the influence of the thickness of a hydrophobic catalyst layer on water transport was studied by using blended catalyst layers with catalyst and the bare carbon black support. Although carbon dilution of catalyst was proven to be useful to control the water distribution of the cells, the performance losses associated for a significant impact in water management does not seem as an attractive option for fuel cell operation. However, the sequential deposition of the catalyst and the bare carbon increase the water recollection in the cathode with minimal performance losses, reversing the effect attained with electroprayed catalyst layers. These results show the way for an effective and passive control of water inside fuel cells, allowing to push water to the anodic or the cathodic side depending on the final application and/or requirements of the cell.

Following the objective of broadening the applications of carbon-based composite layers deposited by electrospray, the carbon black-Nafion layers were studied as corrosion coatings for metallic substrates. *Ex-situ* electrochemical characterization experiments in aqueous acid media show that the electrospray deposited carbon black composite is appropriate for protecting the surface of metal substrates at ambient temperature, attaining complete and stable protective behavior with moderate loadings. Additionally, preliminary experiments coating cathodic gas channel were performed, showing promising results for expelling liquid water when using humidified feed gases. Electrosprayed carbon layers are promisng candidates as coatings for metallic flow-field plates due to their superhydrophobicity, which confers a good corrosion protection and the probably the ability of a better water conduction through the gas channels of the plates.

APPENDIX A

List of figures

APPENDIX B

List of tables

APPENDIX C

List of symbols and abbreviations

ATR	Attenuated total reflectance
CL	Catalyst layer
CPE	Constant phase element
CV	Cyclic voltammetry
CVD	Chemical vapor deposition
DVS	Dynamic vapor sorption
ECSA	Electrochemically active surface area
EDS	Energy-dispersive X-ray spectroscopy
EGA	Evolved gas analysis
EHD	Electrohydrodynamic
EMF	Electromotive force
ESCA	Electron spectroscopy for chemical analysis
ESI	Electrospray ionization
FTIR	Fourier-transform infrared spectroscopy
GDL	Gas diffusion layer
IR	Infrared
LSV	Linear sweep voltammetry
MEA	Membrane-electrode assembly
MID	Multiple ion detection
MPL	Microporous layer
MS	Mass spectrometry
ORR	Oxygen reduction reaction
PEM(FC)	Proton exchange membrane (fuel cell)
PFSA	Perfluorosulfonic acid
Pt/CB	Platinum supported on carbon black

PTFE	Polytetrafluoroethylene
RH	Relative humidity
SEM	Scanning electron microscope
STEM	Scanning transmission electron microscope
TEM	Transmission electron microscope
TG(A)	Thermogravimetric (analysis)
UPD	Underpotential deposition
WCA	Water contact angle
XPS	X-ray photoelectron spectroscopy

A	Electrode area
A_C	Carbon mass specific area
b	Tafel slope
b_a	Anodic Tafel coefficient
b_c	Cathodic Tafel coefficient
C	Concentration of electroactive species
C_{CL}	Electrical capacitance of the catalyst layer
C_d	Double layer capacitance
C_{DL}	Double layer specific capacitance
C_O	Concentration of oxidized species
C_R	Concentration of reduced species
D	Diffusion coefficient
D_{CL}	Diffusion coefficient through the pores of a catalyst layer
E	Cell potential
E_0	Amplitude of voltage signal
E_{cell} / E'	Reversible cell potential
E_{corr}	Corrosion potential
EW	Equivalent weight
F	Faraday constant
f	Area fraction of a liquid-solid interface
f_1 / f_2	Surface area fractions

G	Gibbs free energy
$h\nu$	Energy of photons
I	Cell current
i	Imaginary unit
I_0	Amplitude of current response
I_{corr}	Corrosion current
I_{dl}	Double layer current
i_{lim}	Limiting current
j	Current density
j_0	Exchange current density
j_{corr}	Corrosion current density
j_{DL}	Double layer current density
j_{lim}	Limiting current density
L	Catalyst layer thickness
m_{H2O}	Mass of the water recovered in the exhaust
M_0	Sample dry weight
M_i^{dry}	Dry weight of the ionomer
M_w	Weight of absorbed water
$\bar{M}_w$	Molar weight of water
n	Number of exchanged electrons
n	Constant phase element exponent
Q_{min}	Minimum flow rate
Q_h	Electric charge of hydrogen adsorption/desorption
Q_R	Electric charge of a droplet
R	Radius of a droplet
R	Ideal gas constant
R_{ct}	Charge transfer resistance
R_{dc}	DC internal resistance
R_{hf}	High-frequency resistance (measured at 1 kHz)
R_{local}	Local resistance at catalyst layer active sites

R_{CL}^{D2}	Deuterium mass transport resistance
R_{CL}^{H2}	Hydrogen mass transport resistance
R_{CL}^{mt}	Mass transport resistance of the catalyst layer
R_{foil}^{mt}	Mass transport resistance of the copper foil aperture
R_{GDL}^{mt}	Mass transport resistance of the gas diffusion layer
R_{total}^{mt}	Total mass transport resistance
r_f	Roughness factor
R_p	Polarization resistance
R_Ω	Ohmic resistance
S	Fraction of solid in contact with a liquid
t	Time
T	Temperature
V	Cell voltage
W	Warburg element
W	Electrical power (density)
W_{max}	Maximum power (density)
w_C	Carbon loading
w_i	Water collection from anodic or cathodic exhausts
Y_{CL}	Constant phase element base
Z_0	Impedance modulus
Z_i	Imaginary part of the impedance
Z_r	Real part of the impedance
α	Transfer coefficient
γ	Surface tension
γ	Fraction of platinum surface in the surface of agglomerates
γ_{LV}	Interfacial free energy of liquid-gas interfaces
γ_{SL}	Interfacial free energy of the solid-liquid interfaces
γ_{SV}	Interfacial free energy of the solid-gas interfaces
ε_0	Permittivity of vacuum
η	Discreteness of Pt surface on catalyst agglomerates

η	Overpotential of the activation energy
η_{an}	Activation losses on the anode
η_{ca}	Activation losses on the cathode
η_{tx}	Activation losses due to mass transport
θ	Sinusoidal phase shift
θ	Water contact angle
θ_0	Contact angle on a flat surface
λ	Number of water molecules per sulfonic-acid group
ν	Cyclic voltammetry sweep rate
ρ	Density
τ	Tortuosity of the catalyst layer
ϕ	Porosity of the catalyst layer
ω	Radial frequency